University of Cincinnati

Date: 6/28/2024

I, Andrea Corpolongo, hereby submit this original work as part of the requirements for the degree of Doctor of Philosophy in Geology.

It is entitled:

Neoarchean Microfossils and Microbialites Inform the Search for Extraterrestrial Life in the Solar System

Student's name: **Andrea Corpolongo**

This work and its defense approved by:

Committee member: Annette Rowe, Ph.D.

Committee member: Susannah Porter, Ph.D.

Committee chair: Andrew Czaja, Ph.D.

Committee member: Carlton Brett, Ph.D.

Committee member: Joshua Miller, Ph.D.

48238

Neoarchean Microfossils and Microbialites Inform the Search for Extraterrestrial Life in the Solar System

A dissertation submitted to the Graduate College of the University of Cincinnati

in partial fulfillment of the requirements for the degree of

Doctor of Philosophy

in the Department of Geosciences

of the College of Arts and Sciences

by

Andrea Corpolongo

M.A., Philosophy (Science), University of Cincinnati, 2024

B.S., Plant Biology (Ecology, Evolution, and Systematics), Michigan State University, 2004

Dissertation Committee:

Dr. Andrew D. Czaja (Chair)

Dr. Carlton E. Brett

Dr. Joshua H. Miller

Dr. Annette R. Rowe

Dr. Susannah M. Porter

Dissertation Abstract

The Great Oxygenation Event is the period, between 2.3 and 2.4 billion years ago, when oxygen began to accumulate in Earth's atmosphere. It was arguably the most consequential change in the history of our planet and the life that inhabits it. Knowledge of the events that led to this change is of great scientific interest because it will help us understand how Earth became a planet that can support complex multicellular organisms, including humans, and determine what to look for when planning missions to seek evidence of life beyond Earth, such as NASA's current Mars 2020 mission. This dissertation presents studies of fossilized microorganisms (microfossils) and microbially-influenced carbonate (carbonate microbialites) that formed shortly before the Great Oxygenation Event. Three-dimensional reconstructions along with photomicrography reveal the morphologies and habits of the preserved microbial communities to provide a better understanding of the types of microorganisms that existed just before the Great Oxygenation Event. The results suggest that microorganisms may have evolved to take advantage of transient microoxic-sulfidic interfaces 200 million years before the Great Oxygenation Event. Petrographic examinations and Raman spectroscopy provide insight into the geological processes that led to the preservation of these microfossils and microbialites. Understanding the preservation and detection of life's signatures, or biosignatures, on Earth is both necessary to the study of life on Earth and foundational to planning missions to seek biosignatures elsewhere in the solar system. The results of this work include the first reported instance of early diagenetic silicification that occurred via silica spherule nucleation directly on organic matter in a deep-water environment. To support the interpretation of DUV Raman data collected on Mars, this dissertation presents a comparison of Raman data collected from terrestrial biogenic microbialites with a Mars 2020 analog DUV Raman and fluorescence spectrometer and a visible Raman spectrometer. The results of this work indicate that the positions of peaks in the

fingerprint region of calcite and dolomite DUV Raman spectra are approximately 10 wavenumbers lower than they are in visible Raman spectra, which suggests that data collected with visible Raman spectrometers cannot be relied on to interpret DUV Raman carbonate spectra. Finally, this dissertation presents an early interpretation of the first Raman mapping performed on the surface of another planetary body, which took place during the first science campaign of NASA's Mars 2020 mission. This data interpretation supports the claim that Jezero Crater, the site of the Mars 2020 mission, was once a habitable environment and is currently host to multiple mineral deposits with a high biosignature preservation potential. In addition, this work has provided a foundation for the interpretation of subsequent DUV Raman data collected during the Mars 2020 mission.

Acknowledgements

I am inexpressibly grateful to my husband and child, who uprooted their entire lives because I wanted to study the Great Oxygenation Event. I am nearly as grateful to my advisor, Dr. Andy Czaja, for inexplicably allowing me the opportunity to study the GOE, and so much more, as a member of his lab. Thank you, Andy, for your guidance, patience, and friendship over the last six years.

I also want to thank the many generous people who made the work presented in this dissertation possible. Thank you to my dissertation committee for forcing me to make sense. Thank you to Dr. Ashley Manning-Berg for being the best role model and commiserator I could ask for. Thank you to Dr. Nic Beukes, who sadly passed away last year, for pointing me in the right direction when I first went looking for Neoarchean samples. Thank you to the Albutt family for twice granting me access to their property to collect the samples featured in Chapter II. Thank you, Jove Kohl, for helping me figure out how best to collect serial image scans and how not to collect kerogen from fenestrate microbialites. Thank you, Abby George, for doing all the things! I never would have stopped second guessing myself if you had not made those rectilinear chert puzzles. Thank you to the Mars 2020 science team, and especially the SHERLOC team, for showing me around Jezero Crater and allowing me to contribute to the most awe-inspiring group project I have ever had the honor of taking part in.

Thank you to the funding sources that supported my work, which include the Paleontological Society, NASA, NSF, and GSA.

Finally, thank you, Maynard, for giving me an excuse to take breaks from dissertation writing and bask in the sunshine. (Maynard is a bearded dragon.)

Table of Contents

Chapter I: Introduction

Background and Significance

Interconnections between Precambrian paleontology and astrobiology

Human beings have long wondered how life originated on Earth and whether it exists elsewhere in the universe. The answers to these questions are formally pursued by scientists studying Precambrian paleontology and astrobiology, which are closely intertwined scientific pursuits (e.g., NASEM, 2018). Precambrian paleontologists work to understand how life arose and evolved over approximately 4 billion years of Earth's history, and astrobiologists work to determine whether similar events took place elsewhere in the universe. Although alien life may differ from Earth life in unexpected ways, astrobiologists agree that the search for it must be based upon a robust knowledge of life on Earth (e.g. Meadows et al., 2022; Neveu et al., 2024). This means not only knowledge of what Earth life is, but how it came to be, how it interacts with its environment, and what evidence of its existence it leaves behind. The work of Precambrian paleontologists, who are concerned with determining the conditions that allowed life to arise on Earth, understanding the transition from unicellular to multicellular life, and everything in between, is key to building that knowledge.

As astrobiology-focused space exploration continues, what is learned will, in turn, inform the work of Precambrian paleontologists. For instance, one of the goals of NASA's current Mars 2020 mission is to search for evidence of extinct microbial life in Jezero Crater, Mars (see Chapter IV). During Mars' late Noachian and early Hesperian periods, the 45 km diameter crater hosted an open-basin lake, which is now home to diverse sedimentary rocks that could hold preserved evidence of microbial life that may have once inhabited Jezero Crater (Farley et al.,

2020). Whether or not evidence of ancient life on Mars is found, the results will contribute to our understanding of the origin of life on Earth, which is thought to have occurred during roughly the same period that Jezero Crater was filled with water, and its evolution. If evidence of ancient microbial life is found, it will be an unprecedented opportunity to study life that may have originated separately from life on Earth, which could provide insight into the possible pathways that can result in life's origination. If no evidence of life is found, it will be an equally unprecedented opportunity to study samples from what was once a habitable environment that have never been touched by life, which could offer insight into both the specific circumstances that allowed life to emerge and thrive on Earth and the way that life on early Earth shaped its environment.

This dissertation exemplifies the interconnections between Precambrian paleontology and astrobiology. Chapters II and III discuss evidence of habitable paleoenvironments and ancient microorganisms in the Gamohaan Formation of the Campbellrand-Malmani carbonate platform (CMCP; Transvaal Supergroup, South Africa), a unit deposited during an important point in the coevolution of Earth and life, and Chapter IV discusses early steps in studying a potential habitable paleoenvironment on Mars.

Coevolution of Earth and life: The Great Oxygenation Event

The CMCP formed shortly before oxygen began to accumulate in Earth's atmosphere, which was a pivotal period in Earth's history called the Great Oxygenation Event (GOE; Beukes, 1987; see below). For at least the first 2 billion years of its existence, Earth's atmosphere did not contain significant quantities of oxygen (e.g., Lyons et al., 2014). There is debate as to exactly how low Archean atmospheric oxygen levels were, but it is generally agreed that average levels were at most 10^{-5} PAL, and likely much lower (Pavlov and Kasting, 2002). Atmospheric oxygen

did not rise above 10^{-5} PAL until the early Paleoproterozoic, between 2.4 and 2.3 Ga (Pavlov and Kasting, 2002; Farquhar et al., 2000; Farquhar and Wing, 2003; Bekker et al., 2004; Guo et al., 2009; Ono et al., 2009).

This change in the level of atmospheric oxygen is made evident in the rock record by the disappearance of mass-independently fractionated sulfur isotopes (S-MIF) (Farquhar et al, 2000; Pavlov and Kasting, 2002). The mass independent fractionation of sulfur occurs when UV radiation photolyzes volcanic sulfur dioxide, which produces both elemental sulfur and sulfite (Ono et al., 2003). In the absence of atmospheric oxygen, the elemental sulfur is ultimately incorporated into sulfides and the sulfite is ultimately incorporated into sulfates, which, when preserved in the rock record, preserves the S-MIF signal as well. However, when enough atmospheric oxygen is present, all the sulfur species are oxidized and thus homogenized in the atmosphere or water column and the photochemical S-MIF signal is not preserved (Farquhar and Wing, 2003). Modeling results indicate that the S-MIF signal is lost when atmospheric oxygen reaches 10^{-5} PAL (Pavlov and Kasting, 2002).

Although the GOE is referred to as an "event", the oxygenation of Earth's atmosphere was not instantaneous, even in geologic terms. Instead, according to several lines of evidence, oxygen-rich oases existed prior to the GOE (e.g., Anbar et al., 2007; Lalonde and Konhauser, 2015; Eickmann et al., 2018). There is extensive evidence for the presence of pre-GOE marine oxygen oases associated with the CMCP specifically (e.g., Kendall et al., 2010; Voegelin et al., 2010; Czaja et al., 2012; Ostrander et al., 2020). For example, analyses of trace metals and iron minerals indicate that dissolved oxygen was present at the base of the slope of the CMCP as early as 2.56 Ga (Kendell et al; 2010), molybdenum isotope compositions of CMCP carbonates and shales indicate that marine oxygen was present in the depositional environment at least 2.64

Ga (Voegelin et al., 2010) and repeatedly thereafter (Ostrander et al., 2020). Coupled iron and molybdenum isotope analyses of carbonates and shales indicate the presence of significant dissolved oxygen in the photic zone during the deposition of the CMCP (Czaja et al., 2012). Therefore, the CMCP is an ideal location to look for evidence of the microbial metabolic processes that existed as O_2 was becoming more available in marine environments.

Geologic Context for Chapters II and III

The Campbellrand-Malmani carbonate platform

The CMCP is a well-preserved, microbialite-rich, fossiliferous sequence representing intertidal to below wave base depositional environments that formed in the final 200 million years of the Archean eon (approximately 2.65 to 2.45 Ga; Beukes, 1987; Sumner, 1997b). It occurs across two basins of the Transvaal Supergroup and consists of the Campbellrand Subgroup (Fig. I-1A), which covers 80,000 km^2 of the western region of the Kaapvaal craton in the Griqualand West Basin, and the Malmani Subgroup, which covers 110,000 km^2 of the Transvaal Basin (Beukes, 1987). Chapters II and III of this dissertation are focused on samples from the Campbellrand Subgroup of the CMCP which is minimally altered, with structural disruptions limited to the Griquatown fault zone (Fig. I-1A; Beukes, 1987) and peak metamorphic temperatures of 110 °C to 170 °C, according to mineral phase relations of the overlaying Kuruman Banded Iron Formation (BIF) (Miyano and Beukes, 1984), and 102 °C to 178 °C (± 21 °C), according to the distribution of carbonate isotopologues preserved within its uppermost formation (Levitt et al., 2015). These peak temperatures are consistent with the preservation of organic matter and microfossils (see Chapters II and III).

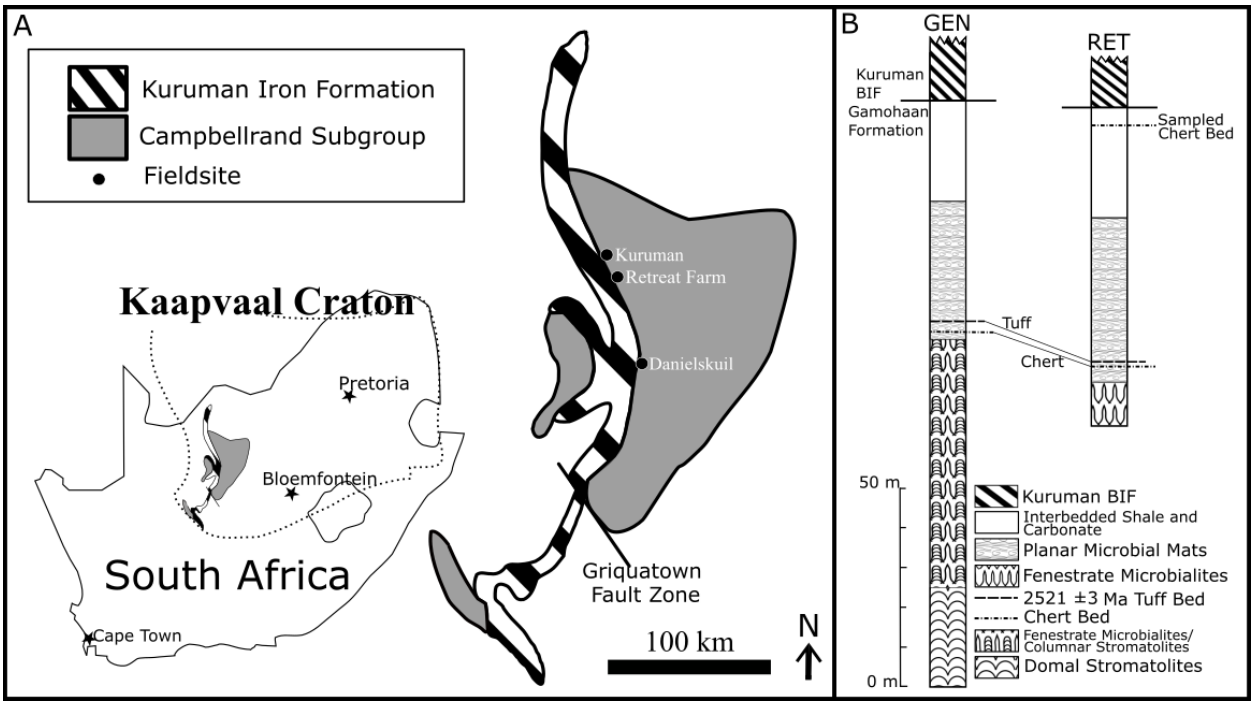

Figure I-1. (A) Simplified geological map showing and the location of the Campbellrand Subgroup on the Kaapvaal Craton in South Africa (left) and the three sampling localities discussed herein, which include a ranch called Retreat Farm (-27.521381°, 23.399681°; RET), Kuruman Kop (-27.382917°, 23.344233°; KUR) near the town of Kuruman, and a farm (-28.104117°, 23.57115°; DSK) near the town of Danielskuil (right). (B) Simplified stratigraphic columns showing a generalized stratigraphy of the Gamohaan Formation (left; labeled GEN) and correlative stratigraphy observed at Retreat Farm (right; labeled RET; see Chapter II). (Map and generalized stratigraphy adapted from Sumner, 1997b and Sumner and Beukes, 2006)

The Gamohaan Formation

The uppermost unit of the Campbellrand Subgroup of the CMCP, where I collected the samples presented here, is the Gamohaan Formation (Fig. I-1). The Gamohaan Formation is conformably overlain by the Kuruman Banded Iron Formation (Beukes, 1987), and its boundaries can be correlated across most of the preserved CMCP (Sumner and Beukes, 2006). It is composed of intertidal to below wavebase carbonate facies with frequent chert in the forms of beds, layers, and nodules (Beukes, 1987; Klein and Beukes, 1989; Beukes et al., 1990; Sumner, 1997a). The age of the Gamohaan Formation is well constrained. U–Pb isotope geochronology of a tuffaceous bed near the midpoint of the formation indicates an age of 2,521 ± 3 Ma (Fig. 1B;

Sumner & Bowring, 1996). U–Pb isotope geochronology of the lower boundary of the Kuruman banded iron formation (BIF), the Klein Naute Shale, indicates an age of 2,484.6 ± 0.34 Ma (Lantink et al., 2019). The depositional rate of the CMCP is thought to be fairly constant, (Sumner and Beukes, 2006). Therefore, the fact that half of the Gamohaan Formation, from the tuffaceous bed near its midpoint to the base of the overlying formation, spans 40 million years indicates that the total formation captures an approximately 80-million-year window of Earth's history.

As discussed above, this window falls at an especially interesting time in the co-evolution of Earth and life, just prior to the Great Oxygenation Event (GOE) and records important details about life's response to the oxygenation of our planet. Bulk and spatially resolved sulfur isotope measurements on pyrites preserved within the Gamohaan Formation record mass-independent fractionation (MIF) of atmospheric sulfur gasses, indicating that atmospheric oxygen levels during the formation's deposition were less than 10^{-5} times PAL (Kaufman et al., 2007; Kamber and Whitehouse, 2007; McLoughlin et al., 2023). However, spatially resolved sulfur isotope measurements indicate that microbial sulfur cycling took place under fluctuating seawater oxygen concentrations during the formation's deposition, even at sub wavebase depths (Kamber and Whitehouse, 2007; McLoughlin et al., 2023; See Chapters II and III for further discussion). Furthermore, isotopically heavy carbon in peritidal carbonates and organic matter (Eroglu et al., 2017) suggest the occurrence of oxygenic photosynthesis within the shallow photic zone during CMCP deposition, which supports the presence of an intermittently oxygenated water column during the deposition of the Gamohaan Formation. Taken together, this evidence indicates that the Gamohaan Formation was deposited as surface marine oxygen levels rose as a result of

oxygen-producing photosynthesis, but before they rose to levels high enough for significant oxygen to build up in the atmosphere.

Table I-1. Details of the major Gamohaan Formation facies.

Facies	Depositional Environment*
Domal Stromatolites with cm- to m-scale synoptic relief; Columnar stromatolites	Intertidal to shallow subtidal; indicated by erosional unconformities, rare channeling, low angle crossbedding
Fenestrate Microbialites	Deep subtidal, sub wavebase; indicated by lack of crossbedding, complex microbial morphology, first facies with continuous deposition across the CMCP indicates formation at the onset of platform drowning
Planar Microbial Mats	Sub wavebase; indicated by lack of crossbedding, continuity with slope facies, continuous deposition across CMCP
Interbedded Shale and Carbonate (Tsineng member)	Sub wavebase; indicated by lack of crossbedding, continuity with slope facies, continuous deposition across CMCP

*Sumner and Grotzinger, 2004; Sumner and Beukes, 2006

The Gamohaan Formation was deposited during a significant transgression, which led to the deposition of progressively deepening facies during the final drowning of the CMCP and ultimately resulted in the deposition of deepwater BIF (Fig. I-1B; Klein and Beukes, 1989; Sumner and Beukes, 2006; Beukes and Gutzmer, 2008). Details regarding the depositional environment of the Gamohaan Formation's major facies are summarized in Table I-1. The base of the Gamohaan Formation consists of centimeter to meter-scale domal stromatolites and columnar stromatolites that formed in intertidal to shallow subtidal depositional environments (Sumner and Beukes, 2006). This is overlain by the fenestrate microbialite facies, which is the first facies to exhibit continuous deposition across the entire CMCP, indicating that it formed at the onset of platform drowning (Sumner and Grotzinger, 2004; Sumner and Beukes, 2006). The planar microbial mat facies, which is interpreted to have formed in a deep sub wavebase environment due to the lack of crossbedding and the fact that it is continuous with planar deposits on the slope of the CMCP and into the basin, overlies the fenestrate microbialite facies

(Sumner and Grotzinger, 2004; Sumner and Beukes, 2006). The planar microbialite mat facies is overlain by interbedded shale and iron-rich carbonate.

The interbedded shale and iron-rich carbonate facies, referred to as the Tsineng member, represents the deepest depositional environment preserved within the formation (Klein and Beukes, 1989). It is thought to have formed at or below the oxic/anoxic interface and is considered a transition zone between the deep planar deposits and the overlying Kuruman BIF (Klein and Beukes, 1989; Beukes et al., 1990; Sumner and Beukes, 2006). The samples discussed herein were collected from chert beds within the interbedded shale and carbonate (Tsineng member) and fenestrate microbialite facies of the Gamohaan Formation, which are further discussed in Chapters II and III, respectively.

Chapter Summaries

In Chapter II, I use optical microscopy, petrographic analysis, Raman spectroscopy, and confocal laser scanning microscopy (CLSM) to investigate the origin and environmental context of microstructures preserved in laminated black chert collected from the Gamohaan Formation of the Campbellrand-Malmani Carbonate Platform (CMCP; Transvaal Supergroup, South Africa; see below). In Chapter III, I describe a paired geochemical and morphological study of morphologically complex microbialites collected from the same formation as the samples in Chapter II. This work was accomplished via optical microscopy, Raman spectroscopy, serial sectioning, and 3D rendering. The work presented in Chapters II and III offers insight into the coevolution of Earth and life and the preservation of life's signatures, or biosignatures. Understanding the preservation and detection of biosignatures on Earth is foundational to the planning of missions to seek biosignatures on other solar system bodies (e.g., NASEM, 2018). Chapter III also presents data collected from biogenic microbialites with a Mars 2020 analogue

instrument, which supports the interpretation of data collected on Mars. In Chapter IV, I present and offer an early interpretation of the first Raman mapping performed on the surface of another planetary body, NASA's Mars 2020 mission, which includes discussion of what those data indicate regarding the potential that habitable paleoenvironments existed in Jezero Crater.

Chapter II: Neoarchean microfossils provide evidence for pre-GOE microbial sulfur-cycling and a deep marine microoxic/euxinic interface

Introduction

Although challenging to interpret, paired morphological and geochemical study of Archean to Paleoproterozoic microfossils provides valuable insight into the early development of life on Earth and biosignature preservation that cannot be obtained through other means (e.g., Schopf et al., 2006; Lepot, 2020; Moore et al., 2023). Microfossils are most often preserved in carbonate, siliciclastic deposits, and chert, with early diagenetic chert being the most likely lithology to host well-preserved microbial body fossils (e.g., Schopf et al., 2006; Lepot, 2020; Moore et al., 2023). As of this writing, well-preserved, chert-hosted, Archean to Paleoproterozoic microfossils have been observed in samples collected from 13 different units located across Western Australia, South Africa, Central Africa, Canada, and China (e.g., Barghoorn and Tyler; 1965; Hofmann and Jackson, 1969; Knoll and Barghoorn, 1976; Knoll et al., 1978; Yun, 1984; Lanier, 1986; Bertrand-Sarfati and Potin, 1994; Sugitani et al., 2010; Sugitani et al., 2013; Schopf et al., 2015; Czaja et al., 2016; Barlow and Van Kranendonk, 2018; Barlow et al., 2024). Of those 13 units, the fossiliferous chert from all but three (Schopf et al., 2015; Czaja et al., 2016; Barlow and Van Kranendonk, 2018; Barlow et al., 2024) formed in intertidal or shallow subtidal depositional environments.

The work presented in this chapter combines petrographic study, Raman spectroscopy, and confocal laser scanning microscopy (CLSM) to assess the biogenicity, depositional environment, and preservation of purported microbial mats and microfossils observed in black chert collected from the Tsineng member of the Gamohaan Formation of the Neoarchean

Campbellrand-Malmani Carbonate Platform, (CMCP; Transvaal Supergroup, South Africa; Figs. I-1 and II-1). The Tsineng member, which is the uppermost unit of the Gamohaan Formation, formed in a deepwater depositional environment shortly before the Great Oxygenation Event (GOE), a pivotal time in the history of life on Earth, which makes it an especially compelling target in the study of Precambrian life (See Chapter I, Geologic Context). The results presented below are a significant addition to our knowledge of Neoarchean life and its preservation in deep marine environments.

Methods

Sample Collection

I collected the samples described in this chapter from a black chert bed within the Tsineng member of the Gamohaan Formation that outcrops at Retreat Farm (RET; -27.521381°, 23.399681°; Fig. I-1). The facies transgression at RET is consistent with that of the upper Gamohaan Formation (Fig. I-1B), the boundaries of which can be correlated across most of the preserved CMCP (Beukes, 1987; Sumner, 1997b; Sumner and Grotzinger, 2004; Sumner and Beukes, 2006). The base of the exposure consists of approximately 11 meters of fenestrate microbialites, which are overlain by an approximately 43-meter-thick facies dominated by planar microbial mats (Fig. I-1B). A microlaminated, fossiliferous black chert bed that is known to outcrop at the well-documented Gamohaan Formation exposures near the towns of Kuruman and Danielskuil is present five meters stratigraphically above the transition from fenestrate microbialites to planar microbial mats (Fig. I-1; Czaja et al., 2016). Approximately 1.5 meters stratigraphically above the chert bed is an outcrop of the 2,521 ± 3 Ma tuff bed that is known to

outcrop at many localities across the Gamohaan Formation (Fig. I-1B; Sumner and Bowring, 1996; Sumner, 1997b).

The planar microbialite mat facies is overlain by the Tsineng member, which is the uppermost member of the Gamohaan Formation (Fig. I-1B; Beukes, 1980). As stated in Chapter I, the Tsineng member is primarily composed of interbedded iron-rich carbonate and shale and is conformably overlain by the Kuruman Banded Iron Formation (BIF; Fig I-1B; Klein and Beukes, 1989). It was deposited in a sub-wavebase, aphotic environment during the final drowning of the CMCP as carbonate deposition shifted to banded iron formation deposition at or below the oxic/anoxic interface (Klein and Beukes, 1989; Beukes et al., 1990; Sumner and Beukes, 2006).

I observed outcrops of Kuruman BIF approximately 130 meters SSE of and 10 meters stratigraphically above the sampled outcrop, which demonstrates that the samples discussed here were collected in the upper portion of the Tsineng member of the Gamohaan Formation (Figs. I-1B and II-1). The sampled outcrop consisted of stratiform black to dark-gray chert with wavy, medium gray microlaminae visible in some regions (Fig. II-1B). It was located at the top of a hill and exposed parallel to the bedding plane (Fig. II-1A).

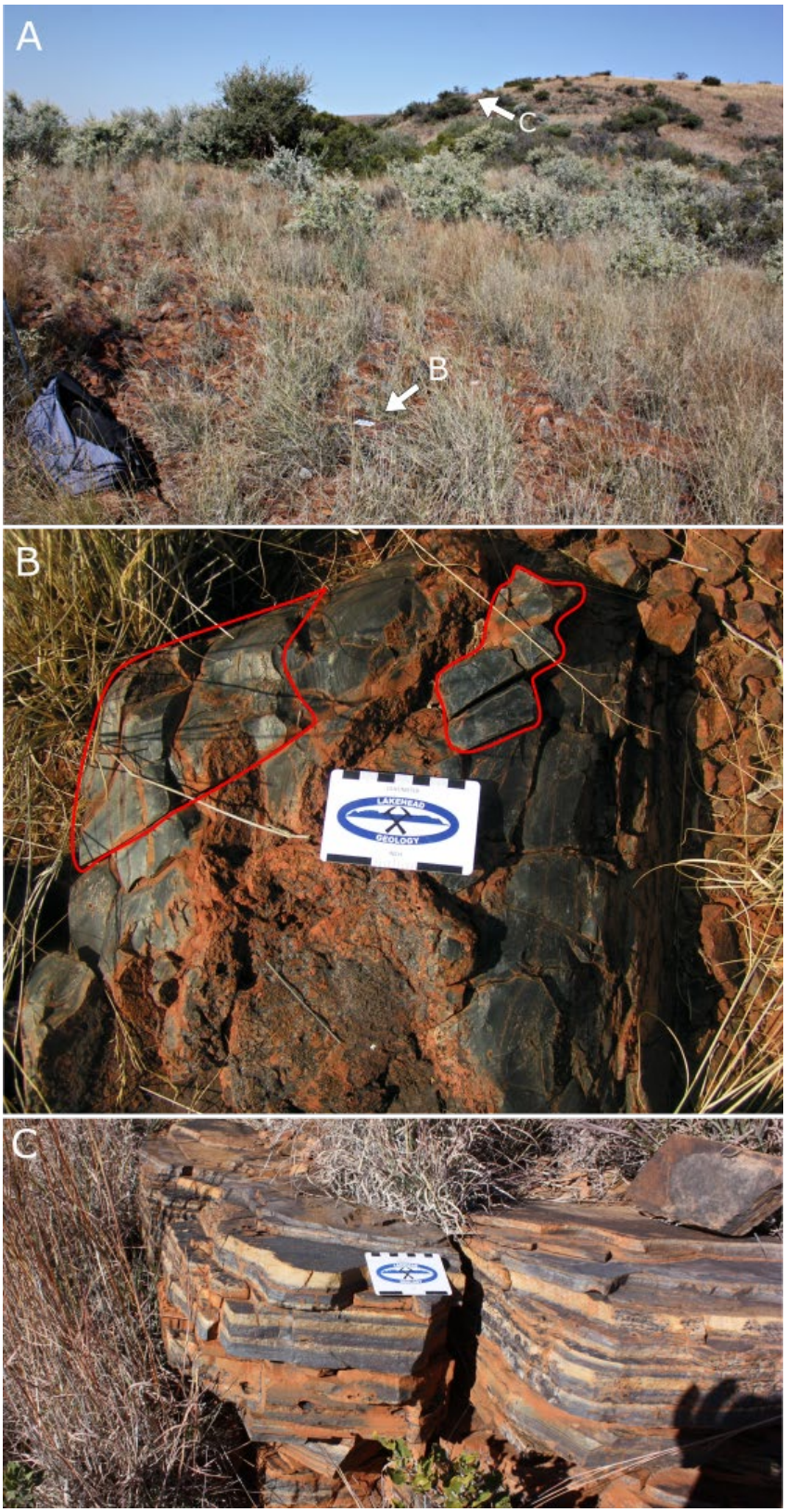

Figure II-1. The sampled outcrop and its context in the field. (A) The area surrounding the outcrop shown in panel B. The white arrow labeled B points to the sampled outcrop within a black chert bed that continues several meters

along strike. The white arrow labeled C indicates an outcrop of the Kuruman Banded Iron Formation (BIF). (B) The sampled outcrop that contained the microfossils described herein. The areas of the outcrop outlined in red are the portions that were collected. (C) An outcrop of Kuruman BIF. This image was taken at the area labeled C in panel A, approximately 130 meters SSE of and 10 meters stratigraphically above the sampled outcrop.

Sample Preparation

I prepared billets from hand samples using a water-cooled, diamond blade rock saw. From these billets, I prepared unpolished thin sections approximately 150 to 250 μm thick for optical microscopy, Raman spectroscopy, and confocal laser scanning microscopy. When optical microscopy of these "thick" thin sections revealed microstructures of interest, I created additional 30 μm thick polished thin sections for petrographic examination under cross-polarized light.

Petrographic Examination

I used an Olympus BX60 microscope, in its transmitted light configuration, to study the petrographic and "thick" thin sections coated with a thin layer of Olympus type F low-florescence immersion oil. I acquired images of thin section-embedded microfossils and other microfeatures with a microscope-mounted Olympus SC50 digital camera. I processed images using Olympus cellSens standard image processing software (version 3.17) and PhotoScape image editing software (version 3.7). For examination under cross-polarized light, I used the same microscope, camera, and software described above, with the addition of an Olympus U-AN analyzer slider and U-POT polarizer as well as a Zeiss quartz first order retardation plate to enhance contrast.

Raman Spectroscopy

I collected Raman spectra with a Horiba T64000 Raman microscope and 457.9 nm laser excitation from a Coherent FreD 90C Ar+ laser with a spot size of approximately 1 to 2 μm and a laser power at the sample of 9 mW. Spectra were collected using a 50X long working distance

objective (NA = 0.50), a 600 g/mm diffraction grating to provide a ~128–2900 cm^{-1} spectral window at a resolution of ~1.5 cm^{-1} between successive spectra points, and a Horiba Symphony II liquid nitrogen cooled (-133ºC) Charge Coupled Device detector. I used the open-source peak fitting software Fityk (version 1.3.1; Wojdyr, 2010) for baseline subtraction and peak fitting of spectra.

Confocal Laser Scanning Microscopy

I collected series of two-dimensional confocal laser scanning microscopic images (z-stacks) with an Olympus FV1000 microscope with a 70 µm confocal aperture, using a 488 nm laser and a 60X oil immersion objective with no filter to produce reflected light images rather than fluorescence images (cf. Czaja et al., 2016). This was necessary because the thin section embedded kerogen did not produce sufficient fluorescence for imaging with 458, 488, 514, 559, or 633 nm laser excitation. I processed the resulting z-stacks using ImageJ image analysis software (Fiji distribution; version 2.9.0/1.53t). I deconvolved the z-stacks with the ImageJ plugin DeconvolutionLab2, using the built-in Richardson-Lucy algorithm and an experimentally obtained point spread function (Sage et al., 2017).

Results

In thin section, RET samples display three dimensionally preserved wavy dark laminae with low inheritance, which are consistent with multiple Archean and Proterozoic features identified as microbial mats preserved in chert (see Grey and Awramik, 2020 for a review of microbialite identification and description; Fig. II-2). The laminae are filmy (i.e., continuous and ≤ 10 µm thick; Figs. II-3B to G and II-4A and B, black arrows) and frequently associated with microscopic siderite and pyrite grains, as identified via Raman spectroscopy (Fig. II-4). Some of the pyrite grains are associated with chert-filled “tails” or tubular microcavities (Fig. II-4).

Together, such pyrite grains and microcavities are commonly referred to as ambient inclusion trails (AIT; e.g., Tyler and Barghoorn, 1963; Knoll and Barghoorn, 1974; McLoughlin et al., 2010; Wacey et al., 2016). The laminae are separated by diffuse gray material and feature frequent fluid escape channels that run between and cut across laminae and often include relatively large voids (up to 1 cm along the longest dimension in cross section; Figs. II-2, blue, white, and red arrows, and II-3). The primary nature of the fluid escape channels is made evident by the stretching and tearing of filmy laminae at their boundaries (Fig. II-3), which could only occur if the channels formed prior to the lithification of the mats, while they remained pliable (Grey and Awramik, 2020). Secondary features, such as mineral veins, would result in sharp disruptions in the preserved layers (Grey and Awramik, 2020).

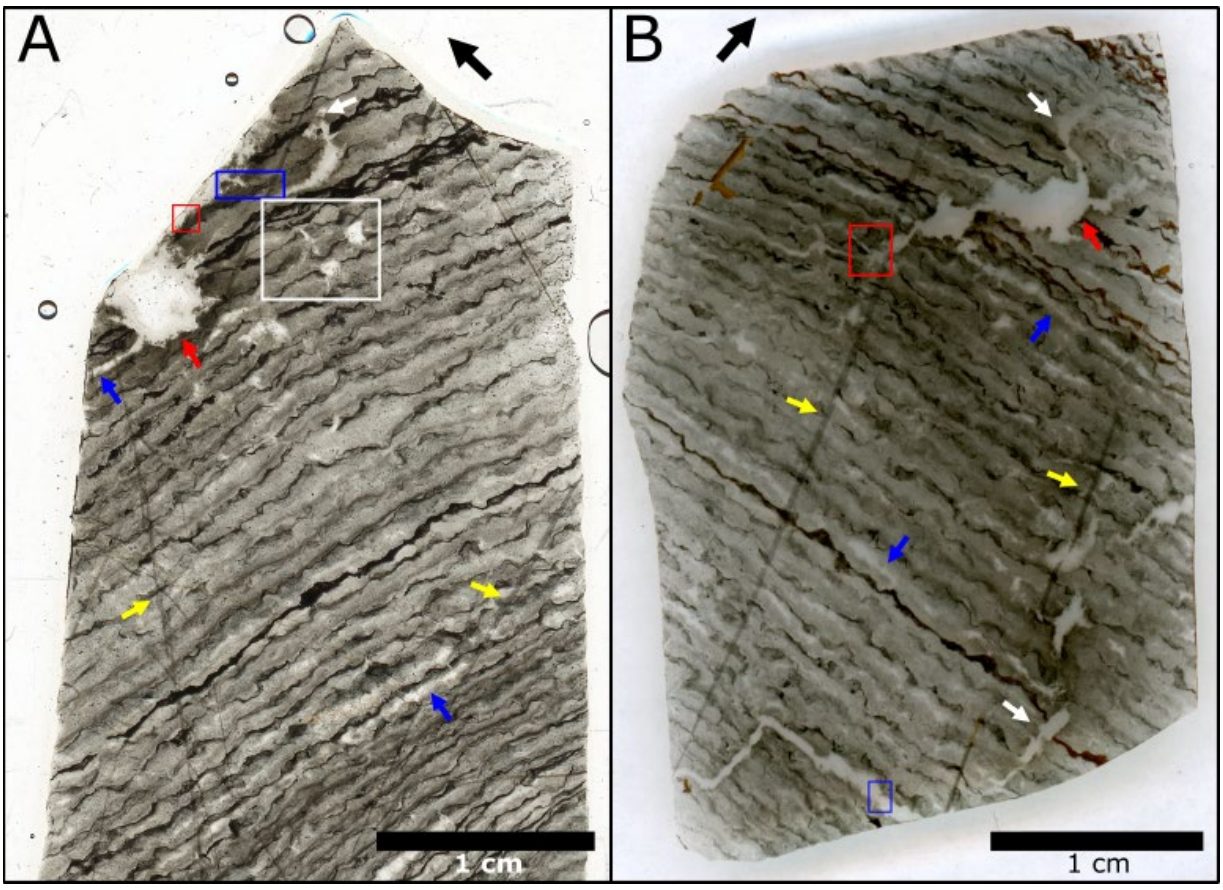

Figure II-2. Thick thin sections prepared from the RET sample, cut perpendicular to bedding. Black arrows indicate the stratigraphic up direction of the laminae. In both panels, blue arrows indicate examples of fluid escape channels that run between laminae. White arrows indicate examples of fluid escape channels that cut across laminae. Red arrows indicate large voids associated with fluid escape channels. Yellow arrows indicate secondary (post lithification) fractures running through the thin section. (A) Scan of a portion of a thick RET thin section showing wavy dark laminae with low inheritance and fluid escape channels. The white box indicates the area imaged in Figure II-3A. The red box indicates the area imaged in Figure II-5A. The blue box indicates the area imaged in Figure II-10A. (B) Scan of a thick RET thin section showing wavy dark laminae with low inheritance and fluid escape channels. The red box indicates the area imaged in Figure II-3F. The blue box indicates the area imaged in Figure II-6A.

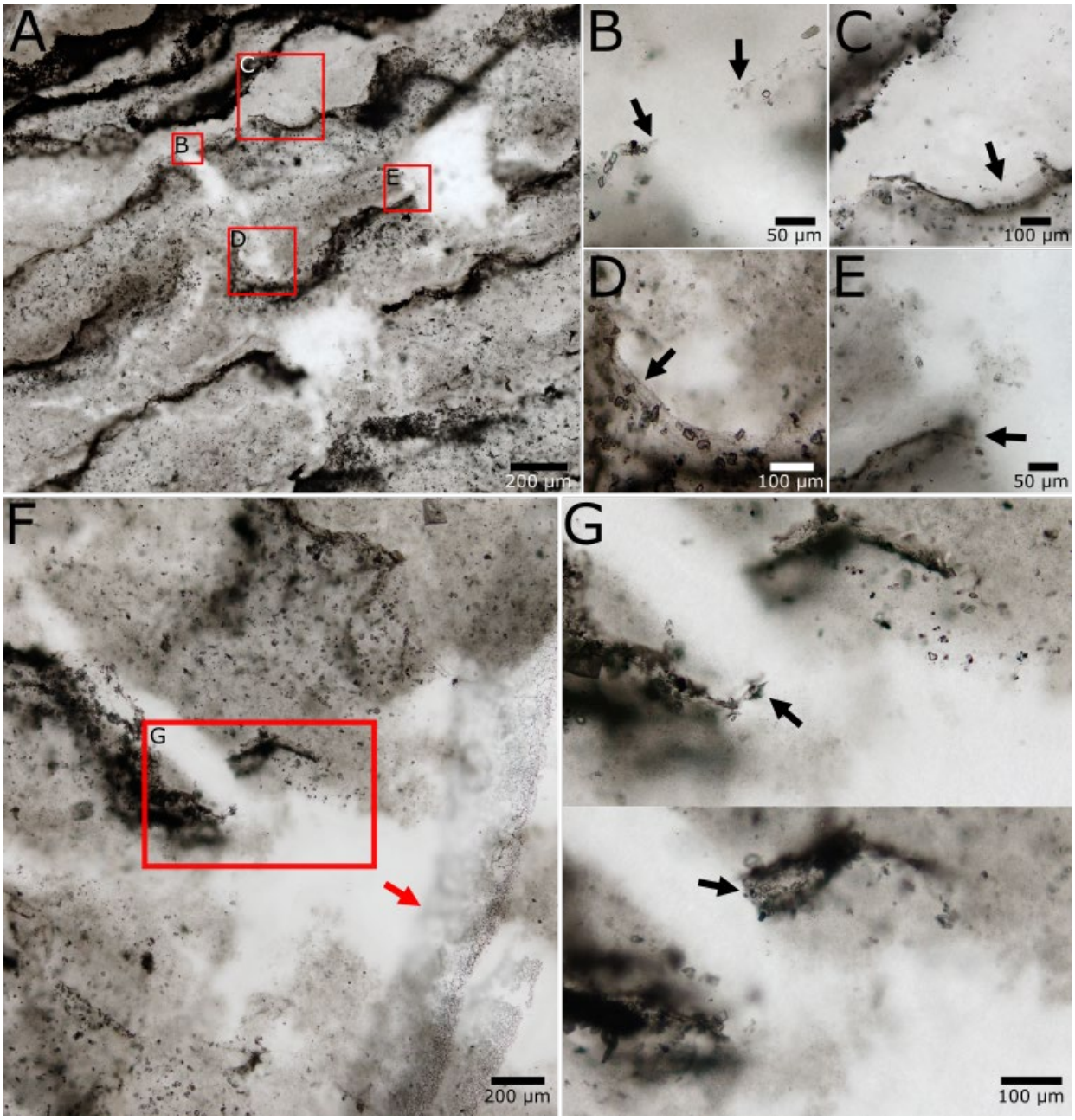

Figure II-3. Photomicrographs that illustrate the primary nature of the fluid escape channels. (A) Corresponds to the area within the white box in Figure II-2A. (B) Corresponds to the area within the red box labeled B in panel A of this figure. The black arrows indicate the edges of a filmy microbial mat that was torn by fluid flowing through a fluid escape channel. (C) Corresponds to the area within the red box labeled C in panel A. The black arrow indicates a section of microbial mat extended along the boundary of a fluid escape channel. (D) Corresponds to the area within the red box labeled D in panel A. The black arrow indicates a section of microbial mat extended along the boundary of a fluid escape channel. (E) Corresponds to the area within the red box labeled E in panel A. The black arrow indicates the torn edge of a microbial mat at the edge of a relatively large void that formed along a fluid escape channel. The gray material that occurs between the filmy microbial mats flows beyond the torn edge and into the void. (F)

Corresponds to the area within the red box in Figure II-2B. Red arrow indicates a secondary fracture within the sample. (G) Corresponds to the area within the red box in panel F (two different focal planes). The black arrows indicate the edges of a filmy microbial mat that was torn by fluid flowing through a fluid escape channel, which are visible at two different focal planes within the thin section. Below the torn microbial mat, some of the gray material that occurs between the mats throughout the sample is visible flowing across the fluid escape channel.

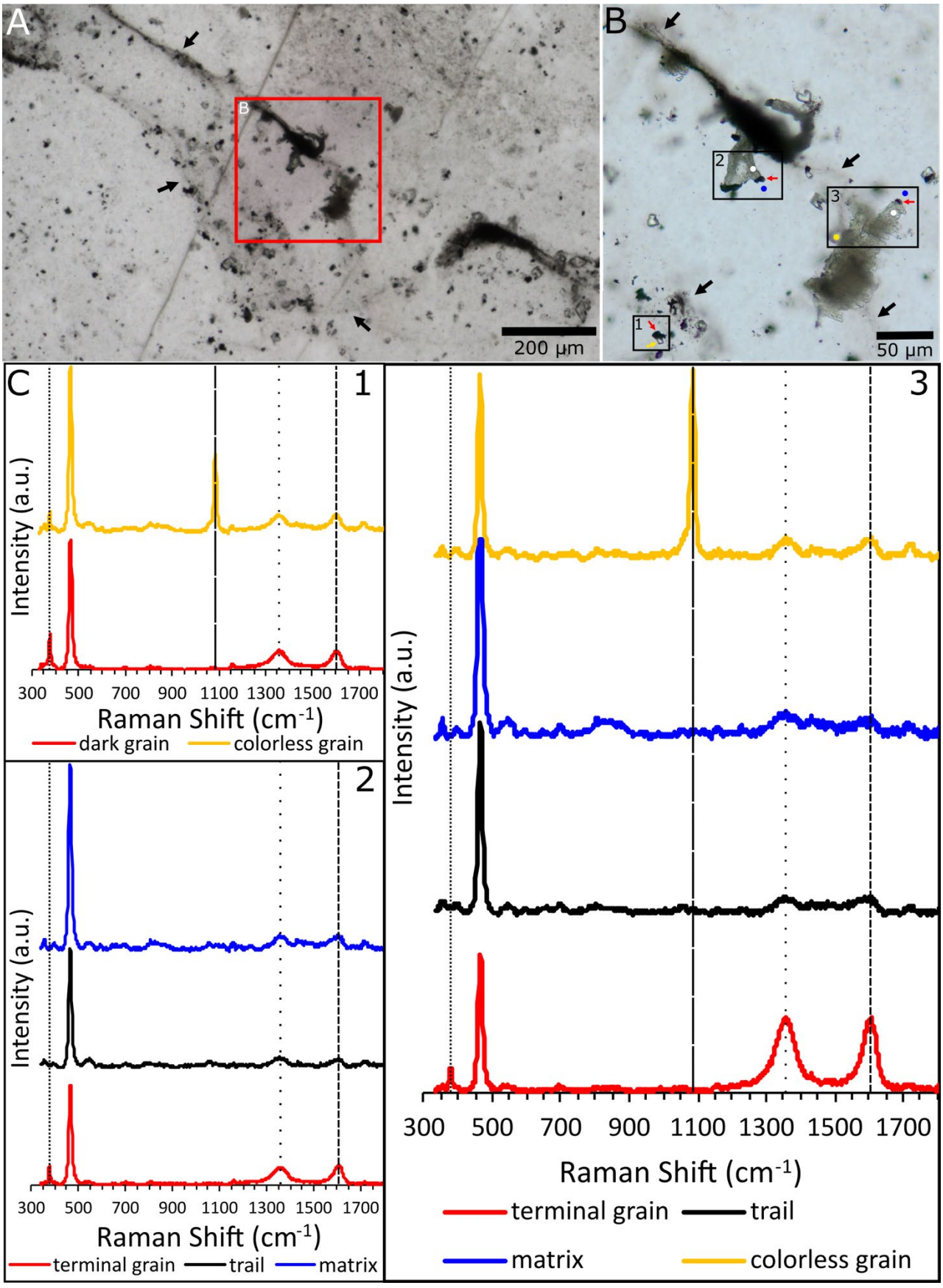
A
B
200 µm
B
2
3
1
50 µm
C
1
Intensity (a.u.)
300 500 700 900 1100 1300 1500 1700
Raman Shift (cm-1)
dark grain
colorless grain
2
Intensity (a.u.)
300 500 700 900 1100 1300 1500 1700
Raman Shift (cm-1)
terminal grain
trail
matrix
3
Intensity (a.u.)
300 500 700 900 1100 1300 1500 1700
Raman Shift (cm-1)
terminal grain
trail
matrix
colorless grain

Figure II-4. Photomicrographs and Raman spectra from a petrographic thin section prepared from the same hand sample as the thin section shown in Figure II-1A. (A) Black arrows point to the edges of a portion of filmy microbial mat, an example of the microbial mats that appear as wavy dark laminae in thin section. The red box indicates the region of the thin section pictured in panel B. (B) Black arrows point to filmy microbial mat. White, red, blue, and yellow arrows and dots within boxes 1, 2, and 3 indicate the spots at which the Raman spectra in panel C were collected. Dots show the exact laser spot. Arrows indicate the microscopic feature that was analyzed when a dot would obfuscate the feature. Box 1 encloses closely associated pyrite (dark, red arrow) and siderite (colorless, yellow arrow) grains that occur within microbial mat. Box 2 encloses a cluster of smooth-walled ambient inclusion trails (AITs) emanating from a relatively thick section of microbial mat. Box 3 encloses a portion of a rough-walled AIT associated with a filmy microbial mat. In boxes 2 and 3 red arrows indicate the terminal pyrite grains, white dots indicate the trail spots, and blue dots indicate the matrix spot at which I collected Raman spectra. The yellow dot indicates a siderite grain. (C) The spectra in panels C1, C2, and C3 correspond to their like-colored dots or arrows in boxes 1, 2, and 3 in panel B. Black spectra correspond to white dots. The closely spaced dotted lines in each spectrum fall at approximately 375 cm^{-1} and indicate the presence of pyrite. The intense peaks at approximately 465 cm^{-1} indicate that the matrix is composed of microcrystalline quartz. The long dash lines fall at approximately 1095 cm^{-1} and indicate the presence of siderite. The loosely spaced dotted lines fall at approximately 1360 cm^{-1} and indicate the kerogen D-band. The short dash lines fall at approximately 1600 cm^{-1} and indicate the kerogen G-band.

Microscopic examination of thick thin sections under transmitted light revealed the presence of locally abundant coccoid microfossils within the fluid escape channels and voids, concentrated along void and channel boundaries (Figs. II-5, II-6, II-7, II-9, II-10). The coccoid microfossils are between 8.9 and 18.8 μm in diameter (mean = 13.4 μm; sd = 1.6 μm; n = 94; Fig. II-7E). There are filament-like structures commonly preserved amongst and attached to the coccoid microfossils. They are <1 μm in diameter, have a wispy appearance, and occur in both tangled bundles that stretch up to approximately 350 μm between clusters of coccoid microfossils and individually attached to singular coccoid microfossils (Figs. II-6 and II-7A and B).

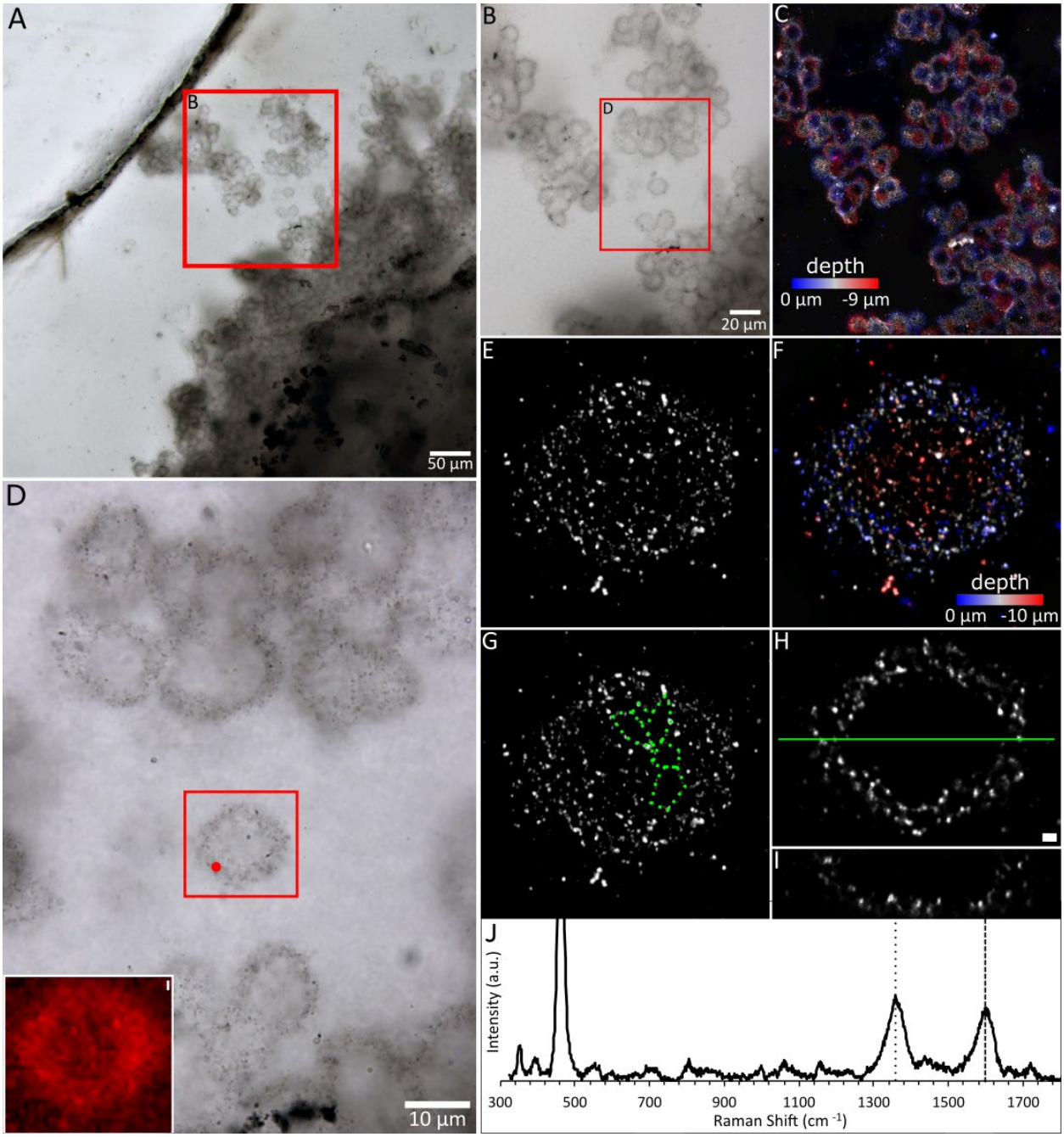

Figure II-5. Photomicrographs, CLSM scans, a Raman map, and a Raman spectrum that illustrate the three-dimensional preservation, reticulate texture, and kerogen composition of the coccoid microfossils. (A) A photomicrograph of the region within the red box in Figure IIA. (B) A higher-magnification photomicrograph of the region within the red box in panel A. (C) A z stack projection of a CLSM image of the clustered coccoid microfossils in the photomicrograph in panel B. (D) A higher-magnification photomicrograph of the region within the red box in panel B. The red dot indicates the point at which the Raman spectrum in panel J was collected. The image inset in the lower left corner of the panel is a Raman map of the coccoid microfossil within the red box. The brightest red areas of the map correspond to the most intense kerogen G-bands detected. The scale bar in the inset is

one micron. (E) The same z stack projection in panel F without a color depth scale. Note the reticulate texture in the center of the microfossil. (F) A CLSM z stack projection of the single coccoid microfossil within the red box in panel D, with depth indicated by the blue-gray-red color scale (bright red = 10 μm deeper into the thin section than the bright blue features). Note that the reticulate texture corresponds to the deep cell wall in the projection. (G) The same CLSM in panel E with some of the polygons that compose the reticulate cell wall texture highlighted in green. (H) The z stack layer at the widest point of the coccoid microfossil featured in panels E to G. The green line indicates the cross section featured in panel I. The scale bar is one micron and applies to panels E to I. (I) A cross section of the z stack projection featured in panels E to G that follows the green line in panel H. (J) The Raman spectrum collected at the point indicated by the red dot in panel D. The intense peak at approximately 465 cm^{-1} indicates that the matrix is composed of microcrystalline quartz. The dotted line falls at approximately 1360 cm^{-1} and indicates the kerogen D-band. The dashed line falls at approximately 1600 cm^{-1} and indicates the kerogen G-band.

Confocal laser scanning microscopy (CLSM) indicates that the microfossils are three-dimensionally preserved within the chert matrix (Figs. II-4C and F, II-5B, and II-6C). The walls of the coccoid microfossils are somewhat diffuse, which makes it difficult to discern their texture in photomicrographs. However, CLSM images of individual coccoids show that the walls have a reticulate texture (Fig. II-4E and G). Raman spectroscopy indicates that the coccoid microfossils are composed of kerogen embedded in a silica matrix (Figs. II-4 and II-5). Coccoid microfossils contain occasional intracellular inclusions. The dark intracellular inclusions observed in some of the coccoid microfossils are composed of kerogen, and the colorless inclusions, which occur more commonly than dark inclusions, are not associated with any compounds other than chert (Fig. II-7A, B, C, D, and F).

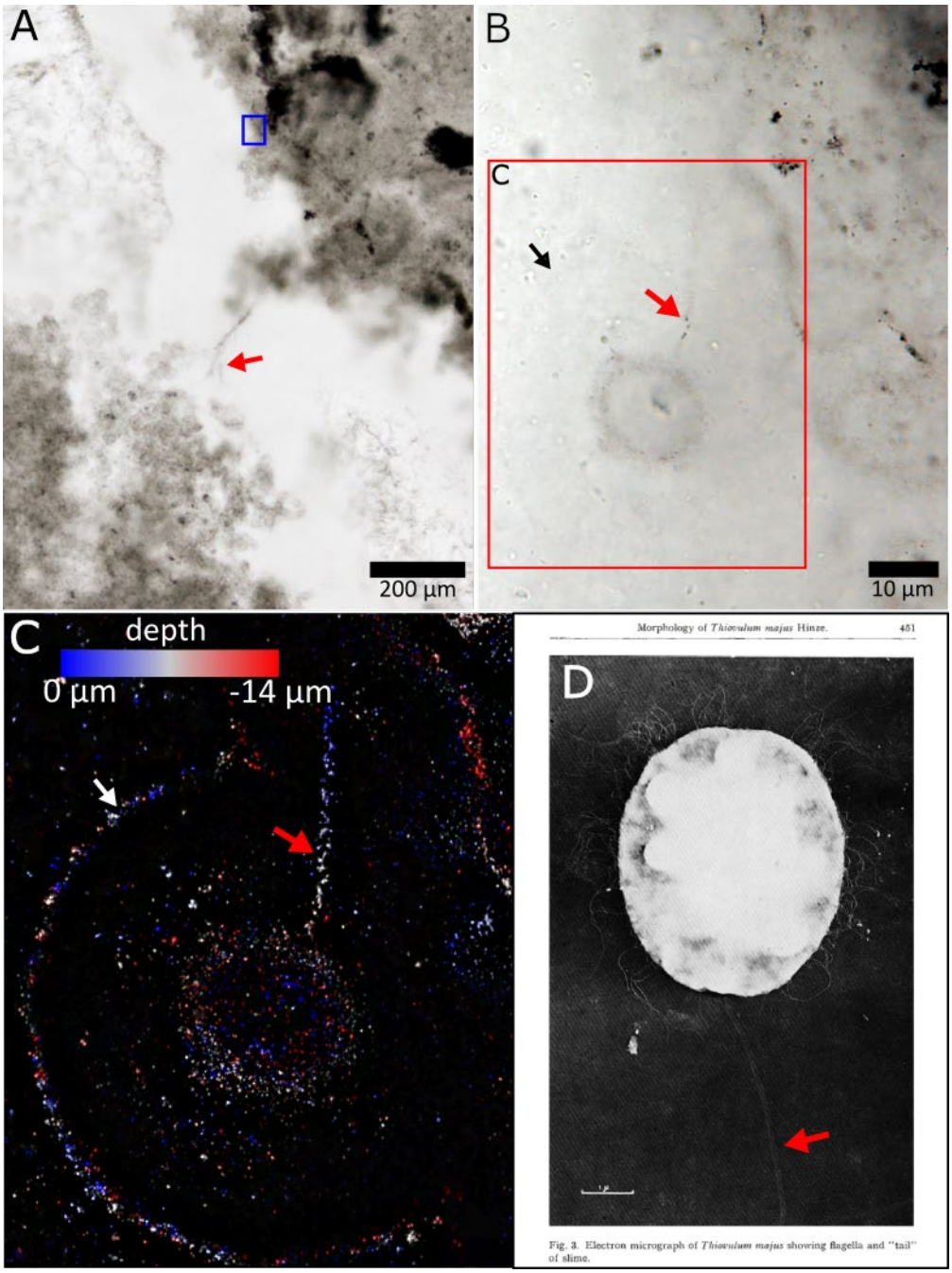

Figure II-6. Photomicrographs and a CLSM z stack projection that feature the wispy filament-like mucous stalks that occur in association with the coccoid microfossils. (A) A photomicrograph of the area within the blue box in Figure II-2B. The blue box indicates the area featured in panel B. The red arrow indicates a bundle of tangled mucous stalks that stretches across a fluid escape channel. (B) A photomicrograph of the area within the blue box in panel A that features a stalked coccoid microfossil. The red arrow points to the mucous stalk. The black arrow indicates a layer within the fibrous chalcedony that lines the fluid escape channel that is only faintly visible in the photomicrograph but highly visible in the CLSM z stack projection in panel C. (C) A CLSM z stack projection of the area within the red box in panel B. Depth is indicated by the blue-gray-red color scale. (Bright red = 14 µm deeper

into the thin section than the bright blue features.) The white arrow indicates the layer within the fibrous chalcedony at the black arrow in panel B. The red arrow indicates the mucous stalk. (D) An electron micrograph of a *Thiovulum majus* cell and its associated mucous stalk (red arrow; De Boer et al., 1961, Figure 3).

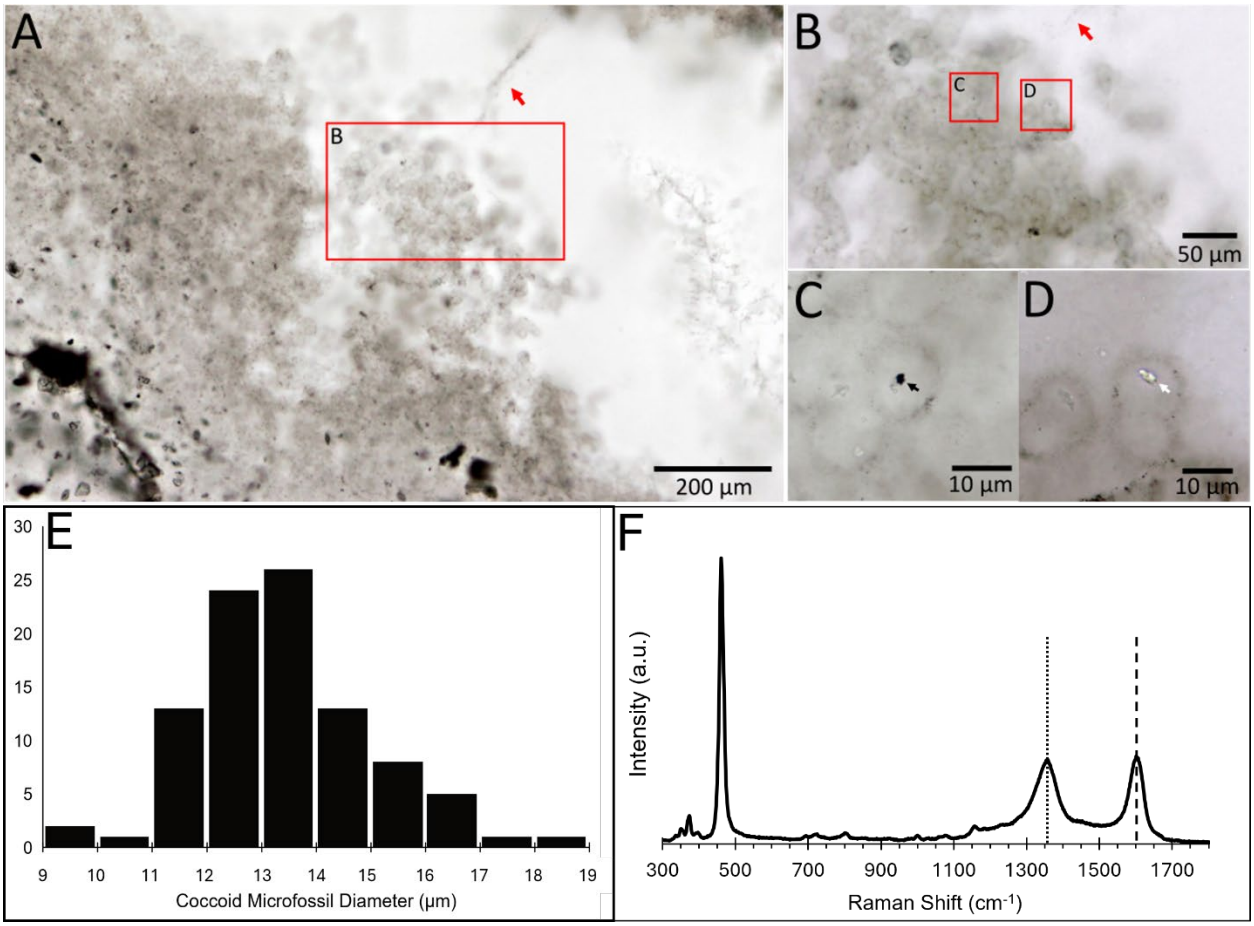

Figure II-7. Photomicrographs, a histogram, and a Raman spectrum indicating the size range of the coccoid microfossils and the kerogen composition of a dark intracellular inclusion within one of the microfossils. (A) A photomicrograph of an area that overlaps with the blue box in Figure II-2B. The red arrow indicates the same bundle of mucous stalks featured in Figure II-6A. (B) A photomicrograph of the area within the red box in panel A. The red arrow indicates a portion of a mucous stalk. (C) A photomicrograph of the area within the red box labeled C in panel B. The black arrow indicates a dark intracellular inclusion. (D) A photomicrograph of the area within the red box labeled D in panel B. The white arrow indicates a clear and colorless cellular inclusion. (E) A histogram indicating the size range of 94 coccoid microfossils. Mean diameter = 13.4 µm (sd = 1.6 µm). (F) A Raman spectrum that was collected on the dark intracellular inclusion featured in panel C. The intense peak at approximately 465 cm^{-1} indicates that the matrix is composed of microcrystalline quartz. The dotted line falls at approximately 1360 cm^{-1} and indicates the kerogen D-band. The dashed line falls at approximately 1600 cm^{-1} and indicates the kerogen G-band.

My examinations of 39 petrographic thin sections in crossed polarized light with a first order retardation plate show that the microbial laminae and microfossils are preserved within microcrystalline chert with a rectilinear (sometimes called “gridwork”) fabric (Figs. II-8 and II-9; Schubel & Simonson, 1990; Hattori, 1996; Dunham, 2018). The rectilinear fabric indicates that the chert is composed of interlocking, fibrous chert spherules that initially formed as silica gel (Fig. II-8; Schuebel and Simonson, 1990). Petrographic analysis also shows that fibrous chalcedony radiates away from the rectilinear microcrystalline chert to line the channels and voids (Fig. II-9B and C). In some instances, the regions of void-lining chalcedony nearest the coccoid microfossils are visible as layered botryoidal chalcedony in transmitted light (Fig. II-9C, black arrow). The largest channels and voids are filled with megacrystalline quartz (Fig II-9B.).

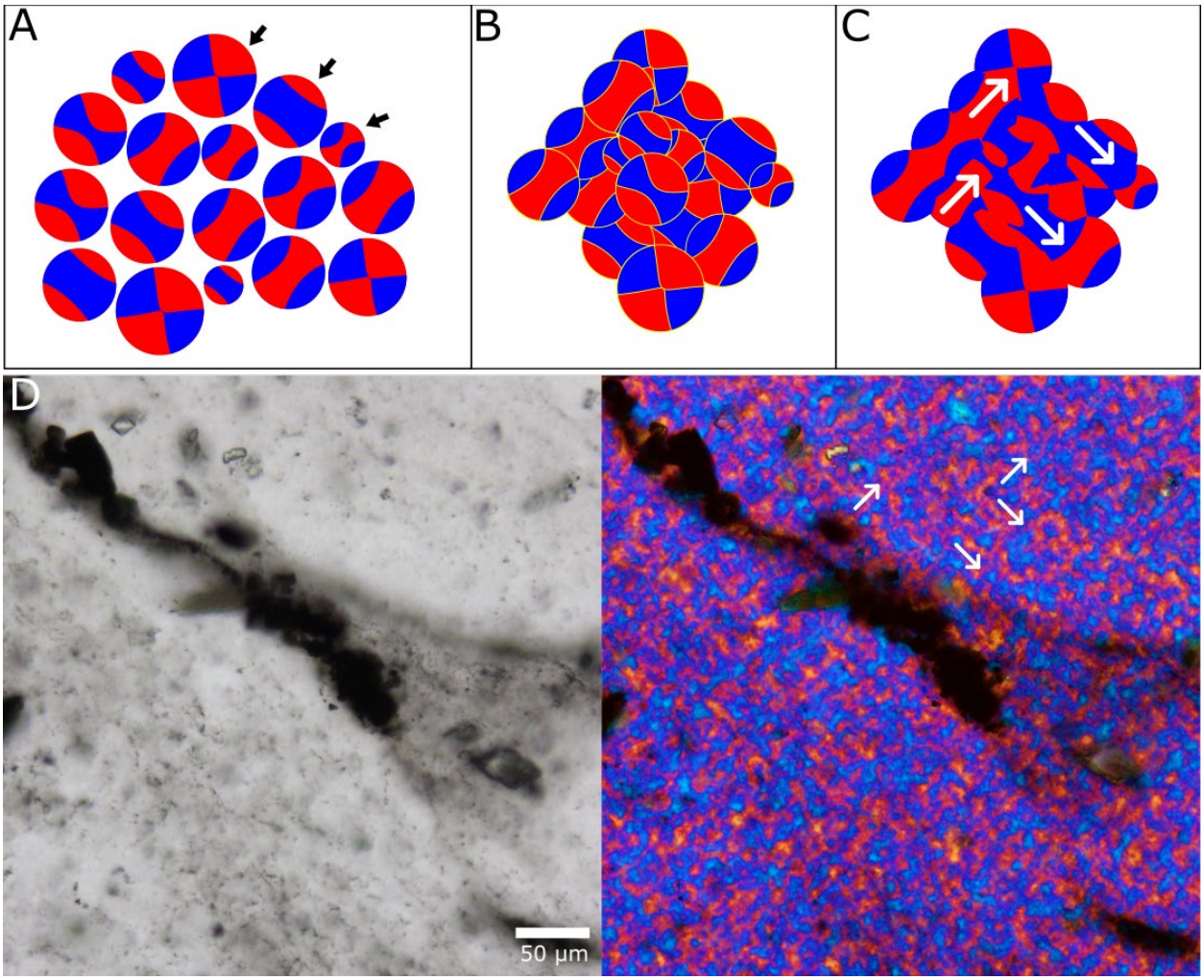

Figure II-8. (A) Illustration of idealized chert spherules as they appear in crossed polarized light with a first order retardation plate. It represents multiple spherules within a thin section that are centered at multiple planes but viewed at a single focal plane. The uppermost arrow points to a spherule that is centered at the focal plane. The center arrow points to a spherule that is centered below the focal plane. The lowest arrow points to a spherule that is centered above the focal plane. In this illustration, the distance between the spherule centers is greater than the combined length of their radii, so the spherules are not interlocking. (B) The same set of spherules in panel A, moved closely together so that the distance between spherule centers is less than the combined length of their radii. In this panel the spherule representations overlap (for the purpose of visualization). The illustrations are outlined in yellow to differentiate individual spherules. (C) The same closely spaced spherules in panel B with the yellow outlines removed and straight edges where spherules meet (rather than overlapping rounded edges as in panel B) to represent interlocking chert spherules. The interlocking spherules display the gridwork pattern of rectilinear chert, which is highlighted by white arrows. (D) Photomicrographs of a filmy mat layer three-dimensionally preserved within a petrographic thin section prepared from the same hand sample as the thin section in Figure II-1B. The image on the left was taken under transmitted light. The image on the right is the same field of view, taken under crossed polarized light with a first order retardation plate. It displays the gridwork pattern of rectilinear chert throughout, highlighted by white arrows.

The red and blue "gridwork" appearance of rectilinear chert occurs because each of its interlocking spherules is composed of elongate fibers. The angle of extinction is the same for each fiber in a spherule, but the fibers are oriented perpendicular to each other within the spherule. The result is apparent extinction at perpendicular angles within each spherule, which is seen as alternating red and blue wedge-shaped regions when viewed under crossed polarized light with a first order retardation plate (Schubel and Simonson, 1990; Dunham, 2018). The schematics in Fig. II-8A to C provide a visual explanation of the gridwork appearance of rectilinear chert.

Discussion

I begin the discussion by detailing evidence that the coccoid microstructures presented here are *bona fide* biogenic microfossils. This is followed by my interpretation of the microbial community that led to the formation of the microfossils and their importance to Precambrian paleontology. Finally, I present a model of the metabolic processes that occurred within the microbial community and the geochemical processes that led to its preservation.

Syngeneity, indigeneity, and biogenicity of coccoid microfossils

In the following paragraphs, I detail multiple lines of evidence, consistent with accepted standards of Precambrian paleontology (e.g., Buick, 1990; Westall, 1999; Brasier et al., 2006; Schopf et al., 2006), indicating that the coccoid microfossils are syngenetic and indigenous to the rock in which they are found and support the claim that they are *bona fide* biogenic microfossils.

Syngeneity and Indigeneity

The rectilinear fabric associated with filmy laminae and microfossils in the RET samples (Figs. II-8 and II-9) suggests that the microfossils are both syngenetic and indigenous to the host rock. As stated above, rectilinear chert is composed of fibrous, interlocking chert spherules

(Scheubel and Simonson, 1990; Dunham, 2018; Fig. II-8). When similar rectilinear fabric is observed in chert samples with microfossils and/or other organic matter that formed in tidal or hot spring depositional environments, it is interpreted as an indication of early diagenetic silicification that occurred because silica spherules nucleated directly on microorganisms, extracellular polymeric substances (EPS), or other organic matter within microbial mats (Dunham, 2018). This interpretation is supported by fossilization experiments which demonstrate that amorphous silica accumulates on actively metabolizing biofilms at room temperature and pressure in artificial seawater at silica concentrations as low as 36 ppm and on extracted extracellular polymeric substance at silica concentrations as low as 90 ppm when the amorphous silica saturation concentration under these conditions is 120 ppm (Moore et al., 2020; Moore et al., 2021).

In the RET samples, rectilinear fabric is associated with only and all of the preserved microbial mats and coccoid microfossils (Fig. II-9). Furthermore, where spherules are not densely packed and nucleation sites can be ascertained (II-9D, yellow circles), some spherule nucleation sites coincide with relatively kerogen-rich coccoid microfossil walls (II-9D, yellow arrows). There is evidence of modern microfractures and meteoric weathering (Fig. II-2, yellow arrows), but the microfossils and kerogen occur in multiple unweathered areas of the samples. Additionally, there is no suggestion of hydrocarbon fluid migration in these samples, nor anywhere in the Gamohaan Formation, that might call the indigeneity of the fossilized organic matter into question (e.g., Rasmussen and Muhling, 2019).

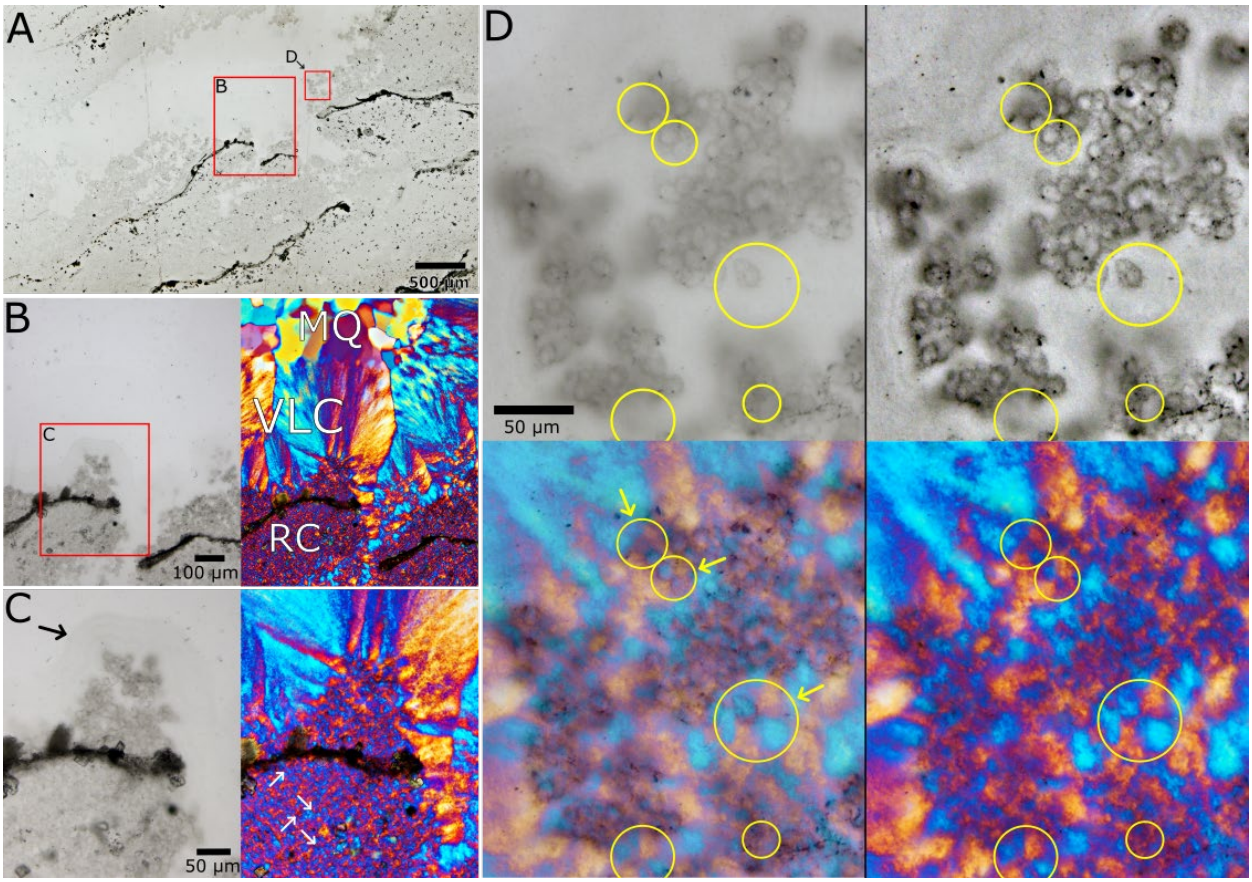

Figure II-9. Photomicrographs taken under unpolarized and cross polarized light with a first order retardation plate. (A) A partial scan of a petrographic thin section prepared from the same sample as the thin section in Figure II-2B. It features the same void that is indicated by the red arrow in Figure II-2B. (B) Photomicrographs of the area within the red box labeled B in panel A. The image on the left was taken under unpolarized light. The image on the right was taken under cross-polarized light with a first order retardation plate. MQ = megacrystalline quartz, VLC = void lining chalcedony, RC = rectilinear chert. (C) Photomicrographs of the area within the red box labeled C in panel B. The image on the left was taken under unpolarized light. The image on the right was taken under cross-polarized light with a first order retardation plate. The black arrow indicates botryoidal chalcedony. The white arrows highlight the gridwork pattern of the rectilinear chert. (D) Photomicrographs of the area within the red box labeled D in panel A. The upper left image shows coccoid microfossils under unpolarized light. The upper right image is the same as the upper left image with enhanced contrast to make microfossils easier to see. The lower right image shows coccoid microfossils under cross-polarized light with a first order retardation plate. The lower left image consists of the lower right image overlain with the upper right image at 50% transparency. Yellow circles indicate the location of chert spherules that are visible under cross-

polarization. Yellow arrows point to instances of spherule centers falling on microfossil cell walls, which indicates that the spherules nucleated on the walls.

Biogenicity

Geologic context

The RET microfossils occur within sedimentary marine rocks (Fig. I-1; Beukes, 1987), which is consistent with the existence of microorganisms. The rocks have been subjected to minimal metamorphism (Miyano and Beukes, 1984; Levitt et al., 2015), which is consistent with the preservation of microfossils. The chert in which they are preserved did not form in or near an environment in which significant abiotic production of organic matter might be expected, such as a hydrothermal vent or serpentinizing system.

In addition, the stratigraphic sequence in which these rocks occur contains abundant evidence of Neoarchean microbial life. The biogenicity of diverse carbonate microbialites in the Gamohaan Formation is well-documented (e.g., Beukes 1987; Sumner, 1997a; Chapter III). Other microfossils have been reported in cherts from the upper units of the Gamohaan Formation. Exceptionally large coccoid microfossils have been observed within the chert bed that lies approximately 5 meters stratigraphically above the transition between fenestrate microbialites and planar microbial mat facies in the Gamohaan Formation (Czaja et al., 2016). Finally, broad filamentous microbial sheaths have been observed in samples of black chert from elsewhere in the Tsineng member (Klein et al., 1987).

Morphology, composition, and preservation

The coccoid morphology of the RET microfossils is consistent with known fossilized and extant microorganisms (e.g., La Rivière and Schmidt, 2006; Schopf et al., 2006; Wood et al., 2017). The coccoid microfossils are hollow, which is consistent with the presence of cell lumen (Figs. II-5, II-6). Their walls have a rough reticulate texture (Fig. II-4E to G), which has been

recognized as a texture of fossilized bacterial walls preserved in chert since the first report of their occurrence (Barghoorn and Tyler, 1965) and their size is consistent with that of several extant types of marine coccoid sulfur-oxidizing bacteria (e.g., La Rivière and Schmidt, 2006) and coccoid cyanobacteria (e.g., Wood et al., 2017). Furthermore, the coccoid microfossils appear to exhibit simple cellular elaborations, described above as wispy filament-like structures, that strongly resemble the stalks of *Thiovulum spp.* (Fig. II-6). The implications of this resemblance are examined in greater detail below.

As mentioned above, Raman spectroscopy indicates that the coccoid microfossils are composed of kerogen, which is an important piece of evidence in support of the conclusion that they are *bona fide* microfossils (Fig. II-5; e.g., Buick, 1990; Schopf et al., 2005). Furthermore, the coccoid microfossils exhibit variable levels of preservation (Fig. II-10). Panels B and C in Figure II-10 show two regions of coccoid microfossils visible within a void and fluid escape channel. The microfossils in panel B are generally well preserved, with continuous cell walls and a rounded shape. The microfossils in panel C exhibit the first stages of bacterial decomposition: discontinuous cell walls and the loss of their rounded shape, which suggests they began to decompose prior to silicification (Fig. II-10C, black arrows; Bartley, 1996; Manning-Berg et al., 2021).

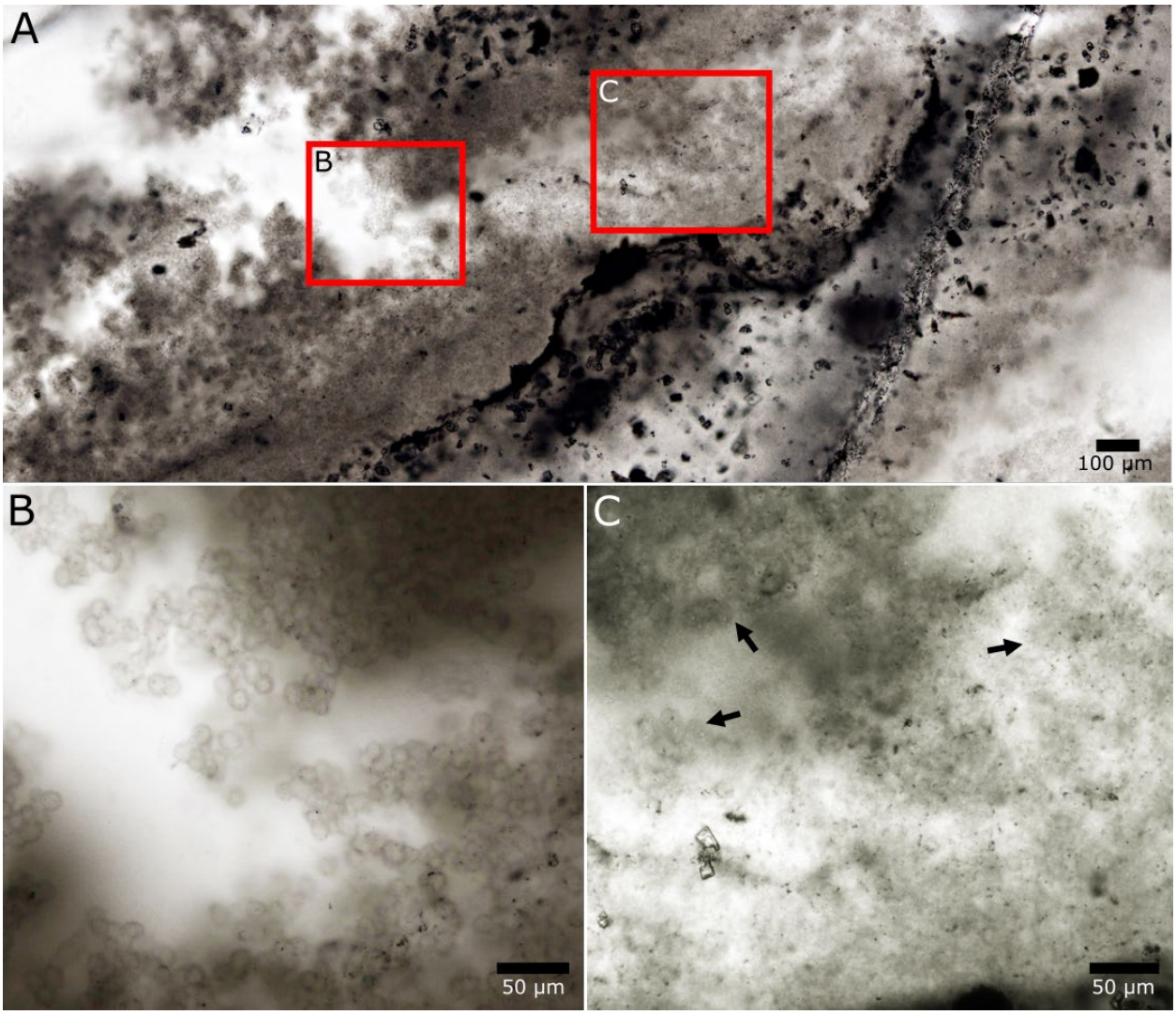

Figure II-10. (A) A photomicrograph of the area within the blue box in Figure II-2A. The red boxes indicate the areas pictured in panels B and C. (B) A photomicrograph of coccoid microfossils with continuous cell walls. (C) A photomicrograph of misshapen coccoid microfossils (black arrows), some of which have discontinuous cell walls (rightmost black arrow).

Potential abiotic formation processes

The coccoid morphology of the RET microfossils is consistent with the morphology of known microorganisms and their context and composition indicate that they are composed of fossilized organic matter. However, their relatively simple morphology means that it is important to carefully consider and rule out abiotic formation processes. There are two known abiotic

formation processes that could produce pseudofossils that are morphologically similar to the RET microfossils and composed of kerogen: the concentration of organic material at mineral grain boundaries and biomorph self-organization (e.g., García Ruiz et al., 2002; Cosmidis and Templeton, 2016; McMahon, 2019).

Mineral grain biomorphs

As described above, the microfossils and microbial mats under consideration here are preserved within spherulitic chert, as indicated by the rectilinear fabric of petrographic thin sections observed under cross-polarized light with a first order retardation plate (Figs. II-8 and II-9; Schubel & Simonson, 1990; Hattori, 1996; Dunham, 2018). While it may seem plausible that the coccoid microfossils described here are pseudofossils that formed at chert spherule boundaries rather than *bona fide* biogenic microfossils, there are several indications that this is not the case, described below.

As explained above, the "gridwork" appearance of spherulitic chert results from the interlocking of closely spaced chert spherules (Fig. II-8). The interlocking nature of the spherules is not consistent with the formation of coccoidal pseudofossils because, as illustrated in Figure II-8, the boundaries do not form coccoidal structures. However, in the occasional instances where preserved organic structures were not tightly packed, spherule nucleation sites were less closely spaced and spherules formed such that the distance between their centers is less than the combined length of their radii, as in panel A of Figure II-8. Those spherules are not interlocking. As a result, I was able to identify the nucleation sites (Fig. II-9D, yellow arrows) and boundaries of some individual chert spherules (Fig. II-9D, yellow circles). If the coccoid microfossils were biomorphs that formed through the coating of chert spherules with organic matter, the spherule nucleation sites would fall at their centers and spherule boundaries would coincide with cell

walls. However, where it is possible to observe spherule nucleation sites, they fall at cell walls rather than centers (Fig. II-9D, yellow arrows), and, where non-interlocking spherule boundaries are visible (Fig. II-9D, yellow circles), they do not coincide with cell walls.

Self-organizing biomorphs

Most abiotic processes that lead to biomorph self-organization yield structures that are morphologically similar to microfossils but composed of minerals rather than organic matter (García Ruiz et al., 2002; Cosmidis and Templeton, 2016; McMahon, 2019). However, one reported abiotic process produces hollow, organic-walled biomorphs, that can form under conditions similar to the RET chert depositional environment. In laboratory experiments, Cosmidis and Templeton (2016) demonstrated that self-organizing biomorphs with simple coccoid and filamentous morphologies can form in sulfide/oxygen gradient tubes that contain yeast extract and/or peptone. Further experiments have demonstrated that these biomorphs can take on a range of morphologies, one of which is similar to the coccoid microfossils preserved here (Fig. II-B; Cosmidis et al., 2019) and that the biomorphs can be preserved through silicification (Nims et al., 2021).

After the initial discovery that self-organizing biomorphs composed of sulfur encapsulated by a carbon membrane can form in sterile, low oxygen, sulfide gradient tubes containing sodium sulfide and yeast extract and/or peptone in an artificial mineral medium (Cosmidis and Templeton, 2016), Cosmidis et al. (2019) performed several experiments using different concentrations of sodium sulfide and dissolved organic compounds. These experiments yielded a range of self-organizing biomorphs, most of which were linear structures and less than 10 μm in diameter (Cosmidis et al., 2019). They frequently appear as stacks of small (<4 μm) prisms protruding from a central axis, up to tens of microns long, and/or feature right angles and

are therefore very unlike the coccoid microfossils reported here (Cosmidis et al., 2019). However, some coccoidal self-organizing biomorphs did form. Experiments using filtered glycine or glucose solution as the organic compound source yielded approximately 1 to 10 μm, holey-surfaced, spherical to subspherical hollow globules that do somewhat resemble the coccoid microfossils (Fig. II-11B; Cosmidis et al., 2019).

It is unlikely that the coccoid microfossils reported here are self-organizing biomorphs such as those reported by Cosmidis et al. (2009) rather than *bona fide* biogenic microfossils. Cosmidis et al. (2019) reported only an approximate size range of 1 to 10 μm for the holey spherical biomorphs, which makes a direct comparison between the size of the biomorphs and the microfossils impossible. However, the biomorphs are significantly smaller than the coccoid microfossils, which are, on average, 13.4 μm in diameter (sd = 1.6 μm; Fig. II-7E). It also appears that a group of the biomorphs that formed under the same conditions exhibit greater variability in size than the coccoid microfossils reported here (Fig. II-11B). In addition, there are no wispy filament-like structures, such as those in Figures II-6 and II-10, associated with the holey spherical biomorphs reported by Cosmidis et al. (2019). However, Cosmidis et al. (2019) noted that the stacked prism biomorphs did form in association with the holey spherical biomorphs. I observed no microstructures resembling the stacked prism biomorphs in the RET samples.

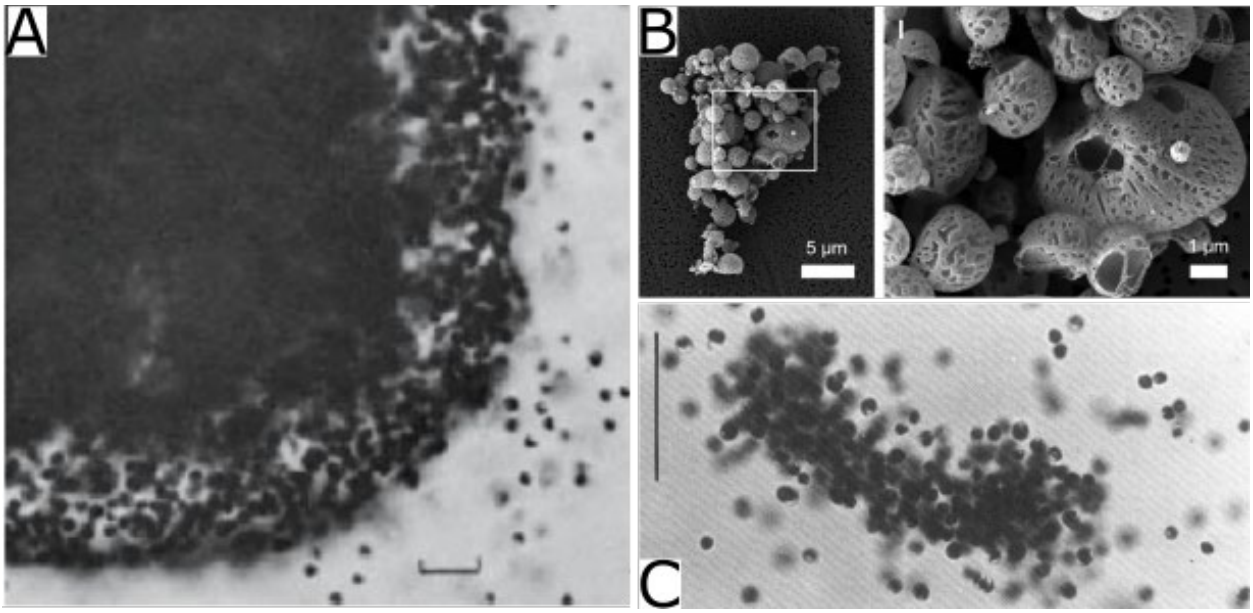

Figure II-11. Images of veil-forming microaerophilic sulfur oxidizing microorganisms and self-organizing biomorphs that resemble the coccoid microfossils presented here. (A) The edge of a veil of *Thiovulum majus* formed around decaying organic matter (La Rivière and Schmidt, 2006, from Figure 5; scale bar = 50 µm). Note the similarity between this image and Figure II-5A. (B) A photomicrograph of a cluster of organomineralized self-organized biomorphs that are morphologically reminiscent of the RET coccoid microfossils (Cosmidis et al., 2019, from Figure 6). (C) An aggregation of *Thiovulum majus* cells described as "mutually entangled in their mucous stalks" (Fenchel, 1994, from Figure 3; scale bar = 100 µm).

Microfossil interpretation: A sulfur-cycling microbial ecosystem at a microoxic/euxinic interface

Several lines of evidence are consistent with the interpretation that the microbial mats and coccoid microfossils presented here may be the remains of a sulfur-cycling microbial community dominated by heterotrophic microbial sulfate reducers and veil-forming microaerophilic sulfur-oxidizing microorganisms (VFMSOM). These lines of evidence, which are discussed in detail below, include the morphology and habit of the coccoid microfossils, previously reported spatially resolved sulfur isotope measurements (Kamber and Whitehouse, 2007), the presence of AITs, and the depth of the env.

Known extant VFMSOMs include the bacteria *Ovobacter propellens* (Fenchel and Thar, 2004), *Thioturbo danicus* (Muyzer et al., 2005), at least one unnamed strain of vibrioid bacteria

(Thar and Fenchel, 2005), and multiple members of the genus *Thiovulum* (e.g., Wirsen and Jannasch, 1978; Fenchel, 1994; Gros, 2017; Bizic et al., 2022; Sylvestre et al., 2022). The most studied of the extant VFMSOMs is *Thiovulum majus. T. majus* are flagellated coccoid to ovoid bacteria that typically measure 5 to 25 µm in diameter (long axis), but some are up to 45 to 50 µm in diameter (Figs. II-6D and II-11A and C; De Boer et al., 1961; Sylvestre et al., 2022; Bizic et al., 2022). They are highly motile chemotactic microorganisms able to anchor themselves in their preferred environment with mucous stalks (Figs. II-6D and II-11A and C; De Boer et al., 1961; Fenchel, 1994). They occur in many environments, notably in marine sediments (e.g., Jørgensen and Revsbech, 1983), caves (Engel et al., 2001; Bizic et al., 2022), sulfide-rich springs (Wirsen and Jannasch, 1978; Valentin-Alverado et al., 2024), and deep-sea hydrothermal vents (Moyer et al., 1995). *T. majus* divide via longitudinal fission, and, like many sulfur-oxidizing microorganisms, frequently contain sulfur inclusions (De Boer et al., 1961; La Rivière and Schmidt, 2006; Marshall et al., 2012; Dahl and Prange, 2006). *T. majus* form conspicuous ephemeral veils at the microoxic-sulfidic interface associated with organic matter that is being broken down by microbial sulfate reducers, including at the sediment-water interface of organic-rich muds (MSR; Fig. II-11A; De Boer et al., 1961; Jørgensen and Revsbech, 1983; Fenchel, 1994; La Rivière and Schmidt, 2006). Their preferred oxygen concentration is from 2 to 10 µM (Cogan and Wolgemuth, 2005).

Microfossil VFMSOM-like morphology and habit

The coccoid microfossils described herein bear a striking resemblance to extant VFMSOMs. The size and shape are consistent with extant VFMSOMs, and the wispy filament-like structures that occur in association with the coccoid microfossils could be preserved examples of the mucous stalks that VFMSOMs form to anchor themselves in their ideal environment. The comparison between an individual coccoid microfossil that is apparently

tethered by a filament-like structure to organic matter at the wall of a fluid escape channel and an electron micrograph of an individual living *Thiovulum majus* cell with its mucous stalk attached (De Boer et al., 1961) in Figure II-6 illustrates how similar the preserved structures are to VFMSOM mucous stalks. Note that both are submicron in diameter (Fig. II-6).

There are also indications that the coccoid microorganisms preserved within the RET samples formed veil-like clusters near deteriorating microbial mats in a way that is similar to way extant VFMSOMs form veils near decaying organic matter today. Compare panel A in Figure II-A with panels A and C in Figure II-11. Figure II-4A features part of a microbial mat in the lower right corner which is surrounded by a halo of tightly packed coccoid microfossils, just as the decaying organic matter in Figure II-11A is surrounded by a halo of tightly packed *Thiovulum majus* cells, which the authors describe as the edge of a *Thiovulum* veil (La Rivière and Schmidt, 2006). The clusters of coccoid microfossils near the apparent veil in Figure II-4A appear quite similar to the cluster of *Thiovulum majus* in Figure II-11C, which the author describes as "mutually entangled in their mucous stalks".

Spatially resolved sulfur isotope measurements

Previously reported spatially resolved sulfur isotope measurements of dispersed pyrite grains preserved within a microlaminated chert sample from the Tsineng member of the Gamohaan Formation yielded $\delta^{34}S$ values from -1.30 to 22.94‰ and $\Delta^{33}S$ values from 0.13 to 7.15‰, with ^{34}S enrichment associated with decreasing $\Delta^{33}S$ (Kamber and Whitehouse, 2007, sample SrKu37). Kamber and Whitehouse (2007) interpreted the significant sulfur isotope variability and negatively correlated isotopic gradients as indications of microbial sulfate reduction under oxygen levels from moderate to microoxic. The microlaminations within the Kamber and Whitehouse (2007) chert sample appear identical to the filmy microbial mats

preserved within the samples presented here (B. Kamber, personal communication, November 6, 2022). While there were no coccoid microfossils preserved within the Kamber and Whitehouse (2007) sample (Balz Kamber, personal communication, November 6, 2022), the sulfur isotope values indicate that the depositional environment of chert beds within the Tsineng member featured the conditions under which modern VFMSOMs thrive (Fig. II-11; e.g., Fenchel, 2004).

Ambient Inclusion Trails (AIT)

The presence of AITs in association with microbial mats (Fig. II-3) suggests that MSR were actively metabolizing during the early silicification of the samples, when the spherulitic chert was still in a gel phase. AITs with terminal pyrite grains and associated organic matter (OM) in chert are hypothesized to form when gasses produced via OM decomposition propel pyrite grains through silica (Knoll and Barghoorn, 1974; Wacey et al., 2016). This process can be entirely abiotic, as Knoll and Barghoorn (1974) suggested regarding AITs observed in Biwabik, Gunflint, and Fortescue cherts. Knoll and Barghoorn (1974) proposed that the Biwabik, Gunflint, and Fortescue AITs formed when H_2S synthesized during thermal decomposition of OM met with iron in solution to form pyrite grains which were subsequently propelled through the chert by continued OM decomposition. In this scenario, the formation and movement of pyrite grains was facilitated by local chert pressure dissolution that resulted from the OM decomposition (Knoll and Barghoorn, 1974).

It was later suggested that AITs might form via the same process described by Knoll and Barghoorn (1974), but due to MSR rather than thermal decomposition of OM (Zhang et al., 2015; Wacey et al., 2016). However, Wacey et al. (2016) questioned how sufficient gas pressure could build up in an environment that also supported active MSR. Silica gel forming on decaying microbial mats is one environment that could allow for this to occur, and I propose that the RET AITs exemplify such an occurrence.

As silica gel begins to form, it may not be viscous enough to allow for the formation of AITs. In such circumstances, any pyrite that formed via MSR would have been preserved as pyrite grains with no associated AITs, which are common in the RET samples (Fig. II-4). However, as gel formation progresses and viscosity increases, it is conceivable that there would be a stage that allows MSR and mineral grain propulsion to occur simultaneously. McLoughlin et al. (2010) proposed that "necking," or a narrowing of the AIT just behind the terminal pyrite grain, could be a sign of AIT formation in silica gel because it suggests that trails closed slightly after formation, as would be expected in a gel matrix. Necking is evident in the AITs within and near box 2 of Figure II-4B.

Microbiology and Preservation

It is certainly possible for MSR to occur in the absence of microbial sulfur oxidation, so long as there is an adequate supply of sulfate. However, modern microbial communities that exist at a microoxic-sulfidic interface such as the environment in which the RET samples formed typically include a variety of sulfate reducing and sulfur oxidizing microorganisms (e.g., Jørgensen et al., 2019). That said, there is no known modern sulfur-cycling microbial community that is perfectly analogous to the community I suggest has been preserved within the RET samples, especially not one in a sub-wavebase, silica-rich marine environment. My proposal for how such a sub-wavebase microbial community came to exist and be preserved in early diagenetic silica in the Neoarchean ocean is illustrated in Figure II-12 and described in the following paragraphs.

In what preceded, I suggested that the rectilinear fabric of the RET samples, paired with the microbial mat associated AITs (Fig. II-3), and previously reported sulfur isotope measurements made on Gamohaan Formation pyrites (Kamber and Whitehouse, 2007;

McLoughlin et al., 2023; Table I-1) indicate that MSR was actively taking place during the early diagenetic silicification of these samples. Where MSR takes place in modern environments, specialized sulfur oxidizing microorganisms are also found (e.g., Jørgensen et al., 2019). Highly motile VFMSOMs specifically evolved to take advantage of transient microoxic-sulfidic interfaces, as would have occurred if MSR were decomposing microbial mats under fluctuating oxygen levels, as suggested by sulfur isotope evidence (Kamber and Whitehouse, 2007; McLoughlin et al., 2023; Table I-1). Once VFMSOMs establish a veil, the veil persists until the oxygen concentration drops too low. While in place, the veil maintains a thin anoxic region in which MSR reduction takes place efficiently, thus providing a steady supply of H_2S to the VFMSOMs which oxidize it to sulfate (or, more accurately, intermediate sulfur species) that fuels the MSR in turn, as illustrated in the inset box in Figure II-12.

The concentration of silica that facilitated the silicification of these samples could have occurred via an iron shuttle mechanism (Fig. II-12). Fischer and Knoll (2009) proposed the iron shuttle mechanism of ferric hydroxide plus silica delivery to basinal sediments to explain the Neoarchean and early Paleoproterozoic deposition of iron formations, specifically citing features of the Kuruman BIF to support their model. This iron shuttle mechanism is based on the tendency of dissolved silica to adsorb onto ferric hydroxides (Fischer and Knoll, 2009).

As illustrated in Figure II-12, dissolved ferrous iron was abundant in the Neoarchean ocean. Fischer and Knoll (2009) suggested that some of the ferrous iron was likely oxidized in the photic zone, either abiotically by microbially derived oxygen, biologically by photosynthetic iron oxidizing microorganisms, or via both of those processes (Fig. II-12). Upon oxidation, iron would have precipitated into the water column as ferric hydroxide. The relatively shallow photic zone would have also been rich with dissolved silica, which was transported to surface waters

due to silicate weathering (Fig. II-12) but not removed because biosilicification had not yet evolved. According to Fischer and Knoll (2009), the proximity of ferric hydroxide and silica in the photic zone along with silica's tendency to adsorb onto ferric hydroxides then resulted in both compounds' delivery to the benthic zone as ferric hydroxide settled to the seafloor (Fig. II-12, inset box). If the Kuruman BIF formed via the iron shuttle, it is reasonable to suggest that this mechanism was at work delivering silica to the benthic zone, perhaps at a slower rate, during the formation of the upper Tsineng member, which, as mentioned previously, is a transition zone between carbonate precipitation and Kuruman BIF (Fig. I-1). The ferric hydroxides that "shuttled" silica to the benthic zone where it nucleated on the microbial mats described herein were likely reduced by microbial iron reducers (MIR), which are often present in modern marine sediments in which microbial sulfur cycling occurs (Fig. II-12; e.g., Jørgensen et al., 2019). The resulting reduced iron would have reacted with CO_2 produced by both MIR and MSR to form siderite and some of the H_2S produced by MSR to form pyrite (Fig. II-12).

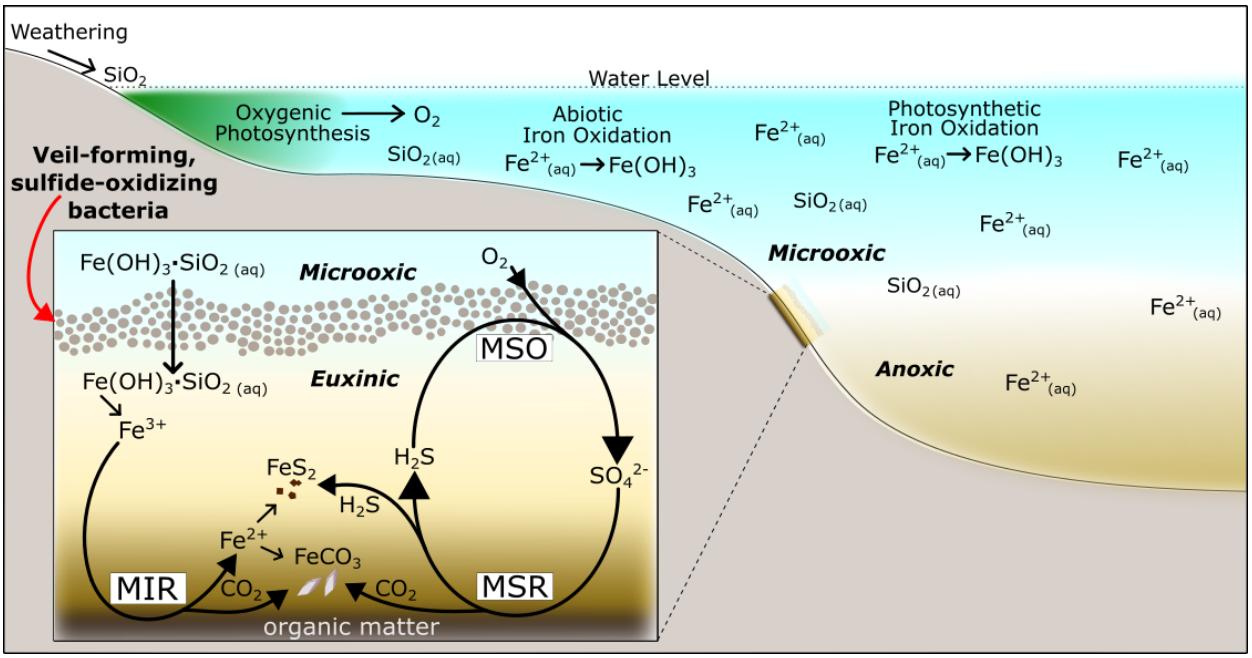

Figure II-12. An illustration of the Neoarchean environment in which the RET samples formed and the specific microbial and geochemical processes that led to their formation. MSO = Microbial Sulfur Oxidation, MSR = Microbial Sulfate Reduction, MIR = Microbial Iron Reduction.

Conclusion

In this chapter, I described a fossilized microbial community preserved in early diagenetic chert collected from the CMCP that is similar to extant sulfur-cycling microbial communities in chemistry, morphology, and habit. My interpretation of the microfossils is consistent with previous work indicating that intermittent microoxic conditions existed below wave base during the final drowning of the CMCP, just prior to the GOE (e.g., Kendall et al., 2010; Voegelin et al., 2010; Czaja et al., 2012; Ostrander et al., 2020). My interpretation that the coccoidal microfossils presented above represent organisms similar to VFMSOMs suggests that microorganisms evolved metabolic strategies that took advantage of marine oxygen well in advance of the GOE, which is supported by phylogenetic analysis suggesting the evolution of oxygen-utilizing enzymes by approximately 3.1 Ga (Jabłońska and Tawfik, 2021).

The results presented in this chapter represent the first reported instance of the early diagenetic silicification of microfossils via the direct nucleation of chert spherules on organic matter in a deep marine environment. This discovery adds to our knowledge of the mechanisms that led to microfossil preservation in chert during the Archean Eon, which are currently poorly understood. Furthermore, the discovery adds to our knowledge of biosignature preservation in general, which informs astrobiology-focused solar system exploration (e.g., NASEM, 2018). To better understand this mode of preservation, Precambrian paleontologists studying organic matter preserved in chert should routinely carry out petrographic investigations to determine if their samples are composed of rectilinear chert.

Chapter III: Morphological reconstruction and spectroscopic analysis of fenestrate microbialites provide insight into a Neoarchean microbial ecosystem and support the interpretation of SHERLOC data

Introduction

Microbialites (*sensu* Burne and Moore, 1987) provide insight into Earth's earliest ecosystems (e.g., Allwood et al., 2006; Noffke et al., 2013; Wacey et al., 2015; Djokic et al., 2017; Homann, 2019; Hickman-Lewis et al., 2020). They are a primary source of both morphological and biogeochemical evidence related to the co-evolution of Earth and life during the Archean Eon (4 to 2.5 Ga), the period of Earth's history during which microbial life first arose and multiple metabolic processes evolved (e.g., Grey and Awramik, 2020; Lepot, 2020). This chapter presents morphological and geochemical analyses of fenestrate microbialites from the Gamohaan Formation of the CMCP (See Chapter I, Geologic Context). These microbialites are of particular interest to those who strive to understand the interactions between Earth's earliest life and its environment because of their well-preserved morphological complexity (Sumner, 1997a; Sumner, 2000) and the fact that they formed during a pivotal period in Earth's history (See Chapter I, Coevolution of Earth and Life: The Great Oxygenation Event).

The CMCP fenestrate microbialites are organosedimentary carbonates exhibiting three-dimensionally preserved black, kerogen-rich structures (Sumner, 1997a; Beukes et al., 1990). They occur in the Gamohaan and Nauga Formations (Campbellrand subgroup) and the Frisco and Fairfield Formations (Malmani subgroup) of the CMCP (Beukes, 1987; Sumner, 1997a; Wright and Altermann, 2000; Sumner and Grotzinger, 2004; Sumner and Beukes, 2006; Schröder et al., 2009; Rivera and Sumner, 2014; Warke et al., 2019). Their delicate

morphologies along with the lack of cross-bedding and stratigraphic setting of the facies in which they occur indicate that they formed in deep subtidal environments (Sumner, 1997a; Sumner and Grotzinger, 2004; Sumner and Beukes, 2006).

The morphology of the CMCP fenestrate microbialites is well-known and their biogenicity is well-accepted (Sumner, 1997a; Sumner, 2000; Wright and Altermann, 2000; Schröder et al., 2009; Stevens et al., 2011; Rivera and Sumner, 2014; Warke et al., 2019). The fenestrate microbialites feature seven morphological end-members: planar laminae, contorted laminae, tented structures, irregular columnar structures, cuspate structures, plumose structures, and net structures (Sumner, 1997; Sumner, 2000; Stevens et al., 2011; Rivera and Sumner, 2014). The seven morphological endmembers are composed of various combinations of support structures, laminae, and linear structures in association with herringbone carbonate that formed contemporaneously with microbial growth and voids filled with carbonate cements (Sumner, 1997a; Sumner 2000).

Although the biogenicity and morphological complexity of the CMCP fenestrate microbialites is well-established, the factors that led to the formation of their distinctive morphological features are not known. When Beukes (1987) first described cuspate microbialites from the Gamohaan Formation, he suggested that their morphology was the result of phototactic cyanobacteria-like microorganisms competing for sunlight. Since that time researchers have noted that the tented and cuspate microbialite structures are morphologically similar to various modern cyanobacteria-dominated microbial mats, especially mats featuring pinnacles and ridges in perennially ice-covered Antarctic lakes (e.g., Sumner, 1997a; Rivera and Sumner, 2014; Warke et al., 2019). The modern microbial mat pinnacles and ridges are not perfect analogues to the fenestrate microbialite structures because, while they do include laminae and linear

structures, they lack support structures (Sumner et al., 2016), which are characteristic of CMCP fenestrate microbialites (Sumner, 1997a).

In a description of cuspate microbialites that occur within the Sulky Formation of the Mesoproterozoic Dismal Lakes Group (Arctic Canada) that are morphologically similar to the cuspate and tented microbialites of the Gamohaan Formation, Bartley et al. (2015) also suggested that the morphologically complex microbialites resulted from interactions between microbial communities with motile components. Specifically, Bartley et al. (2015) suggested that the vertical supports might have been dominated by motile filamentous cyanobacteria or sulfur-oxidizing bacteria and the draping laminae dominated by anaerobic heterotrophs, possibly including microbial sulfate-reducers (MSR).

These microbialites are typically preserved in carbonate, but the specific chemistry of the matrix (calcite or dolomite) varies at the micron scale. This is thought to result from dolomitization of original calcite (Beukes, 1987; Beukes et al., 1990) but the details of how this localized dolomitization occurs are not understood. Multiple non-exclusive processes have been proposed to explain the localized dolomitization of the CMCP fenestrate microbialites. Beukes et al. (1990) proposed that large-scale dolomitization of Gamohaan Formation microbialites is the result of fluid alteration during early diagenesis that also resulted in recrystallization and segregation of kerogen to grain margins. Beukes et al. (1990) also proposed that hyper-local dolomitization is the result of fluid alteration along microfractures during burial diagenesis. Wright and Altermann (2000) proposed that localized dolomitization associated with kerogen-rich features is the result of MSR liberating magnesium ions from $MgSO_4$ during very early diagenesis. In this scenario, the authors accepted the hypothesis that the microbialites were formed by cyanobacteria and suggested that MSR was associated with cyanobacterial

degradation. In contrast to the Wright and Altermann (2000) hypothesis, Warke et al. (2019) proposed that dolomitization associated with kerogen-rich microbialites resulted from microbially-influenced dolomite nucleation that took place when actively growing microbial structures released Mg^{2+} in response to changes in salinity or alkalinity.

This chapter reports the results of 3D reconstructions, petrographic examinations, and co-located geochemical analyses of Gamohaan fenestrate microbialites at the mm to micro-scale. These data address several key questions about the microbial system. First, the detailed observations of microbialite morphologies offer insight into the processes that led to their morphological complexity. Second, combining the fine scale microbialite morphological data with collocated geochemical analyses allows for an assessment of the geochemical preservation of the microbialites and understanding of the heterogeneous and localized dolomitization found within (Beukes et al., 1990; Wright and Alterman, 2000; Warke et al., 2019). These data also will support the interpretation of data collected in Jezero Crater, Mars by the Mars 2020 rover and connect this work to that reported in Chapter IV.

Methods

Sample Collection

The samples described in this chapter were collected from the fenestrate microbialite facies of the Gamohaan Formation at two different, well studied localities: Kuruman Kop near the town of Kuruman (Fig. III-1A to C; -27.382917°, 23.344233°), and a farm near the town of Danielskuil (Fig. III-1D to F; -28.104117°, 23.57115°). Throughout this chapter, I refer to the sample collected at Kuruman Kop as KUR and the sample collected near Danielskuil as DSK. The specific hand samples used in this study were selected from among many Gamohaan

Formation fenestrate microbialite samples for their lack of recrystallization and distinctive morphological features, which are discussed in detail below.

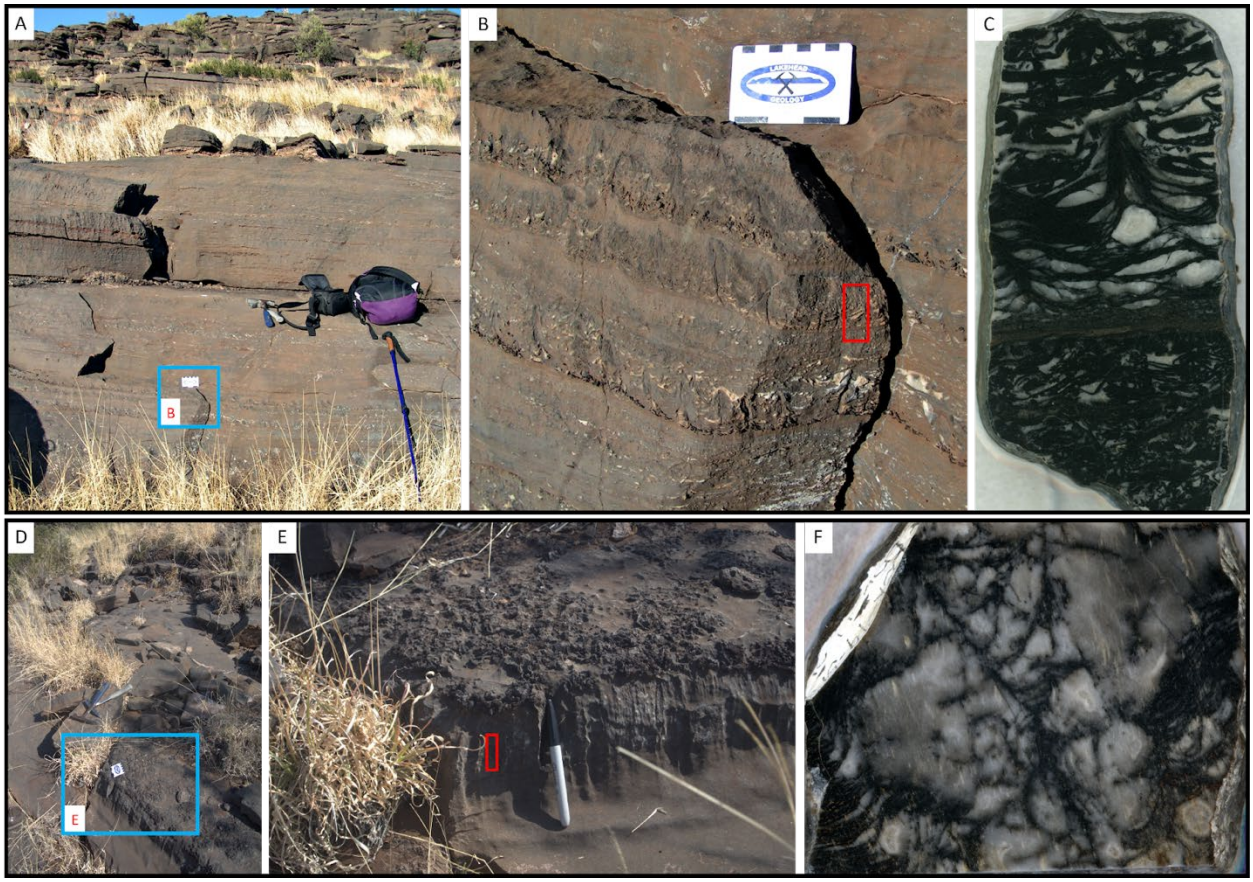

Figure III-1. Images of fenestrate microbialites at multiple scales. A) The sampling locality of sample KUR, at Kuruman Kop. The blue box outlines the region in panel B. B) The outcrop of fenestrate carbonate microbialite sampled at Kuruman Kop. The red box outlines the approximate portion of the KUR sample from which the billet used for 3D reconstruction was cut. C) A single scanned face of the KUR sample, showing dark, kerogen-rich, morphologically complex microbial structures. D) The sampling locality of sample DSK, near the town of Danielskuil. The blue box indicates the approximate area of the outcrop seen in panel E, from a different orientation. The left edge of the blue box corresponds to the foreground of panel E. E) The outcrop of fenestrate carbonate microbialite that was sampled near Danielskuil. The red box outlines the approximate portion of the DSK sample from which the billet used for 3D reconstruction was cut. F) A single scanned face of the DSK sample, showing dark, kerogen-rich, morphologically complex microbial structures. The microbialite scans in panels C and F are oriented with the stratigraphic up position at the top. See figures 4 and 5 for microbialite scale.

Visible Raman Spectroscopy

To investigate the hypotheses that localized dolomitization in the CMCP fenestrate microbialites is microbially-influenced (Wright and Altermaan, 2000; Warke et al., 2019) and verify the organic composition of apparent microbial features, thirty Raman spectra were collected at ten morphologically distinct points (Figs. III-2 and III3; three spectra were collected within tens of microns of each other at each point) on the imaged KUR and DSK microbialite samples. The visible Raman data discussed in the section titled SHERLOC Analogue Data includes these 30 spectra, as well as 82 additional spectra collected on the KUR, DSK, and two additional Gamohaan fenestrate microbialite samples.

Visible Raman measurements were collected using a Horiba T64000 Raman microscope and 457.9 nm laser excitation from a Coherent FreD 90C Ar+ laser with a spot size of approximately 1 to 2 μm and a laser power at the sample of 9 mW. Spectra were collected using a 50X long working distance objective (NA = 0.50). I used a 600 g/mm diffraction grating to provide a ~128–2900 cm^{-1} spectral window at a resolution of ~1.5 cm^{-1} between spectral data points. Raman scatter was detected with a Horiba Symphony II liquid nitrogen cooled (-133ºC) CCD.

Deep Ultraviolet (DUV) Raman Spectroscopy

One hundred and seven DUV Raman spectra were collected from the same four fenestrate microbialite samples described above using the Analogue Complimentary Raman for Operations oN Mars (ACRONM) SHERLOC analogue instrument at NASA's Johnson Space Center in Houston, TX. ACRONM was built according to the specifications of MOBIUS, the SHERLOC breadboard instrument, which is housed at the Jet Propulsion Laboratory (Abbey et

al., 2017). Laser excitation at a wavelength of 248.5794 nm was produced by a PhotonSystems NeCu70-248 hollow cathode laser. Spectra were collected using a 20 Hz laser rep rate with each pulse having a 40 μs width and ~4.7 μj/pulse energy at the sample. The incident laser beam was focused to a ~50 μm annular beam on the sample surface using a 5X objective. The Raman scattering was dispersed using a Horiba Scientific iHR 320 spectrometer. A 2,400 g/mm diffraction grating was used to provide a ~400–4,900 cm^{-1} spectral window at a resolution of ~2 cm^{-1} between spectral data points. Raman spectra were detected using a Horiba Scientific back-thinned Synapse Plus CCD that is thermoelectrically cooled to −75°C.

Spectral Processing

The open-source peak fitting software Fityk (version 1.3.1; Wojdyr, 2010) was used for baseline subtraction and peak fitting of spectra. Following the kerogen peak fitting protocol described by Kouketsu et al. (2014), I used Fityk's Voight fit function to determine Raman peak positions and find the full width at half maximum (FWHM) of kerogen D1 bands. I used Fityk's Lorentzian fit function to determine Raman peak centers (Demtroder, 2008).

3D Reconstruction

3D reconstructions of microbialite morphology were created using a combination of serial image scanning and image processing via the open-source image analysis software Fiji. Fiji is an updated distribution of the software imageJ that facilitates the sharing of community-developed software components, or plugins, for biological-image analysis (Schindelin et al., 2012). The process I used is based on methodology developed at the Keck Center for Active Visualization in Earth Sciences at the University of California, Davis (Stevens et al., 2011; Rivera and Sumner, 2014), which I adapted to the Fiji platform.

To perform serial scanning, I first created billets of the studied microbialites. For each set of scans, I polished the billet surface with 30 μm grit polishing film, removing approximately 50 μm of sample material each time, and scanned the surface at 3200 dpi resolution with an Epson Perfection V600 Photo flatbed scanner. I repeated this process to create a series of 150 scans of each sample. Each 3D reconstruction discussed below was made using a set of 150 scans represents approximately 7.5 mm of sample material.

To create 3D reconstructions, I first converted each set of scans to an image stack in Fiji. I then used the Fiji plugin Linear Stack Alignment with SIFT (default parameters) to align the images within each stack. The Linear Stack Alignment with SIFT plugin uses a cascade filtering approach to extract distinctive scale and rotation invariant image features, based on a method developed by Lowe (2004), to match features in consecutive stack images, allowing for image alignment. After image alignment, I cropped the image stacks in Fiji to remove background features and billet edges from the images.

I used the Fiji plugin Volume Viewer (projection mode, trilinear interpolation, sampling of 1.0, thermal look-up table (LUT), 3D Fill, default alpha settings) to create 3D image projections from the aligned and cropped image stacks. For this method, it was necessary to manually set the z-aspect ratio of each stack to a value that was appropriate to the dimensions of each image stack and the thickness of the material removed from the billet surface between scans within the Volume Viewer user interface. The physical dimensions of the slabs, pixel resolutions of the images, and the thickness of material removed between each scan was used to find the micron-to-pixel ratio for each image stack. Those values were used to calculate z-Aspect ratios of 1.1 for sample KUR and 1.3 for sample DSK.

This method requires the selection of a pixel color from an image within the image stack to be fully opaque, with the opacity of all other voxels weighted according to the alpha settings. For the 3D reconstructions presented below, I selected RGB (0, 0, 0), or black, pixels to be fully opaque. Thus, pixels approaching RGB (255, 255, 255), or white, approach full transparency. The thermal LUT used for 3D projections renders opaque voxels white, so the darkest morphological structures in the microbialite samples appear white and features that were white or near white in the microbialite samples are transparent. Fiji's 3D Viewer plugin (default settings, adjust transfer function for desired opacity) was used to produce rotating 3D reconstructions of each sample, which are available as supplemental files (S1 and S2).

Petrographic Examination

Although the 3D reconstructions produced via the above method allow observation of mesoscopic microbialite morphology, the relatively low resolution (50 μm) along the z-axis of the 3D reconstructions makes it difficult to observe microscopic textures preserved within thos mesoscopic structures. Therefore, petrographic examinations of thin sections were prepared from the same hand samples (Figs. III-8, III-9, and III-10). Olympus BX60 and BX53 microscopes in transmitted light configuration were used to study petrographic (approximately 30 μm) and "thick" (approximately 200 μm) thin sections coated with a thin layer of Olympus type F low-florescence immersion oil. Images of thin section-embedded microbial structures were acquired with an Olympus SC50 digital camera mounted on the microscope. Images were processed with Olympus cellSens standard image processing software (version 3.17), and PhotoScape image editing software (version 3.7).

Results and Discussion

Visible Raman Spectroscopy and Raman Geothermometry

Visible Raman spectroscopy confirms that the Gamohaan microbialites are composed of calcite, high magnesium calcite, and dolomite and that the kerogen content is concentrated in the black microbial structures (Tables III-1 and III-2, Fig. III-4). The carbonate peaks are discussed in detail below, under the subheading dolomitization. Kerogen is indicated by two main Raman bands: the D-band (disordered) centered at approximately 1360 cm^{-1} and the G-band (graphitic) centered at approximately 1600 cm^{-1}. I observed D- and G-bands in all spectra collected at dark structures within the microbialites (Figs. III-2 and III-3; Tables III-1 and III-2). In general, the kerogen bands in DSK spectra are less intense relative to the carbonate peaks than the kerogen bands in KUR spectra (Fig. III-4), which is consistent with the greater density of microbial structures (Figs. III-5 and III-6) and higher kerogen content of the KUR sample.

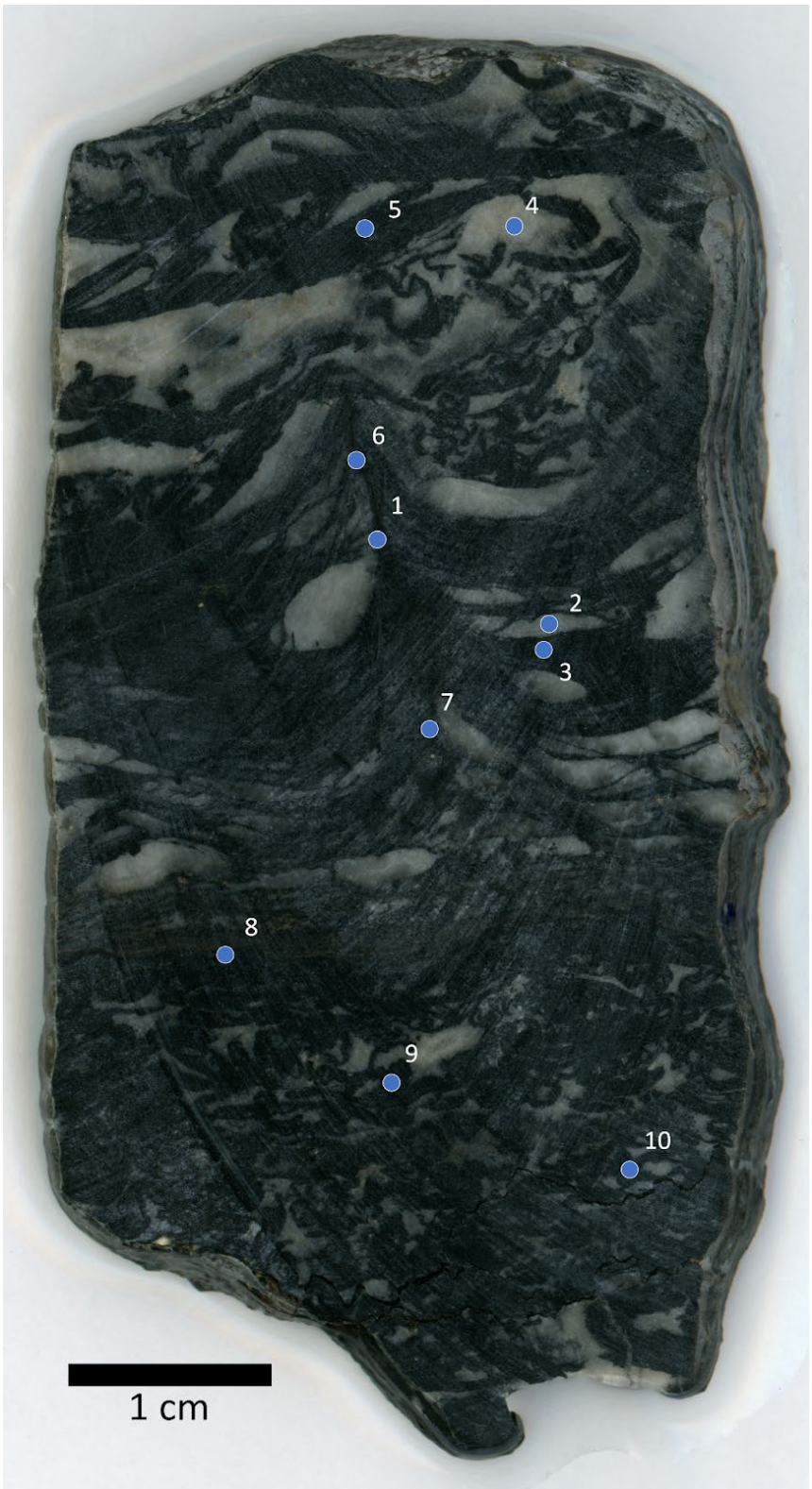

Figure III-2. Unpolished slab of sample KUR, oriented with the stratigraphic up position at the top. Blue dots indicate Raman analysis spots. Their numbers correspond to the numbers in Figure III-4A and Table III-1.

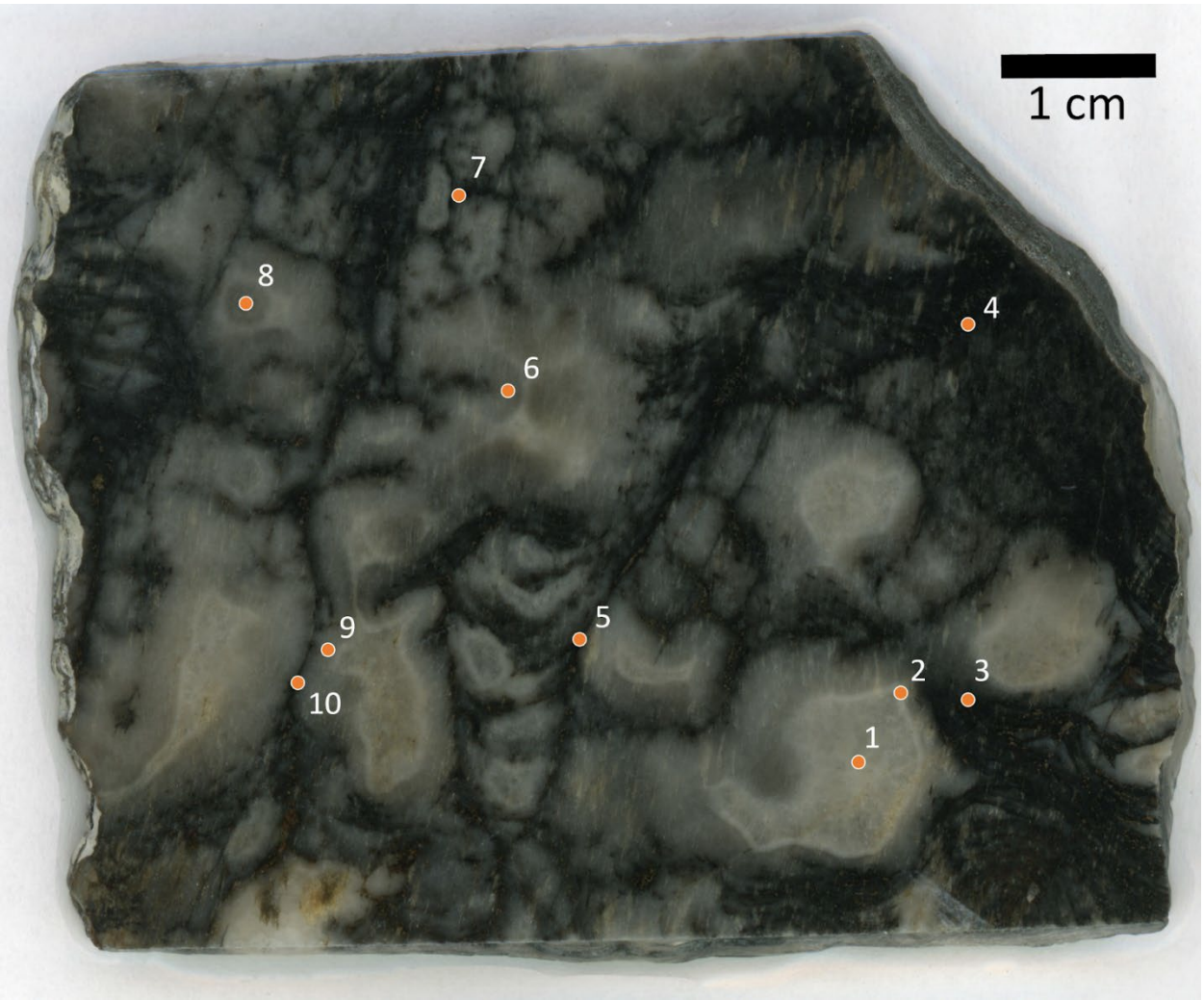

Figure III-3. Unpolished slab of sample DSK, oriented with the stratigraphic up position at the top. Orange dots indicate Raman analysis spots. Their numbers correspond to the numbers in Figure III-4B and Table III-2.

Kerogen D- and G- bands are composed of multiple bands that are attributed to various kerogen components. The exact number and positions of the bands that compose the D- and G-bands is a subject of debate, but typically four to six possible bands are identified in deconvoluted kerogen spectra (see Henry et al., 2019 and Schito et al., 2023 for recent reviews of the debate). The D-band reflects the presence of disordered organic matter and is composed of a main D1-band that can be accompanied by one to three less intense bands that are likely associated with the presence of aliphatic hydrocarbon chains (Henry et al., 2019; Schito et al.,

2023). The G-band is composed of a main G1-band that appears at 1582 cm^{-1} in crystalline graphite Raman spectra (Henry et al., 2019; Schito et al., 2023). The G1-band can be accompanied by one or two less intense bands that are likely associated with defects and the presence of hydrogen, oxygen, and other non-carbon atoms.

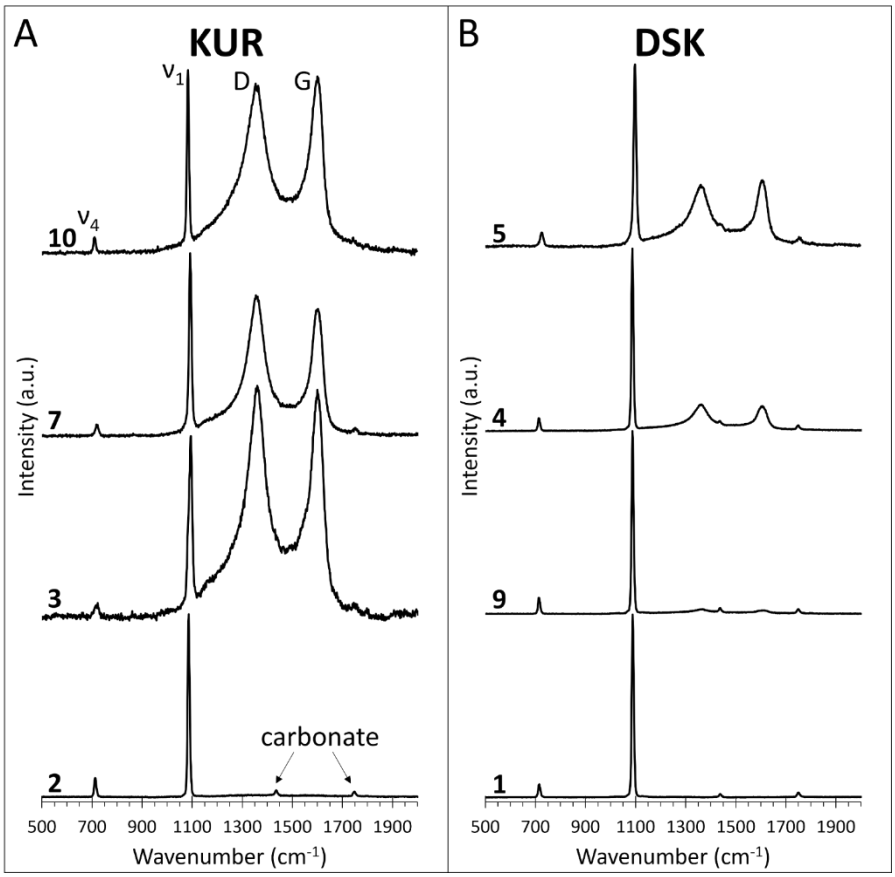

Figure III-4. Representative Raman spectra of the KUR and DSK samples, baseline subtracted and normalized to the ν_1 carbonate peak. Spectra are numbered according to their collection spot, as labeled in Figures S1 and S2. The carbonate and kerogen peaks discussed in this paper are labeled in spectrum 10 of panel A. Two secondary carbonate peaks that are not discussed in this paper are labeled in spectrum 2 of panel A. A) KUR spectra **2**. Spectrum collected from void fill (Fig. S1, point 2) showing no kerogen detection and calcite with 0 to 5.5 mol% $MgCO_3$ **3**. Spectrum collected from draping laminae (Fig. S1, point 3) showing kerogen and calcite with 20 to 50 mol% $MgCO_3$ **7**. Spectrum collected from a support structure (Fig. S1, point 7) showing kerogen and calcite with 20 to 50 mol% $MgCO_3$ **10**. Spectrum collected from contorted laminae (Fig. S1, point 10) showing kerogen and calcite. B) DSK spectra **1**. Spectrum collected from void fill (Fig. S2, point 1) showing no kerogen and calcite with 10.5 to 20 mol% $MgCO_3$. **9**. Spectrum collected from herringbone calcite (Fig. S2, point 9) showing a weak kerogen signal and calcite with 10.5

to 20 mol% $MgCO_3$ **4**. Spectrum collected from draping laminae (Fig. S2, point 4) showing kerogen and calcite with 10.5 to 20 mol% $MgCO_3$ **5**. Spectrum collected from a support surface (Fig. S2, point 5) showing kerogen and dolomite detections. See the section of this chapter titled Dolomitization below for a discussion of the carbonate peaks in these spectra.

As kerogen approaches thermal maturity, it loses heteroatoms and aliphatic hydrocarbons, eventually becoming molecularly indistinguishable from graphite. The changes that kerogen undergoes when heated result in predictable changes to its characteristic Raman bands. Therefore, several researchers have proposed geothermometry approaches based on various parameters of kerogen Raman spectra, including the full width at half maximum (FWHM) of the D- and G-bands, D- and G-band positions, the ratio of D- and G-band intensity, and the ratio of or total D- and G-band area (see Henry et al., 2019 and Schito et al., 2023 for recent reviews).

Table III-1. KUR Raman data, including morphological features and kerogen and carbonate peak parameters. Point numbers correspond to labeled points in Figure III-2.

Point	Associated Feature	D1-Band Center (cm^{-1})	D1-Band FWHM (cm^{-1})	G-band Center (cm^{-1})	Carbonate v_1 (cm^{-1})	Carbonate v_4 (cm^{-1})
5	Contorted Lamina	1359	77	1604	1084	711
		1359	77	1604	1085	712
		1362	53	1603	1085	712
9	Contorted Lamina	1359	89	1602	1083	710
		1358	69	1603	1083	710
		1360	63	1604	1084	710
10	Contorted Lamina	1358	86	1600	1083	711
		1358	75	1604	1083	711
		1354	91	1603	1083	711
3	Draped Lamina	1360	65	1603	1093	717
		1358	69	1600	1095	722
		1362	60	1601	1090	714
8	Planar Lamina	1364	83	1611	1092	719
		1369	86	1612	1092	719
		1367	71	1612	1092	719
1	Support	1366	73	1610	1094	722
		1368	70	1611	1094	719
		1366	74	1610	1094	718
6	Support	1363	60	1607	1096	723
		1357	66	1598	1085	713
		1363	59	1605	1095	722
7	Support	1357	63	1603	1092	720
		1356	80	1603	1092	719
		1358	61	1602	1093	721
2	Void	ND	ND	ND	1086	713
		ND	ND	ND	1088	714
		ND	ND	ND	1087	713
4	Void	ND	ND	ND	1087	714
		ND	ND	ND	1091	719
		ND	ND	ND	1091	718

ND indicates that there was no detection of the indicated band at that point.
Carbonate peak fitting errors are ± 0.06 to 1.5 cm^{-1}.
D1-band peak fitting errors are ± 0.8 to 11.5 cm^{-1}.
G-band peak fitting errors are ± 0.3 to 4.7 cm^{-1}.

Table III-2. DSK Raman data, including morphological features and kerogen and carbonate peak parameters. Point numbers correspond to labeled points in Figure III-3.

Point	Associated Feature	D1-Band Center (cm^{-1})	D1-Band FWHM (cm^{-1})	G-band Center (cm^{-1})	Carbonate ν_1 (cm^{-1})	Carbonate ν_4 (cm^{-1})
2	Herringbone	1359	NA	1604	1088	715
		1364	NA	1608	1088	715
		1363	NA	1603	1088	715
6	Herringbone	1365	NA	1608	1088	715
		1362	NA	1604	1089	715
		1355	NA	1605	1088	714
8	Herringbone	1360	NA	1606	1088	715
		ND	ND	ND	1087	714
		1357	NA	1605	1087	714
9	Herringbone	1363	70	1606	1088	715
		1362	70	1607	1088	715
		1361	69	1606	1088	715
7	Linear	1361	67	1605	1087	713
		1365	NA	1601	1088	715
		1363	52	1600	1087	714
5	Support	1360	81	1604	1097	725
		1368	NA	1608	1089	716
		1365	50	1604	1088	715
10	Support	1358	73	1605	1088	715
		1357	NA	1610	1088	715
		1366	52	1601	1088	715
3	Draped Lamina	1364	NA	1604	1088	715
		1362	NA	1602	1088	714
		1361	81	1608	1088	714
4	Draped Lamina	1359	72	1605	1087	715
		1361	72	1608	1088	715
		1363	74	1606	1087	714
1	Void	ND	ND	ND	1089	716
		ND	ND	ND	1089	716
		ND	ND	ND	1088	715

ND indicates that there was no detection of the indicated band at that point.
NA indicates that Raman bands were not intense enough to fit according to Kouketsu et al., 2014.
Carbonate peak fitting errors are ± 0.06 to 1.5 cm^{-1}.
D1-band peak fitting errors are ± 0.8 to 11.5 cm^{-1}.
G-band peak fitting errors are ± 0.3 to 4.7 cm^{-1}.

Several Raman geothermometry approaches involve deconvolving kerogen spectra into three or four bands, depending on spectral characteristics, and finding the FWHM of the D1-band in the deconvoluted spectrum. Using that approach, Kouketsu et al. (2014) showed that the D1-band FWHM closely correlates with peak metamorphic temperature when that temperature falls between 150 and 400°C, with an error of approximately ±30°C. The correlation is described by the following equation:

$$T(°C) = -2.15(\text{D1-FWHM}) + 478 \quad \text{(Equation III-1)}$$

In all KUR and DSK spectra with adequately intense kerogen bands, I deconvolved the bands according to the protocol of Kouketsu et al. (2014) and determined the FWHM for the D1-band in each (Tables III-1 and III-2). Table III-3 shows the range of peak metamorphic temperatures calculated for the KUR and DSK samples according to Equation III-1. KUR and DSK D1-band FWHM indicate possible peak metamorphic temperatures between 282 and 366 ± 30ºC. The average D1-band FWHM in the KUR and DSK correspond to similar peak metamorphic temperatures of 323 and 332 ± 30°C. Although the range is similar between the two samples, it is markedly different from the peak temperature range of approximately 100 to 180°C that is indicated by mineral phase relations and clumped isotope geothermometry (Miyano and Beukes, 1984; Levitt et al., 2015).

The discrepancy between the Raman geothermometry results presented here and the results of previous geothermometry efforts indicates that additional investigation into the thermal history of the CMCP is warranted. However, it is not necessarily due to a difference in peak metamorphic temperatures between samples. Rather than reflecting the thermal history of the samples, the Raman geothermometry results could be due to unknown factors that impact the

accuracy of previously reported kerogen-based Raman geothermometry methods (e.g., Kouketsu et al, 2014), which could include influences of the host rock, the presence of catalysts, the composition of the starting material, the age of the material, or other factors.

Table III-3. Maximum, minimum, and average kerogen D-band full width half maxima (FWHM) in KUR and DSK spectra after peak fitting, followed by the corresponding peak metamorphic temperatures, according to Kouketsu et al., 2014. The greatest FWHM corresponds to the lowest peak metamorphic temperature.

Sample	Maximum FWHM (cm^{-1})	Minimum FWHM (cm^{-1})	Average FWHM (cm^{-1})	Minimum Temperature (°C)	Maximum Temperature (°C)	Average Temperature (°C)
KUR	91	53	72 (σ=10.2)	282 ± 30°C	364 ± 30°C	323 ± 30°C
DSK	81	52	68 (σ=9.9)	304 ± 30°C	366 ± 30°C	332 ± 30°C

The starting material and age of the kerogen in the fenestrate microbialite samples differ significantly from that of the kerogen Kouketsu et al. (2014) used in their study. Kouketsu et al. calibrated their Raman geothermometer using samples from the Jurassic period to the Eocene epoch, meaning that the oldest samples were at most ~200 million years old (2014). The starting materials of 200-million-year-old kerogen would have contained organic molecules not produced by Neoarchean lifeforms, such as steranes, making them different from the starting materials of 2.5 billion-year-old kerogen. This difference may be reflected in the Raman spectra of the kerogen.

The time that has passed since the Archean kerogen formed is an order of magnitude greater than the time that has passed since the Jurassic kerogen formed. As explained above, the FWHM of the kerogen D1-band is known to decrease as aliphatic molecules and heteroatoms are eliminated from the material. This process, known as aromatization, occurs more rapidly as temperatures increase. However, the rate of aromatization may be high enough at relatively low temperatures that, over billions of years, the D-band parameters change to the extent that it appears as though the kerogen was exposed to high temperatures. This would only be apparent in

Archean sedimentary rock that has never been exposed to high metamorphic temperatures, which is a rare occurrence.

Morphology

Mesoscopic Structures Observed in 3D Reconstructions

The KUR 3D reconstruction reveals five horizons, each with morphologically distinct kerogen-rich structures (Fig. III-5). I identified the structures of each horizon according to the established terminology described in the introduction (Sumner, 1997a; Sumner, 2000). The lowest horizon, which occupies the bottom 2.3 cm of the slab, consists of contorted laminae (Fig. III-5D, E, and F, lower white outline). Immediately above this horizon is a 0.4 cm layer of planar laminae (Fig. III-5D, E, and F, orange outline). Above the planar laminae is a 2.2 cm horizon in which the laminae transition from planar laminae to cuspate structures with millimeter-scale relief (Fig. III-5D, E, and F, green outline). Above the cuspate horizon is a ~1 cm tall tented structure consisting of a narrow support structure, which is only partially visible in my reconstruction (Fig. III-5E, pink outline), over which filmy laminae drape (Fig III-5D, E, and F, cyan outline). The uppermost horizon, which takes up the remainder of the slab, again contains randomly oriented contorted laminae (Fig III-5D, E, and F, upper white outline).

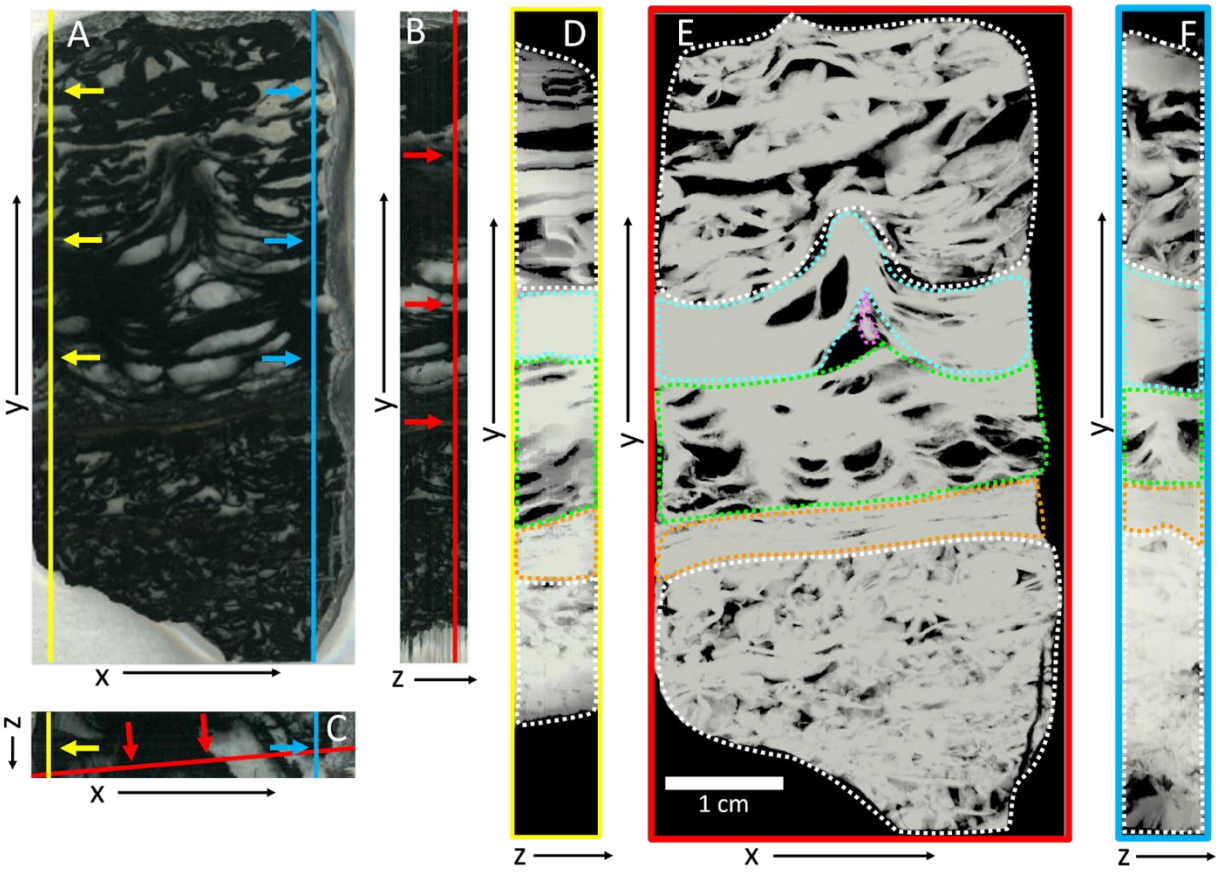

Figure III-5. Three-dimensional reconstruction of sample KUR (~6.8 x 3.0 x 0.8 cm slab of fenestrate microbialite from Kuruman Kop; see Figure 2). Panels A, B, and C are true-color renderings of the center XY, YZ, and XZ planes of the KUR scan stack, respectively. Panels D, E, and F are views of a 3D reconstruction of the stack. The white structures of the reconstruction correspond to the black structures in the original images. The yellow lines in panels A and C indicate the plane shown in panel D and the yellow arrows indicate which face of that plane is shown. The blue lines in panels A and C indicate the plane shown in panel F and the blue arrows indicate which face of that plane is shown. The red line in panel B indicates the axis around which the plane pivoted to create the view in panel E. The red line in panel C indicates the plane shown in panel E. The red arrows in panels B and C indicate the face of the plane shown in panel E. In panels D, E, and F, white outlines indicate contorted laminae, orange outlines indicate planar laminae, green outlines indicate wavy/peaked laminae, pink outline indicates a support structure, and cyan outlines indicate draping laminae. See also the supplemental GIFs showing the entire image stack used for this reconstruction and a rotating view of the reconstruction, and Fig. III-7A, which is a cartoon representation of the morphological structures in KUR.

Instead of distinct horizons like those in KUR, the DSK 3D reconstruction reveals a configuration of interconnected support structures (Fig. III-6D, E, F, and G, pink outlines), linear

structures (as described by Rivera and Sumner, 2014; Fig. III-6D, E, F, and G, green outlines), and filmy laminae (Fig. III6F, cyan outline). The leftmost pink outline in Figure III-6D indicates a support surface that spans the full depth of the DSK reconstruction. This support surface is also visible in the upper region of panels F and G of Figure III-6, where it is again outlined in pink. Unlike the partially visible KUR support structure, which extends vertically like a support pole in the center of draping laminae, this DSK support is wall-like in that it extends vertically and horizontally in space. Such wall-like support surfaces have been called irregular surfaces (Sumner, 1997a). DSK also features support structures that extend linearly vertically to horizontally, but not along a wall-like plane. Support walls and support structures in DSK support draping laminae (Fig. III-6F, cyan outline) and linear structures (Fig. III-6D, E, F, and G, green outlines). Like support structures, the linear structures in DSK extend vertically to horizontally, but not along a wall-like plane. Linear structures are similar to support structures, but they tend to be less dense with kerogen, which makes them appear fainter in 3D reconstruction (Fig. III-6D, E, F, and G). In addition, linear structures extend between and connect support structures but do not support other linear structures or laminae as support structures do.

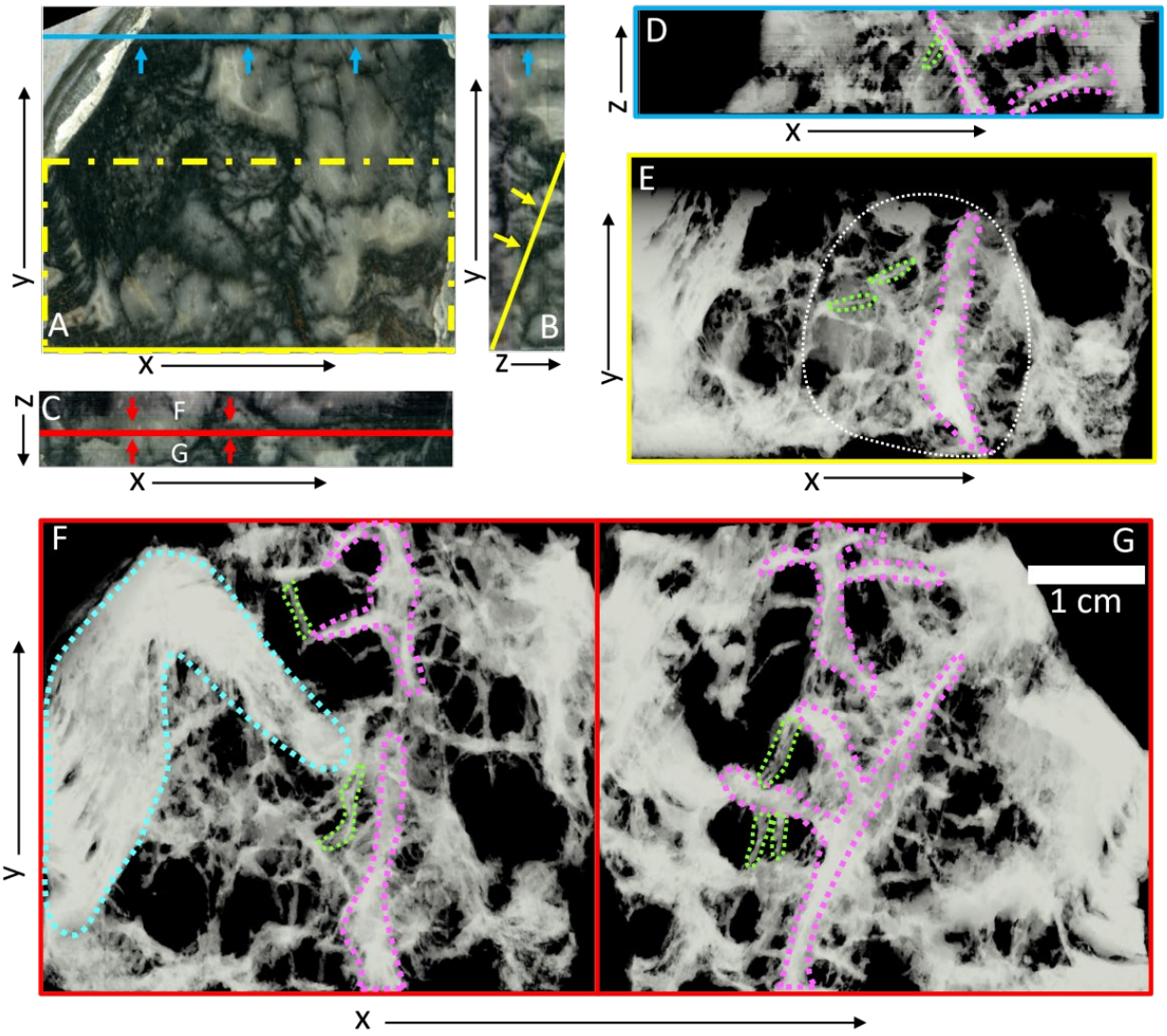

Figure III-6. Three-dimensional reconstruction of fenestrate microbialites from sample DSK (~5.2 x 4.3 x 0.8 cm slab from a farm near Danielskuil; see Figure 2) exhibiting plumose microbialite morphology. Panels A, B, and C are true-color renderings of the center XY, YZ, and XZ planes of the DSK scan stack, respectively. Panels D, E, F, and G are views of a 3D reconstruction of the stack. The white structures of the reconstruction correspond to the black structures in the original images. The blue lines in panels A and B indicate the plane shown in panel D and the blue arrows indicate which face of that plane is shown. The dashed yellow box in panel A indicates the approximate outline of the plane shown in panel E, with the lower side of the box at the surface of the scan stack and the upper side of the box reaching the bottom of the stack. The yellow line in panel B indicates the plane shown in panel E and the yellow arrows indicate which face is shown. The red line in panel C indicates the plane shown in panels F and G and the red arrows indicate which face of that plane is shown in each panel. In panels D, E, F, and G, pink outlines indicate select support surfaces and structures, green outlines indicate select linear structures, the cyan outline indicates laminae, and the white circle surrounds a radial configuration of support and linear structures. See also the supplemental GIFs of

the entire image stack used for this reconstruction and a rotating view of the reconstruction and Fig. III-7B, which is a cartoon representation of the morphological structures in DSK.

The configuration of support surfaces, vertical to horizontal support structures, and linear structures in DSK includes an arrangement of support and linear structures radiating away from a support surface (Fig. III-6E, encircled in white). This radial arrangement is consistent with the morphology of plumose microbialites as described by Sumner (1997a) and Rivera and Sumner (2014). In particular, support surfaces are characteristic of plumose microbialites (Stevens et al., 2011; River and Sumner, 2014). There is no obvious support structure associated with the draping laminae in the DSK 3D reconstruction (Fig. III-6F, cyan outline), but a central support structure is visible supporting draping laminae in the same region in a thin section prepared from the hand sample used for the 3D reconstruction (Fig. III-8A, cyan outline, and B). Lower in the thin section, the same support structure is supporting radially arrayed plumose microbialite morphology (Fig. III-8A, white outline), which indicates that this structure is intermediate between plumose and tented microbialite morphology.

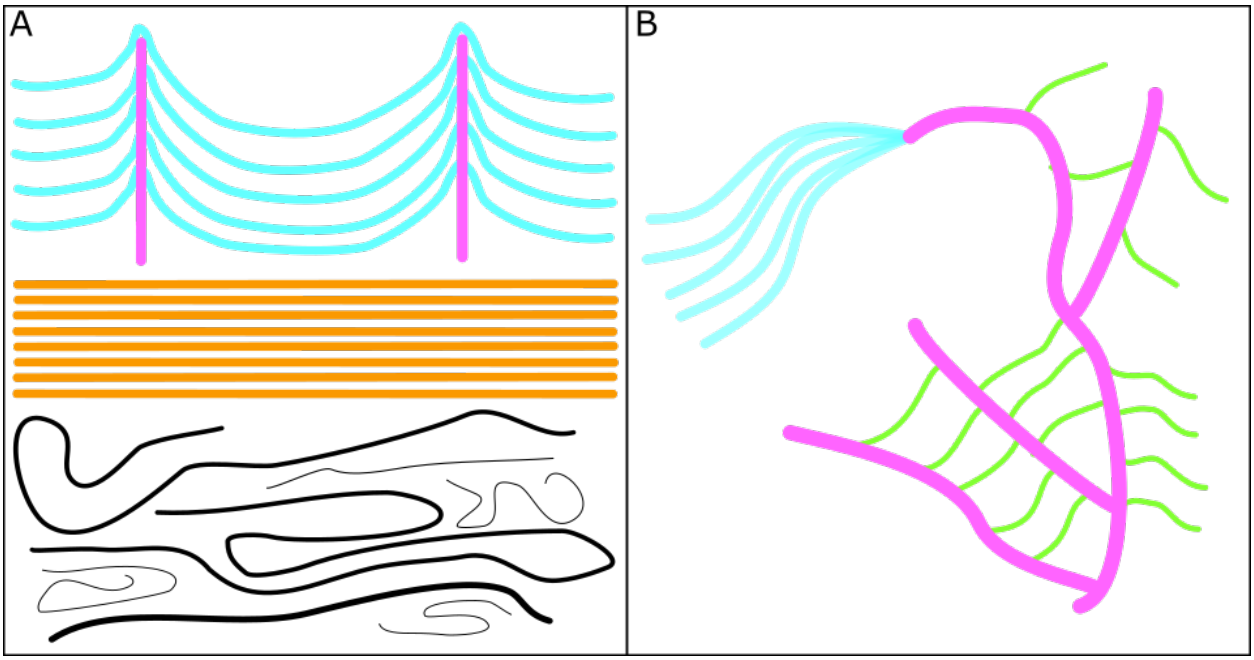

Figure III-7. Schematics illustrating the mesoscopic morphology revealed in our 3D reconstructions of Gamohaan formation carbonate microbialites. A. A simplified illustration of the mesoscopic morphological structures observed in KUR that includes support structures (pink), draping laminae (cyan), planar laminae (orange), and contorted laminae (black). B. A simplified illustration of the mesoscopic morphological structures observed in DSK that includes support structures (pink), linear features (green), and draping laminae (cyan). The color of each morphological structure (support, planar laminae, etc.) other than the contorted laminae in panel A corresponds to the color in which the same type of morphological structure is outlined in Figs. 4, 5, 6, and 8. Contorted laminae in Figs. 4 and 8 are outlined in white.

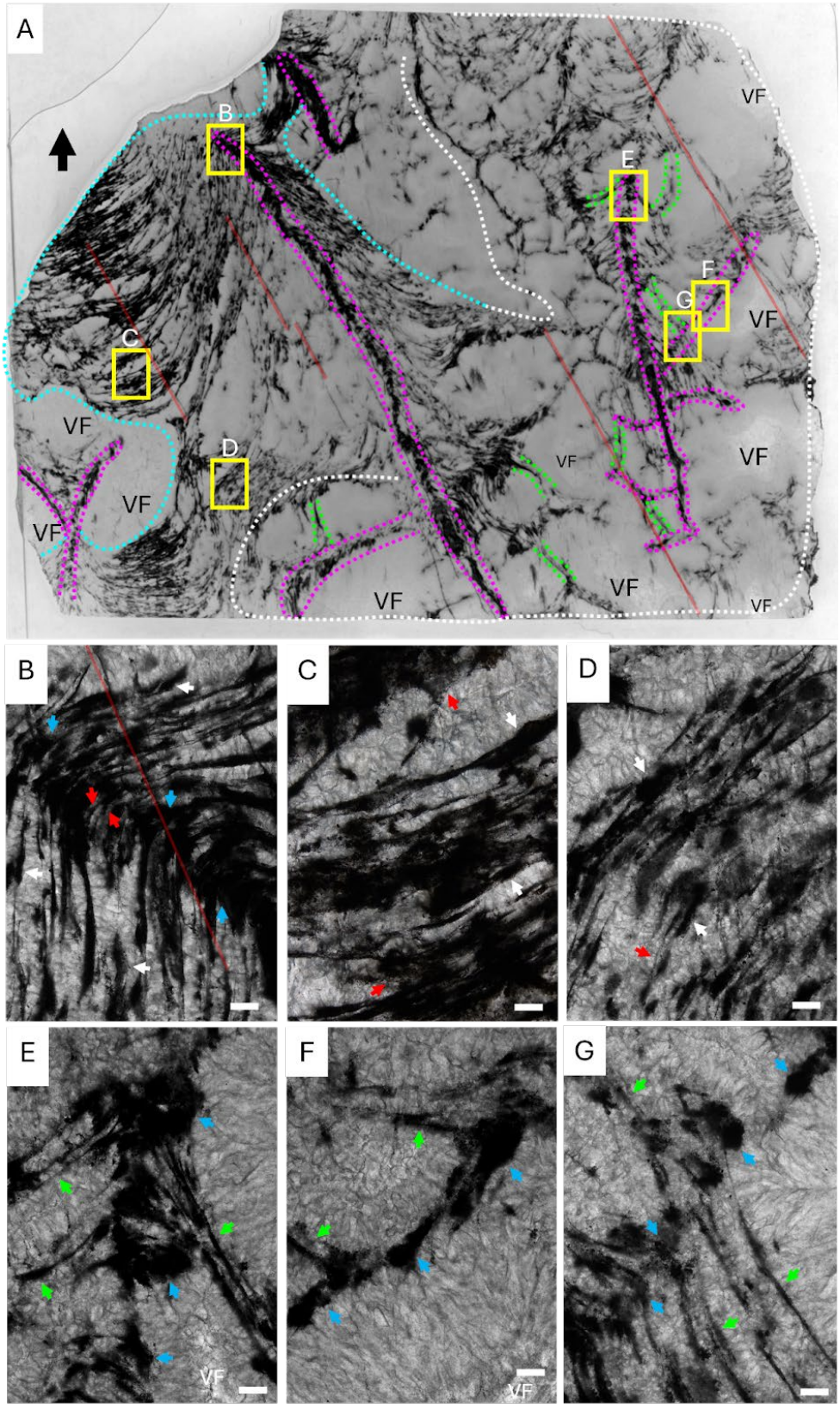
A
B
C
D
E
F
G
VF
VF
VF
VF
VF
VF
VF
VF
VF
VF
B
C
D
E
F
G
VF
VF

Figure III-8. Photomicrographs of morphological structures within a thick thin section of the DSK sample. A. Scan of the thin section with yellow boxes indicating the locations of each of the structures in panels B through G. Colored dashed outlines correspond to morphological features as described in Figure 5. Only some examples of support and linear structures are outlined because highlighting all of them would obscure the image. The cyan outline around draping lamiae is continuous with the white outline around radial plumose structures to indicate that the morphologies grade into each other. Transparent red lines in panels A and B highlight examples of parallel microfractures that traverse DSK, which can be seen as straight, thin, dark lines across the scan. B. Support structure and draping laminae. White arrows point to examples of OM clots associated with laminae, blue arrows point to examples of clotted OM within the support structure, red arrows point to examples of laminae passing through the support structure. C and D. Draping laminae. White arrows point to examples of OM clots. Red arrows point to laminae intersecting with the surface of the thin section. E and F. Support structures and linear features. Green arrows point to linear features with associated and blue arrows point to clotted OM within support structures. G. Support structure and linear features. Green arrows point to linear features with associated clotted OM and blue arrows point to clotted OM within the support structure. VF indicates void filling carbonate. The remaining matrix is herringbone carbonate. B to G scale bars = 200 μm.

Microscopic Textures

Previous researchers have hypothesized that certain microscopic textures preserved within Gamohaan fenestrate microbialite structures suggest the original nature of the microorganisms that formed those structures. Sumner (1997a) described the filmy laminae preserved within the Gamohaan microbialites as “very fine laminae defined by organic inclusions” that provide “strong evidence for the presence of microbial communities that influenced the morphology” of the microbialites. Sumner (2000) further suggested that the filmy laminae “are the remnants of microbial mats composed of filamentous microbes with diameters of only a few microns.” Within contorted laminae, Wright and Altermann (2000) noted that the parallel organization of “elongate strands” indicates their “original filamentous nature.”

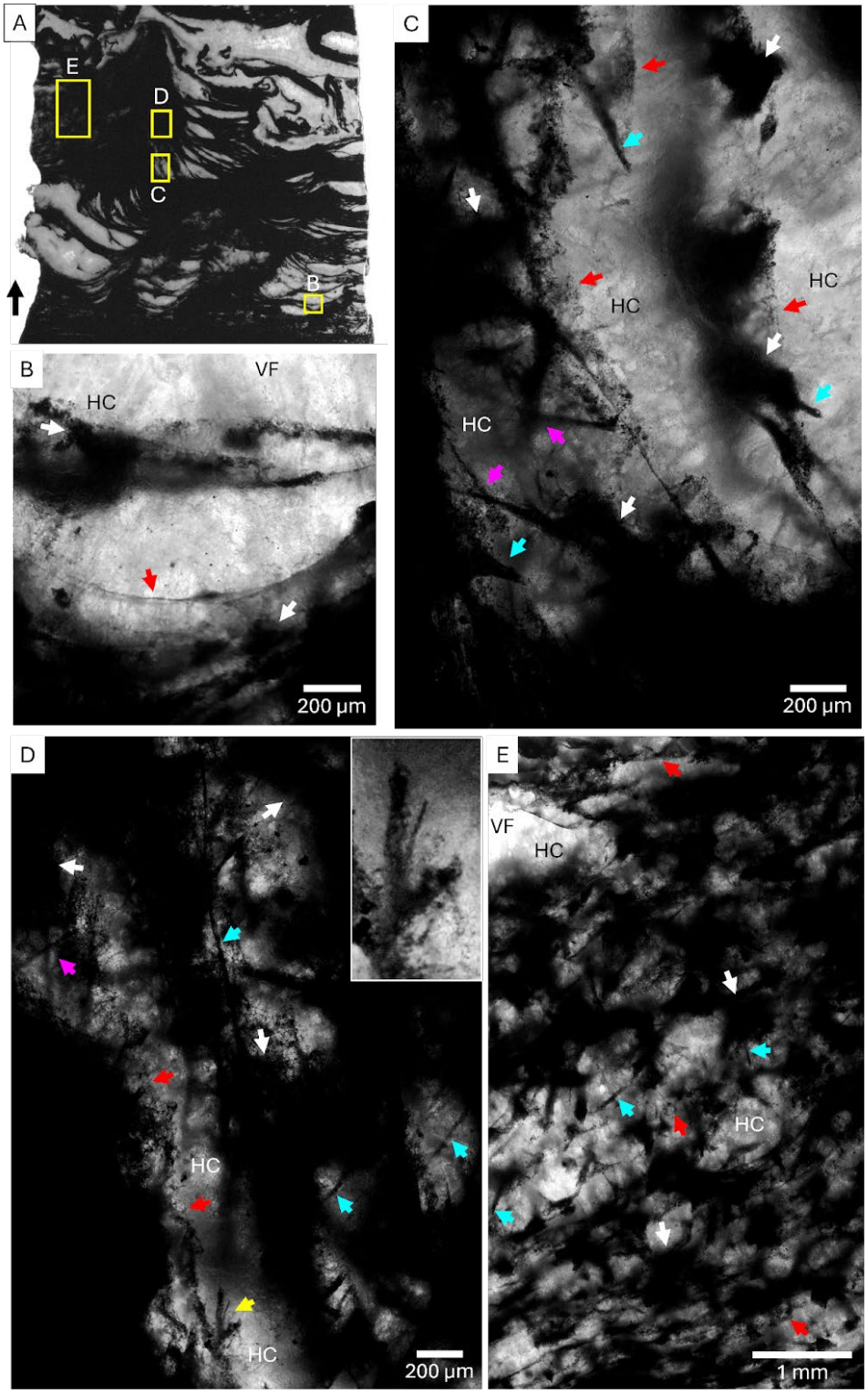

Figure III-9. Photomicrographs of morphological structures within a thick thin section of the KUR sample. A. Partial scan of the thin section with yellow boxes indicating the locations of each structure imaged in panels B through E. The thick thin section was prepared from the same billet as the petrographic thin section in Figure III-10 and therefore

features the same morphological structures as those outlined in Fig. III-10A. In all panels, HC indicates herringbone carbonate that formed contemporaneously with microbial growth and VF indicates void filling carbonate that formed after microbial growth ceased. B. Draping laminae between support structures within a cuspate structure. The red arrow indicates hyaline film. C to E. Draping laminae within a tented structure. Red arrows point to the edges of distinctive laminae where they intersect with the surface of the thin section. Cyan arrows indicate linear features that follow the same plane as the draping laminae. Pink arrows indicate instances in which the linear features cross over each other. The yellow arrow indicates a bundle of linear features separating into multiple linear features, shown in greater detail in the inset image.

Petrographic study of the KUR sample revealed filmy laminae within cuspate structures similar to those Sumner (2000) suggested were originally composed of narrow filamentous microbes (Fig. III-9B, red arrow). However, the laminae within the tented structure have a granular rather than filmy texture. Furthermore, the laminae of the tented structure are associated with filament-like linear features that do not occur in any other laminae within thin sections prepared from KUR or DSK samples (Fig. III-9C to E, cyan, pink, and white arrows; III-10C, pink arrow).

The filament-like linear features within the draping laminae of the tented structure in KUR are approximately 10 to 50 μm wide (Fig. III-9, cyan and pink arrows). Where tented structure laminae intersect obliquely with the thin section surface, segments of filament-like linear features up to several hundred microns long can be seen following the plane of the draping lamina in which they are found (Fig. III-9C and D, cyan arrows). Where laminae intersect with the surface approximately perpendicularly, only short segments of the filament-like structures can be seen (Fig. III-9E, cyan arrows). The filament-like linear features are not arranged in parallel within the laminae. There are several examples of filament-like linear features crossing over each other within draping laminae (Fig. III-9C and D, pink arrows) and one instance in which an apparent bundle of linear features separates into three distinct filament-like linear features (Fig. III-9D, yellow arrow and inset image).

Draping laminae in cuspate and tented structures in both the KUR and DSK samples and linear structures in the DSK sample are associated with clots of OM that appear to be continuous with the structures (Figs. III-8B to G; III-9C to D; III-10C, E, F, G, and I, white arrows). The support structures in KUR and DSK samples are entirely composed of similarly textured clotted OM (Figs. III-8B, E to G; III-10D, E, and G, blue arrows). In some cases, laminae pass through the clotted OM within support structures (Fig. III-8B, red arrows). Planar laminae in the KUR sample are associated with compact masses of OM rather than clotted OM (Fig. III-10H and I, cyan arrows). Unlike the OM clots, there are compact OM masses associated with planar laminae that are discontinuous with the laminae. They occur between laminae, often not in contact with the laminae (Fig. III-10H, I, K, cyan arrows). In one instance a collection of compact OM masses formed between the planar and contorted laminae horizons (Fig. III-10K). The collection is approximately triangular in cross section, with a height of approximately 1.2 mm and a diameter at its base of approximately 1.8 mm.

The contorted laminae in petrographic thin sections prepared from sample KUR are composed of elongate parallel features (Figs. III-10B and J) and appear very similar to the contorted laminae in Figure 7 of Wright and Altermann (2000). Wright and Altermann described the elongate parallel features as “elongate strands and remnant sheaths” and, as mentioned above, suggested that their presence indicated the “original filamentous nature” of the microorganisms that formed the contorted laminae. In photomicrographs, the features appear strand-like (Figs. III-10B and J), but the elongate parallel features appear to be rolled laminae rather than strands in the serial images of the KUR 3D reconstruction reported here (KUR z-stack GIF). This observation does not eliminate the possibility of an “original filamentous nature” for the contorted laminae. However, it indicates that the filaments were more likely “a

few microns" in diameter, like those Sumner (2000) suggested formed the draping laminae of cuspate structures, rather than *Siphonophycus*-like microbial sheaths, as some have interpreted (Wright and Altermann, 2000; Warke et al., 2019). Neither the OM clots that are associated with draping laminae nor the compact OM masses that are associated with planar laminae occur in association with the contorted laminae.

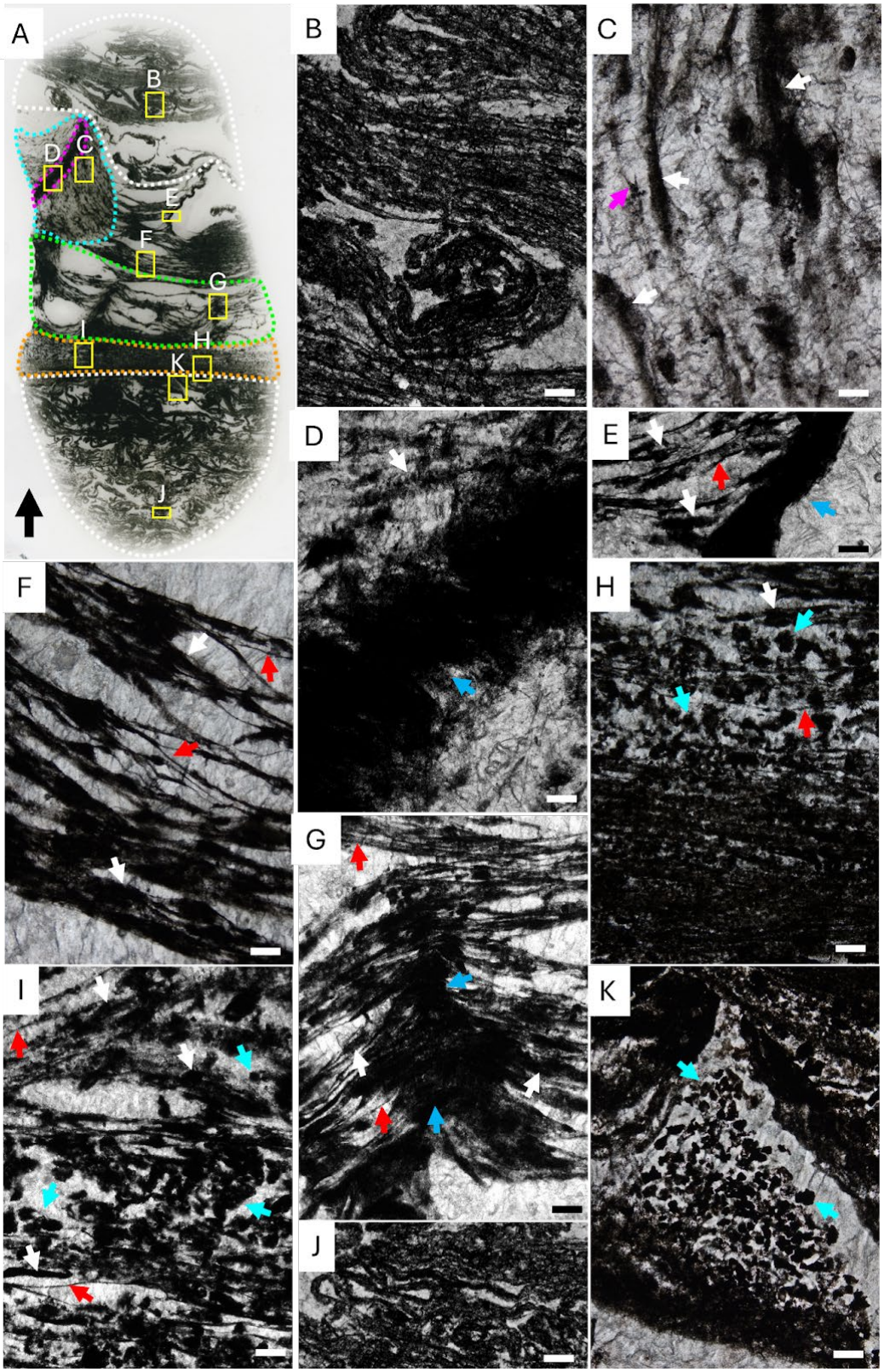
A
B
C
D
E
F
G
H
I
J
K

Figure III-10. Photomicrographs of morphological structures within a petrographic thin section of the KUR sample. A. Scan of the thin section with yellow boxes indicating the locations of each of the structures in B to K. Colored dashed outlines correspond to morphological features as described in Figure 4. B. Contorted laminae in the upper horizon showing parallel features like those that Wright and Altermann (2000) suggested were indicative of the "original filamentous nature" of the microorganisms. C. Draping laminae of a tented structure. White arrows indicate examples of OM clots. D. Support structure of a tented structure. White arrow indicates an example of an OM clot within the laminae. The black feature running diagonally through the panel is the support structure, which consists of clotted OM, blue arrow. E. draping laminae that terminate at a support structure. White arrows indicate examples of OM clots within laminae. Red arrow indicates an example of a filmy lamina. The blue arrow indicates the support structure. F. Laminae (red arrows) within an area of the thin section that is transitional between cuspate and tented structures. Note the presence of OM clots (white arrows) and lack of compact OM masses. G. A support structure (blue arrows) within cuspate structures. Red arrows indicate laminae. H. Planar laminae. Red indicates a lamina. The white arrow indicates an example of an OM clot and the cyan arrows indicate examples of compact OM masses. I. Planar laminae (lower red arrow) transitioning to overlying draping laminae (upper red arrow). Note that the OM masses transition from mostly compact (cyan arrows) to mostly clotted (white arrows) as the laminae transition from planar to draping. J. Contorted laminae in the lower horizon showing bundles of parallel features that are narrower than the bundles in panel B. K. Compact OM masses piled in a space between planar and contorted laminae. B to K scale bars = 200 μm.

Microbial Community Interpretation

Th 3D reconstructions of Gamohaan fenestrate microbialite morphologies presented here are consistent with previous suggestions that their morphological complexity results from interacting microbial communities with motile components. Variations in microscopic textures preserved within the microbialite structures (Figs. III-8, III-9, and III-10) further support the conclusion that morphologically distinct structures within the fenestrate microbialites were formed by different microbial communities. The association of filament-like linear structures with the filmy laminae of a tented structure (Figs. III-9 and III-10, cyan and pink arrows)

Table III-4. Results from previous sulfur isotope measurements in pyrites preserved within Gamohaan fenestrate microbialites showing the source study, the morphology of the microbialite in which the measured pyrite was preserved, reported $\Delta^{33}S$ values, the sulfur source indicated by $\Delta^{33}S$ values, reported $\delta^{34}S$ values, and the sulfide formation process indicated by $\delta^{34}S$ values (Kamber and Whitehouse, 2007; McLoughlin et al., 2023).

Study	Sample Morphology	$\Delta^{33}S$ values	Sulfur Source	$\delta^{34}S$ values	Sulfide Formation
Kamber and Whitehouse (2007)	Pyrite spheroid in contorted laminae	-0.91 to -0.35‰	Sulfate formed via atmospheric photochemistry	-8 to +4‰, increasing from spheroid core to rim	MSR in a sulfate-limited environment
McLoughlin et al. (2023)	Pyrite spheroid in contorted laminae	-0.35 to +0.11‰	Sulfate formed via atmospheric photochemistry	-3.9 to +10‰, not increasing from core to rim	MSR in a sulfate-rich environment
McLoughlin et al. (2023)	Dispersed pyrite grains in contorted laminae	+1.7 to +12.6‰	Sulfate formed via atmospheric photochemistry and oxidized bacterially produced sulfides	+3.1 to +30.6‰	MSR under a fluctuating chemocline, in moderately oxygenated to dysoxic or anoxic waters
McLoughlin et al. (2023)	Pyrite grains in cuspate support structure and draping laminae	+7.7 to +10.5‰	S_n formed via atmospheric photochemistry	+4.8 to +12.0‰	Microbial sulfur disproportionation

Combining the 3D reconstructions and petrographic investigations presented above with previously reported spatially resolved sulfur isotope measurements (Kamber and Whitehouse, 2007; McLoughlin et al., 2023; Table III-4), suggests some specific microbial interactions that might have contributed to their morphology. The pyrite sulfur isotope values reported by Kamber and Whitehouse (2007) and McLoughlin et al. (2023) indicate that MSR and sulfur disproportionating microorganisms (SDM) were among the microorganisms that contributed to the formation of the Gamohaan fenestrate microbialites, which suggests the presence of a flourishing system of sulfur cycling microorganisms. The reported sulfur isotope values also suggest that at least some of those sulfur cycling microorganisms existed in a fluctuating moderately oxygenated to dysoxic environment (McLoughlin et al., 2023; Table III-4). Fluctuating low oxygen levels are consistent with the presence of oxygenic photosynthetic microorganisms in nearshore waters. However, higher oxygen concentration would be expected

if the Gamohaan fenestrate microbialites were the remains of phototactic cyanobacteria-like microorganisms, as suggested by Beukes (1987).

The presence of OM clots within draping laminae, similarly textured clotted OM within support structures, and compact OM among the planar laminae (Figs. III-8, III-9, and III-10, white, blue, and cyan arrows) may support the claim that the microorganisms that formed the Gamohaan fenestrate microbialites included MSR. Modern MSR are a diverse group of microorganisms that includes motile, rod-shaped bacteria that migrate within microbial mats in search of optimal growing conditions and are known to flocculate, creating compact aggregates with dysoxic centers, in response to increased oxygen levels (e.g., Krekeler et al., 1997; Krekeler et al., 1998; Sigalevich et al, 2000). The clotted OM are consistent with populations of MSR migrating upwards in search of sulfate under dysoxic to anoxic conditions. Modern motile, rod-shaped bacteria that migrate in this way are only a few microns in their longest dimension (Krekeler et al., 1997). Microorganisms of this size have never been preserved as assured recognizable individual microfossils in Archean to Paleoproterozoic rocks, but clusters of such MSR could be preserved as clotted OM. Furthermore, the compact OM masses, which are associated with planar laminae (Fig. III-10H, I, and K), may represent populations of MSR that underwent flocculation in response to rising oxygen levels. Because the plumose microbialites preserved within DSK commonly feature the same clotted OM observed within cuspate and tented microbialites but do not feature any compact OM masses (Fig. III-8, blue and white arrows), the plumose morphology may have arisen during periods when oxygen levels were consistently low.

The amorphous appearance of the clotted OM is likely a primary texture rather than a taphonomic artifact because it occurs in association with well-preserved, delicate textures, such

as the hyaline filmy lamina in Figure III-9B, and because the texture is consistently associated with specific mesoscale morphological features. It is unlikely that a taphonomic process that imparted an amorphous texture on organic matter would, for example, impact a support structure without impacting the laminae passing through that structure, as in Figure III-8B.

Dolomitization

Raman spectroscopy was used to assess dolomitization in the KUR and DSK samples. Calcite ν_1 and ν_4 Raman peaks occur at approximately 1080 to 1090 cm^{-1} and 710 to 720 cm^{-1}, respectively, and dolomite ν_1 and ν_4 peaks occur at approximately 1095 to 1105 cm^{-1} and 720 to 730 cm^{-1}, respectively (Gunasekaran et al., 2006; Buzgar and Apopei, 2009; Armbruster and Danisi, 2016). In magnesian calcite, or calcite in which less than 50% of the Ca^{2+} has been replaced by Mg^{2+}, the ν_1 and ν_4 peak positions increase linearly with increasing magnesium content. Using data collected from carbonate and dolomite standards as well as biogenic magnesian calcite of known composition, Borromeo et al. (2017) demonstrated that the linear relationship between ν_1 and ν_4 peak positions allows for the estimation of magnesium content in carbonates in the solid solution between calcite and dolomite using Raman spectra.

Following Borromeo et al. (2017), I plotted the average ν_1 and ν_4 peak positions of three Raman spectra collected within tens of microns of each other at each of ten morphologically distinct spots on both the KUR and DSK samples (Fig. III-11; see Figs. III-2 and III-3 for Raman analysis spots and Tables III-1 and III-2 for peak positions). The resulting plot indicates very different patterns of dolomitization in my KUR and DSK samples. In my analysis, the magnesium content of KUR varies between morphological structures while the magnesium content of DSK is fairly consistent across the entire sample.

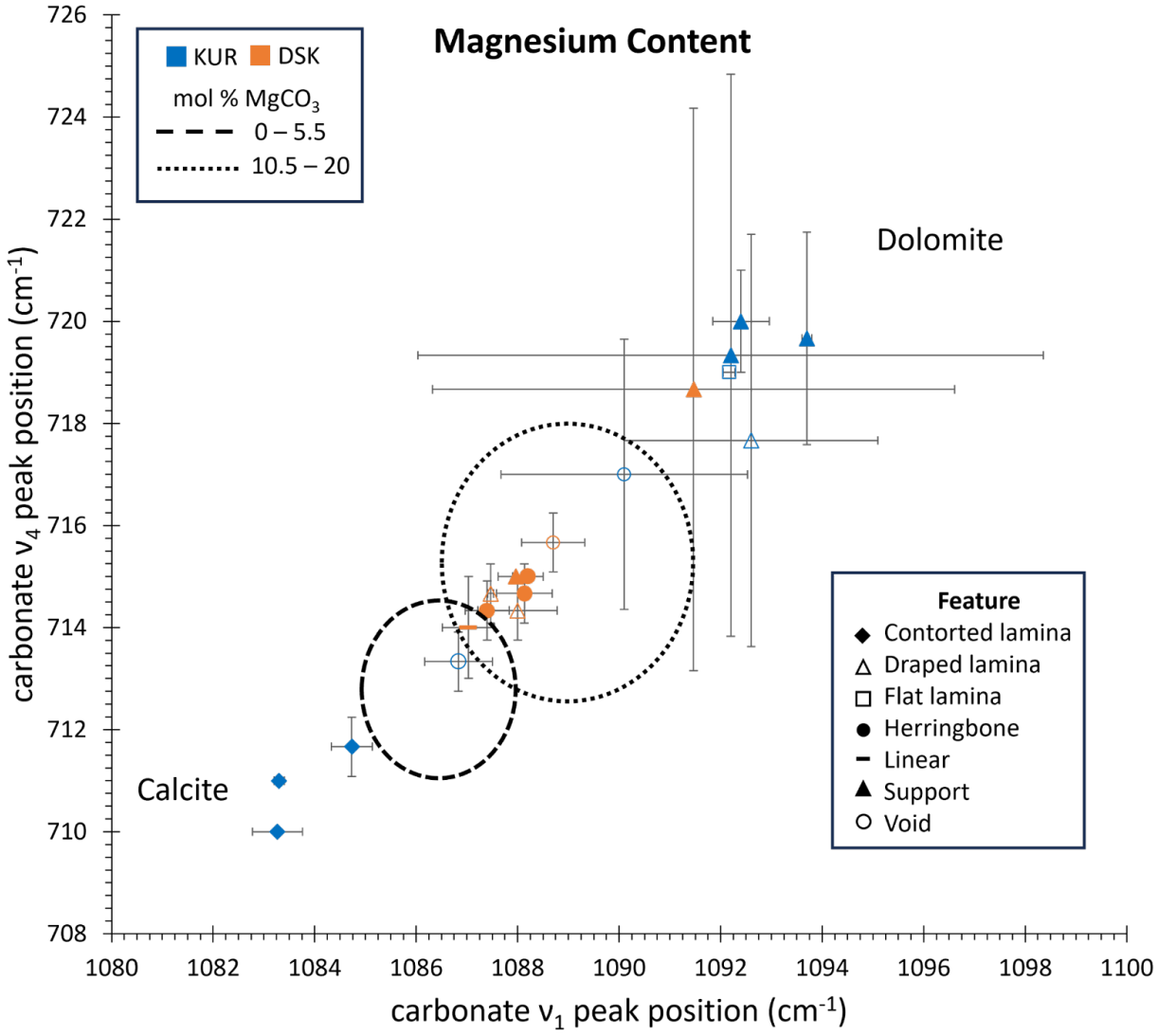

Figure III-11. Plot of ν_4 versus ν_1 peak positions in Raman spectra collected from KUR and DSK samples. KUR data is plotted in blue. DSK data is plotted in orange. Point shapes indicate microbialite morphology at the analysis spot. Each data point falls at the average ν_4 and ν_1 peak positions in the three Raman spectra collected at each analysis spot. Error bars represent one standard deviation of those averages. The dashed circle indicates the region of the plot in which samples with 0 to 5.5 mol% $MgCO_3$ occur and the dotted circle indicates the region of the plot in which samples with 10.5 to 20 mol% $MgCO_3$ occur, as determined by Borromeo et al.'s (2017) analysis of magnesian calcite samples of known composition.

Nine out of ten of the DSK analysis spots are closely clustered within the region of the plot that Borromeo et al. (2017) found corresponds to 10.5 to 20% mol $MgCO_3$, with one of

those falling in the region that overlaps with the 0 to 5.5% $MgCO_3$ region (Fig. III-11). The remaining DSK analysis spot is an outlier that lies in the >20 mol% $MgCO_3$ region. The outlier DSK spot has the second greatest standard deviation of the data points on the plot. This is because one of the three points at this spot has ν_1 and ν_4 peak positions of 1097 and 725 cm^{-1}, which are consistent with dolomite, but the peak positions of the other two points would put them within the 10.5 to 20% mol $MgCO_3$ cluster (Table III-2). The hyper-localized nature of this dolomitization and the presence of microfractures across the DSK sample (Fig. III-8) suggest that it is the result of fluid alteration during burial diagenesis, as described by Beukes et al. (1990). The relatively even magnesium content across the DSK sample likely reflects regional fluid alteration during early diagenesis, again as described by Beukes et al. (1990). DSK's sub-dolomite magnesium content and minimal recrystallization suggests that the alteration event occurred at a relatively low temperature, alteration fluids may have had a low magnesium content, or the alteration event may have been brief.

The magnesium content of the KUR sample at each of the ten analysis spots ranges from approximately 0% mol $MgCO_3$ (calcite) to approximately 50 mol% $MgCO_3$ (dolomite) (Fig. III-11). Of the ten KUR analysis spots, three fall on contorted laminae, one falls on draping laminae, one falls on planar laminae, three fall on support structures, and two fall on voids (Table III-1; Fig. III-2). The three contorted laminae spots all fall in the pure calcite region of the plot, the two void spots are in the 0 to 20% mol $MgCO_3$ region, and the remaining spots, which fell on planar or draping laminae and support structures, fall in the >20 mol% $MgCO_3$ region (Table III-1; Figs. III-11 and III-2).

The KUR dolomitization results are not consistent with regional fluid alteration, and the KUR sample lacks microfractures that would allow for localized fluid alteration during burial

diagenesis. Furthermore, these results provide no obvious support for either Wright and Altermann's (2000) or Warke et al.'s (2019) hypothesis. In both cases, localized dolomitization was hypothesized to be a microbially-influenced process. The fact that the KUR sample void fill analysis spots fell in the 0 to 20% mol $MgCO_3$ region while the analysis spots that fell on contorted laminae fell in the pure calcite region is inconsistent with dolomitization via a microbially-influenced process, if it is assumed that the microbial communities that formed all morphological structures influenced dolomitization in the same way. Instead, the KUR dolomitization results may be an indication that different microbial communities preserved within the Gamohaan microbialites influenced dolomitization in different ways.

SHERLOC Analogue Data

In addition to the work reported above, which was primarily undertaken to better characterize the microbial community and diagenetic processes that led to the formation of the Gamohaan fenestrate microbialites, I also analyzed these samples with the deep ultraviolet (DUV) Raman and fluorescence spectrometer, ACRONM, which is housed at Johnson Space Center (see Methods, above). ACRONM was designed as an analogue to SHERLOC (Scanning Habitable Environments with Raman and Luminescence for Organics and Chemicals), the DUV Raman and fluorescence spectrometer on the Perseverance Rover, which is currently carrying out NASA's Mars 2020 mission (See Chapter IV).

The comparisons of DUV Raman spectra collected with ACRONM and visible Raman spectra from the KUR and DSK samples is of interest to the Mars 2020 mission because carbonates are common in Jezero Crater (e.g., Chapter IV) and, unlike visible Raman spectra, there are very few published DUV Raman spectra of minerals. As a result, the interpretation of

DUV Raman data often relies on databases of visible Raman spectra, which may not be appropriate.

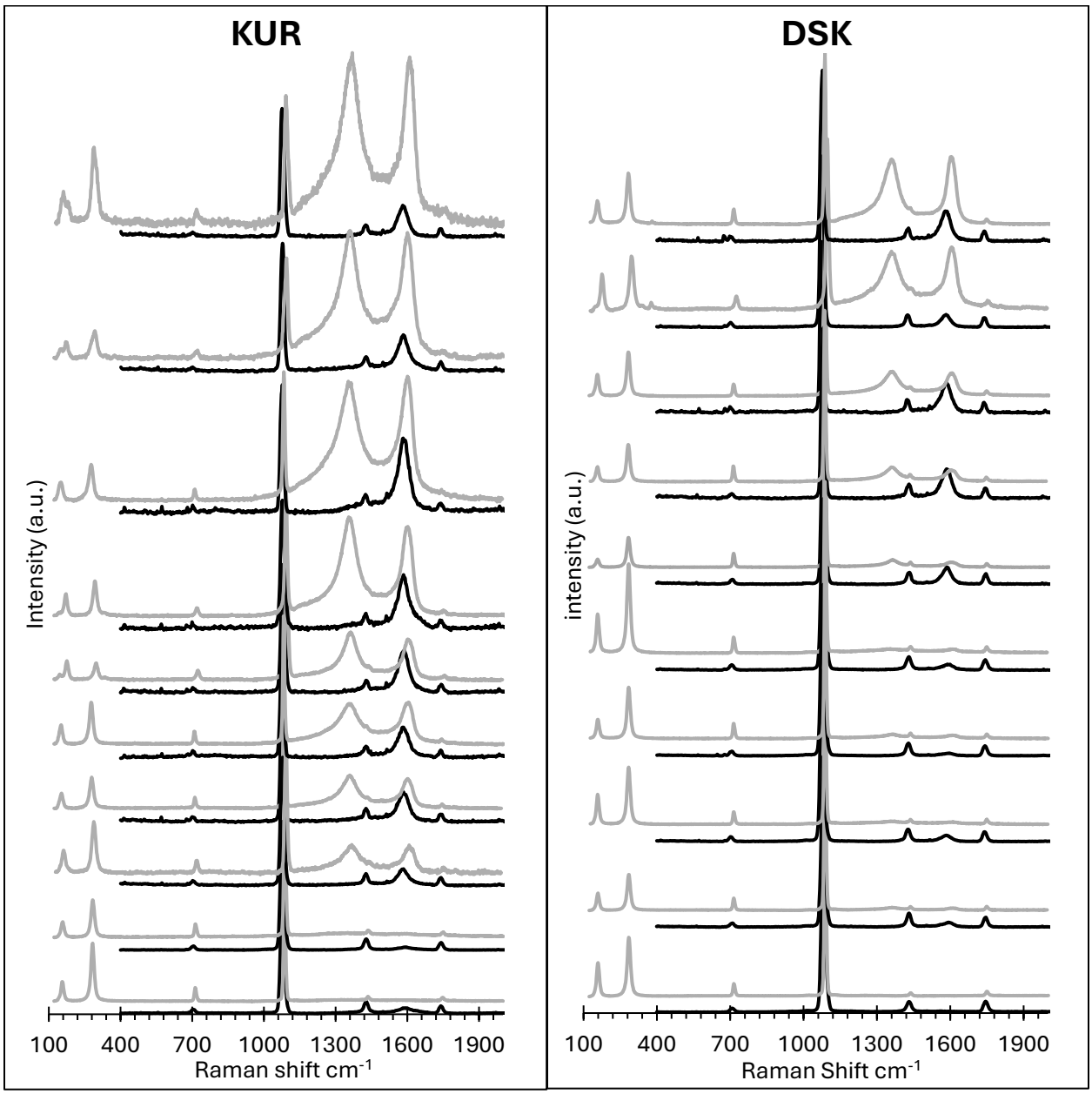

Figure III-12. Collocated visible (gray) and DUV (black) Raman spectra collected at the spots indicated in Figures III-2 and III-3. Note the differences between the DUV and visible Raman ν_1 peak positions, even though the spectra were collected at the same spots on each sample.

Figure III-12 displays 10 pairs of collocated DUV and visible Raman spectra from each of the samples. Notice that the ν_1 and ν_4 carbonate peaks within several collocated pairs fall several wavenumbers apart. After observing these discrepancies in the collocated Raman spectra, I plotted the ν_1 and ν_4 carbonate positions of all the DUV (n = 107) and visible (n = 112) spectra that I have collected on Gamohaan Formation fenestrate microbialite samples, again following Borromeo et al., 2017 (Fig. III-13). This data set includes spectra collected from the KUR and DSK samples discussed above as well as two additional samples. All of the samples are unpolished slabs.

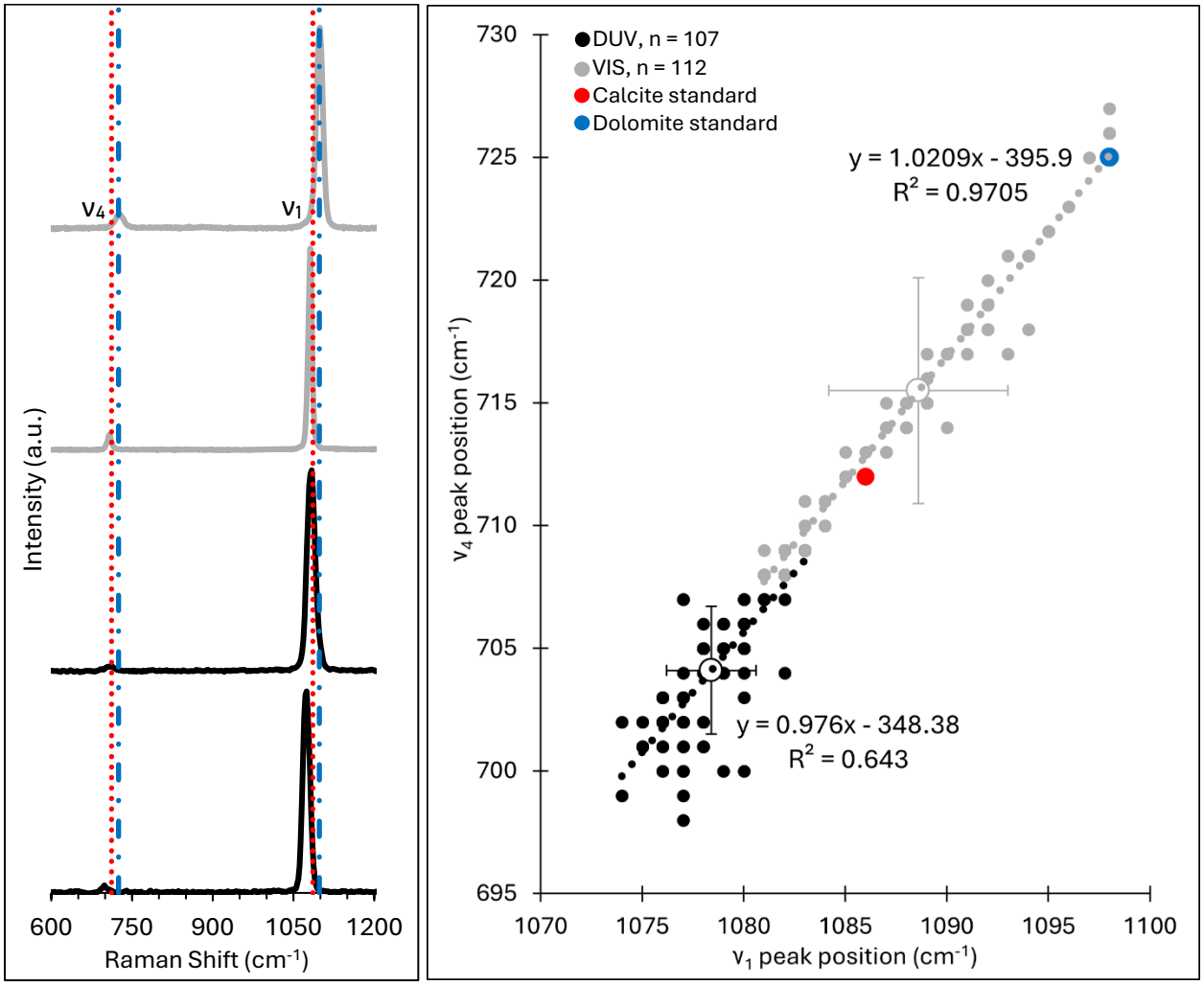

Figure III-13. The left panel shows the spectra exhibiting the most extreme ν_1 and ν_4 peak positions in this data set. From top to bottom, the spectra show the highest peak positions among visible Raman spectra, the lowest peak positions among visible spectra, the highest peak positions among DUV spectra, and the lowest peak positions among DUV spectra. The red dashed lines indicate the ν_1 and ν_4 peak positions of a pure calcite crystal, and the blue

dashed lines indicate peak positions of a dolomite standard under 532 nm laser excitation (Borromeo et al., 2017). The right panel is a plot of ν_1 (x-axis) against ν_4 (y-axis) peak positions from DUV (black) and visible (gray) Raman spectra. The red and blue points indicate the same standard calcite and dolomite peak positions shown in the left panel. The black and gray open points indicate the average DUV and visible peak positions, error bars indicate 1σ.

There are three important differences between the DUV and visible Raman spectra collected on the Gamohaan fenestrate microbialites. First, the average peak positions in Raman spectra are approximately 10 cm^{-1} lower in DUV than visible spectra. The average ν_1 peak positions are 1088.6 cm^{-1} ($\sigma = 4.4$) in visible Raman spectra and 1078.4 cm^{-1} ($\sigma = 2.2$) in DUV spectra and the average ν_4 peak positions are 715.5 ($\sigma = 4.6$) in visible and 704.1 ($\sigma = 2.6$) in DUV spectra (Fig. III-13, hollow points). Second, the linear relationship between ν_1 and ν_4 peak positions is weaker in DUV spectra (Fig III-13.). This may be due to broader peaks in DUV spectra, which result in less precise peak fitting. Third, the ν_1 and ν_4 peak positions do not vary as widely in DUV spectra as they do in visible spectra, which is visually apparent in the plot and indicated by the lower σ of average DUV peak positions (Fig. III-13). This suggests that Raman scatter resulting from DUV laser excitation may not be as sensitive to magnesium substitution in calcite as it is under visible laser excitation. Further investigation is needed to determine whether these and/or additional spectral differences between DUV and visible Raman spectra occur when collected on a more diverse set of carbonate samples.

Conclusion

The 3D reconstructions and petrographic examinations presented here, combined with previously reported sulfur isotope data, suggest that CMCP fenestrate microbialites may be the remains of a diverse community of sulfur-cycling microorganisms, perhaps like that proposed by Bartley et al. (2015) to explain morphologically complex fenestrate microbialites that occur in the Mesoproterozoic Sulky Formation. Additionally, the presence of compact OM, which may be

the remains of MSR that flocculated in response rising oxygen concentrations, in association with cuspate and tented structures but absent from plumose structures may indicate that the morphological differences between cuspate/tented and plumose microbialites are due to variations in oxygen levels, with plumose structures forming under dysoxic to anoxic conditions and cuspate/tented structures forming when oxygen concentrations reach moderate levels. *In situ* sulfur isotope measurements of pyrite grains associated with specific microbialite structures in Gamohaan fenestrate microbialites would provide evidence to support or dispute this hypothesis.

Visible Raman data from the DSK sample show evidence of localized dolomitization via both non-microbially-influenced pathways proposed by Beukes et al. (1990). Visible Raman data from the KUR sample is inconsistent with the non-microbially-influenced dolomitization processes, but neither is it entirely consistent with the microbially-influenced dolomitization processes proposed by Wright and Altermann (2000) and Warke et al. (2019), which assume that all the microbial communities preserved within the CMCP fenestrate microbialites influenced dolomitization in the same way. However, the KUR results are consistent with the possibility that different microbial communities preserved within the microbialites influenced dolomitization in different ways. This hypothesis could be tested by collecting many more Raman spectra associated with morphologically distinct microbialite features from samples with no evidence of non-microbially-influenced dolomitization and looking for correlations between magnesium content and morphology.

The visible Raman data reported here also raise questions about the interpretation of Raman data collected on both Earth and Mars. Visible Raman data call the thermal history of the Gamohaan Formation and/or the accuracy of Raman geothermometry performed on Archean kerogen into question while DUV Raman data indicate a need for caution when interpretating

SHERLOC data based on the results of visible Raman spectroscopy, particularly carbonate spectra.

Chapter IV: SHERLOC Raman Mineral Class Detections of the Mars 2020 Crater Floor Campaign – as published in JGR: Planets, 2023

Andrea Corpolongo, Ryan S. Jakubek, William Abbey, Sanford A. Asher, Desirée Baker, Luther W. Beegle, Eve L. Berger, Rohit Bhartia, Adrian J. Brown, Aaron S. Burton, Sergei V. Bykov, Emily Cardarelli, Edward A. Cloutis, Pamela Conrad, Andrew D. Czaja, Lauren DeFlores, David Flannery, Teresa Fornaro, Marc Fries, Nikole C. Haney, Keyron Hickman-Lewis, Linda Kah, Carina Lee, Francis M. McCubbin, Michelle Minitti, Richard V. Morris, Joseph Razzell Hollis, Ryan Roppel, Eva L. Scheller, Sunanda Sharma, Svetlana Shkolyar, Sandra Siljeström, Kim Steadman, Andrew Steele, Kyle Uckert, Brittan V. Wogsland, Anastasia Yanchilina

Abstract

The goals of NASA's Mars 2020 mission include searching for evidence of ancient life on Mars, studying the geology of Jezero crater, understanding Mars' current and past climate, and preparing for human exploration of Mars. During the mission's first science campaign, the Perseverance rover's SHERLOC deep UV Raman and fluorescence instrument collected microscale, two-dimensional Raman and fluorescence images on ten natural (unabraded) and abraded targets on two different Jezero crater floor units: Séítah and Máaz. We report SHERLOC Raman measurements collected during the Crater Floor Campaign and discuss their implications regarding the origin and history of Séítah and Máaz. The data support the conclusion that Séítah and Máaz are mineralogically distinct igneous units with complex aqueous alteration histories and suggest that the Jezero crater floor once hosted an environment capable of supporting microbial life and preserving evidence of that life, if it existed.

Introduction

On 18th February 2021, NASA's Mars 2020 mission Perseverance rover began exploring Jezero crater with the primary goal of searching for evidence of ancient life on Mars. Other goals

include studying the geology of the region, understanding Mars' current and past climate, and preparing for human exploration (Farley et al., 2020). These goals are being addressed through *in situ* analyses by the rover's instruments and collection of a suite of compelling samples to be returned to Earth by future Mars Sample Return (MSR) missions.

The first campaign of the Mars 2020 mission was an exploration of the floor of Jezero crater (Sun et al., 2022; Fig. 1). During this campaign, the rover investigated two major units, Séítah and Máaz, on the floor of Jezero crater that had been identified from orbital data before surface operations commenced (Stack et al., 2020). (Note that special characters and accents in target, rock, and unit names are omitted in many Mars 2020 documents because they cannot be included in code used to communicate with Perseverance. As a result, alternate spellings, such as , Seitah, Maaz, and Chal, are often used for features with accents or special characters in their names.) The older unit, Séítah, previously referred to as the Crater Floor Fractured 1 (CF-F-1) Unit, is light-toned, ridged, and fractured. Séítah is overlain by Máaz, previously referred to as the Crater Floor Fractured Rough (CF-Fr) Unit, which is light-toned and polygonally fractured. Results from the Perseverance payload during the Crater Floor Campaign indicate that both Máaz and Séítah are igneous in origin (Horgan et al., 2022). Máaz is characterized by the presence of abundant pyroxene (Schmidt et al., 2022; Udry et al., 2022), while Séítah is an olivine cumulate (Brown et al., 2022: Farley et al., 2022; Liu et al., 2022; Nuñez et al., 2022; Wiens et al., 2022). The transition between the Séítah and Máaz units is highlighted in cyan in Figure 1. The contact between the two units is obscured by regolith and not observable, however Séítah and Máaz vary in elevation by approximately 10 meters along Artuby ridge (Fig. 1), a resistant feature along the southern margin of the portion of the Séítah unit that Perseverance explored (Sun et al., 2022).

The Crater Floor Campaign addressed several objectives of the Mars 2020 mission by contributing to a scientific understanding of the geology of Jezero crater, seeking rocks with a high probability of preserving ancient biosignatures and looking for potential biosignatures within rocks of the Séítah and Máaz units, and documenting the geological context of the first set of samples collected for possible future return to Earth. This paper reports spectral maps collected by SHERLOC (Scanning Habitable Environments with Raman and Luminescence for Organics and Chemicals), an arm mounted deep UV (DUV) Raman spectrometer (Bhartia et al., 2021). The maps are paired with high resolution (10.1 μm/pixel) grayscale images collected by the co-boresighted Autofocus Contex Imager (ACI), enabling mapping of the location where each Raman spectrum was collected on the target surface. In addition, the Wide Angle Topographic Sensor for Operations and eNgineering camera (WATSON) provides macro-scale, color images of the Raman scan targets. Combining the image color of WATSON images with the high resolution of the ACI images produces colorized ACI images that allow for the identification of individual mineral grains and the detection of associations between minerals and any detected organic matter. These capabilities make SHERLOC and WATSON of central importance to achieving the geological and astrobiological objectives of the Mars 2020 mission.

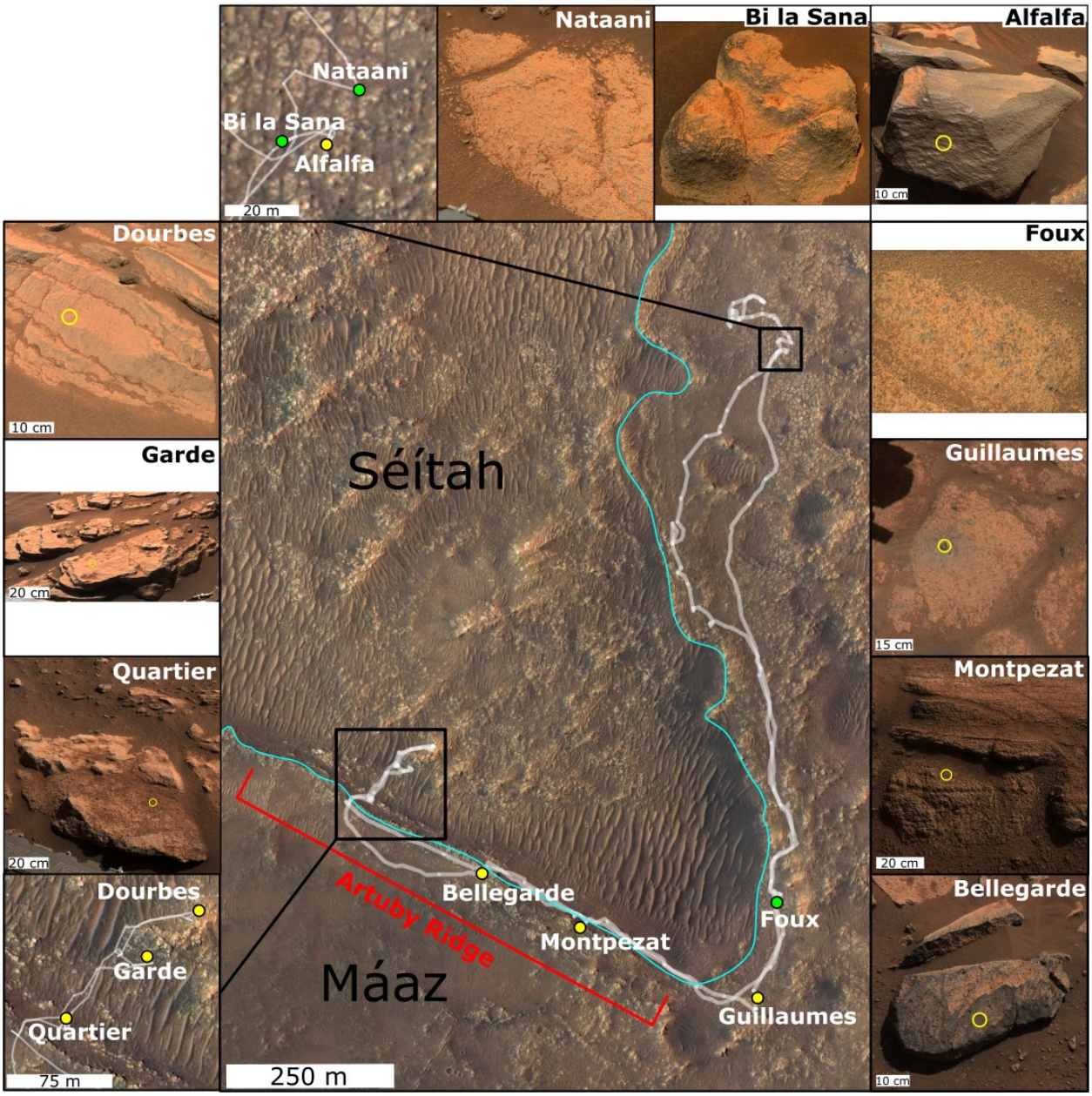

Figure 1. Map of the Crater Floor Campaign traverse (central image and insets, based on HiRISE imagery) and natural and abraded targets analyzed by proximity science, including SHERLOC and WATSON, through sol 370 (smaller images around the periphery, imaged by the MastCam-Z instrument on the Perseverance rover). The white path on the map shows Perseverance's traverse. The cyan line marks the approximate contact between the Séítah formation below and the Máaz formation above. The red bracket indicates Artuby Ridge. Targets analyzed are indicated along the route. The yellow circles on most targets indicate the location of abrasion patches (see subsequent figures). Those without yellow circles were not abraded.

Methods

SHERLOC is a deep UV (DUV) Raman and fluorescence spectrometer designed to detect, characterize, and spatially resolve organics and minerals on the Martian surface (Bhartia et al., 2021). A 248.6 nm DUV laser is used for excitation and takes advantage of increased scattering Raman cross section from Rayleigh Law and resonance enhancement, allowing for the detection of small quantities of organics and minerals. Many molecules, when excited, fluoresce at wavelengths above ~270 nm, at intensities many orders of magnitude greater than the intensities of typical Raman peaks, making it difficult to impossible to detect any Raman scattering that might coincide with such strong fluorescence bands. Unlike longer wavelength lasers (near-UV, visible, or near IR) the DUV Raman window is energetically separated from the fluorescence window, allowing for Raman and fluorescence spectra to be obtained in non-overlapping spectral regions (Tarcea et al., 2007; Bhartia et al., 2012; Eshelman et al., 2014; Montagnac et al., 2021). The depth of field of the SHERLOC instrument is ±500 μm to accommodate the surface roughness of the abraded patch however, it is expected that the Raman response is coming from a 100-200 μm depth of penetration (Bhartia et al., 2021, Carrier et al., 2019). The DUV laser-injection filter optical coating attenuates < 800 cm^{-1}, limiting detection of primary Raman bands of many silicates and oxides. In addition, DUV absorbing minerals (i.e., some Fe containing minerals) can attenuate the depth of penetration into a material and reduce signal to noise ratios (SNR) (Morris et al., 2022; Razzell Hollis et al., 2021a).

SHERLOC is an arm-mounted instrument, which allows it to be moved into proximity of an analysis target. With no change in arm position, an internal scanning mirror rasters the deep UV laser beam across the sample surface. With a maximum area of 7 x 7 mm, Raman/fluorescence spectra are acquired at discrete points with a beam diameter of ~100 μm

(Bhartia et al., 2021). Prior to each spectrum scan, the Autofocus Context Imager (ACI) is used to acquire 10.1 μm/pixel resolution grayscale images of the target surface. This provides context for the spectral maps and is used to focus the spectrometer/laser. Color images acquired by WATSON have a spatial resolution ranging from 16 to 150 μm/pixel and are used for targeting SHERLOC observations and textural analysis (Bhartia et al., 2021; Edgett et al., 2012). SHERLOC is designed to simultaneously collect Raman and fluorescence data on the same CCD with a single readout. To reduce noise, the CCD readout is binned into 3 regions, a Raman region ~ 800 to 4000 cm^{-1} (250 to 273 nm) and two fluorescence regions (274 to 337 and 338 to ~370 nm). Each region has a separate wavenumber calibration, previously discussed in detail (Uckert et al., 2021).

2.1 Scan Procedures

In this paper, we use the following nomenclature to describe SHERLOC Raman measurements (Fig. S1). A "target" refers to the specific rock or abraded patch on which data were collected, such as "Nataani" or "Guillaumes," while a "scan" refers to a specific Raman hyperspectral map that was collected on a target. Each Raman scan is named using the nomenclature "#0001_name_#2_#3", wherein #0001 denotes the sol on which the scan was performed, name refers to the target and describes the parameters of the scan, #2 is the laser pulses per each point spectrum within a scan, and #3 is the scan number used to differentiate between multiple scans of the same parameter made on the same sol. Each individual spectrum within a scan is referred to as a "point," and each point within a scan is assigned a number according to the order it occurred in the scan. The first Raman spectra collected within a scan falls at the upper left corner of the hyperspectral map. Collection continues in a serpentine pattern, such that the final spectra in a 100 point scan falls at the lower left corner of the map. High Dynamic Range (HDR) scans

consist of 100 points with 780 μm spacing for an image size of 7 x 7 mm. Detail scans consist of 100 points with 100 μm spacing for an image size of 1 x 1 mm. Survey scans consist of 1296 points with fixed spacing between them (50, 144, or 200 μm, depending on the scan template) and 10 or 15 pulses per point. For example, the scan name "0083_Nataani HDR_50_1" describes the first HDR scan performed on Nataani using 50 pulses per point on sol 83 of the Mars 2020 mission.

For each scan SHERLOC performs, single spectra are obtained by first collecting a dark spectrum with no incident laser light and then collecting the active spectrum with the laser firing. The dark scan is then subtracted from the active spectrum to produce the reported Raman spectrum. SHERLOC spectra have a ~10 cm^{-1}/pixel resolution with a Raman spectral range of ~800–4000 cm^{-1}. The potential to observe Raman bands in the spectral range below 800 cm^{-1} is limited because SHERLOC's laser-injection filter has reduced transmission in this region and the 252.9 nm laser plasma line is observed at ~650 cm^{-1}. However, very strong bands below 800 cm^{-1} can be observed (Bhartia et al., 2021; Uckert et al., 2021; Razzell Hollis et al., 2021a).

We performed scans on both natural and abraded targets. Targets were abraded using Perseverance's Rock Abrasion Tool (RAT), which is ~45 mm in diameter and capable of creating smooth-bottomed abraded patches up to ~1 cm deep. After abrasion, abraded patches are cleaned of dust and cuttings by the gaseous dust removal tool (gDRT), which blasts the abraded target with a high-velocity jet of nitrogen gas (Farley et al., 2020; Moeller et al., 2021). The targets described below as abraded targets were abraded and cleaned as described prior to scanning. Any targets described below as natural targets were neither abraded nor cleaned with the gDRT prior to scanning.

2.2 Data Analysis Procedures

We examined each individual Raman spectrum in each scan. We considered any band with a FWHM of 30 cm^{-1} (~3 pixels) or more a potential Raman signal. We assigned each single spectrum containing observable Raman signals to its respective mineral class via comparison to standard spectra obtained through laboratory measurements with the SHERLOC Brassboard instrument, an analogue DUV Raman and fluorescence instrument housed at the NASA Jet Propulsion Laboratory (described in detail by Razzell-Hollis et al., 2021a,b) and ACRONM (Analogue Complementary Raman for Operations oN Mars) (see section S4.1 for a discussion of SHERLOC analogue instruments). All peak centers were determined with a Gaussian fit function, through the open-source peak fitting software Fityk (version 1.3.1; Wojdyr, 2010).

In section 3.0, we display the SHERLOC Raman data through Raman spectral assignments overlain on each scan's associated ACI image. These spectral assignment maps are accompanied by colorized ACI images overlaid with white rings that indicate the location of each point in the scan. The spectral positioning calculations were validated from images of ACI calibration measurements where dust mobilization could be observed. Spectral map/ACI overlays are accurate to within ~44 μm near the center of maps, and within 115 μm at the 7x7 mm map corners in the HDR overlays. The points at the start of each scan (scans start at the upper left corner) have less location uncertainty than points at the end of the map scan because of robotic arm drift, which can add up to ~30 μm of uncertainty. Each laser shot hits the scanned surface as an annulus ~100 μm in diameter. The white rings overlying the colorized ACI images are ~200 μm in diameter so that the location being analyzed is visible.

We used Bayer-encoded 8-bit WATSON color and grayscale ACI image products for this study to most closely represent the raw data from the image detector. To generate secondary image products, we performed further processing on both WATSON and ACI products using a custom

Python script to register multiple images for a single target to create an overlay. ACI companded image products and WATSON companded or companded z-stack range images (~4 cm to 10 cm standoff) images were used in all cases. “Colorized” ACI images used for correlating spectral, color, and textural information were generated as previously described (Scheller et al., 2022).

2.3 Spectra Signal-to-Noise Analysis

In order to quantitatively assign confidence to SHERLOC mineral detections, we developed a statistical procedure involving comparing apparent signal intensities to a calculated median root-mean-squared-deviation (RMSD) of the noise for each scan. We first calculated the noise RMSD in the 2500–3000 cm^{-1} region of Raman spectra for every individual spectrum in each scan. This “silent” region was selected for its lack of signal in any spectrum, excluding cosmic ray artifacts. Then we determined the median of the noise RMSD values for each scan. We used the median to avoid contributions from any RMSD values that were inflated by cosmic rays, background fluorescence, and other spectral effects. The RMSD noise values differed between Raman images but generally occur in the 20-50 count range.

We designated single spectra Raman bands with intensities ≥3X the noise RMSD as statistically significant signals. This designation criterion is based on the International Union of Pure and Applied Chemistry’s limit of detection for the probability of a data point being statistically above a normally distributed noise background (McNaught & Wilkinson, 1997). The peak position error for SHERLOC Raman bands with intensities ≥3X the noise RMSD is ≤±~4.0 cm^{-1}. We used mean spectra to assign detections to mineral classes. By doing so, we obtained spectra with maximum peak intensities ≥10X the noise RMSD, which have a peak position error of <±~1 cm^{-1}. Combined with the ±1.8 cm^{-1} uncertainty in the wavenumber calibration (Fries et al. 2022), the peak wavenumber error of the most intense peaks in spectra used to assign mineral classes is

approximately ±2-3 cm^{-1}. However, the error for any specific peak in a single spectrum is dependent on signal-to-noise ratio and can be estimated using the work of Lenz and Ayres 1992 as described in section S1.0 of the supporting information. In the main text, the peak wavenumber values reported are approximate values for a mineral class assignment and are only meant to qualitatively describe the spectra for discussion. As described in the supporting information, most mineral class assignments were assigned based on multiple Raman bands, and for mineral classes where only one band is present (carbonate, pyroxene, and silicate), the bands have distinctive Raman shifts. Thus, the mineral class assignments are not peak wavenumber error limited.

In the context of this paper, signals with ≥3X the noise RMSD are qualitatively observed with high confidence while those <3X are observed with less confidence. For these reasons, in the ACI-Raman image overlay figures presented in section 3, we differentiate between Raman signals ≥3X and <3X the RMSD noise as a first-order indicator of the assignment confidence. To make this distinction, we label assignments made based on Raman signals ≥3X the noise with capital letters and those made based on signals <3X the noise with lowercase letters. In the text, we describe assignments made based on Raman signals ≥3X the noise as definitive and assignments made based on signals <3X the noise as probable or possible.

2.4 Background Spectral Features

It is important to note several spectral features observed as background in SHERLOC Raman spectra. These features are characterized by Raman scans collected with no target at the laser focus, referred to as the stowed arm scans. We collected HDR_100, _250, and _500 scans with SHERLOC in the stowed position. We detected a weak Raman peak of fused silica that originated from Raman scattering of the instrument optics, seen as broad peaks at ~480 cm^{-1} and

~800 cm^{-1} (section S2). This background feature is of sufficiently weak intensity that it is observed only in spectra with ≥500 pulses/point. In addition, the fused silica background is distinct from all Raman signals obtained from sample targets and does not interfere with spectral analysis.

We also observed narrow peaks occurring at specific wavenumbers more frequently than would be expected if they were occurring randomly. These peaks are artifacts of the dark spectrum subtraction process described in section 2.1. Most of the artifact peaks occur at wavenumbers that are irrelevant to the spectral assignments in this paper. However, we observed narrow peaks at 970 cm^{-1} and/or 981 cm^{-1} in ~20% of the stowed arm spectra, which increases the uncertainty of spectral assignments relying on peaks at or near these wavenumbers. At the time of writing, the SHERLOC team is working to determine the cause and mitigate the influence of these artifacts. See section S3 for a detailed discussion of this topic.

Results

SHERLOC scanned 10 targets during the Crater Floor Campaign: three from Séítah (all abraded surfaces) and seven from Máaz (three natural and four abraded surfaces) (Fig. 1). SHERLOC successfully performed within operating capabilities on Mars, becoming the first Raman spectrometer to map mineral composition in context on the surface of another planetary body.

In sections 3.1 and 3.2, beginning with the stratigraphically lower Séítah targets and moving upsection to Máaz targets, we report the results of SHERLOC's microscale mineral mapping on the Jezero Crater floor. For each target, we describe textural features of the scanned rock surfaces revealed by WATSON imagery (Wogsland et al., this issue), report mineral detections facilitated

by SHERLOC Raman spectroscopy at each target, and highlight associations between textural features and mineral detections.

Mineral assignments reported below are to mineral class only, not to mineral species, with the exception of sodium perchlorate assignments reported in section 3.2.1. Assignments include undefined silicate (labeled silicate throughout the text), carbonate, olivine, perchlorate/phosphate, perchlorate, sodium perchlorate, pyroxene, and sulfate. Class assignments were made by comparing fitted mean or individual SHERLOC spectra (as specified in the individual reports below) to standard spectra collected with the DUV SHERLOC analogue instruments Brassboard and ACRONM, as shown in figures 2 through 8.

Spectra assigned to undefined silicate feature a broad band centered at ~1050 cm^{-1} that is similar to broad bands between 900 to 1200 cm^{-1} observed in some silicate spectra collected on ACRONM. The bands are qualitatively similar to ACRONM spectra of plagioclase feldspar (Figs. 2, 3, 6, 7, 8). However, the identifying Raman peaks of feldspars (and many other silicates) occur below 800 cm^{-1}, in the spectral range that is obscured by SHERLOC's laser-injection filter and laser plasma line. Some of the broad bands centered at ~1050 cm^{-1} could represent detections of amorphous silica, as amorphous silica would yield spectra with a similar feature (Fu et al., 2017). However, the broad nature of these bands is also similar to broad bands centered between 1000 and 1020 cm-1 in augite, labradorite, and bytownite spectra collected on Brassboard (Razzell-Hollis et al., 2021a), which further indicates that SHERLOC scans of crystalline silicates may yield broad spectral features. As a result, we cannot make more specific mineral assignments of spectra featuring broad bands centered at ~1050 cm^{-1} at this time, as they may represent detections of crystalline or amorphous mineral phases. The SHERLOC team is actively working to determine exactly how the laser injection filter effects peak intensity and

placement in the spectral range below 800 cm^{-1}. This work will be reported in a future publication. Unlike other silicates, the Raman spectra of olivine and pyroxene have identifying peaks above 800 cm^{-1}, allowing us to assign SHERLOC spectra to these mineral classes.

The dominant peaks in pyroxene and sulfate Raman spectra can fall within the same spectral range, of ~970 cm^{-1} to 1050 cm^{-1} (e.g., Razzell Hollis et al., 2021a). We differentiated between these assignments based on the presence of characteristic secondary peaks and hydration features in sulfate spectra, and by confirming pyroxene assignments with data collected by PIXL, Perseverance's micro-X-Ray fluorescence spectrometer, when possible. The dominant peaks of perchlorate and phosphate fall in a partially overlapping spectral range, between ~950 cm^{-1} and 970 cm^{-1}. Where we observed peaks in this range, we distinguished between phosphate and perchlorate based on the presence of secondary perchlorate peaks. Where we observed peaks between ~950 cm^{-1} and 970 cm^{-1} with no secondary peaks, we assigned spectra to perchlorate/phosphate. Criteria for all mineral assignments reported below are discussed in greater detail in the supporting information (section S4).

3.1 Séítah Targets

3.1.1 Dourbes

The Dourbes abrasion, which was approximately 7 mm deep, was made on sol 251 on Brac, an outcrop of the Bastide member of the Séítah formation that featured centimeter to decimeter scale layering (Fig. 1). The pre-abrasion surface of Brac was fluted from apparent wind abrasion and dust coated (Fig. S2A). The lowest relief areas of the surface of Brac were filled with coarse regolith and fine-grained gravel. Two core samples retrieved from Brac, Salette and Coulettes, are associated with the Dourbes abrasion. The abraded surface of Dourbes features ~1–3 mm

angular light gray-to-green and dark brown-to-black mineral grains (Figs. 2A-C). The gray-to-black grains are highly reflective. These grains are frequently rimmed by a light tan material and a reddish-brown material occurs in the spaces between them. The surface of Dourbes has no pitting or staining.

SHERLOC scans of Dourbes include 0257_Dourbes Survey_15_1, 0257_Dourbes HDR_500_1, 0269_Dourbes Survey_15_1, 0269_Dourbes Detail_500_1, 0269_Dourbes Detail_500_2, and 0269_Dourbes Detail_500_3 (Fig. 2). The individual spectra from the Dourbes Survey scans contain no discernible peaks. The mean spectra of each of these scans has a very weak possible silicate band (see section S4.2), a weak possible O-H stretching band, and the background fused silica spectra discussed in section 2.4 (Fig. S1b). The remaining scans contain spectra consistent with olivine, carbonate, pyroxene, sulfate, and perchlorate or phosphate in addition to silicate (Figs. 2B-D).

Olivine was the most common detection in 0257_Dourbes HDR_500_1 (Fig. 2B). Thirty-eight percent of the points in this scan were definitively assigned to olivine and a further 8% were assigned as probable olivine. The dominant peak in the mean spectrum of all points in 0257_Dourbes HDR 500_1 definitively assigned to olivine is centered at 827 cm^{-1} (Fig. 2D). The olivine standard spectrum in figure 3D was collected with Brassboard from a natural forsterite sample (WARDS) and exhibits a primary peak centered at 844 cm^{-1}. Neither SHERLOC nor Brassboard has the spectral resolution required to resolve the doublet at ~820 cm^{-1} and ~850 cm^{-1} that is typically observed in olivines and can be used to determine olivine composition (Chopelas, 1991; Kuebler et al., 2006; Razzell Hollis et al., 2021a). Correlating SHERLOC's unresolved olivine doublets to olivine Fo content is beyond the scope of this paper, as changes in

the unresolved band position and width are controlled by the relative positions and intensities of the individual ~820 and ~850 cm^{-1} bands (see section S4.3).

Carbonate and pyroxene were also prominent detections in this scan, with 5% of the points definitively assigned to carbonate, 6% assigned probable carbonate, 4% definitively assigned to pyroxene, and 5% assigned probable pyroxene. In addition, one point was definitively assigned to silicate and two were assigned as probable silicates. One point in this scan was definitively assigned to sulfate. The mean spectrum of all points in 0257_Dourbes HDR 500_1 definitively assigned to pyroxene is centered at 993 cm^{-1}, which is consistent with the augite spectrum collected by Brassboard (Fig. 2D). The comparison to a standard augite spectrum is not a formal mineral species assignment, which will require a detailed investigation that is beyond the scope of this paper. This peak could also be consistent with hydrated sulfate species. We determined that the Dourbes points assigned to pyroxene are unlikely to be sulfate because they lack detectable hydration features and because PIXL, Perseverance's micro-X-Ray fluorescence spectrometer that provides spatially resolved elemental abundances, detected silicon, magnesium, and aluminum, but no sulfur, in the region of these detections, which is consistent with the presence of pyroxene (Razzell Hollis et al., 2022).

The three Dourbes Detail scans yielded sulfate, carbonate, olivine, silicate, perchlorate, and phosphate or perchlorate detections. Scan 0269_Dourbes Detail_500_1 is dominated by sulfate detections surrounded by carbonate detections, much like the larger carbonate rimmed sulfate in Quartier (Figs. 4C; see section 3.1.3). The dominant peak in the mean spectrum of all points in 0269_Dourbes Detail 500_1 assigned to sulfate only is centered at 1022 cm^{-1}, represented by the vertical solid red line in figure 2D. This mean spectrum also has weak secondary peaks at 1141 cm^{-1} and 1220 cm^{-1}, represented by the dotted and dashed vertical red lines in figure 2D, and an

OH stretching mode band (Fig. S10b). The primary peak in the Dourbes sulfate spectrum agrees closely with the primary peak of a synthetic magnesium sulfate (Macron Chemicals) spectrum collected on Brassboard, which is centered at 1019 cm^{-1} (Fig. 4D). The secondary peaks of the Brassboard magnesium sulfate spectrum are at 1150 cm^{-1} and 1274 cm^{-1}. While these peaks do not correspond directly to the secondary peaks in the Dourbes sulfate spectrum, the secondary peaks of magnesium sulfate are reported to vary between ~1060 cm^{-1} and ~1260 cm^{-1}, depending on the hydration state of the mineral (Wang et al., 2006). The sulfate detections are concentrated on a sub-millimeter light brown to white grain (Figs. 2C and 9B).

The single definitive perchlorate or chlorate detection in Dourbes is at point 11 of scan 0269_Dourbes Detail_500_1 (Figs. 2C and S12). This detection co-occurs with a definitive sulfate detection and falls at the edge of the light brown to white sulfate grain, adjacent to carbonate detections. We made this perchlorate assignment based on the presence of a peak at 932 cm^{-1}, which is consistent with the primary peak of several different perchlorate and chlorate species (see section S4.8).

The dominant peak in the mean spectrum of all points in 0269_Dourbes Detail 500_1 assigned to carbonate is centered at 1083 cm^{-1}, represented by the vertical cyan line in figure 2D. This peak corresponds closely to the 1084 cm^{-1} peak in the Brassboard terrestrial calcite standard spectrum (WARDS #49–5860) (Fig. 2). The similarity between these spectra could suggest that the Dourbes carbonates are primarily calcite (see section S4.4). However, this comparison is made with a mean spectrum of all carbonate points in the scan, so it is likely that carbonates with different cations are contributing to the average peak position. Furthermore, minerals containing iron cations can absorb DUV laser radiation (Morris et al., 2022; Razzell Hollis et al., 2021a and b). This effect would have interfered with data acquisition if any of the detected carbonates

contained iron. Therefore, we cannot assign SHERLOC carbonate detections to specific mineral species. The carbonate detections correspond to reddish-brown grains, primarily at the edge of the sulfate grain.

Scan 0269_Dourbes Detail_500_2 is the only SHERLOC scan of the Séítah formation in which the most common mineral detection is silicate. It also features olivine, carbonate, and perchlorate or phosphate detections. The band in the mean spectrum of all points in 0269_Dourbes Detail 500_1 assigned to silicate is centered at 1065 cm^{-1} and has a FWHM of 180 cm^{-1} (Fig. 2D). This mean spectrum is similar to a labradorite spectrum standard collected with ACRONM. However, this similarity is not sufficient to assign the Dourbes silicate spectra to labradorite (Fig. 2D). The silicate detections correspond with micron scale light gray-to-blue mineral grains. See section S4.2 for additional details regarding silicate detections during the Crater Floor Campaign.

The perchlorate or phosphate peak in the mean spectrum of the three perchlorate or phosphate spectra in 0269_Dourbes Detail_500_2 is centered at ~958 cm^{-1} (Fig. 4D). This falls between the dominant peak of a sodium perchlorate standard spectrum (collected with Brassboard from a sample of synthetic sodium perchlorate hydrate powder, Sigma Aldrich 310514) and that of a series of eleven natural and synthetic phosphate standards (collected with ACRONM and includes the minerals fluorapatite, hydroxylapatite, chlorapatite, whitlockite, and merrillite), which makes a confident mineral assignment difficult (Fig. 2D). We observed no hydration features in the Dourbes perchlorate/phosphate spectra. Assignment of SHERLOC Raman peaks between ~950 cm^{-1} and 990 cm^{-1} is further complicated by the presence of relatively frequent artifacts at 970 cm^{-1} and 981 cm^{-1} in SHERLOC scans (see sections 2.4 and S3). These artifacts are easily identified when they occur in the absence of Raman signal. However, if they occur in a

spectrum with a Raman signal between ~950 cm^{-1} and 990 cm^{-1}, they may artificially shift the center of the Raman peak.

Scan 0269_Dourbes Detail_500_3 detected olivine, carbonate, and, at a single point that overlaps with 0269_Dourbes Detail_500_1, sulfate. The dominant peak in the mean spectrum of all points in 0269_Dourbes Detail 500_3 assigned to olivine only is centered at 834 cm^{-1}. The olivine detections in the lower left corner of this scan correspond with a relatively large, reflective, dark brown-to-black euhedral mineral crystal and are not directly associated with carbonate detections (Fig. 2C). Olivine detections in the upper left corner of this scan fall on a smaller, subhedral, black mineral crystal and are adjacent to carbonate detections that fall on a light reddish-brown grain (Fig. 2C).

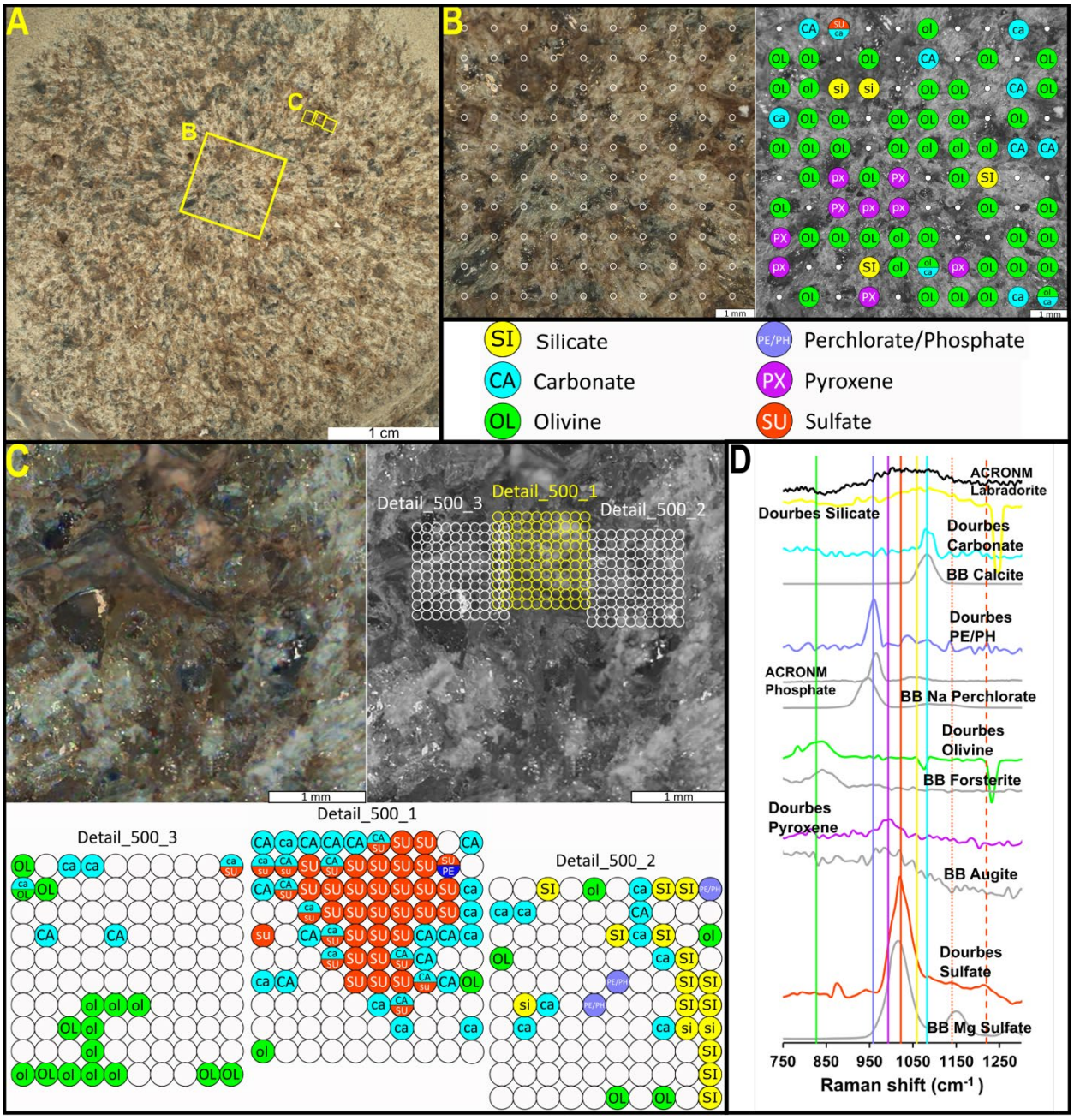

Figure 2. SHERLOC Raman mineral identifications from Dourbes. A) The abrasion patch imaged by WATSON (image ID SI1_0257_0689775622_738FDR_N0080000SRLC00006_000095J01). Yellow boxes indicate the location of the scans performed. B) Colorized (left) and grayscale (right) ACI images (image ID SC3_0257_0689786306_125FDR_N0080000SRLC11421_0000LMJ01) of the region of the abrasion patch bounded by the larger yellow box in panel A. The white circles in panel B indicate the locations of SHERLOC analysis spots. Mineral identifications are indicated in the right panel. C) Colorized (left) and grayscale (right) ACI images (image ID SC3_0269_0690851147_347FDR_N0080000SRLC11373_0000LMJ02) of the region of the abrasion patch bounded by the smaller yellow boxes in panel A. The white and yellow circles in the upper right subpanel of panel C

indicate the locations of SHERLOC analysis spots for three 1 mm^2 Detail scans. The lower three subpanels show mineral identifications for these three Detail scans. D) Representative Raman spectra of minerals detected with high confidence from the abrasion patch and spectra of mineral standards collected on the SHERLOC Brassboard instrument at JPL and the ACRONM instrument at JSC. Vertical lines indicate peak centers. Spectra are offset along the y-axis for clarity.

3.1.2 Garde

The abrasion patch Garde, which was approximately 11 mm deep, was made on sol 206 on the upper surface of a platy layered outcrop of the Bastide member of the Séítah formation, called Bastide (Fig.1). The Bastide member is characterized by pronounced tabular layering, with most layers 1–3 cm thick and some 10–40 cm thick layers (Farley et al., 2022). The pre-abrasion surface of Garde was dust-coated, with occasional 2-3 mm, angular, elongate, gray-to-green mineral grains visible through the dust (Fig. S2B). Similar grains were recognized in SuperCam RMI images of relatively fresh outcrop surfaces and identified as olivine (Farley et al., 2022). The surface also exhibited infrequent millimeter scale pitting. No coring was attempted at this outcrop and no core samples are associated with the Garde abrasion.

The abraded surface of Garde has a relatively homogeneous texture (Fig. 3A). It features reflective, light-to-dark gray-green, angular, millimeter-scale mineral grains in a fine-grained light-toned matrix and reflective, dark gray-to-black angular mineral grains that range in size from approximately 1–3 mm across. These are associated with light brown and reddish brown millimeter-scale mineral grains. The surface has no pitting or staining.

SHERLOC scans of Garde include 0207_Garde Survey_15_1, 0207_Garde HDR_500_1, 0207_Garde HDR_500_2, 0208_Garde Detail_500_1, 0208_Garde Detail_500_2, and 0208_Garde Detail_500_3. The Garde survey scan does not contain any spectra with Raman

signals strong enough to assign. The remaining scans contain Raman spectra corresponding to olivine, carbonate, silicate, and perchlorate or phosphate, as well as possible pyroxene (Fig. 3D).

Olivine was the primary mineral we detected in all of the HDR and Detail scans performed on Garde; 21% of the combined 500 points of these scans were definitively assigned to olivine, and an additional 14% were assigned as probable olivine (Fig. 3B-C). The dominant peak in the mean spectrum of all points in 0208_Garde Detail_500_1 assigned to olivine is centered at 830 cm^{-1}, represented by the vertical green line in figure 3D. The points in Garde assigned to olivine generally fall on the reflective gray-green mineral grains.

We also detected carbonate across all of the Garde HDR and Detail scans, with 7% of the 500 points definitively assigned to carbonate and an additional 11% assigned to probable carbonate (Fig. 3B-C). The dominant peak of the mean spectrum of all points in scan 0208_Garde Detail_500_1 assigned to carbonate is centered at 1085 cm^{-1}, represented by the vertical cyan line in figure 3D. However, as in the Dourbes carbonate detections, this assignment is to mineral class only, not species. The points assigned to carbonate fall on light brown and reddish brown grains that are closely associated with the olivine grains.

All three of the Garde Detail scans contain Raman spectra that are consistent with perchlorate or phosphate. The dominant peak of a mean spectrum of all points in scan 0208_Garde Detail_500_1 assigned to perchlorate or phosphate is centered at 956 cm^{-1}, represented by the vertical lavender-blue line in figure 3D. As in Dourbes, this peak falls between the dominant peak of perchlorate and phosphate standards analyzed by SHERLOC analogue instruments (see sections 3.1 and S4.8) and cannot be confidently assigned to either mineral. We did not observe hydration features in the Garde spectra assigned

perchlorate/phosphate. The points assigned to perchlorate or phosphate in the Garde Detail scans generally fall on non-reflective light gray grains.

The spectra in scan 0208_Garde Detail_500_1 assigned to perchlorate or phosphate also feature a fluorescence band located at ~340 nm (Scheller et al., 2022). The ~340 nm fluorescence feature could result from organic species and/or from trivalent cerium (Ce3+) within a phosphate crystal structure (Shkolyar et al., 2021). The possible presence of (Ce3+) fluorescence may support a phosphate assignment for these spectra. However, the fluorescence spectral assignment is not straightforward (see section S4.6).

Scans 0207_Garde HDR_500_2, 0208_Garde Detail_500_1, and 0208_Garde Detail_500_3 contain points assigned to silicate. The silicate detections fall on dark gray non-reflective grains and are often associated with perchlorate or phosphate detections in the Detail scans (Figs. 3B-C). The mean spectrum of all points in scan 0208_Garde Detail_500_1 assigned to silicate features a broad band centered at 1057 cm^{-1}, represented by the vertical yellow line in figure 3D. This band is qualitatively similar to one seen in a labradorite spectrum collected by ACRONM (see section S4.2) SHERLOC also detected possible pyroxene at six points across 0207_Garde HDR_500_1, 0207_Garde HDR_500_2, and 0208_Garde Detail_500_3. The mean spectrum of these six spectra features a peak at ~1020 cm^{-1}, which most closely matches a spectrum collected from diopside on Brassboard. However, the comparison to a standard diopside spectrum is not a formal mineral assignment, which will require a detailed investigation beyond the scope of this paper.

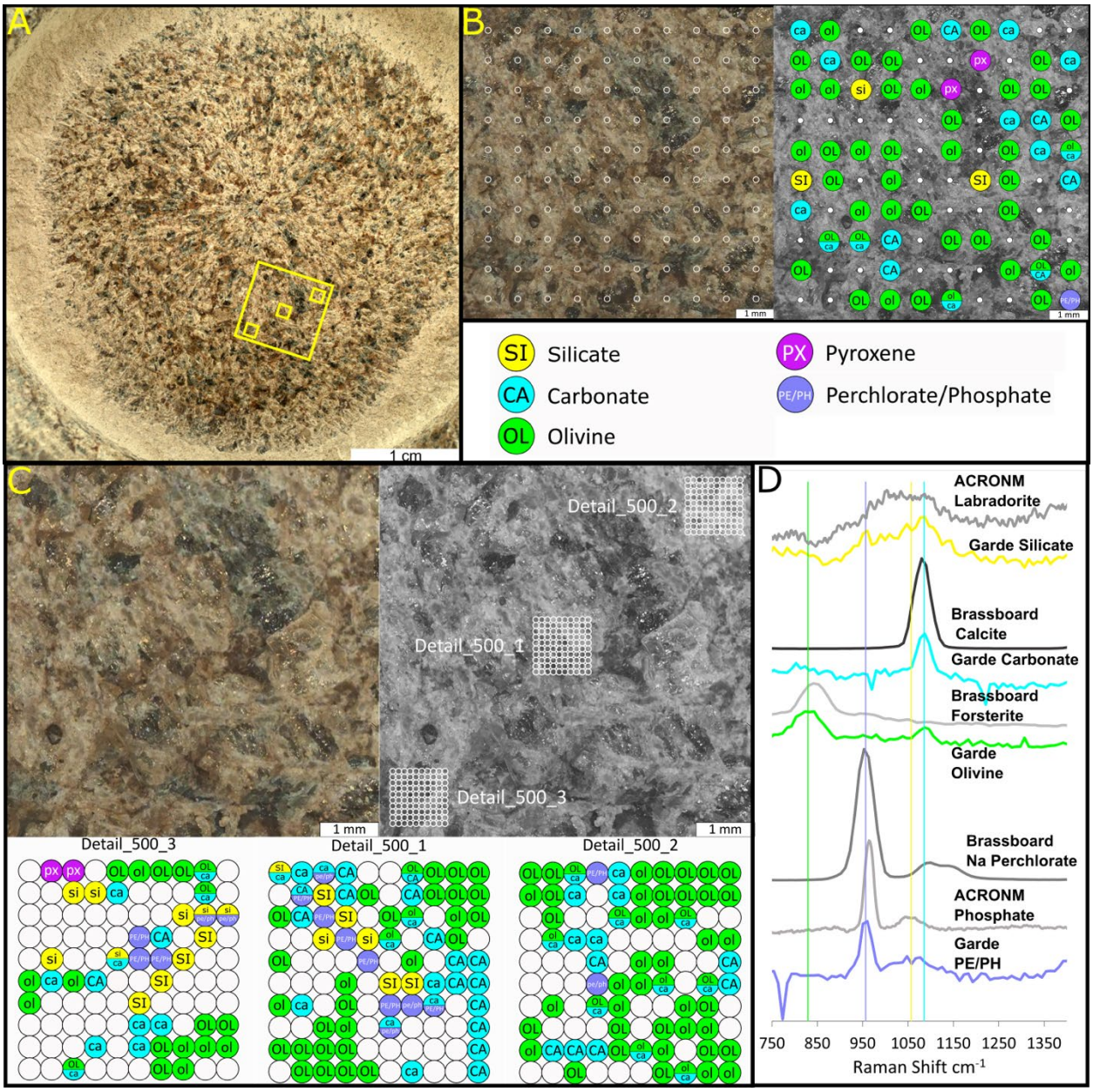

Figure 3. SHERLOC Raman mineral identifications from Garde. A) The abrasion patch imaged by WATSON (image ID SIF_0206_0685226491_804FDR_N0071836SRLC01024_0000LMJ01). Yellow boxes indicate the location of scans. B) Colorized (left) and grayscale (right) ACI images (image ID SC3_0208_0685436606_980FDR_N0071836SRLC11372_0000LMJ01) of the region of the abrasion patch bounded by the larger yellow box in panel A. The white circles in panel B indicate the locations of SHERLOC analysis spots for scan 0207_Garde HDR_500_2. Mineral identifications are indicated in the right panel. C) Upper Panel: Colorized (left) and grayscale (right) ACI images (image ID SC3_0208_0685432316_968FDR_N0071836SRLC11370_0000LMJ01) of the region of the abrasion patch where the Detail scans occurred. The white circles on the grayscale ACI image in panel C indicate the locations of SHERLOC

analysis spots of three 1 mm^2 Detail scans. The lower subpanel shows mineral identifications for the Detail scans. D) Representative Raman spectra of minerals detected with high confidence and spectra of mineral standards collected on the SHERLOC Brassboard instrument at JPL. Vertical lines indicate peak centers. Spectra are offset along the y-axis for clarity.

3.1.3 Quartier

The Quartier abrasion patch, which was approximately 7 mm deep, was made on sol 292 on Issole, a weathered, tabular outcrop of the Issole member of the Séítah formation, near the contact of the Séítah and Máaz formations (Fig. 1). The pre-abrasion surface of Quartier exhibited multiple textures: centimeter-scale platy features, rounded bumps that were up to approximately one centimeter tall, and a patchy covering of coarse regolith to fine-grained gravel (Fig. S2C). It also featured occasional rounded centimeter-scale pebbles. Quartier is associated with two core samples from the Issole outcrop: Robine and Malay. Abrading Quartier revealed prominent dark gray-to-black angular 1–5 mm mineral grains associated with smaller and less abundant light-to-dark gray minerals that are sometimes rimmed with light reddish-brown material (Fig. 4A). These gray-to-black mineral grains exist within a light colored matrix. The surface also features scattered, irregularly shaped, bright white mineral grains and closely associated reddish-brown mineral grains. SHERLOC scans of Quartier focused on an area that is dominated by bright white and reddish-brown grains, with some dark gray-to-black grains (Figs. 4A and B).

SHERLOC scans of Quartier include 0293_Quartier Survey_15_1, 0293_Quartier HDR_500_1, 0304_Quartier Survey_15_1 (which had 50 μm spacing), 0304_Quartier Detail_500_1, 0304_Quartier Detail_500_2, 0304_Quartier Detail_500_3, and 0304_Quartier Detail_500_4. (Fig. 4). All of the Quartier scans, including the survey scans, contain spectra that correspond to

sulfate. The Quartier HDR and Detail scans also contain spectra corresponding to carbonate, olivine, undefined silicate, perchlorate, and perchlorate or phosphate (Fig. 4B-D).

Carbonate and sulfate were the most abundant minerals detected in 0293_Quartier HDR_500_1 (Fig. 4B). Eighteen percent of the points in this scan were definitively assigned to carbonate and an additional 18% were assigned as probable carbonate. The dominant peak of the mean spectrum of all points in 0293_Quartier HDR_500_1 definitively assigned to carbonate, with no second assignment, is centered at 1085 cm^{-1}, represented by the vertical cyan line in figure 2D. Twelve percent of the points were definitively assigned to sulfate and an additional 9% were assigned as probable sulfate. The mean spectrum of all points in 0293_Quartier HDR_500_1 definitively assigned to sulfate has a primary peak centered at 1011 cm^{-1} and no clear secondary peaks.

The sulfate detections in 0293_Quartier HDR_500_1 are generally collocated with a patch of bright white mineral grains, while the carbonate detections fall on reddish-brown mineral grains surrounding the sulfate grains (Fig. 4B). A single point in this scan was assigned as probable olivine. This detection falls on a highly reflective, light gray mineral that is surrounded by carbonate (Fig 4B). The spectrum of one point definitively assigned to sulfate in this scan also contains a peak at 952 cm^{-1} assigned to perchlorate or phosphate. This point falls partially on bright white grains and partially on a small brown grain within the patch of bright white mineral grains (Figs. 4B). Two points in the 0293_Quartier HDR_500_1 scan were definitively assigned to silicate and one point was identified as a probable silicate. The silicate detections fall on dark gray-to-black mineral grains (Fig. 4B).

The four Quartier Detail scans, which were focused on the bright white mineral grains, are dominated by sulfate detections (Figs. 4C). Of the 400 combined points in the Quartier Detail

scans, we definitively assigned 66% to sulfate and assigned 11% probable sulfate. As in the HDR scan of Quartier, the sulfate detections were collocated with the bright white mineral grains. The mean spectrum of all points in 0304_Quartier Detail_500_1 definitively assigned to sulfate only has a primary peak centered at 1015 cm^{-1}, represented by the vertical red line in figure 4D, and secondary peaks at 1133 cm^{-1} and 1221 cm^{-1}, represented by dashed and dotted vertical red lines, respectively (Fig. 4D). The primary peak of the representative Quartier sulfate spectrum and the secondary peak at 1133 cm^{-1} are near the primary and secondary peaks of a gypsum standard (WARDS #46–3798) spectrum collected on Brassboard, which has peaks at 1009 cm^{-1} and 1129 cm^{-1} (Fig. 4D). The secondary peak at 1221 cm^{-1} in the Quartier sulfate spectrum does not correspond to any peak in the Brassboard gypsum spectrum. However, the primary peak in the Quartier sulfate spectrum also has good agreement with the primary peak of the synthetic magnesium sulfate (Macron Chemicals) spectrum collected on Brassboard, which is centered at 1019 cm^{-1}, and the two secondary magnesium sulfate peaks that can vary between ~1060 cm^{-1} and ~1260 cm^{-1}, according to hydration state (Wang et al., 2006; Fig. 4D). The representative Quartier sulfate spectrum has a broad band with two peaks at 3229 cm^{-1} and 3415 cm^{-1}, which is consistent with OH stretching mode bands seen in hydrated sulfates (Fig. S10b). Further investigation is needed to establish the primary cation and hydration states of Quartier sulfates at individual points within the Quartier scans, but the mean spectrum presented in figures 4D and S10b suggests that the bright white minerals of Quartier may be a mixture of calcium and magnesium sulfate at various levels of hydration.

In addition to sulfate, the Quartier Detail scans detected carbonate, olivine, perchlorate/chlorate, and perchlorate or phosphate. Three definitive carbonate detections, one in 0304_Quartier Detail_500_1 and two in 0304_Quartier Detail_500_2, fall on small, reddish-brown mineral

grains at the margins of sulfate grains within or at the edge of the bright white patch of sulfate. Only one definitive olivine assignment was made in the Quartier Detail scans. It was at a point that was also definitively assigned to sulfate and falls on small, light gray grains at a boundary between dark gray and bright white grains (Fig. 4C). We definitively assigned three points in 0304_Quartier Detail_500_1 to perchlorate or chlorate with unknown cation, all of which were also definitively assigned sulfate. The perchlorate/chlorate assignments were made based on the presence of peaks at 938 cm^{-1}, 935 cm^{-1}, and 931 cm^{-1}, which are consistent with the primary peaks in ACRONM spectra collected from several different oxychlorine species (Fig. S12). The points assigned perchlorate/chlorate fall on light gray-to-brown material at the boundary between a bright white and dark gray-to-black grain (Fig. 4C).

We assigned eight points in the Quartier Detail scans to perchlorate or phosphate. Six of these points are also assigned to sulfate, one is also assigned to carbonate, and one is also assigned to both sulfate and carbonate. The perchlorate or phosphate peak in the mean spectrum of the eight perchlorate or phosphate spectra is centered at ~959 cm^{-1} (Fig. 4D) and cannot be definitively assigned to perchlorate or phosphate (see sections S4.6 and S4.8). Most of these detections are associated with hydrated sulfate detections. The single perchlorate/chlorate detection in 0304_Quartier Detail_500_2 that is not associated with sulfate has no discernable hydration features. Like the points assigned perchlorate/chlorate, these points fall on light gray-to-brown material at the boundaries of bright white mineral grains.

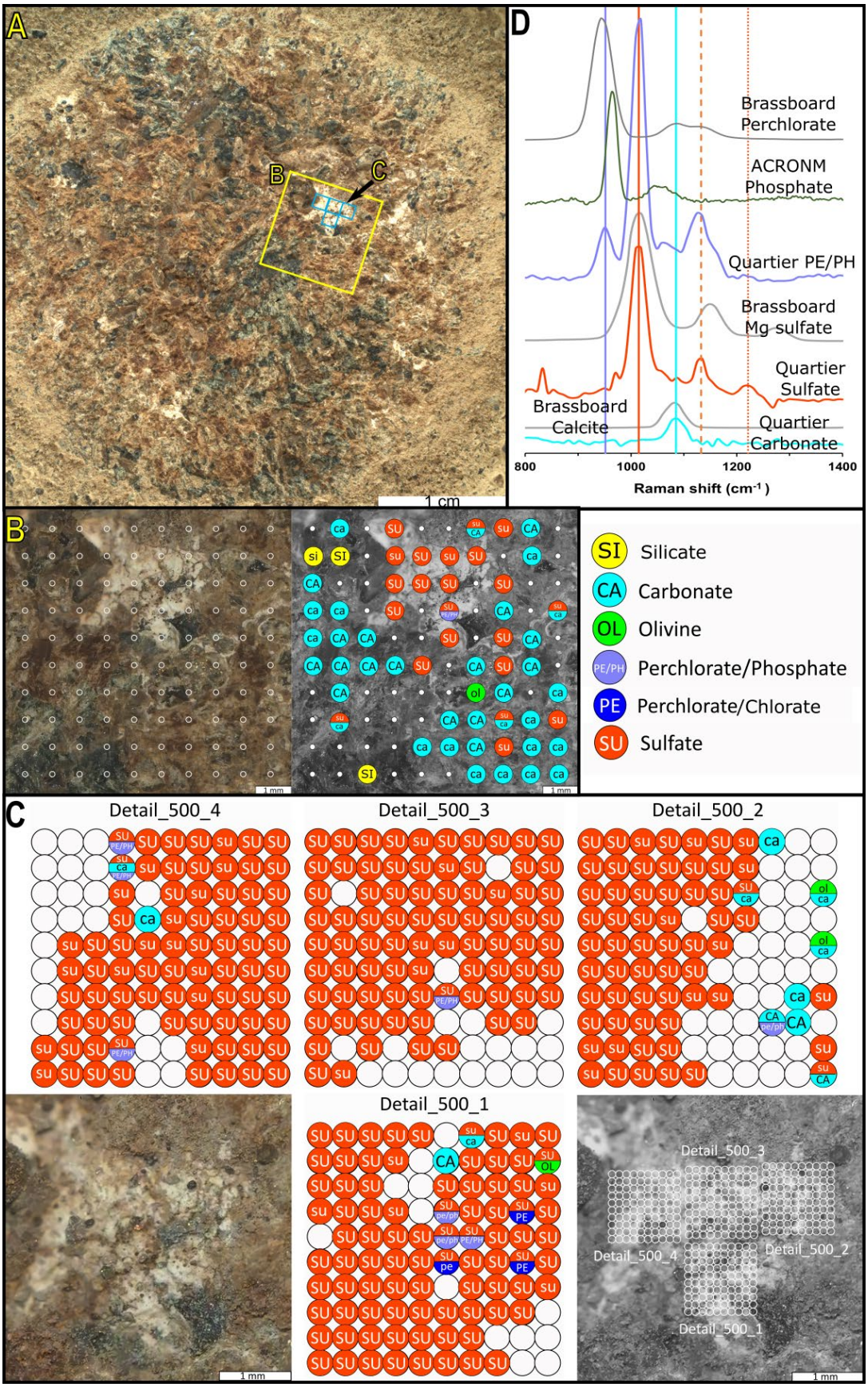
A
B
C
1 cm
D
Brassboard Perchlorate
ACRONM Phosphate
Quartier PE/PH
Brassboard Mg-sulfate
Quartier Sulfate
Brassboard Calcite
Quartier Carbonate
800
1000
1200
1400
Raman shift (cm-1)
B
1 mm
1 mm
SI Silicate
CA Carbonate
OL Olivine
PE/PH Perchlorate/Phosphate
PE Perchlorate/Chlorate
SU Sulfate
C
Detail_500_4
Detail_500_3
Detail_500_2
Detail_500_1
1 mm
Detail_500_3
Detail_500_4
Detail_500_2
Detail_500_1
1 mm

Figure 4. SHERLOC Raman mineral identifications from Quartier. A) The abrasion patch imaged by WATSON (image ID SIF_0292_0692866773_550FDR_N0090000SRLC00702_0000LMJ01). The yellow box indicates the location of the HDR scan and blue boxes indicate the location of the Detail scans. B) Colorized (left) and grayscale (right) ACI images (image ID SC3_0293_0692982585_671FDR_N0090000SRLC10600_0000LMJ01) of the region of the abrasion patch bounded by the larger yellow box in panel A. The white circles in panel B indicate the locations of SHERLOC analysis spots for 0293_Quartier HDR_500_1. Mineral identifications are indicated in the right panel. C) Colorized (bottom left) and grayscale (bottom right) ACI (image ID SC3_0304_0693962423_667FDR_N0090000SRLC11373_0000LMJ01) images of the region of the abrasion patch where the Detail scans occurred. The white circles on the grayscale ACI image in panel C indicate the locations of SHERLOC analysis spots for four 1 mm^2 Detail scans. The other four subpanels show mineral identifications for Quartier Detail scans. D) Representative Raman spectra of minerals detected with high confidence from the abrasion patch and spectra of mineral standards collected on the SHERLOC Brassboard instrument at JPL. Vertical lines represent peak centers. Spectra are offset along the y-axis for clarity.

3.2 Máaz Targets

3.2.1 Guillaumes

Guillaumes was the first abraded patch of the Mars 2020 mission, made on sol 160. This abrasion, which was approximately 8 mm deep, was on a low-relief, polygonal outcrop of the Roubion member of the Máaz formation, also called Roubion (Fig.1). The pre-abrasion surface of the target appeared degraded, granular, and flaky, with regolith embedded in the lowest points and rounded pebbles up to ~5 mm in size across it (Fig. S2D). Meter-scale, friable, low-relief, polygonal outcrops are characteristic of the Roubion member, which is at least ~5 m thick and interpreted to be the stratigraphically lowest member of the Máaz formation (Farley et al., 2022). The attempt to core this target produced a borehole and cuttings, but no core was recovered (Simon et al., 2022). The Guillaumes abrasion (Fig. 5A) revealed millimeter-scale, interlocking, light and dark mineral grains. Slightly larger, irregularly shaped bright white mineral grains were also present. The abraded surface featured pits and crevices up to approximately 5 mm in

diameter. The surface was discontinuously stained by dark brown material, particularly in and near the pits.

SHERLOC Guillaumes scans included 0161_Guillaumes Survey_15_1, 0161_Guillaumes HDR_100_1, 0161_Guillaumes HDR_100_2, 0161_Guillaumes HDR_300_1, 0162_Guillaumes HDR_250_1 and 0162_Guillaumes HDR_250_2. The sol 161 scans covered an area of the abraded surface that was primarily composed of interlocking light and dark mineral grains with extensive dark brown staining while the sol 162 scans covered an area of interlocking light and dark grains with both irregular bright white mineral grains and discontinuous dark brown staining (Figs. S3A-C, 5A-B).

The sol 161 scans yielded only two spectra with Raman peaks that could be assigned to a mineral class (Fig. S3A-B). The limited Raman signal observed in this scan may be the result of iron oxide minerals coating much of the area this scan covered, which is suggested by the brown staining on the abraded surface (Figs. S3A-B, 5A). The two assigned points are point ten of 0161_Guillaumes HDR_100_2 and point ten of 0161_Guillaumes HDR_300_1, which are approximately collocated; both are assigned to perchlorate with an unknown cation.

In the sol 162 scans, we observed numerous spectra of sodium perchlorate, perchlorate with no cation assignment, and sulfate, in agreement with Scheller et al. (2022), along with a single possible silicate spectra (Figs. 5, S3). The perchlorate and sulfate detections generally fall on irregular bright white mineral grains. The representative Guillaumes sodium perchlorate spectrum in figure 5C is the mean spectrum of the points in scan 0162_Guillaumes HDR_250_1 assigned to sodium perchlorate with no second assignment (Fig 5B). The dominant peak of this spectrum is centered at 952 cm^{-1}, represented by the vertical solid blue line in figure 5C. The secondary peaks in this spectrum are centered at 1091 cm^{-1} and 1150 cm^{-1}, represented by

vertical dashed and vertical dotted blue lines in figure 5C, respectively. The signal to noise ratios of both the primary and secondary peaks in the individual Guillaumes spectra assigned to sodium perchlorate were greater than ten. For SHERLOC spectra with S/N > 10, the standard deviation of the fitted peak position error is less than 1.2 cm^{-1} (see section S1). As a result, we can confidently assign these Guillaumes detections to a specific mineral species. The peaks of the representative Guillaumes sodium perchlorate spectrum directly correspond to the peaks of the sodium perchlorate (Sigma Aldrich 310514) standard spectrum collected on the Brassboard. In addition to peaks at ~950 cm^{-1}, ~1090 cm^{-1}, and ~1150 cm^{-1}, the Brassboard spectrum features a hydration peak centered at ~3500 cm^{-1} that is approximately three times as intense as the peak at ~1090 cm^{-1}. We did not observe a potential hydration peak in any individual or averaged Guillaumes sodium perchlorate spectra.

The representative Guillaumes perchlorate spectrum in figure 5C is the mean spectrum of the points in scan 0162_Guillaumes HDR_250_1 definitively assigned to perchlorate with no second assignment (Fig 5B). The dominant peak of this spectrum is centered at 950 cm^{-1}. Secondary peaks were not discernible in individual spectra assigned to perchlorate with unknown cation. However, the mean spectrum displays a weak peak at ~1090 cm^{-1}, which corresponds to the most intense secondary peak in the Brassboard spectrum, and the primary peak corresponds to the primary sodium perchlorate peak, suggesting that the perchlorate spectra represent weak sodium perchlorate detections. This mean spectrum also exhibits a weak peak that corresponds with the primary peak of the sulfate spectra detected in Guillaumes, which demonstrates the close association of perchlorate and sulfate in this target.

The representative Guillaumes sulfate spectrum in figure 5C is the mean spectrum of the points in scan 0162_Guillaumes HDR_250_1 assigned to sulfate with no second assignment (Fig. 5).

The dominant peak of this spectrum is centered at 1017 cm^{-1} and the secondary peak is centered at 1123 cm^{-1}, represented by the solid and dashed vertical red lines in figure 5C, respectively. This spectrum also exhibits a weak, broad OH stretching band with two peaks at 3287 cm^{-1} and 3498 cm^{-1}. Similarly to the sulfate spectra observed in Quartier scans, peak positions in the representative Guillaumes sulfate spectrum are consistent with some features of several different Brassboard sulfate spectra, including gypsum, epsomite (CVS epsom salts), natural kieserite (JPL mineral collection), and synthetic magnesium sulfate (Macron Chemicals). This suggests that the sulfates detected in Guillaumes may have mixed calcium and magnesium cations, but further investigation is needed before mineral species assignments are made. The mean Guillaumes sulfate spectrum also features a weak peak that corresponds with the primary perchlorate peak, again demonstrating the close association of these two minerals in Guillaumes.

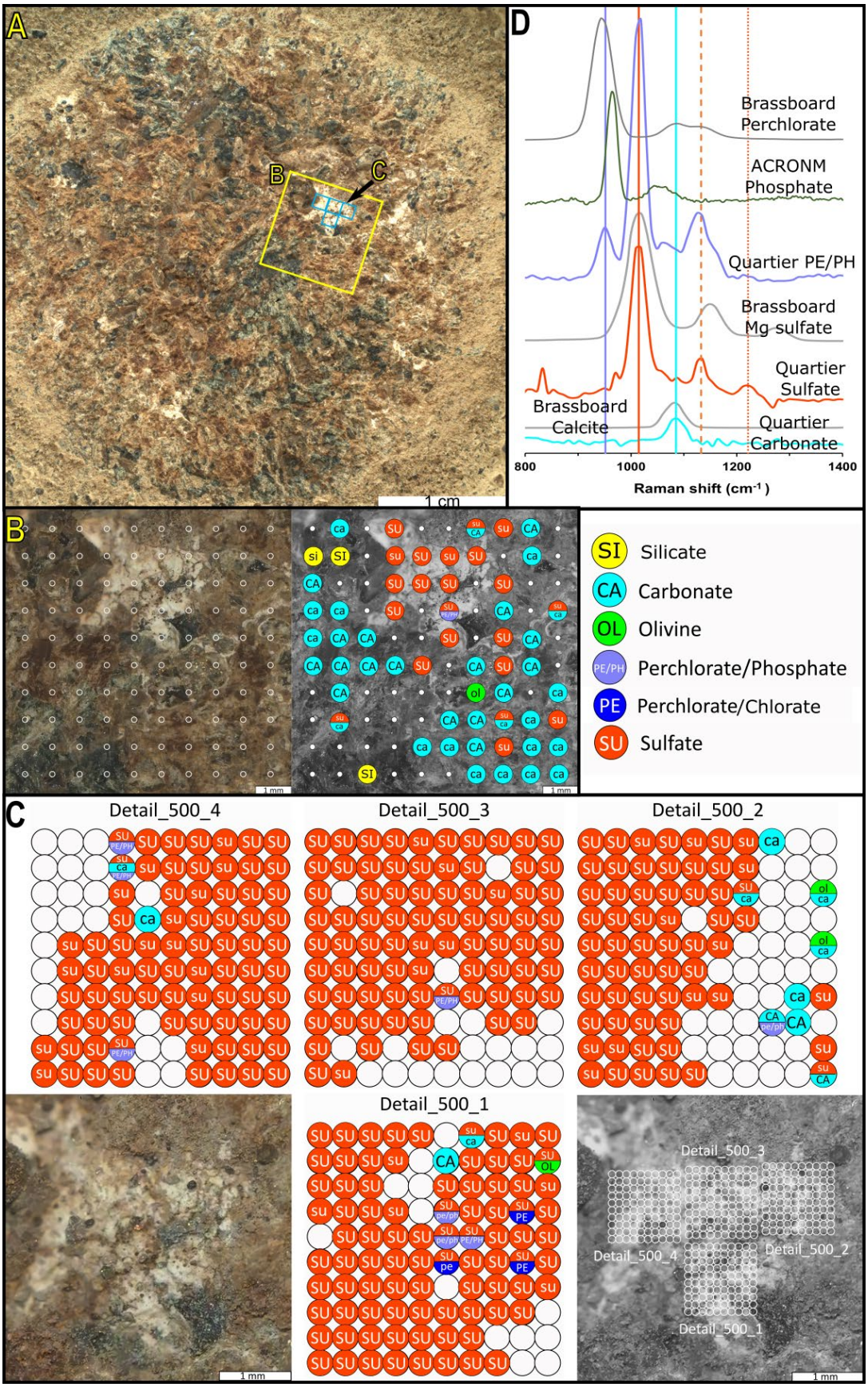
A
B
C
1 cm
D
Brassboard Perchlorate
ACRONM Phosphate
Quartier PE/PH
Brassboard Mg-sulfate
Quartier Sulfate
Brassboard Calcite
Quartier Carbonate
800
1000
1200
1400
Raman shift (cm-1)
B
1 mm
1 mm
SI Silicate
CA Carbonate
OL Olivine
PE/PH Perchlorate/Phosphate
PE Perchlorate/Chlorate
SU Sulfate
C
Detail_500_4
Detail_500_3
Detail_500_2
Detail_500_1
1 mm
Detail_500_3
Detail_500_4
Detail_500_2
Detail_500_1
1 mm

Figure 5. SHERLOC Raman mineral identifications from scan 0162_Guillaumes HDR_250_1. A) The abrasion patch imaged by WATSON (image ID SI1_0160_0681181210_679FDR_N0060000SRLC00003_000095J01). Yellow boxes indicate the location of the scans performed. The left box corresponds to HDR scans performed on sol 161 (Fig. S3). The right box corresponds to HDR scans performed on sol 162. B) colorized (left) and grayscale (right) ACI images (image ID SC3_0162_0681352993_195FDR_N0060000SRLC11420_0000LMJ01) of the region of the abrasion patch bounded by the right yellow box in panel A. The white circles in panel B indicate the locations of SHERLOC analysis spots. Mineral identifications from scan 0162_Guillaumes HDR_250_1 are indicated in the right panel. C) Representative Raman spectra of minerals detected with high confidence from the abrasion patch and spectra of mineral standards collected on the SHERLOC Brassboard instrument at JPL. Vertical lines indicate peak centers. Spectra are offset along the y-axis for clarity.

3.2.2 Foux

SHERLOC scanned the natural target Foux on sol 141. SHERLOC also scanned two other natural targets during the Crater Floor Campaign (see section 3.2.5). Like Guillaumes, Foux was a low-relief, polygonal outcrop of the Roubion member of the Máaz formation. Its surface was somewhat similar to the unabraded surface of Guillaumes. It appeared degraded and had regolith settled into its recesses. It also featured occasional rounded pebbles, up to ~5 mm in size (Fig. S2E). The most notable difference between the surface of Foux and the unabraded surface of Guillaumes was the presence of a purplish coating on Foux (Garczynski et al., 2022).

Scans of Foux included 0141_Foux Survey_15_1, 0141_Foux HDR_100_1, 0141_Foux HDR_100_2, and 0141_Foux HDR_300_1. As in the other two natural targets of the Crater Floor Campaign, Nataani and Bi La Sana (see section 3.2.5), but unlike scans of the abraded targets, the Foux scans produced no single Raman spectra that could be given a mineral assignment. This was expected, as SHERLOC is optimized for analyzing dust-free surfaces with low relief, conditions that were not met on the surface of Foux, Nataani or Bi la Sana. The median and average spectra of all of the Foux scans showed silicate bands centered between ~1040 cm^{-1} and

~1050 cm^{-1} (Fig. S5) and the fused silica background spectral signature peaks at ~480 cm^{-1} and ~800 cm^{-1} discussed in section 2.4 (Fig. S4b).

3.2.3 Montpezat

The Montpezat abrasion, which was approximately 8 mm deep, was made on sol 346 on Rimplas, an outcrop of the Artuby member of the Máaz formation. The surface of Rimplas is coarse-grained and exhibits 1–10 centimeter thick layers with variable erosion resistance between layers (Fig. 1). A coarse-grained surface texture and decimeter thick layers are characteristic of the Artuby member (Farley et al., 2022). The pre-abrasion surface of the Montpezat target looked very similar to that of Guillaumes and Foux, with course regolith and fine gravel packed into recesses between bumps up to ~5mm tall, occasional, rounded, sub-centimeter pebbles, and small patches of purplish coating (Fig. S2F). Rimplas was not an intended coring target and the Montpezat abrasion is not associated with any sample cores.

The abraded surface of Montpezat appears highly altered compared to that of the other abraded targets (Fig. 6A). It is uneven, perhaps due to pitting that is similar to but more extensive than that seen on Guillaumes. The surface also exhibits extensive staining with dark brown-to-black material. Furthermore, it is partially covered in fine material that is likely cuttings from the abrasion process, possibly because the gDRT used a smaller volume of nitrogen gas to clean Montpezat than it used for previous targets. The least altered or occluded portion of the surface of Montpezat was targeted for SHERLOC scanning, but there is reddish brown staining over much of the scanned surface. The scanned surface exhibits sub-millimeter to millimeter sized interlocking white to dark gray-blue grains.

SHERLOC scans of Montpezat included 0349_Montpezat Survey_15_1 and 0349_ Montpezat HDR_500_1 scans. No points in the Montpezat Survey scan had a discernible Raman signal. The 0394_Montpezat HDR_500_1 scan revealed silicate, carbonate, and perchlorate or phosphate spectral signatures. Seventeen single spectra display silicate signatures, however, only four of those assignments were made with high confidence. We observed three carbonate and three perchlorate or phosphate spectra in the scan. All carbonate spectra and one of the perchlorate or phosphate spectra are of low confidence. Figure 6C shows the mean spectrum of all 0349_Montpezat HDR_500_1 definitively assigned to silicate and the mean spectrum of the two points definitively assigned to perchlorate or phosphate. These peaks are centered at 1050 cm^{-1} and 959 cm^{-1} respectively. The Montpezat HDR scan also contains one spectrum with a low, broad band centered at ~1600 cm^{-1}, which may be a graphitic (G) band. The point with the possible G band is indicated by a capital G on a white background in figure 6B. A report from the SHERLOC team that discusses the context and implications of this detection is forthcoming.

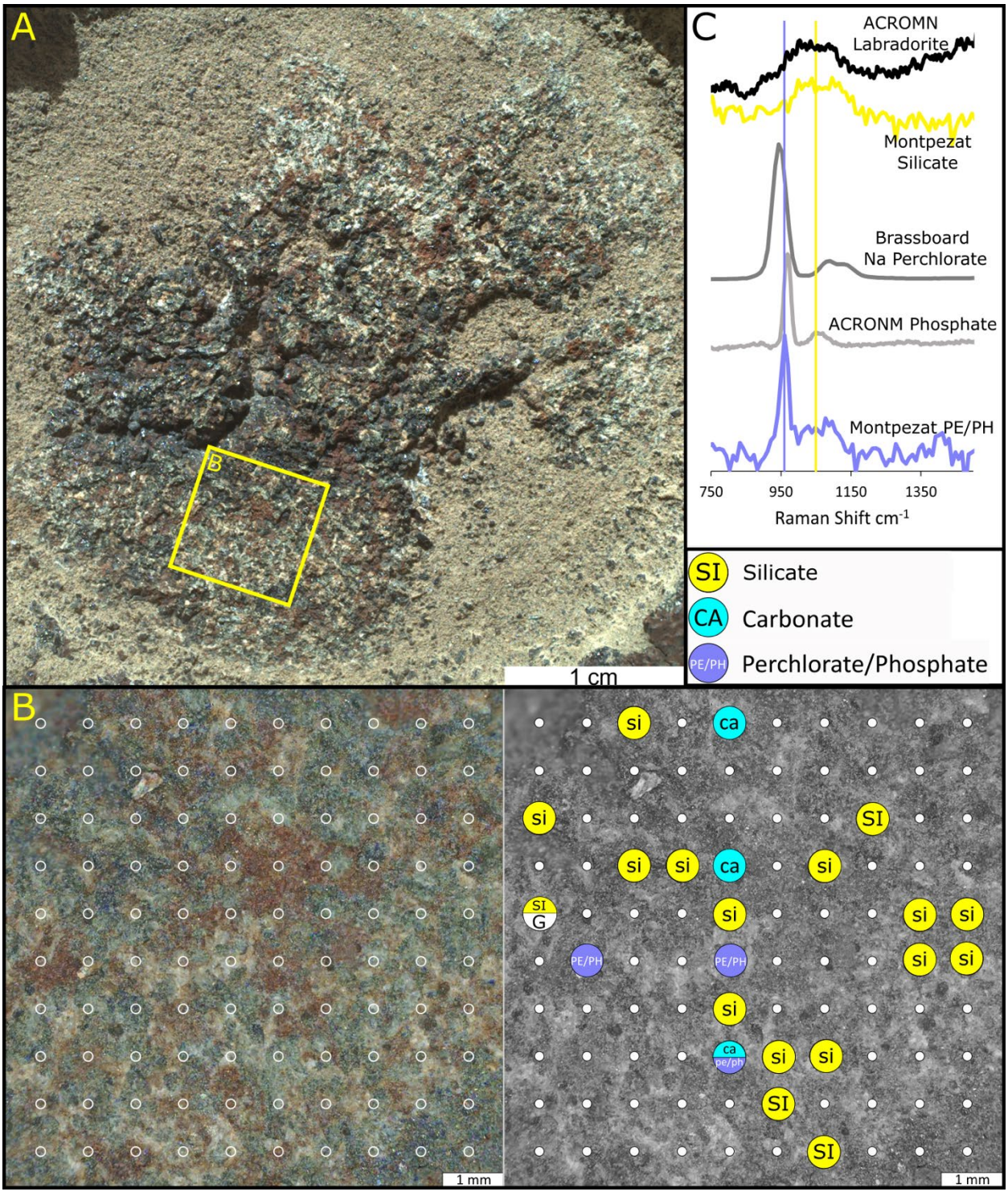

Figure 6. SHERLOC Raman mineral identifications from the 0349_Montpezat HDR_500_1 scan of target Montpezat. A) The abrasion patch imaged by WATSON (image ID SIF_0346_0697661461_972FDR_N0092982SRLC01034_0000LMJ01). The yellow box indicates the location of the scan. B) Colorized (left) and grayscale (right) ACI images (image ID

SC3_0349_0697954126_179FDR_N0092982SRLC10600_0000LMJ01) of the region of the abrasion patch bounded by the yellow box in panel A. The white circles in panel B indicate the locations of SHERLOC analysis spots. Mineral identifications are indicated in the right panel. C) Representative Raman spectra from the abrasion patch of minerals detected with high confidence, and mineral standard spectra collected on the SHERLOC Brassboard instrument at JPL and the ACRONM instrument at JSC. Spectra are offset along the y-axis for clarity.

3.2.4 Bellegarde

The Bellegarde abrasion, which was approximately 8 mm deep, was made on sol 185 on a small blocky boulder (approximately 40 cm across; Fig. 1) of the Rochette member of the Máaz formation. The boulder was chosen as the second target for abrasion and coring in part because it did not appear to be highly weathered (Fig. S2G), indicating a high likelihood for successful core recovery. In fact, the first two successful cores of the Mars 2020 mission, Montdenier and Montagnac, were retrieved from this boulder (Simon et al., 2022). The erosion-resistant Rochette member is approximately 30 to 50 cm thick and often exhibits centimeter scale layering (Farley et al., 2022). The Rochette member caps the crest of Artuby ridge (Sun et al., 2022).

The abraded surface of Bellegarde (Fig. 7A) features sub-millimeter, interlocking, white to dark green-gray mineral grains. We also observed some larger, bright white mineral grains rimmed by a tan material on the surface of Bellegarde. The surface of Bellegarde is partially stained by a reddish-brown material.

SHERLOC scans of Bellegarde include 0186_Bellegarde Survey_15_1, 0186_Bellegarde HDR_250_1, and 0186_Bellegarde HDR_250_2. The data from these scans indicate that Bellegarde contains silicate, perchlorate or phosphate, and sulfate spectral signatures. As reported by Scheller et al. (2022), the Bellegarde Survey scan detected sulfate associated with the largest cluster of bright white minerals in the upper left region of the scan. Only 17 of 200 total spectra across both Bellegarde HDR scans show Raman spectral signatures. The low level of

Raman signals in Bellegarde may be due to the presence of iron oxide minerals at the target surface, which is suggested by the reddish-brown staining. Most Bellegarde mineral detections are on regions of the target that have no staining.

The 17 mineral detections in the Bellegarde HDR scans include three definitive and seven probable silicate, which fall on dark gray grains; four probable sulfate, which are only sometimes associated with bright white grains; and two definitive and one probable perchlorate or phosphate, which fall on medium to dark gray grains. Figure 7C shows the mean spectrum of all 0186_Bellegarde HDR_250_2 definitively assigned to silicate and the mean spectrum of the two points definitively assigned to perchlorate or phosphate. These peaks are centered at 1036 cm^{-1} and 955 cm^{-1} respectively. The peak centered at 1036 cm^{-1} is qualitatively similar to the band in a labradorite spectrum collected by ACRONM and assigned to silicate (Fig. 7C).

As in Garde, the Bellegarde spectra assigned to perchlorate or phosphate also feature a fluorescence band at ~340 nm (Scheller et al., 2022). The ~340 nm fluorescence feature could result from organic species and/or from trivalent cerium (Ce^{3+}) within a phosphate crystal structure (Shkolyar et al., 2021). Therefore, the ~340 nm fluorescence feature may support a phosphate assignment for these detections (see section S4.6). Data acquired by Perseverance's SuperCam instrument revealed the presence of an anhydrous sodium perchlorate signature associated with a bright white patch of mineral grains at Bellegarde that was not analysed by SHERLOC, similar to that detected by both SHERLOC and SuperCam at Guillaumes (see section 3.2.1; Meslin et al., 2022). Taken together, these analyses suggest that both phosphate and perchlorate may be present in the Bellegarde abrasion.

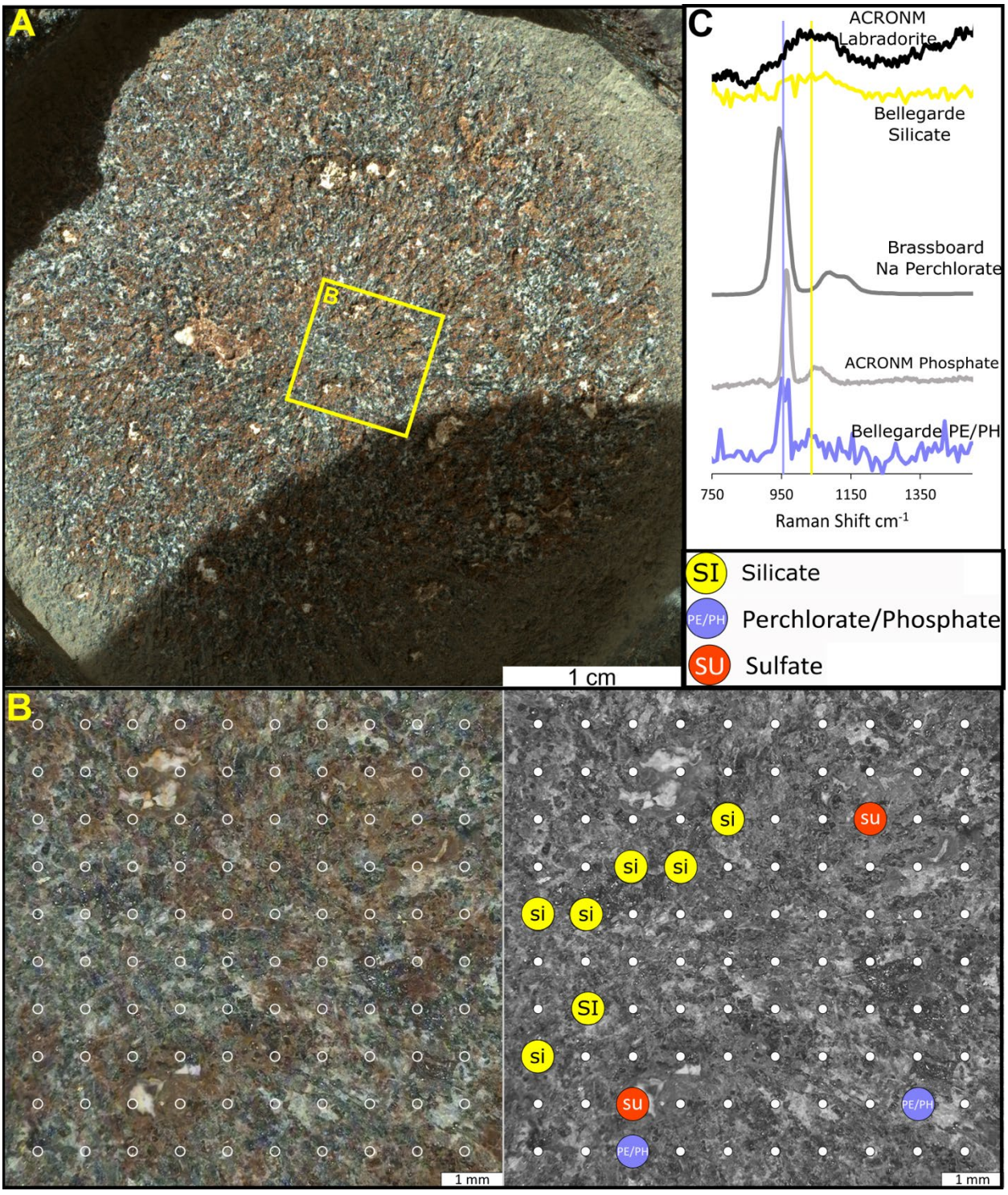

Figure 7. SHERLOC Raman mineral identifications from scan 0186_Bellegarde HDR_250_2 of the target Bellegarde. A) The abrasion patch imaged by WATSON (image ID SIF_0185_0683368184_652FDR_N0070000SRLC00720_0000LMJ01). The yellow box indicates the location of the HDR. B) Colorized (left) and grayscale (right) ACI images (image ID

SC3_0186_0683479674_054FDR_N0070000SRLC11420_0000LMJ02) of the region of the abrasion patch bounded by the yellow box in panel A. The white circles in panel B indicate the locations of SHERLOC analysis spots. Mineral identifications are indicated in the right panel. C) Representative Raman spectra from the abrasion patch of minerals detected with high confidence, and mineral standard spectra collected on the SHERLOC Brassboard instrument at JPL and the ACRONM instrument at JSC) Vertical lines indicate peak centers. Spectra are offset along the y-axis for clarity.

3.2.5 Nataani and Bi la Sana

SHERLOC's first two sets of scans on Mars were performed on the natural targets Nataani, on sol 83, and Bi la Sana, on sol 98 (Fig. S2H-I). These targets are expressions of the Nataani member of the Máaz formation, which overlies the Rochette member, according to ground penetrating radar data (Farley et al., 2022).

Scans on Nataani included 0083_Nataani Survey_10_1, which yielded no detectable Raman signal; 0083_Nataani HDR_5_1, which yielded no detectable Raman signal; 0083_Nataani HDR_50_1, which displayed the fused silica background peaks at ~480 cm^{-1} and 800 cm^{-1} (see sections 2.4 and S2) in the mean and median spectra; and 0083_Nataani HDR_100_1, which displayed the fused silica background signal and an silicate band centered at ~1055 cm^{-1} in the mean and median spectra (Fig. S5). Unlike most survey scans in the Crater Floor Campaign, which had 144 μm spacing, 0083_Nataani Survey_10_1 had 200 μm spacing.

The sol 98 set of scans of the natural target Bi la Sana included 0098_Bi la Sana Survey_15_1, 0098_Bi la Sana HDR_100_1, 0098_Bi la Sana HDR_100_2, and 0098_Bi la Sana HDR_300_1. All Bi la Sana scans displayed the fused silica background signal and an silicate band centered at ~1050 cm^{-1} in the mean and median spectra (Fig. S5).

While Raman mineral detections were minimal in the natural target scans of the Crater Floor Campaign, compared to the abraded target scans, it is noteworthy that the same silicate signature observed in many abraded target scans also appears in several of the natural target scans.

3.2.6 Alfalfa

The Alfalfa abrasion, which was approximately 9 mm deep, was made on sol 367 on Sid, a boulder in the Ch'aɬ member of the Máaz formation (Fig. 1). The Ch'aɬ member overlies the Nataani member (Farley et al., 2022) Sid is a blocky, apparently structureless, gray boulder and a typical representative of the Ch'aɬ member. The light tan-to-gray pre-abrasion surface of Sid was polished and fluted by wind abrasion and relatively dust free (Fig. S2J). Two core samples, Ha'ahóni and Atsá, were retrieved from Sid. The Alfalfa abrasion revealed interlocking, sub-millimeter to ~ 5 mm bright white, brown, gray, and black mineral grains (Fig. 8A). The largest of the grains are bright white, lath-like, and highly reflective. There is patchy reddish brown coloration across the entire abraded surface.

SHERLOC scans of Alfalfa include 0370_Alfalfa Survey_15_1 and 0370_Alfalfa HDR_500_1. The Alfalfa scans contain predominantly silicate spectra with minor components of carbonate and perchlorate or phosphate. In the single HDR Raman scan collected on alfalfa, silicate comprised 44 of the 100 spectra with 30 detections of high confidence. The mean spectrum of the definitive silicate detections contains a broad band centered at 1053 cm^{-1}, which is qualitatively similar to a broad band in a labradorite spectrum collected by ACRONM (Fig. 8C).Carbonate and perchlorate or phosphate peaks were found in 5 and 3 spectra respectively. Two of the perchlorate or phosphate assignments were of high confidence and only one of the carbonate assignments was of high confidence. The mean spectrum of the two definitively assigned perchlorate or phosphate detections has a peak centered at 949 cm^{-1} (Fig. 8C).

Several of the silicate detections are associated with bright white, highly reflective mineral grains, including a large lathe-like crystal. This mineral morphology suggests that the Alfalfa silicate detections may be plagioclase feldspar minerals. The carbonate detections fall on light

brown to red regions of the surface and the perchlorate or phosphate detections appear to fall at the margins of angular, black mineral grains. No mineral detections fell on the reddest regions of the target surface, which may indicate that the red color is the result of the presence of iron cations (Fig 8B), since ferric iron cations can absorb DUV laser radiation (Morris et al., 2022; Razzell Hollis et al., 2021a and b).

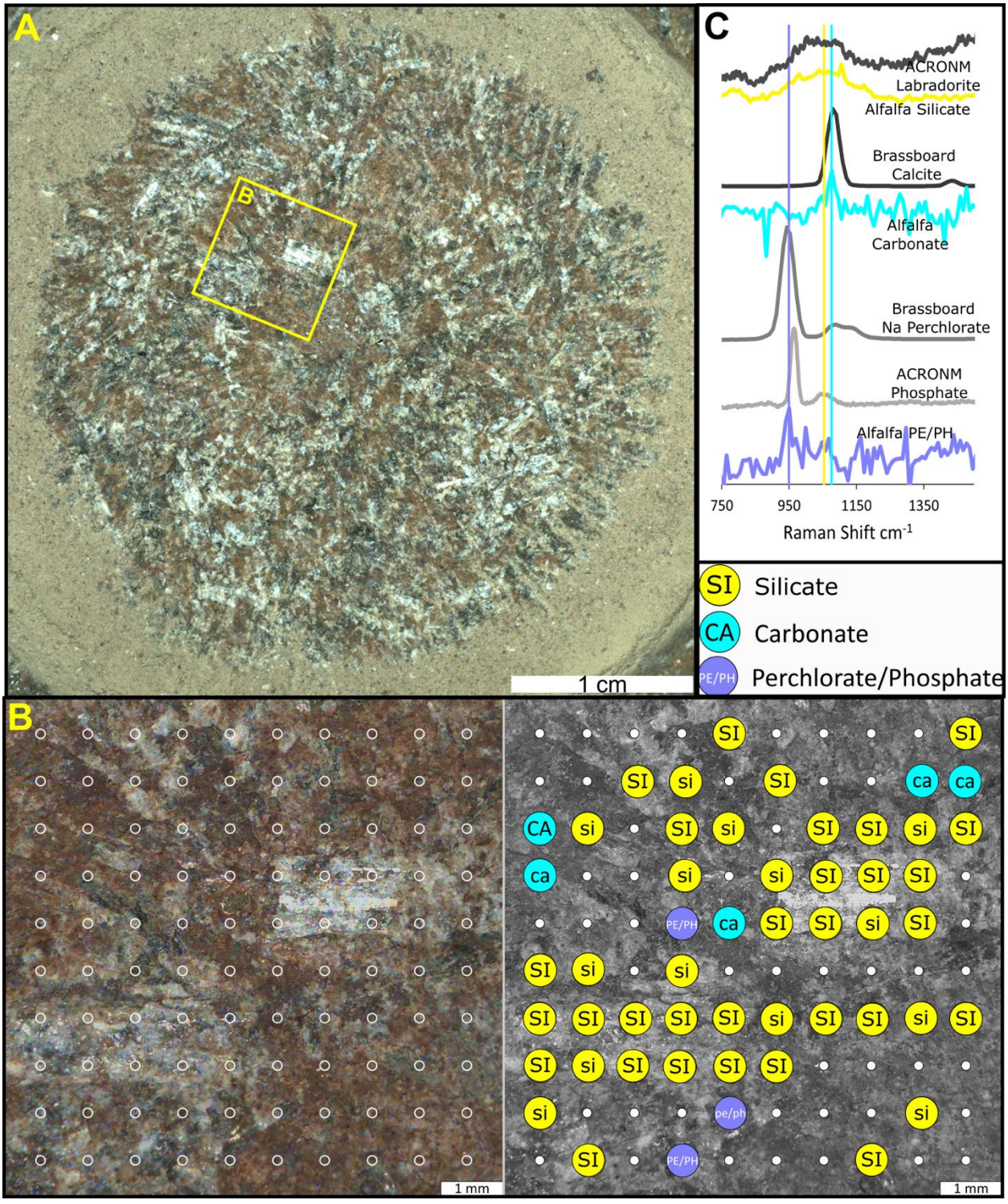

Figure 8. SHERLOC Raman mineral identifications from scan 0370_Alfalfa HDR_500_1 of target Alfalfa. A) The abrasion patch imaged by WATSON (image ID SIF_0367_0699544277_375FDR_N0110108SRLC08029_0000LMJ01). The yellow box indicates the location of the Alfalfa HDR scan. B) Colorized (left) and grayscale (right) ACI images (image ID

SC3_0370_0699816293_742FDR_N0110108SRLC10600_0000LMJ01) of the region of the abrasion patch bounded by the yellow box in panel A. The white circles in panel B indicate the locations of SHERLOC analysis spots. Mineral identifications are indicated in the right panel. C) Representative Raman spectra from the abrasion patch of minerals, and mineral standard spectra collected on the SHERLOC Brassboard instrument at JPL and the ACRONM instrument at JSC. Vertical lines indicate peak centers. Spectra are offset along the y-axis for clarity.

Discussion

SHERLOC scans of the three abraded Séítah targets and four abraded Máaz targets described above support the conclusions that the Séítah unit is an olivine cumulate and Máaz is a less mafic igneous unit. In addition, the SHERLOC scans reveal that, between them, the Séítah and Máaz units may record the histories of at least three different aqueous alteration events on the floor of Jezero Crater, including olivine carbonation and sulfate dominated salt deposition in Séítah, and sodium perchlorate dominated salt deposition in Máaz. The iron oxides present on the four Máaz targets (Weins et al., 2022) are also likely the result of aqueous alteration. Ultimately, the data acquired by SHERLOC during the Crater Floor Campaign show evidence that Jezero Crater was once a chemically active aqueous environment with the potential to host and preserve evidence of microbial life.

Figure 9 shows that the three most common mineral class detections in SHERLOC scans of Séítah targets were olivine, carbonate, and sulfate. Olivine and carbonate detections dominated scans in targets Dourbes and Garde, while minimal olivine was detected in Quartier. Scans of Quartier and Dourbes both revealed patches of sulfate, while Garde scans detected no sulfate. The minimal olivine detections in Quartier and lack of sulfate detection in Garde may not reflect a major difference in the mineralogy of these targets. The discrepancies may, instead, reflect the SHERLOC team’s decision to focus Quartier scans on the bright white patches of the target and the patchy nature of salt deposits in the Séítah formation.

We observe gray grains similar to the one that corresponds with a definitive olivine spectrum in 0304_Quartier Detail_500_1 across the surface of Quartier, sometimes rimmed by light reddish-brown material (Fig. 4A). These gray grains appear similar to grains identified as olivine in Dourbes and Garde and the reddish-brown material looks similar to carbonate that was associated with the olivine in Dourbes and Garde (Figs. 2, 3). While it is possible that Bastide, the outcrop that hosted the Garde abrasion (Fig.1), contains no sulfate deposits, it is equally likely that the Garde abrasion and scans simply did not sample Bastide's sulfate deposits. As demonstrated by the sulfate detected in Dourbes (Fig. 2), Séítah sulfate deposits are not all as visually prominent as the sulfate detected in Quartier (Figs. 4).

The closely associated olivine and carbonate detections in Garde and Dourbes suggest that the olivine cumulate Séítah unit was exposed to at least one aqueous alteration event, during which partial carbonation of olivine took place (Figs. 2 and 3). In particular, detail maps of Dourbes reveal a euhedral olivine crystal with no directly associated carbonate sitting less than one millimeter away from a subhedral olivine grain with adjacent carbonate grains (Fig. 2C). Sulfate deposits in both Dourbes and Quartier are rimmed by carbonate that is both spectrally and morphologically similar to the carbonate associated with olivine in Dourbes and Garde (Figs. 2, 3, 4). This suggests that all of the carbonates in Séítah formed via the same process, olivine carbonation, and that Séítah's sulfate was deposited later by a sulfate-rich brine, in pore space generated during olivine carbonation through cracking caused by the pressure of carbonate crystal formation (e.g., Xing et al., 2018).

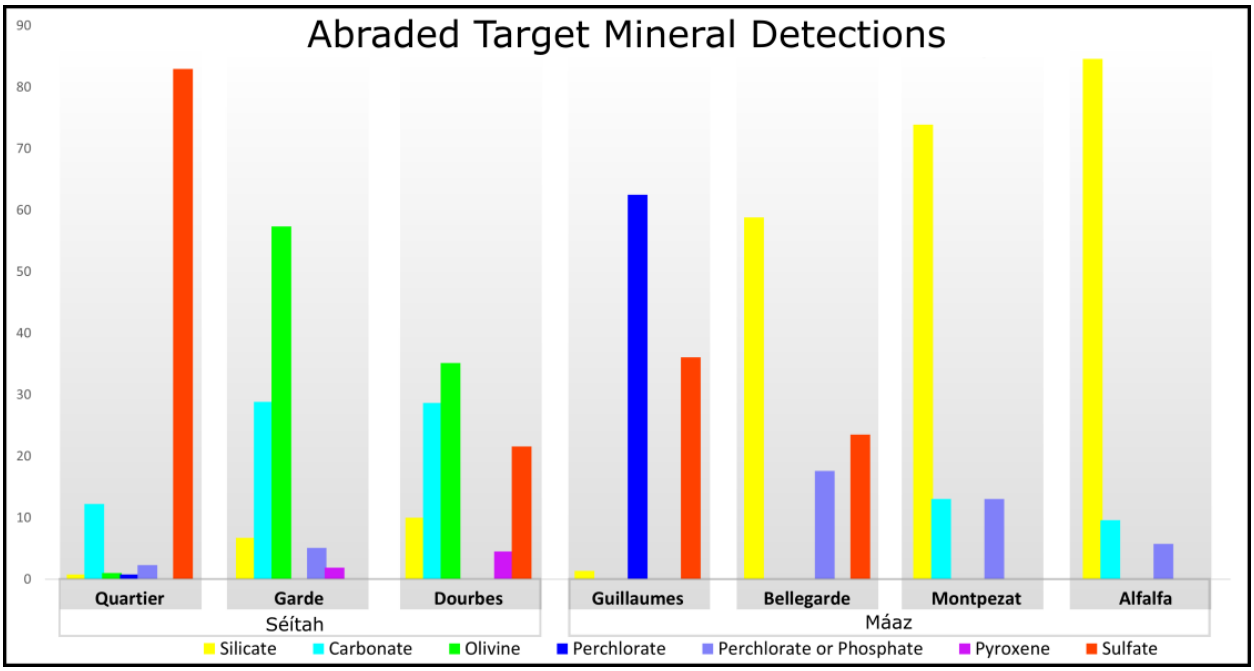

Figure 9. A) This graph presents, for each abraded target of the Crater Floor Campaign, the percent of detections of each mineral class out of the total SHERLOC mineral detections per target. Each group of bars associated with each target adds up to 100 percent. Data are presented in this way to correct for the differences in Raman signal intensities between targets discussed in section 4.1. Séítah formation targets are on the left (Quartier, Garde, and Dourbes) and Máaz targets are on the right (Guillaumes, Bellegarde, Montpezat, and Alfalfa).

Figure 9 shows that the three most common mineral detections in SHERLOC scans of Máaz targets were silicate, sodium perchlorate, and sulfate. It is important to note the widespread presence of iron oxides in Máaz (Weins et al., 2022). Iron oxides can absorb deep UV laser radiation and attenuate the spectral signatures of any underlying material (Razzell Hollis et al., 2021a; Morris et al., 2022). In all four of the Máaz targets, mineral detections are negatively correlated with the red-to-brown material on their surfaces, which appears consistent with the presence of iron oxide (Figs. 5-8). This indicates that SHERLOC's mineral detections in the Máaz formation were limited by the absorption of DUV laser radiation by iron oxide.

Farley et al. (2022) report that the totality of data collected during the Mars 2020 Crater Floor campaign indicates that the Máaz and Séítah units either originated from two different sources or represent different layers of a single differentiated magma body. The different rock-forming mineral detections of (non- olivine or pyroxene) silicate in the Máaz targets Bellegarde, Montpezat, and Alfalfa, and olivine and pyroxene detections in Séítah targets further supports Farley et al.'s interpretation (Fig. 9).. SHERLOC's microscale mapping of Máaz targets reveals that similar spectra assigned to silicate correspond to grains with very different morphologies. Silicate detections in Montpezat and Bellegarde map to sub-millimeter dark blue-gray grains; in Alfalfa, the detections correspond to mm-scale reflective white lathe-like crystals (Figs. 6-8). Although the (non- olivine or pyroxene) silicate spectra reported above were all compared to the same standard labradorite spectrum, the broad bands that led us to assign the spectra to silicate are centered at different wavenumbers: 1050 cm^{-1}, 1036 cm^{-1}, and 1053 cm^{-1} in Montpezat, Bellegarde, and Alfalfa, respectively. The variable grain morphology and Raman band placement in Máaz silicate detections suggests that they correspond to at least two different silicate mineral species, and some may actually be amorphous silica detections.

Perchlorate and sulfate detected in Guillaumes and Bellegarde scans are evidence of a third possible aqueous alteration event on the floor of Jezero Crater. While the Guillaumes and Bellegarde salt deposits are similar in morphology to the deposits in Dourbes and Quartier, they differ in mineralogy. The deposits in Dourbes and Quartier were predominantly sulfate, with only minor perchlorate contributions (see sections 3.1.1 and 3.1.3). In contrast, SHERLOC mineral detections on the white patch of minerals in Guillaumes were dominated by perchlorate that can, in some cases, be identified as sodium perchlorate, with lesser, but still significant, sulfate contributions (see section 3.2.1). SHERLOC scans of Bellegarde detected definitive sulfate

signatures alongside perchlorate or phosphate signatures and SuperCam detected a definitive sodium perchlorate signature (Meslin et al., 2022; see section 3.2.4). Taken together, these SHERLOC and PIXL detections suggest that the salts in Guillaumes and Bellegarde precipitated from a perchlorate-sulfate-bearing brine as it percolated through the Máaz formation rocks.

The mineral detections discussed above are consistent with a changing, habitable aqueous environment that was capable of supporting microbial life and preserving evidence of that life, if it existed. In low-temperature terrestrial environments, carbonation of mafic to ultramafic rocks, which SHERLOC data from Séítah formation targets indicate occurred in the Jezero Crater lake, produces hydrogen that can fuel low-density microbial communities (e.g. Fones et al., 2019; Twing et al., 2017; Woycheese et al., 2015). Terrestrial sulfate and perchlorate brines, similar to the brines that likely deposited the sulfate and perchlorate that SHERLOC detected in Jezero Crater, can host microbial life (e.g., Cesur et al., 2022: Fox-Powell & Cockell., 2018; Heinz et al., 2019, 2020). Furthermore, terrestrial sulfate minerals can trap and preserve organic molecules within their structure (eg., Aubrey et al, 2006; Kotler et al., 2008; Schopf et al., 2012; Shkolyar and Farmer, 2018), and halite- and perchlorate-rich hypersaline subsurface deposits in the Atacama Desert can preserve organic molecules for millions of years (Fernández-Remolar et al., 2013).

Conclusion

During the Mars 2020 Crater Floor Campaign, SHERLOC was the first Raman spectrometer to map mineral composition in context on the surface of another planetary body. The microscale mineral maps of abraded Séítah and Máaz targets SHERLOC produced during this campaign reveal differing igneous protoliths with aqueous alteration histories indicating that

the Jezero crater floor was once a habitable aqueous environment and highlight the importance of the proposed Mars Sample Return mission.

SHERLOC data acquired during the Crater Floor Campaign allowed us to identify evidence of olivine carbonation, a process that releases hydrogen and is therefore potentially capable of supporting microbial metabolic processes and units bearing sulfate and perchlorate salts, which are known to preserve organic molecules over long periods of time in terrestrial Mars analogue environments (Aubrey et al., 2006; Kotler et al., 2008; Fernández-Remolar et al., 2013; Schopf et al., 2012; Shkolyar and Farmer, 2018). These mineral assignments were made with high confidence, and suggest that the return of Crater Floor Campaign samples associated with Dourbes (Salette or Coulettes) and Quartier (Robine or Malay) in Séítah, where we observed evidence of both olivine carbonation and sulfate deposition, and Bellegarde (Montdenier or Montagnac) in Máaz, where we observed evidence of perchlorate and sulfate deposition, could bring preserved evidence of microbial life that may have existed in Jezero Crater.

SHERLOC scans performed on the floor of Jezero Crater also yielded data that does not allow for straightforward phase assignments, such as the apparent detections of silicate signatures that are common, but associated with differing rock textures, in the Máaz targets Montpezat, Bellegarde, and Alfalfa. Return of Crater Floor Campaign samples associated with Bellegarde (Montdenier or Montagnac) and Alfalfa (Ha'ahóni or Atsá) will allow for laboratory analyses of the sub-millimeter dark blue-gray grains in Bellegarde and large, reflective, lathe-like, white grains in Alfalfa that will provide more definitive, fine scale phase identifications that will facilitate an understanding of the discrepancies in silicate mineral detections between SHERLOC and other Perseverance instruments.

Acknowledgments

We thank the entire Perseverance rover team. The work described in this paper was partially carried out at the Jet Propulsion Laboratory, California Institute of Technology, under a contract with the National Aeronautics and Space Administration. Funding: A.C. was supported by a National Science Foundation Graduate Research Fellowship (award number 2035701). Funding for R.S.J was provided as an Advanced Curation project run by the NASA Astromaterials Acquisition and Curation Office, Johnson Space Center. ADC and AC were supported by the Mars 2020 Returned Sample Science Participating Scientist Program (NASA award number 80NSSC20K0237). EAC thanks the Canadian Space Agency (grant #EXPCOI4) and the Natural Sciences and Engineering Research Council (grant #RGPIN-2021-02995). E.L.S. was supported by a NASA Earth and Space Science Fellowship (NESSF) (grant 80NSSC18K1255) and the SHERLOC Co-I funds of B.L.E. J.R.H. was supported by a NASA Postdoctoral Program fellowship. J.R.H., A.S., L.W.B., R.B., P.G.C., M.F., F.M.M., and A.S.B. were supported by the 107415 Mars 2020 Phase-E. A.J.W. was supported by the NASA M2020 Participating Scientist Program. T.F. was supported by the Italian Space Agency (ASI) grant agreement ASI/INAF n. 2017-48-H-0. S.S. acknowledges funding from the Swedish National Space Agency (contracts 137/19 and 2021-00092). This work was supported in part by the ISFM Mission Enabling Work Package and the Johnson Space Center. Author contributions: Entire team performed data analysis and interpretation and participated in editing this manuscript. A.C. and R.S.J. contributed equally to the manuscript. Special thanks go to E.L.B. for figure making. L.W.B. and R.B. are the principal and deputy investigators of the SHERLOC instrument. Competing interests: We declare no competing interests. The data used for the study are available on NASA's Planetary Data System (Beegle et al., 2021).

Chapter V: Conclusion

Concluding Remarks

The work presented in Chapters II and III adds to a field of study that began in earnest in 1965 with the first discovery of microfossils preserved in black cherts from the 1.88 Ga Gunflint Formation (Barghoorn and Tyler, 1965). Since that discovery, paleontologists have looked to the Precambrian rock record for evidence of Earth's earliest life and the evolution of key metabolic processes that have reshaped our planet, especially the emergence of oxygenic photosynthesis (e.g., Cloud, 1968; Anbar et al., 2007; Lyons et al., 2014). More recently, the field of astrobiology has also looked to the Precambrian rock record to inform the search for life beyond Earth (e.g., Des Marais et al., 2003), as in NASA's ongoing Mars 2020 mission (see Chapter IV).

For over two decades, geochemical research has indicated that at least some marine oxygenation occurred via oxygenic photosynthesis hundreds of millions of years prior to the Great Oxygenation Event (e.g., Eigenbrode and Freeman, 2006; Anbar et al., 2007; Czaja et al., 2012; Planavsky et al., 2014; Satkoski et al., 2015; Ostrander et al., 2020; Robbins et al., 2023). Recent phylogenetic analysis indicates that O_2 utilizing enzymes may have evolved as early as 3.1 Ga, suggesting O_2 may have been circulating through the biosphere up to 800 million years before it became a stable feature of Earth's atmosphere (Jabłońska and Tawfik, 2021). The discovery of what may be the remains of Neoarchean microbial sulfur cycling community that took advantage of a microoxic environment, reported in Chapter II, further supports the claim that microorganisms evolved specialized lifestyles in response to the presence of marine O_2 well before the GOE. Furthermore, the preservation of this microbial community in early diagenetic spherulitic chert is an unusual example of microfossils preserved in a sub-wavebase depositional environment. The nucleation of spherulitic chert on organic matter in this deepwater

environment adds to our understanding of microfossil preservation on the early Earth and the potential for biosignature preservation elsewhere in the solar system.

The morphological reconstructions of Gamohaan Formation fenestrate microbialites reported in Chapter III offer another possible example of Neoarchean microorganisms responding to intermittent marine oxygenation in a sub-wavebase environment. Raman analyses of the fenestrate microbialites also raise important questions about the interpretation of Raman data collected on both Earth and Mars. Visible Raman data presented in Chapter III call the thermal history of the Gamohaan Formation, which has long been studied as a rare example of minimally altered Neoarchean rock, and/or the accuracy of Raman geothermometry performed on Archean kerogen into question. DUV Raman data presented in Chapter III suggest that caution is needed when attempting to interpretate SHERLOC data based on the results of visible Raman spectroscopy, particularly carbonate spectra, and that a more extensive library of DUV Raman mineral spectra is needed for confident SHERLOC data interpretation.

Finally, this dissertation presents the initial interpretations of DUV Raman spectra collected by the SHERLOC instrument in the first science campaign of NASA's Mars 2020 mission. This work has provided a foundation for subsequent SHERLOC data analyses in which researchers have, for example, examined associations between potential organic compounds and minerals detected in Jezero Crater (Sharma et al., 2023) and investigated the implications that hydrated sulfates on the floor of Jezero Crater have for the crater's alteration history, past habitability, and biosignature preservation potential (Siljeström et al., 2024). In addition, the spectral processing workflow my coauthors and I developed while writing this paper provided a starting point for the development of SHERLOC data treatment standards (e.g., Jakubek et al., 2023; Uckert et al., 2024; Jakubek et al., submitted). This work has also helped to inform

researchers studying Mars analog sites on Earth (e.g., Magnuson et al., 2023; Bruschini et al., 2024).

Future Directions

Following graduation, I will build on the work presented here as a postdoctoral researcher and Mars 2020 science team collaborator in Dr. Andrew Czaja's lab. The aim of my postdoctoral project is to explore cutting edge and novel analytical techniques capable of detecting collocated morphological and geochemical biosignatures and appropriate for studying the samples collected in Jezero Crater, Mars that are delivered to Earth via Mars Sample Return. This postdoctoral project is an opportunity to further study biosignature preservation and detection in the Neoarchean samples discussed above with the potential to further inform the search for evidence of Precambrian life on Earth and life elsewhere in the solar system. As a member of Dr. Czaja's lab, I will also contribute to a burgeoning project to determine why Raman geothermometry yields higher peak metamorphic temperatures than those indicated by mineral phase relations and clumped isotope geothermometry (See Chapter III).

Whether during my upcoming postdoctoral project or in a future role, I am eager to test the interpretations of Gamohaan Formation microfossils and microbialites presented in Chapters II and III. Avenues that I intend to pursue include *in situ* sulfur isotope measurements and experimental silicification of veil-forming microaerophilic sulfur oxidizing microorganisms (VFMSOM). *In situ* sulfur isotope measurements of pyrite grains preserved within the RET chert samples discussed in Chapter II could support or dispute the suggestion that the microbial mats and microfossils preserved within those samples are the remains of a sulfur-cycling microbial community that included organisms that are analogous to modern VFMSOMs. Similarly, *in situ*

sulfur isotope measurements of pyrite grains associated with specific microbialite structures in Gamohaan fenestrate microbialites could help assess whether marine oxygen concentration influenced microbialite morphology, as suggested in Chapter III. Experimental silicification of VFMSOMs could determine whether these microorganisms encourage the deposition of amorphous silica in the same way that cyanobacteria do (Moore et al., 2020; Moore et al., 2021). The results of this work would support or dispute the claim that the organic-matter-associated spherulitic chert observed in RET samples is the result of chert spherule nucleation on organic matter (See Chapter II).

References

Abbey, W. J., Bhartia, R., Beegle, L. W., DeFlores, L., Paez, V., Sijapati, K., Sijapati, S., Williford, K., Tuite, M., Hug, W., & Others. (2017). Deep UV Raman spectroscopy for planetary exploration: The search for in situ organics. *Icarus*, *290*, 201–214.

Adcock, C. T., Hausrath, E. M., Forster, P. M., Tschauner, O., & Sefein, K. J. (2014). Synthesis and characterization of the Mars-relevant phosphate minerals Fe- and Mg-whitlockite and merrillite and a possible mechanism that maintains charge balance during whitlockite to merrillite transformation. *American Mineralogist*, *99*(7), 1221–1232. https://doi.org/10.2138/am.2014.4688

Anbar, A. D., Duan, Y., Lyons, T. W., Arnold, G. L., Kendall, B., Creaser, R. A., Kaufman, A. J., Gordon, G. W., Scott, C., Garvin, J., & Buick, R. (2007). A Whiff of Oxygen Before the Great Oxidation Event? *Science*, *317*(5846), 1903–1906. https://doi.org/10.1126/science.1140325

Allwood, A. C., Walter, M. R., Kamber, B. S., Marshall, C. P., & Burch, I. W. (2006). Stromatolite reef from the Early Archaean era of Australia. *Nature*, *441*, 714–718. https://doi.org/10.1038/nature04764

Armbruster, T., & Danisi, R. M. (Eds.). (2016). *Highlights in mineralogical crystallography*. Walter de Gruyter GmbH. https://rruff.info/about/downloads/HMC1-30.pdf

Barghoorn, E. S., & Tyler, S. A. (1965). Microorganisms from the Gunflint Chert. *Science*, *147*(3658), 563–575. https://doi.org/10.1126/science.147.3658.563

Barlow, E. V., & Van Kranendonk, M. J. (2018). Snapshot of an early Paleoproterozoic ecosystem: Two diverse microfossil communities from the Turee Creek Group, Western Australia. *Geobiology*, *16*(5), 449–475. https://doi.org/10.1111/gbi.12304

Barlow, E. V., House, C. H., Liu, M.-C., Wetherington, M. T., & Van Kranendonk, M. J. (2024). Distinctive microfossil supports early Paleoproterozoic rise in complex cellular organisation. *Geobiology*, *22*(1), e12576. https://doi.org/10.1111/gbi.12576

Bartley, J. K. (1996). Actualistic Taphonomy of Cyanobacteria: Implications for the Precambrian Fossil Record. *PALAIOS*, *11*(6), 571. https://doi.org/10.2307/3515192

Bartley, J. K., Kah, L. C., Frank, T. D., & Lyons, T. W. (2015). Deep-water microbialites of the Mesoproterozoic Dismal Lakes Group: Microbial growth, lithification, and implications for coniform stromatolites. *Geobiology*, *13*(1), 15–32. https://doi.org/10.1111/gbi.12114

Beegle, L. W., Bhartia, R., Deen, Robert G., Padgett, D., Algermissen, S., Dunn, A. E., Toole, N. T., Crombie, M. K., Arena, N. W., Oij, S. L., Abarca, H. E., Slavney, S. (2021). Mars 2020 SHERLOC Bundle. NASA Planetary Data System. https://doi.org/10.17189/1522643

Bekker, A., Holland, H. D., Wang, P.-L., Rumble, D., Stein, H. J., Hannah, J. L., Coetzee, L. L., & Beukes, N. J. (2004). Dating the rise of atmospheric oxygen. *Nature*, *427*(6970), 117–120. https://doi.org/10.1038/nature02260

Bertrand-Sarfati, J., & Potin, B. (1994). Microfossiliferous cherty stromatolites in the 2000 Ma Franceville Group, Gabon. *Precambrian Research*, *65*(1–4), 341–356. https://doi.org/10.1016/0301-9268(94)90112-0

Beukes, N. J. (1980). Lithofacies and stratigraphy of the Kuruman and Griquatown iron-formations, Northern Cape Province, South Africa. *Transactions of the Geological Society of South Africa*, *83*, 69–86.

Beukes, N. J. (1987). Facies relations, depositional environments and diagenesis in a major early Proterozoic stromatolitic carbonate platform to basinal sequence, Campbellrand Subgroup, Transvaal Supergroup, Southern Africa. *Sedimentary Geology*, *54*(1–2), 1–46. https://doi.org/10.1016/0037-0738(87)90002-9

Beukes, N. J., & Gutzmer, J. (2008). Origin and Paleoenvironmental Significance of Major Iron Formations at the Archean-Paleoproterozoic Boundary. *Society of Economic Geologists Rviews*, *15*, 5–47.

Beukes, N. J., Klein, C., Kaufman, A. J., & Hayes, J. M. (1990). Carbonate petrography, kerogen distribution, and carbon and oxygen isotope variations in an early Proterozoic transition from limestone to iron-formation deposition, Transvaal Supergroup, South Africa. *Economic Geology*, *85*(4), 663–690. https://doi.org/10.2113/gsecongeo.85.4.663

Beyssac, O., Goffé, B., Chopin, C., & Rouzaud, J. N. (2002). Raman spectra of carbonaceous material in metasediments: A new geothermometer. *Journal of Metamorphic Geology*, *20*(9), 859–871. https://doi.org/10.1046/j.1525-1314.2002.00408.x

Bhartia, R., Beegle, L. W., DeFlores, L., Abbey, W., Razzell Hollis, J., Uckert, K., et al. (2021). Perseverance's Scanning Habitable Environments with Raman and Luminescence for Organics and Chemicals (SHERLOC) Investigation. *Space Science Reviews*, *217*, 58. https://doi.org/10.1007/s11214-021-00812-z

Bhartia, R., Hug, W. F. and Reid, R. D. (2012). Improved sensing using simultaneous deep UV Raman and fluorescence detection. Proc. SPIE 8358, *Chemical, Biological, Radiological, Nuclear, and Explosives (CBRNE) Sensing XIII*, 83581A https://doi.org/10.1117/12.920170

Bizic, M., Brad, T., Ionescu, D., Barbu-Tudoran, L., Zoccarato, L., Aerts, J. W., Contarini, P.-E., Gros, O., Volland, J.-M., Popa, R., Ody, J., Vellone, D., Flot, J.-F., Tighe, S., & Sarbu, S. M. (2022). Cave Thiovulum (Candidatus Thiovulum stygium) differs metabolically and genomically from marine species. The ISME Journal, 1–14. https://doi.org/10.1038/s41396-022-01350-4

Borromeo, L., Zimmermann, U., Andò, S., Coletti, G., Bersani, D., Basso, D., Gentile, P., Schulz, B., & Garzanti, E. (2017). Raman spectroscopy as a tool for magnesium estimation in Mg-calcite. *Journal of Raman Spectroscopy*, *48*(7), 983–992. https://doi.org/10.1002/jrs.5156

Brasier, M., McLoughlin, N., Green, O., & Wacey, D. (2006). A fresh look at the fossil evidence for early Archaean cellular life. *Philosophical Transactions of the Royal Society B: Biological Sciences, 361*(1470), 887–902. https://doi.org/10.1098/rstb.2006.1835

Brown, A. J., Wiens, R. C., Maurice, S., Uckert, K., Tice, M., Flannery., D., et al. (2022). A Komatitite succession as an analog for the olivine bearing rocks at Jezero (abstract). 53rd Lunar and Planetary Science Conference.

Buick, R. (1990). Microfossil Recognition in Archean Rocks: An Appraisal of Spheroids and Filaments from a 3500 M.Y. Old Chert-Barite Unit at North Pole, Western Australia. *PALAIOS, 5*(5), 441–459. https://doi.org/10.2307/3514837

Burne, R. V., & Moore, L. S. (1987). Microbialites; organosedimentary deposits of benthic microbial communities. *PALAIOS*, *2*(3), 241–254. https://doi.org/10.2307/3514674

Buzgar, N., & Apopei, A. I. (2009). The Raman study of certain carbonates. *Geologie*, *55*(2). https://doi.org/10.13140/2.1.1358.3368

Buzgar, N., Buzatu, A., & Sanislav, I. V. (2009). The Raman study of certain sulfates. *Analele Stiintifice Ale Universitatii Al. I. Cuza*, *55*, 5–23.

Carrier, B. L., Abbey, W. J., Beegle, L. W., Bhartia, R., & Liu, Y. (2019). Attenuation of Ultraviolet Radiation in Rocks and Minerals: Implications for Mars Science. *Journal of Geophysical Research: Planets*, *124*(10), 2599–2612. https://doi.org/10.1029/2018JE005758

Cesur, R. M., Ansari, I. M., Chen, F., Clark, B. C., & Schneegurt, M. A. (2022). Bacterial Growth in Brines Formed by the Deliquescence of Salts Relevant to Cold Arid Worlds. *Astrobiology*, *22*(1), 104–115. https://doi.org/10.1089/ast.2020.2336

Chopelas, A. (1991.). Single crystal Raman spectra of forsterite, fayalite, and monticellite. *American Mineralogist, 76*(7-8), 1101-1109.

Cloud, P. E., Gruner, J. W., & Hagen, H. (1965). Carbonaceous Rocks of the Soudan Iron Formation (Early Precambrian). Science, 148(3678), 1713–1716. https://doi.org/10.1126/science.148.3678.1713

Cloutis, E.A., McCormack, K.A., Bell, J.F., Hendrix, A.R., Bailey, D.T., Craig, M.A., Mertzman, S.A., Robinson, M.S., and Riner, M.A. (2008) Ultraviolet spectral reflectance properties

of common planetary minerals. Icarus 197:321–347. https://doi.org/10.1016/j.icarus.2008.04.018

Cogan, N. G., & Wolgemuth, C. W. (2005). Pattern Formation by Bacteria-Driven Flow. *Biophysical Journal*, *88*(4), 2525–2529. https://doi.org/10.1529/biophysj.104.053348

Cosmidis, J., & Templeton, A. S. (2016). Self-assembly of biomorphic carbon/sulfur microstructures in sulfidic environments. *Nature Communications, 7*(1). https://doi.org/10.1038/ncomms12812

Cosmidis, J., Nims, C. W., Diercks, D., & Templeton, A. S. (2019). Formation and stabilization of elemental sulfur through organomineralization. *Geochimica et Cosmochimica Acta*, *247*, 59–82. https://doi.org/10.1016/j.gca.2018.12.025

Currie, K. L., Knutson, J.,Temby, P. A. (1992). The Mud Tank carbonatite complex, central Australia-an example of metasomatism at mid-crustal levels. *Contributions to Mineralogy and Petrology, 109*(3).

Czaja, A. D., Beukes, N. J., & Osterhout, J. T. (2016). Sulfur-oxidizing bacteria prior to the Great Oxidation Event from the 2.52 Ga Gamohaan Formation of South Africa. *Geology*, *44*(12), 983–986. https://doi.org/10.1130/G38150.1

Czaja, A. D., Johnson, C. M., Roden, E. E., Beard, B. L., Voegelin, A. R., Nägler, T. F., Beukes, N. J., & Wille, M. (2012). Evidence for free oxygen in the Neoarchean ocean based on coupled iron–molybdenum isotope fractionation. *Geochimica et Cosmochimica Acta*, 86, 118–137. https://doi.org/10.1016/j.gca.2012.03.007

Dahl, C., & Prange, A. (2006). Bacterial Sulfur Globules: Occurrence, Structure and Metabolism. Microbiology Monograph, 1, 21–51. https://doi.org/DOI 10.1007/7171_002

De Boer, W. E., La Rivière, J. W. M., & Houwink, A. L. (1961). Observations on the morphology of *Thiovulum majus* Hinze. *Antonie van Leeuwenhoek, 27*(1), 447–456. https://doi.org/10.1007/BF02538470

Demtroder, W. (2008). *Laser Spectroscopy: Basic Principles* (4th ed., Vol. 1). Springer Berlin Heidelberg. https://doi.org/10.1007/978-3-540-73418-5

Des Marais, D. J., Allamandola, L. J., Benner, S. A., Boss, A. P., Deamer, D., Falkowski, P. G., Farmer, J. D., Hedges, S. B., Jakosky, B. M., Knoll, A. H., Liskowsky, D. R., Meadows, V. S., Meyer, M. A., Pilcher, C. B., Nealson, K. H., Spormann, A. M., Trent, J. D., Turner, W. W., Woolf, N. J., & Yorke, H. W. (2003). The NASA Astrobiology Roadmap. Astrobiology, 3(3). https://doi.org/10.1089/153110703769016299

Djokic, T., Van Kranendonk, M. J., Campbell, K. A., Walter, M. R., & Ward, C. R. (2017). Earliest signs of life on land preserved in ca. 3.5 Ga hot spring deposits. *Nature Communications*, *8*(1), 15263. https://doi.org/10.1038/ncomms15263

Dunham, J. I. (2018). *Understanding Early Diagenetic Silicification: Petrographic Fabrics within Proterozoic Microfossiliferous Chert* [Master's thesis, University of Tennessee]. https://trace.tennessee.edu/utk_gradthes/5350

Edgcomb, V. P., Bernhard, J. M., Summons, R. E., Orsi, W., Beaudoin, D., & Visscher, P. T. (2014). Active eukaryotes in microbialites from Highborne Cay, Bahamas, and Hamelin Pool (Shark Bay), Australia. *The ISME Journal*, *8*(2), 418–429. https://doi.org/10.1038/ismej.2013.130

Edgett, K. S., Yingst, R. A., Ravine, M. A., Caplinger, M. A., Maki, J. N., Ghaemi, F. T., Schaffner, J. A., Bell, J. F., Edwards, L. J., Herkenhoff, K. E., Heydari, E., Kah, L. C., Lemmon, M. T., Minitti, M. E., Olson, T. S., Parker, T. J., Rowland, S. K., Schieber, J., Sullivan, R. J., … Goetz, W. (2012). Curiosity's Mars Hand Lens Imager (MAHLI) Investigation. *Space Science Reviews*, *170*(1–4), 259–317. https://doi.org/10.1007/s11214-012-9910-4

Eigenbrode, J. L., & Freeman, K. H. (2006). Late Archean rise of aerobic microbial ecosystems. *Proceedings of the National Academy of Sciences, 103*(43), 15759–15764. https://doi.org/10.1073/pnas.0607540103

Eickmann, B., Hofmann, A., Wille, M., Bui, T. H., Wing, B. A., & Schoenberg, R. (2018). Isotopic evidence for oxygenated Mesoarchaean shallow oceans. *Nature Geoscience*, *11*(2), 133–138. https://doi.org/10.1038/s41561-017-0036-x

Engel, A. S., Porter, M. L., Kinkle, B. K., & Kane, T. C. (2001). Ecological Assessment and Geological Signi cance of Microbial Communities from Cesspool Cave, Virginia. *Geomicrobiology Journal*, *18*, 259–274.

Eroglu, S., van Zuilen, M. A., Taubald, H., Drost, K., Wille, M., Swanner, E. D., Beukes, N. J., & Schoenberg, R. (2017). Depth-dependent δ13C trends in platform and slope settings of the Campbellrand-Malmani carbonate platform and possible implications for Early Earth oxygenation. *Precambrian Research*, *302*, 122–139. https://doi.org/10.1016/j.precamres.2017.09.018

Eshelman, E., Daly, M.G., Slater, G., Dietrich, P. and Gravel, J.F. (2014). An ultraviolet Raman wavelength for the in-situ analysis of organic compounds relevant to astrobiology. *Planetary and Space Science*, *93*, 65-70.

Farley, K. A., Williford, K. H., Stack, K. M., Bhartia, R., Chen, A., de la Torre, M., Hand, K., Goreva, Y., Herd, C. D. K., Hueso, R., Liu, Y., Maki, J. N., Martinez, G., Moeller, R. C., Nelessen, A., Newman, C. E., Nunes, D., Ponce, A., Spanovich, N., … Wiens, R. C. (2020). Mars 2020 Mission Overview. *Space Science Reviews*, *216*(8), 142. https://doi.org/10.1007/s11214-020-00762-y

Farley, K. A., Stack, K., M., Horgan, B. H. N., Tarnas, J., Sun, V. Z., Shuster, D. L., et al. (2022). Aqueously altered igneous rocks on the floor of Jezero crater, Mars. *Science,* https://doi.org/10.1126/science.abo2196

Farquhar, J. (2000). Atmospheric Influence of Earth's Earliest Sulfur Cycle. Science, 289(5480), 756–758. https://doi.org/10.1126/science.289.5480.756

Farquhar, J., & Wing, B. A. (2003). Multiple sulfur isotopes and the evolution of the atmosphere. *Earth and Planetary Science Letters, 213*(1–2), 1–13. https://doi.org/10.1016/S0012-821X(03)00296-6

Fenchel, T. (1994). Motility and chemosensory behaviour of the sulphur bacterium Thiovulum majus. *Microbiology*, *140*(11), 3109–3116. https://doi.org/10.1099/13500872-140-11-3109

Fenchel, T., & Thar, R. (2004). "Candidatus Ovobacter propellens": A large conspicuous prokaryote with an unusual motility behaviour. FEMS Microbiology Ecology, 48(2), 231–238. https://doi.org/10.1016/j.femsec.2004.01.013

Fernández-Remolar, D. C., Chong-Díaz, G., Ruíz-Bermejo, M., Harir, M., Schmitt-Kopplin, P., Tziotis, D., Gómez-Ortíz, D., García-Villadangos, M., Martín-Redondo, M. P., Gómez, F., Rodríguez-Manfredi, J. A., Moreno-Paz, M., De Diego-Castilla, G., Echeverría, A., Urtuvia, V. N., Blanco, Y., Rivas, L., Izawa, M. R. M., Banerjee, N. R., … Parro, V. (2013). Molecular preservation in halite- and perchlorate-rich hypersaline subsurface deposits in the Salar Grande basin (Atacama Desert, Chile): Implications for the search for molecular biomarkers on Mars. *Journal of Geophysical Research: Biogeosciences*, *118*(2), 922–939. https://doi.org/10.1002/jgrg.20059

Fischer, W. W., & Knoll, A. H. (2009). An iron shuttle for deepwater silica in Late Archean and early Paleoproterozoic iron formation. *Geological Society of America Bulletin*. https://doi.org/10.1130/B26328.1

Fones, E. M., Colman, D. R., Kraus, E. A., Nothaft, D. B., Poudel, S., Rempfert, K. R., Spear, J. R., Templeton, A. S., & Boyd, E. S. (2019). Physiological adaptations to serpentinization in the Samail Ophiolite, Oman. *The ISME Journal*, *13*(7), 1750–1762. https://doi.org/10.1038/s41396-019-0391-2

Fox-Powell, M. G., & Cockell, C. S. (2018). Building a Geochemical View of Microbial Salt Tolerance: Halophilic Adaptation of Marinococcus in a Natural Magnesium Sulfate Brine. *Frontiers in Microbiology*, *9*, 739. https://doi.org/10.3389/fmicb.2018.00739

Fu, X., Wang, A., & Krawczynski, M. J. (2017). Characterizing amorphous silicates in extraterrestrial materials: Polymerization effects on Raman and mid-IR spectral features of alkali and alkali earth silicate glasses: Characterizing amorphous silicates in

extraterrestrial materials. Journal of Geophysical Research: Planets, 122(5), 839–855. https://doi.org/10.1002/2016JE005241

Garcia-Ruiz, J. M. (2003). Self-Assembled Silica-Carbonate Structures and Detection of Ancient Microfossils. Science, 302(5648), 1194–1197. https://doi.org/10.1126/science.1090163

Garczynski, B. J., Bell, J. F., Horgan, B. H. N., Johnson, J. R., Rice M. S., Vaughan, J. I., et al. (2022). Perseverance and the purple coating: A MASTCAM-Z multispectral story (abstract). 53rd Lunar and Planetary Science Conference.

Grey, K., & Awramik, S. (2020). *Handbook for the study and description of microbialites*. Geological Survey of Western Australia.

Grey, K., & Sugitani, K. (2009). Palynology of Archean microfossils (c. 3.0Ga) from the Mount Grant area, Pilbara Craton, Western Australia: Further evidence of biogenicity. *Precambrian Research*, *173*(1–4), 60–69. https://doi.org/10.1016/j.precamres.2009.02.003

Gros, O. (2017). First description of a new uncultured epsilon sulfur bacterium colonizing marine mangrove sediment in the Caribbean: Thiovulum sp. strain karukerense. *FEMS Microbiology Letters*, *364*(18). https://doi.org/10.1093/femsle/fnx172

Gunasekaran, S., Anbalagan, G., & Pandi, S. (2006). Raman and infrared spectra of carbonates of calcite structure. *Journal of Raman Spectroscopy*, *37*(9), 892–899. https://doi.org/10.1002/jrs.1518

Guo, Q., Strauss, H., Kaufman, A. J., Schröder, S., Gutzmer, J., Wing, B., Baker, M. A., Bekker, A., Jin, Q., Kim, S.-T., & Farquhar, J. (2009). Reconstructing Earth's surface oxidation

across the Archean-Proterozoic transition. *Geology, 37*(5), 399–402. https://doi.org/10.1130/G25423A.1

Hattori, I., Umeda, M., Nakagawa, T., & Yamamoto, H. (1996). From chalcedonic chert to quartz chert: Diagenesis of chert hosted in a Miocene volcanic-sedimentary succession, central Japan. *Journal of Sedimentary Research*, *66*(1), 163–174.

Heinz, J., Krahn, T., & Schulze-Makuch, D. (2020). A New Record for Microbial Perchlorate Tolerance: Fungal Growth in NaClO4 Brines and its Implications for Putative Life on Mars. *Life*, *10*(5), 53. https://doi.org/10.3390/life10050053

Heinz, J., Waajen, A. C., Airo, A., Alibrandi, A., Schirmack, J., & Schulze-Makuch, D. (2019). Bacterial Growth in Chloride and Perchlorate Brines: Halotolerances and Salt Stress Responses of *Planococcus halocryophilus*. *Astrobiology*, *19*(11), 1377–1387. https://doi.org/10.1089/ast.2019.2069

Henry, D. G., Jarvis, I., Gillmore, G., & Stephenson, M. (2019). Raman spectroscopy as a tool to determine the thermal maturity of organic matter: Application to sedimentary, metamorphic and structural geology. *Earth-Science Reviews*, *198*, 102936. https://doi.org/10.1016/j.earscirev.2019.102936

Hickman-Lewis, K., Westall, F., & Cavalazzi, B. (2020). Diverse communities of Bacteria and Archaea flourished in Palaeoarchaean (3.5–3.3 Ga) microbial mats. *Palaeontology*, *63*(6), 1007–1033. https://doi.org/10.1111/pala.12504

Hofmann, H. J., & Jackson, G. D. (1969). Precambrian (Aphebian) microfossils from Belcher Islands, Hudson Bay. *Canadian Journal of Earth Sciences*, *6*(5), 1137–1144. https://doi.org/10.1139/e69-115

Homann, M. (2019). Earliest life on Earth: Evidence from the Barberton Greenstone Belt, South Africa. *Earth-Science Reviews*, *196*, 102888. https://doi.org/10.1016/j.earscirev.2019.102888

Horgan B. H. N., Rice, M. S., Garczynski, B. J., Johnson J. R., Stack, K. M., Vaughan, J. I., et al. (2022). Mineralogy, morphology, and geochronological significance of the Máaz formation and the Jezero Crater Floor (abstract). 53rd Lunar and Planetary Science Conference.

Huang, E., Chen, C. H., Huang, T., Lin, E. H., Xu, J. (2000). Raman spectroscopic characteristics of Mg-Fe-Ca pyroxenes. *American Mineralogist, 85*, 3-4.

Hurowitz, J. A., Tice, M. M., Allwood, A. C., Cable, M. L., Bosak, T., Broz, A., Caravaca, G., Clark, B. C., Dehouck, E., Fairén, A. G., Gomez, F., Grotzinger, J., Gupta, S., Johnson, J. R., Kah, L. C., Kalucha, H., Labrie, J., Li, A. Y., Mandon, L., … Yanchilina, A. (2023). *THE PETROGENETIC HISTORY OF THE JEZERO CRATER DELTA FRONT FROM MICROSCALE OBSERVATIONS BY THE MARS 2020 PIXL INSTRUMENT*. Luna are Planetary Science Conference, 2023, The Woodlands, Texas, United States.

Ishibashi, H., Arakawa, M., Ohi, S., Yamamoto, J., Miyake, A., Kagi, H. (2008). Relationship between Raman spectral pattern and crystallographic orientation of a rock-forming mineral: a case study of Fo_{89} Fa_{11} olivine. *Journal of Raman spectroscopy, 39*(11).

Jabłońska, J., & Tawfik, D. S. (2021). The evolution of oxygen-utilizing enzymes suggests early biosphere oxygenation. *Nature Ecology & Evolution, 5*(4), 442–448. https://doi.org/10.1038/s41559-020-01386-9

Jørgensen, B. B., & Revsbech, N. P. (1983). Colorless Sulfur Bacteria, *Beggiatoa* spp. And *Thiovulum* spp., in O 2 and H 2 S Microgradients. *Applied and Environmental Microbiology*, *45*(4), 1261–1270. https://doi.org/10.1128/aem.45.4.1261-1270.1983

Jørgensen, B. B., Findlay, A. J., & Pellerin, A. (2019). The Biogeochemical Sulfur Cycle of Marine Sediments. *Frontiers in Microbiology*, *10*, 849. https://doi.org/10.3389/fmicb.2019.00849

Kaufman, A. J., Johnston, D. T., Farquhar, J., Masterson, A. L., Lyons, T. W., Bates, S., Anbar, A. D., Arnold, G. L., Garvin, J., & Buick, R. (2007). Late Archean Biospheric Oxygenation and Atmospheric Evolution. *Science, 317*(5846), 1900–1903. https://doi.org/10.1126/science.1138700

Kamber, B. S., & Whitehouse, M. J. (2007). Micro-scale sulphur isotope evidence for sulphur cycling in the late Archean shallow ocean. *Geobiology*, *0*(0), 061221060249002-??? https://doi.org/10.1111/j.1472-4669.2006.00091.x

Kendall, B., Reinhard, C. T., Lyons, T. W., Kaufman, A. J., Poulton, S. W., & Anbar, A. D. (2010). Pervasive oxygenation along late Archaean ocean margins. *Nature Geoscience*, *3*(9), 647–652. https://doi.org/10.1038/ngeo942

Klein, C., Beukes, N. J., & Schopf, J. W. (1987). Filamentous microfossils in the early proterozoic transvaal supergroup: Their morphology, significance, and paleoenvironmental setting. *Precambrian Research*, *36*(1), 81–94. https://doi.org/10.1016/0301-9268(87)90018-0

Klein, C., & Beukes, N. J. (1989). Geochemistry and sedimentology of a facies transition from limestone to iron-formation deposition in the early Proterozoic Transvaal Supergroup,

South Africa. *Economic Geology*, *84*(7), 1733–1774. https://doi.org/10.2113/gsecongeo.84.7.1733

Knoll, A. H., & Barghoorn, E. S. (1974). Ambient Pyrite in Precambrian Chert: New Evidence and a Theory. Proceedings of the National Academy of Sciences, 71(6), 2329–2331. https://doi.org/10.1073/pnas.71.6.2329

Knoll, A. H., & Barghoorn, E. S. (1976). A Gunflint-type microbiota from the Duck Creek dolomite, Western Australia. *Origins of Life*, *7*(4), 417–423. https://doi.org/10.1007/BF00927937

Knoll, A. H., Barghoorn, E. S., & Awramik, S. M. (1978). New Microorganisms from the Aphebian Gunflint Iron Formation, Ontario. *Journal of Paleontology*, *52*(5), 976–992.

Knoll, A. H., Worndle, S., & Kah, L. C. (2013). Covariance of microfossil assemblages and microbialite textures across an upper Mesoproterozoic carbonate platform. *PALAIOS*, *28*(7), 453–470. https://doi.org/10.2110/palo.2013.p13-005r

Kouketsu, Y., Mizukami, T., Mori, H., Endo, S., Aoya, M., Hara, H., Nakamura, D., & Wallis, S. (2014). A new approach to develop the Raman carbonaceous material geothermometer for low-grade metamorphism using peak width: Raman CM geothermometer using FWHM. *Island Arc*, *23*(1), 33–50. https://doi.org/10.1111/iar.12057

Krekeler, D., Sigalevich, P., Teske, A., Cypionka, H., & Cohen, Y. (1997). A sulfate-reducing bacterium from the oxic layer of a microbial mat from Solar Lake (Sinai), *Desulfovibrio oxyclinae* sp. Nov. *Archives of Microbiology*, *167*(6), 369–375. https://doi.org/10.1007/s002030050457

Krekeler, D., Teske, A., & Cypionka, H. (1998). Strategies of sulfate-reducing bacteria to escape oxygen stress in a cyanobacterial mat. *FEMS Microbiology Ecology*.

Kuebler, K. E., Jolliff, B. L., Wang, A., & Haskin, L. A. (2006). Extracting olivine (Fo–Fa) compositions from Raman spectral peak positions. *Geochimica et Cosmochimica Acta*, *70*(24), 6201–6222. https://doi.org/10.1016/j.gca.2006.07.035

La Rivière, J. W. M., & Schmidt, K. (2006). Morphologically Conspicuous Sulfur-Oxidizing Eubacteria. In M. Dworkin, S. Falkow, E. Rosenberg, K.-H. Schleifer, & E. Stackebrandt (Eds.), *The Prokaryotes* (pp. 941–954). Springer New York. https://doi.org/10.1007/0-387-30747-8_40

Lalonde, S. V., & Konhauser, K. O. (2015). Benthic perspective on Earth's oldest evidence for oxygenic photosynthesis. *Proceedings of the National Academy of Sciences*, *112*(4), 995–1000. https://doi.org/10.1073/pnas.1415718112

Lanier, W. P. (1986). Approximate Growth Rates of Early Proterozoic Microstromatolites as Deduced by Biomass Productivity. *PALAIOS*, *1*(6), 525. https://doi.org/10.2307/3514705

Lantink, M. L., Davies, J. H. F. L., Mason, P. R. D., Schaltegger, U., & Hilgen, F. J. (2019). Climate control on banded iron formations linked to orbital eccentricity. *Nature Geoscience*, *12*(5), 369–374. https://doi.org/10.1038/s41561-019-0332-8

Lenz, D. D., & Ayres, T. R. (1992). Errors Associated with Fitting Gaussian Profiles to Noisy Emission-Line Spectra. *Publications of the Astronomical Society of the Pacific*, *104*(681), 1104–1106.

Lepot, K. (2020). Signatures of early microbial life from the Archean (4 to 2.5 Ga) eon. *Earth-Science Reviews*, 209, 103296. https://doi.org/10.1016/j.earscirev.2020.103296

Levitt, N. P., Johnson, C. M., Eiler, J. M., Satkoski, A. M., & Beard, B. L. (2015). *Burial History of the Neoarchean Campbellrand-Malmani Carbonate Platform*: 5th International Clumped Isotope Workshop Applications of Clumped Isotope Measurements, University of South Florida, St. Petersburg, Florida.

Lieftink, D. J., Nijland, T. G., Maijer, C. (1994). The behavior of rare-earth elements in high-temperature Cl-bearing aqueous fluids; results from the Odegardens Verk natural laboratory. *The Canadian Mineralogist, 32*(1).

Litasov, K. D., & Podgornykh, N. M. (2017). Raman spectroscopy of various phosphate minerals and occurrence of tuite in the Elga IIE iron meteorite. *Journal of Raman Spectroscopy, 48*(11).

Liu, Y., Tice, M. M., Schmidt, M. E., Treiman, A. H., Kizovski, T. V., Hurowitz, J. A., et al. (2022). An olivine cumulate outcrop on the floor of Jezero crater, Mars. *Science,* https://doi.org/10.1126/science.abo2756

Lowe, D. G. (2004). Distinctive Image Features from Scale-Invariant Keypoints. *International Journal of Computer Vision*, *60*(2), 91–110. https://doi.org/10.1023/B:VISI.0000029664.99615.94

Luo, G., Ono, S., Beukes, N. J., Wang, D. T., Xie, S., & Summons, R. E. (2016). Rapid oxygenation of Earth's atmosphere 2.33 billion years ago. Science *Advances, 2*(5), e1600134. https://doi.org/10.1126/sciadv.1600134

Lyons, T. W., Reinhard, C. T., & Planavsky, N. J. (2014). The rise of oxygen in Earth's early ocean and atmosphere. *Nature*, *506*(7488), 307–315. https://doi.org/10.1038/nature13068

Machel, H. G. (2004). Concepts and models of dolomitization: A critical reappraisal. In C. J. R. Braithwaite, G. Rizzi, & G. Darke (Eds.), The Geometry and Petrogenesis of Dolomite Hydrocarbon Reservoirs (pp. 7–63). The Geological Society of London. https://doi.org/10.1144/GSL.SP.2004.235.01.02

Manning-Berg, A., Selly, T., & Bartley, J. K. (2021). Actualistic approaches to interpreting the role of biological decomposition in microbial preservation. *Geobiology*, gbi.12475. https://doi.org/10.1111/gbi.12475

Marshall, I. P. G., Blainey, P. C., Spormann, A. M., & Quake, S. R. (2012). A Single-Cell Genome for Thiovulum sp. *Applied and Environmental Microbiology*, *78*(24), 8555–8563. https://doi.org/10.1128/AEM.02314-12

Mason, H. E., McCubbin, F. M., Smirnov, A., and Phillips, B. L. (2009). Solid-state NMR and IR spectroscopic investigation of the role of structural water and F in carbonate-rich fluorapatite. *American Mineralogist, 94*(4).

McCubbin, F. M., Hauri, E. H., Elardo, S. M., Vander Kaaden, K. E., Wang, J., Shearer Jr, C. K. (2012), Hydrous melting of the Martian mantle produced both depleted and enriched shergottites. *Geology, 40*(8).

McCubbin, F. M., Phillips, B. L., Adcock, C. T., Tait, K. T., Steele, A., Vaughn, J. S., Fries, M.D., Atudorei, V., Vander Kaaden, K. E., and Hausrath, E. M. (2018). Discreditation of bobdownsite and the establishment of criteria for the identification of minerals with

essential monofluorophosphate (PO_3F^{2-}). *American Mineralogist: Journal of Earth and Planetary Materials, 103*(8).

Mcloughlin, N., Staudigel, H., Furnes, H., Eickmann, B., & Ivarsson, M. (2010). Mechanisms of microtunneling in rock substrates: Distinguishing endolithic biosignatures from abiotic microtunnels: Mechanisms of microtunneling in rock substrates. *Geobiology*, *8*(4), 245–255. https://doi.org/10.1111/j.1472-4669.2010.00243.x

McLoughlin, N., Li, M., Wacey, D., Martin, L. A. J., Shen, Y., & Beukes, N. J. (2023). Microbial sulphur-cycling and atmospheric signatures in the 2.52 Ga Gamohaan Formation, South Africa | Elsevier Enhanced Reader. *Earth and Planetary Science Letters*, *602*. https://doi.org/10.1016/j.epsl.2022.117941

McMahon, S. (2019). Earth's earliest and deepest purported fossils may be iron-mineralized chemical gardens. Proceedings of the Royal Society B: Biological Sciences, 286(1916), 20192410. https://doi.org/10.1098/rspb.2019.2410

McNaught, A. D., Wilkinson, A. (1997). Compendium of chemical terminology. Blackwell Science.

Meadows, V., Graham, H., Abrahamsson, V., Adam, Z., Amador-French, E., Arney, G., Barge, L., Barlow, E., Berea, A., Bose, M., Bower, D., Chan, M., Cleaves, J., Corpolongo, A., Currie, M., Domagal-Goldman, S., Dong, C., Eigenbrode, J., Enright, A., … Young, L. (2022). Community Report from the Biosignatures Standards of Evidence Workshop (arXiv:2210.14293). arXiv. https://doi.org/10.48550/arXiv.2210.14293

Meslin, P.-Y., Forni, O., Beck, P., Cousin, A., Beyssac, O., Lopez-Reyes, G., et al.. (2022). Evidence for perchlorate and sulfate salts in Jezero Crater, Mars, from SuperCam observations (abstract). 53rd Lunar and Planetary Science Conference.

Miyano, T., & Beukes, N. J. (1984). Phase relations of stilpnomelane, ferri-annite, and riebeckite in very low-grade metamorphosed iron-formations. *South African Journal of Geology*, *87*(2), 111-124.

Moeller, R. C., Jandura, L., Rosette, K., Robinson, M., Samuels, J., Silverman, M., et al. (2021). The Sampling and Caching Subsystem (SCS) for the Scientific Exploration of Jezero Crater by the Mars 2020 Perseverance Rover. *Space Science Reviews*, *217*(1), 5. https://doi.org/10.1007/s11214-020-00783-7

Montagnac, G., Hao, J., Pedreira-Segade, U., & Daniel, I. (2021). Detection of nucleotides adsorbed onto clay by UV resonant Raman spectroscopy: A step towards the search for biosignatures on Mars. *Applied Clay Science*, *200*, 105824. https://doi.org/10.1016/j.clay.2020.105824

Moore, K. R., Pajusalu, M., Gong, J., Sojo, V., Matreux, T., Braun, D., & Bosak, T. (2020). Biologically mediated silicification of marine cyanobacteria and implications for the Proterozoic fossil record. *Geology*, *48*(9), 862–866. https://doi.org/10.1130/G47394.1

Moore, K. R., Gong, J., Pajusalu, M., Skoog, E. J., Xu, M., Feliz Soto, T., Sojo, V., Matreux, T., Baldes, M. J., Braun, D., Williford, K., & Bosak, T. (2021). A new model for silicification of cyanobacteria in Proterozoic tidal flats. *Geobiology*, *19*(5), 438–449. https://doi.org/10.1111/gbi.12447

Moore, K. R., Daye, M., Gong, J., Williford, K., Konhauser, K., & Bosak, T. (2023). A review of microbial-environmental interactions recorded in Proterozoic carbonate-hosted chert. *Geobiology*, *21*(1), 3–27. https://doi.org/10.1111/gbi.12527

Morris, R. V., Haney, N. C., Jakubek, R. S., Fries, M. D., Clark, J. V., Lee, L., and Mertzman, S. A. (2022). Relative detectability of iron-bearing phases for the Mars 2020 SHERLOC deep UV Raman instrument: 1. Focusing on carbonates (abstract). 53rd Lunar and Planetary Science Conference.

Morrison, P. R., & Mojzsis, S. J. (2021). Tracing the Early Emergence of Microbial Sulfur Metabolisms. *Geomicrobiology Journal*, *38*(1), 66–86. https://doi.org/10.1080/01490451.2020.1812773

Moyer, C. L., Dobbs, F. C., & Karl, D. M. (1995). Phylogenetic diversity of the bacterial community from a microbial mat at an active, hydrothermal vent system, Loihi Seamount, Hawaii. *Applied and Environmental Microbiology*, *61*(4), 1555–1562. https://doi.org/10.1128/aem.61.4.1555-1562.1995

Muyzer, G., Yildirim, E., Van Dongen, U., Kühl, M., & Thar, R. (2005). Identification of " Candidatus Thioturbo danicus," a Microaerophilic Bacterium That Builds Conspicuous Veils on Sulfidic Sediments. Applied and Environmental Microbiology, 71(12), 8929–8933. https://doi.org/10.1128/AEM.71.12.8929-8933.2005

NASEM (National Academies of Sciences, Engineering, and Medicine). 2018. *An Astrobiology Science Strategy for the Search for Life in the Universe*. The National Academies Press, Washington, D.C. https://doi.org/10.17226/25252.

Neveu, M., Quinn, R., Barge, L. M., Craft, K. L., German, C. R., Getty, S., Glein, C., Parra, M., Burton, A. S., Cary, F., Corpolongo, A., Fifer, L., Gangidine, A., Gentry, D., Georgiou, C. D., Haddadin, Z., Herbold, C., Inaba, A., Jordan, S. F., … Yang, Z. (2024). Future of the Search for Life: Workshop Report. Astrobiology, 24(1), 114–129. https://doi.org/10.1089/ast.2022.0158

Nims, C., Lafond, J., Alleon, J., Templeton, A. S., & Cosmidis, J. (2021). Organic biomorphs may be better preserved than microorganisms in early Earth sediments. Geology. https://doi.org/10.1130/G48152.1

Noffke, N., Christian, D., Wacey, D., & Hazen, R. M. (2013). Microbially Induced Sedimentary Structures Recording an Ancient Ecosystem in the *ca.* 3.48 Billion-Year-Old Dresser Formation, Pilbara, Western Australia. *Astrobiology*, *13*(12), 1103–1124. https://doi.org/10.1089/ast.2013.1030

Núñez, J. I., Johnson J. R., Horgan B. H. N., Rice M. S., Vaughan A., Tate, C., et al. (2022).Stratigraphy and mineralogy of the deposits within Séítah region on the floor of Jezero Crater, Mars as seen with Mastcam-Z (abstract). 53rd Lunar and Planetary Science Conference.

O'shea, D. C., Bartlett, M. L., Young, R. A. (1974). Compositional analysis of apatites with laser-Raman spectroscopy: (OH, F, Cl) apatites. *Archives of Oral Biology, 19*(11).

Olson, S. L., Kump, L. R., & Kasting, J. F. (2013). Quantifying the areal extent and dissolved oxygen concentrations of Archean oxygen oases. *Chemical Geology, 362*, 35–43. https://doi.org/10.1016/j.chemgeo.2013.08.012

Ono, S., Eigenbrode, J. L., Pavlov, A. A., Kharecha, P., Rumble, D., Kasting, J. F., & Freeman, K. H. (2003). New insights into Archean sulfur cycle from mass-independent sulfur isotope records from the Hamersley Basin, Australia. Earth and Planetary Science Letters, 213(1–2), 15–30. https://doi.org/10.1016/S0012-821X(03)00295-4

Ono, S., Beukes, N. J., & Rumble, D. (2009). Origin of two distinct multiple-sulfur isotope compositions of pyrite in the 2.5Ga Klein Naute Formation, Griqualand West Basin, South Africa. *Precambrian Research, 169*(1–4), 48–57. https://doi.org/10.1016/j.precamres.2008.10.012

Ostrander, C. M., Kendall, B., Olson, S. L., Lyons, T. W., Gordon, G. W., Romaniello, S. J., Zheng, W., Reinhard, C. T., Roy, M., & Anbar, A. D. (2020). An expanded shale δ98Mo record permits recurrent shallow marine oxygenation during the Neoarchean. *Chemical Geology, 532*, 119391. https://doi.org/10.1016/j.chemgeo.2019.119391

Ostrander, C. M., Nielsen, S. G., Owens, J. D., Kendall, B., Gordon, G. W., Romaniello, S. J., & Anbar, A. D. (2019). Fully oxygenated water columns over continental shelves before the Great Oxidation Event. *Nature Geoscience, 12*(3), 186–191. https://doi.org/10.1038/s41561-019-0309-7

Pavlov, A. A., & Kasting, J. F. (2002). Mass-Independent Fractionation of Sulfur Isotopes in Archean Sediments: Strong Evidence for an Anoxic Archean Atmosphere. *Astrobiology, 2*(1), 27–41. https://doi.org/10.1089/153110702753621321

Planavsky, N. J., Asael, D., Hofmann, A., Reinhard, C. T., Lalonde, S. V., Knudsen, A., Wang, X., Ossa Ossa, F., Pecoits, E., Smith, A. J. B., Beukes, N. J., Bekker, A., Johnson, T. M., Konhauser, K. O., Lyons, T. W., & Rouxel, O. J. (2014). Evidence for oxygenic

photosynthesis half a billion years before the Great Oxidation Event. Nature Geoscience, 7(4), 283–286. https://doi.org/10.1038/ngeo2122

Rasmussen, B., & Muhling, J. R. (2019). Organic-rich microfossils produced by oil infiltration of hollow silicified bacteria: Evidence from the ca. 340 Ma Red Dog Zn-Pb deposit, Alaska. *Geology*, *47*(12), 1107–1111. https://doi.org/10.1130/G46346.1

Razzell Hollis, J., Abbey, W., Beegle, L. W., Bhartia, R., Ehlmann, B. L., Miura, J., Monacelli, B., Moore, K., Nordman, A., Scheller, E., Uckert, K., & Wu, Y.-H. (2021a). A deep-ultraviolet Raman and Fluorescence spectral library of 62 minerals for the SHERLOC instrument onboard Mars 2020. Planetary and Space Science, 209, 105356. https://doi.org/10.1016/j.pss.2021.105356

Razzell Hollis, J., Ireland, S., Abbey, W., Bhartia, R., & Beegle, L. W. (2021b). Deep-ultraviolet Raman spectra of Mars-relevant evaporite minerals under 248.6 nm excitation. *Icarus,* 357, 114067. https://doi.org/10.1016/j.icarus.2020.114067

Razzell Hollis, J., Moore., K. R., Sharma, S., Beegle, L., Grotzinger, J. P., Allwood, A., et al., (2022). The power of paired proximity science observations: Co-located data from SHERLOC and PIXL on Mars. *Icarus., 387*(15). https://doi.org/10.1016/j.icarus.2022.115179

Rivera, M. J., & Sumner, D. Y. (2014). Unraveling the three-dimensional morphology of Archean microbialites. *Journal of Paleontology*, *88*(4), 719–726. https://doi.org/10.1666/13-084

Sage, D., Donati, L., Soulez, F., Fortun, D., Schmit, G., Seitz, A., Guiet, R., Vonesch, C., & Unser, M. (2017). DeconvolutionLab2: An open-source software for deconvolution microscopy. *Methods*, *115*, 28–41. https://doi.org/10.1016/j.ymeth.2016.12.015

Scheller, E.L., Razzell Hollis, J., Cardarelli, E. L., Steele, A., Beegle, L. W., Bhartia, R., et al. 2022). Aqueous alteration processes and implications for organic geochemistry in Jezero crater, Mars. *Science, 378*(6624). *https://doi.org/10.1126/science.abo5204*

Schindelin, J., Arganda-Carreras, I., Frise, E., Kaynig, V., Longair, M., Pietzsch, T., Preibisch, S., Rueden, C., Saalfeld, S., Schmid, B., Tinevez, J.-Y., White, D. J., Hartenstein, V., Eliceiri, K., Tomancak, P., & Cardona, A. (2012). Fiji: An open-source platform for biological-image analysis. *Nature Methods*, *9*(7), 676–682. https://doi.org/10.1038/nmeth.2019

Schito, A., Muirhead, D. K., & Parnell, J. (2023). Towards a kerogen-to-graphite kinetic model by means of Raman spectroscopy. *Earth-Science Reviews*, *237*, 104292. https://doi.org/10.1016/j.earscirev.2022.104292

Schopf, J. W., Kudryavtsev, A. B., Agresti, D. G., Czaja, A. D., & Wdowiak, T. J. (2005). Raman Imagery: A New Approach to Assess the Geochemical Maturity and Biogenicity of Permineralized Precambrian Fossils. *Astrobiology*, *5*(3), 333–371. https://doi.org/10.1089/ast.2005.5.333

Schopf, J. W., Kudryavtsev, A. B., Czaja, A. D., & Tripathi, A. B. (2006). Evidence of Archean life: Stromatolites and microfossils. *Precambrian Research, 158*(3–4), 141–155. https://doi.org/10.1016/j.precamres.2007.04.009

Schopf, J. W., Farmer, J. D., Foster, I. S., Kudryavtsev, A. B., Gallardo, V. A., & Espinoza, C. (2012). Gypsum-Permineralized Microfossils and Their Relevance to the Search for Life on Mars. *Astrobiology*, *12*(7), 619–633. https://doi.org/10.1089/ast.2012.0827

Schopf, J. W., Kudryavtsev, A. B., Walter, M. R., Van Kranendonk, M. J., Williford, K. H., Kozdon, R., Valley, J. W., Gallardo, V. A., Espinoza, C., & Flannery, D. T. (2015). Sulfur-

cycling fossil bacteria from the 1.8-Ga Duck Creek Formation provide promising evidence of evolution's null hypothesis. *Proceedings of the National Academy of Sciences*, *112*(7), 2087–2092. https://doi.org/10.1073/pnas.1419241112

Schmidt, M. E., Allwood A., Christian, J., Clark, B. C., Flannery, D., Hennecke, J., et al. (2022). Highly differentiated basaltic lavas examined by PIXL in Jezero Crater (abstract). 53rd Lunar and Planetary Science Conference.

Schröder, S., Beukes, N. J., & Sumner, D. Y. (2009). Microbialite–sediment interactions on the slope of the Campbellrand carbonate platform (Neoarchean, South Africa). *Precambrian Research*, *169*(1–4), 68–79. https://doi.org/10.1016/j.precamres.2008.10.014

Schubel, K. A., & Simonson, B. M. (1990). Petrography and Diagenesis of Cherts From Lake Magadi, Kenya. *Journal of Sedimentary Petrology*, *60*(5), 761–776.

Sharma, S., Roppel, R. D., Murphy, A. E., Beegle, L. W., Bhartia, R., Steele, A., Hollis, J. R., Siljeström, S., McCubbin, F. M., Asher, S. A., Abbey, W. J., Allwood, A. C., Berger, E. L., Bleefeld, B. L., Burton, A. S., Bykov, S. V., Cardarelli, E. L., Conrad, P. G., Corpolongo, A., … Yanchilina, A. (2023). Diverse organic-mineral associations in Jezero crater, Mars. *Nature*, 1–9. https://doi.org/10.1038/s41586-023-06143-z

Shkolyar, S., & Farmer, J. D. (2018). Biosignature Preservation Potential in Playa Evaporites: Impacts of Diagenesis and Implications for Mars Exploration. *Astrobiology*, *18*(11), 1460–1478. https://doi.org/10.1089/ast.2018.1849

Shkolyar, S., Lalla, E., Konstantinidis, M., Cote, K., Daly, M. G., & Steele, A. (2021). Detecting Ce^{3+} as a biosignature mimicker using UV time-resolved laser-induced fluorescence and

Raman spectroscopy: Implications for planetary missions. *Icarus*, *354*, 114093. https://doi.org/10.1016/j.icarus.2020.114093

Sigalevich, P., Meshorer, E., Helman, Y., & Cohen, Y. (2000). Transition from Anaerobic to Aerobic Growth Conditions for the Sulfate-Reducing Bacterium *Desulfovibrio oxyclinae* Results in Flocculation. *Applied and Environmental Microbiology*, *66*(11), 5005–5012. https://doi.org/10.1128/AEM.66.11.5005-5012.2000

Siljeström, S., Czaja, A. D., Corpolongo, A., Berger, E. L., Li, A. Y., Cardarelli, E., Abbey, W., Asher, S. A., Beegle, L. W., Benison, K. C., Bhartia, R., Bleefeld, B. L., Burton, A. S., Bykov, S. V., Clark, B., DeFlores, L., Ehlmann, B. L., Fornaro, T., Fox, A., … Zorzano, M.-P. (2024). Evidence of Sulfate-Rich Fluid Alteration in Jezero Crater Floor, Mars. Journal of Geophysical Research: Planets, 129(1), e2023JE007989. https://doi.org/10.1029/2023JE007989

Simon, J. I., Amundsen, H. E. F., Beegle, L. W., Bell J., Benison, K. C., Berger., E. L., et al. (2022). Sampling of Jezero Crater Máaz Formation by Mars 2020 Perseverance rover (abstract). 53rd Lunar and Planetary Science Conference.

Simon, J. I., Hickman-Lewis, K., Cohen, B. A., Mayhew, L. E., Shuster, D. L., Debaille, V., Hausrath, E. M., Weiss, B. P., Bosak, T., Zorzano, M.-P., Amundsen, H. E. F., Beegle, L. W., Bell III, J. F., Benison, K. C., Berger, E. L., Beyssac, O., Brown, A. J., Calef, F., Casademont, T. M., … Williford, K. H. (2023). Samples Collected From the Floor of Jezero Crater With the Mars 2020 Perseverance Rover. *Journal of Geophysical Research: Planets*, *128*(6), e2022JE007474. https://doi.org/10.1029/2022JE007474

Stack, K. M., et al. (2020). Photogeologic Map of the Perseverance Rover Field Site in Jezero Crater Constructed by the Mars 2020 Science Team. Space Science Reviews, 216(8), 127. https://doi.org/10.1007/s11214-020-00739-x

Stevens, E. W., Sumner, D. Y., Harwood, C. L., Crutchfield, J. P., Hamann, B., Kreylos, O., Puckett, E., & Senge, P. (2011). Understanding Microbialite Morphology Using a Comprehensive Suite of Three-Dimensional Analysis Tools. *Astrobiology*, *11*(6), 509–518. https://doi.org/10.1089/ast.2010.0560

Sudarsanan, K. T., & Young, R. A. (1969) Significant precision in crystal structural details. Holly Springs hydroxyapatite. *Acta Crystallographica Section B, 25*(8).

Sugitani, K., Lepot, K., Nagaoka, T., Mimura, K., Van Kranendonk, M., Oehler, D. Z., & Walter, M. R. (2010). Biogenicity of Morphologically Diverse Carbonaceous Microstructures from the ca. 3400 Ma Strelley Pool Formation, in the Pilbara Craton, Western Australia. *Astrobiology*, *10*(9), 899–920. https://doi.org/10.1089/ast.2010.0513

Sugitani, K., Mimura, K., Nagaoka, T., Lepot, K., & Takeuchi, M. (2013). Microfossil assemblage from the 3400Ma Strelley Pool Formation in the Pilbara Craton, Western Australia: Results form a new locality. *Precambrian Research*, *226*, 59–74. https://doi.org/10.1016/j.precamres.2012.11.005

Sumner, D. Y., & Bowring, S. A. (1996). U/Pb geochronologic constraints on deposition of the Campbellrand Subgroup, Transvaal Supergroup, South Africa. *Precambrian Research*, *79*(1–2), 25–35. https://doi.org/10.1016/0301-9268(95)00086-0

Sumner, D. Y. (1997a). Late Archean Calcite-Microbe Interactions: Two Morphologically Distinct Microbial Communities That Affected Calcite Nucleation Differently. *PALAIOS*, *12*(4), 302. https://doi.org/10.2307/3515333

Sumner, D. Y. (1997b). Carbonate precipitation and oxygen stratification in late Archean seawater as deduced from facies and stratigraphy of the Gamohaan and Frisco formations, Transvaal Supergroup, South Africa. *American Journal of Science*, *297*(5), 455–487. https://doi.org/10.2475/ajs.297.5.455

Sumner, D. Y. (2000). Microbial vs Environmental Influences on the Morphology of Late Archean Fenestrate Microbialites. In R. E. Riding & S. M. Awramik (Eds.), *Microbial Sediments* (pp. 307–314). Springer Berlin Heidelberg. https://doi.org/10.1007/978-3-662-04036-2_33

Sumner, D. Y., & Grotzinger, J. P. (2004). Implications for Neoarchaean ocean chemistry from primary carbonate mineralogy of the Campbellrand-Malmani Platform, South Africa. *Sedimentology*, *51*(6), 1273–1299. https://doi.org/10.1111/j.1365-3091.2004.00670.x

Sumner, D. Y., & Beukes, N. J. (2006). Sequence Stratigraphic Development of the Neoarchean Transvaal carbonate platform, Kaapvaal Craton, South Africa. *South African Journal of Geology*, *109*(1–2), 11–22. https://doi.org/10.2113/gssajg.109.1-2.11

Sun, V. Z., Hand, K. P., Stack, K. M., Farley, K. A., Milkovich, S., Kronyak, R., et al. (2022). Exploring the Jezero Crater floor: Overview of results from the Mars 2020 Perseverance Rover's first science campaign (abstract). 53rd Lunar and Planetary Science Conference.

Sylvestre, M.-N., Jean-Louis, P., Grimonprez, A., Bilas, P., Collienne, A., Azède, C., & Gros, O. (2022). *Candidatus* Thiovulum sp. strain imperiosus: The largest free-living

Epsilonproteobacteraeota *Thiovulum* strain lives in a marine mangrove environment. *Canadian Journal of Microbiology*, *68*(1), 17–30. https://doi.org/10.1139/cjm-2021-0101

Tarcea, N., Harz, M., Rösch, P., Frosch, T., Schmitt, M., Thiele, H., Hochleitner, R., & Popp, J. (2007). UV Raman spectroscopy—A technique for biological and mineralogical in situ planetary studies. *Spectrochimica Acta Part A: Molecular and Biomolecular Spectroscopy*, *68*(4), 1029–1035. https://doi.org/10.1016/j.saa.2007.06.051

Thar, R., & Fenchel, T. (2005). Survey of Motile Microaerophilic Bacterial Morphotypes in the Oxygen Gradient above a Marine Sulfidic Sediment. *Applied and Environmental Microbiology, 71*(7), 3682–3691. https://doi.org/10.1128/AEM.71.7.3682-3691.2005

Tice, M., Hurowitz, J., Siebach, K. L., Moreland, E. L., Kizovski, T. V., Schmidt, M. E., O'Neill, L. P., Treiman, A. H., Clark, B., & Jones, M. W. M. (2024). *Regional Paleoenvironments Recorded in Sedimentary Rocks of the Western Fan-Delta, Jezero Crater, Mars*. 55th Lunar and Planetary Science Conference, The Woodlands, Texas, United States.

Twing, K. I., Brazelton, W. J., Kubo, M. D. Y., Hyer, A. J., Cardace, D., Hoehler, T. M., McCollom, T. M., & Schrenk, M. O. (2017). Serpentinization-Influenced Groundwater Harbors Extremely Low Diversity Microbial Communities Adapted to High pH. *Frontiers in Microbiology*, *8*. https://doi.org/10.3389/fmicb.2017.00308

Tyler, S. A., & Barghoorn, E. S. (1963). Ambient pyrite grains in Precambrian cherts. American Journal of Science, 261(5), 424–432. https://doi.org/10.2475/ajs.261.5.424

Uckert, K., Bhartia, R., Beegle, L. W., Monacelli, B., Asher, S. A., Burton, A. S., Bykov, S. V., Davis, K., Fries, M. D., Jakubek, R. S., Hollis, J. R., Roppel, R. D., & Wu, Y.-H. (2021). Calibration of the SHERLOC Deep Ultraviolet Fluorescence–Raman Spectrometer on the

Perseverance Rover. Applied Spectroscopy, 75(7), 763–773. https://doi.org/10.1177/00037028211013368

Udry, A., Sautter, V., Cousin, A., Wiens, R. C., Forni, O., Benzerara, K., et al. (2022). A Mars 2020 Perseverance SuperCam perspective on the igneous nature of the Máaz formation at Jezero crater, Mars (abstract). 53rd Lunar and Planetary Science Conference.

Valentin-Alvarado, L. E., Fakra, S. C., Probst, A. J., Giska, J. R., Jaffe, A. L., Oltrogge, L. M., West-Roberts, J., Rowland, J., Manga, M., Savage, D. F., Greening, C., Baker, B. J., & Banfield, J. F. (2024). Autotrophic biofilms sustained by deeply sourced groundwater host diverse bacteria implicated in sulfur and hydrogen metabolism. *Microbiome*, *12*(1), 15. https://doi.org/10.1186/s40168-023-01704-w

Voegelin, A. R., Nägler, T. F., Beukes, N. J., & Lacassie, J. P. (2010). Molybdenum isotopes in late Archean carbonate rocks: Implications for early Earth oxygenation. *Precambrian Research*, *182*(1–2), 70–82. https://doi.org/10.1016/j.precamres.2010.07.001

Wacey, D., Noffke, N., Cliff, J., Barley, M. E., & Farquhar, J. (2015). Micro-scale quadruple sulfur isotope analysis of pyrite from the ~3480 Ma Dresser Formation: New insights into sulfur cycling on the early Earth. *Precambrian Research*, *258*, 24–35. https://doi.org/10.1016/j.precamres.2014.12.012

Wacey, D., Saunders, M., Kong, C., & Kilburn, M. R. (2016). A new occurrence of ambient inclusion trails from the ~1900-million-year-old Gunflint Formation, Ontario: Nanocharacterization and testing of potential formation mechanisms. *Geobiology*, *14*(5), 440–456. https://doi.org/10.1111/gbi.12186

Warke, M. R., Edwards, N. P., Wogelius, R. A., Manning, P. L., Bergmann, U., Egerton, V. M., Kimball, K. C., Garwood, R. J., Beukes, N. J., & Schröder, S. (2019). Decimeter-scale mapping of carbonate-controlled trace element distribution in Neoarchean cuspate stromatolites. *Geochimica et Cosmochimica Acta*, *261*, 56–75. https://doi.org/10.1016/j.gca.2019.07.004

Walrafen, G. E., Krishnan, P. N. (1981). Raman spectrum of pressure compacted fused silica. *The Journal of Chemical Physics, 74*(9).

Wang, A., Freeman, J. J., Jolliff, B. L., & Chou, I.-M. (2006). Sulfates on Mars: A systematic Raman spectroscopic study of hydration states of magnesium sulfates. *Geochimica et Cosmochimica Acta, 70*(24), 6118–6135. https://doi.org/10.1016/j.gca.2006.05.022

Westall, F. (1999). The nature of fossil bacteria: A guide to the search for extraterrestrial life. *Journal of Geophysical Research: Planets*, *104*(E7), 16437–16451. https://doi.org/10.1029/1998JE900051

Wiens, R. C., Udry, A., Mangold, N., Beyssac, O., Quantin, C., Sautter, V., et al. (2022). Composition and density stratification observed by SuperCam in the first 300 sols in Jezero Crater (abstract). 53rd Lunar and Planetary Science Conference.

Wirsen, C. O., & Jannasch, H. W. (1978). Physiological and morphological observations on Thiovulum sp. Journal of Bacteriology, 136(2), 765–774. https://doi.org/10.1128/jb.136.2.765-774.1978

Wojdyr, M. (2010). *Fityk*: A general-purpose peak fitting program. *Journal of Applied Crystallography*, *43*(5), 1126–1128. https://doi.org/10.1107/S0021889810030499

Wood, S. A., Rhodes, L., Smith, K., Lengline, F., Ponikla, K., & Pochon, X. (2017). Phylogenetic characterisation of marine Chroococcus-like (Cyanobacteria) strains from the Pacific region. *New Zealand Journal of Botany*, *55*(1), 5–13. https://doi.org/10.1080/0028825X.2016.1205634

Woycheese, K. M., Meyer-Dombard, D. R., Cardace, D., Argayosa, A. M., & Arcilla, C. A. (2015). Out of the dark: Transitional subsurface-to-surface microbial diversity in a terrestrial serpentinizing seep (Manleluag, Pangasinan, the Philippines). *Frontiers in Microbiology*, *6*. https://doi.org/10.3389/fmicb.2015.00044

Wright, D. T., & Altermann, W. (2000). Microfacies development in Late Archaean stromatolites and oolites of the Ghaap Group of South Africa. *Geological Society, London, Special Publications*, *178*(1), 51–70. https://doi.org/10.1144/GSL.SP.2000.178.01.05

Wu, Z., Wang, A., & Ling, Z. (2016). Spectroscopic study of perchlorates and other oxygen chlorides in a Martian environmental chamber. Earth and Planetary Science Letters, 452, 123–132. https://doi.org/10.1016/j.epsl.2016.07.044

Wu, B., Liu, F., Fang, W., Yang, T., Chen, G.-H., He, Z., & Wang, S. (2021). Microbial sulfur metabolism and environmental implications. *Science of The Total Environment*, *778*, 146085. https://doi.org/10.1016/j.scitotenv.2021.146085

Xing, T., Zhu, W., Fusseis, F., & Lisabeth, H. (2018). Generating porosity during olivine carbonation via dissolution channels and expansion cracks. *Solid Earth*, *9*(4), 879–896. https://doi.org/10.5194/se-9-879-2018

Yun, Z. (1984). A Gunflint type of microfossil assemblage from early Proterozoic stromatolitic cherts in China. *Nature*, *309*(5968), 547–549. https://doi.org/10.1038/309547a0

Zapata, F., Garcia-Ruiz, C. (2018). The discrimination of 72 nitrate, chlorate and perchlorate salts using IR and Raman spectroscopy. *Spectrochimica Acta A, 189.*

Zerkle, A. L. (2005). Biogeochemical signatures through time as inferred from whole microbial genomes. *American Journal of Science*, *305*(6–8), 467–502. https://doi.org/10.2475/ajs.305.6-8.467

Zhang, Y.-T., She, Z.-B., & Papineau, D. (2015). Ambient inclusion trails (AITs) in the Ediacaran Doushantuo Formation, south China: New observations and a refined model. *Goldschmidt 2015*.

Appendix A: Supporting Information for SHERLOC Raman Mineral Class Detections of the Mars 2020 Crater Floor Campaign

Introduction

This supporting information includes figures to aid in interpreting the main text; more thorough explanations of the peak position error calculation, background artifacts, and SHERLOC analogue instruments that were provided in the main text; and additional details regarding our mineral class assignment criteria.

Text S1 Raman Spectral Peak Position Error

An understanding of the error in peak position assignments is essential for distinguishing between mineral Raman spectra with primary Raman bands in similar spectral locations. As stated in the main text, Raman band positions were determined by fitting the peaks to gaussian functions. Gaussian functions were used because the SHERLOC instrument slit function dominates the shape of the observed Raman band and is well-approximated as a Gaussian. While the spectral resolution is ~10cm^{-1}/pixel, fitting the spectrum significantly decreases the peak position error because all data points across the full width of the band (~8 for SHERLOC bands that are slit function dominated) contribute information on the peak position. Lenz and Ayres (1992) derived the equations for calculating peak position error from a gaussian fit. The error is dependent on the number of points across the band's full width and the S/N ratio of the data. We find that for a S/N = 3 the error is ±~4.0 cm^{-1} and for S/N = 10 the error is ~1.2 cm^{-1}. While the S/N differs for each individual spectrum for all mineral detections we have single spectra with S/N>10 and by averaging numerous spectra we can obtain a spectrum with S/N>10 resulting in an error of <±1 cm^{-1}. For averaged spectra we check that the bandwidth of the peak is similar to

the SHERLOC slit function bandwidth of ~40 cm^{-1} to ensure only one peak position is being averaged. If multiple peaks are being averaged, then the average spectrum bandwidth will be significantly broadened. These analysis techniques aid in the differentiation between minerals with similar peak positions.

S2. Stowed Arm Scan Measurements

The median spectrum of every SHERLOC scan was examined to determine the most prevalent Raman spectra in each scan with high S/N. We found common features observed in the median spectrum for every scan of every target. These features include broad bands at ~480 cm-1, 800 cm-1 and 1050 cm-1 (Figure S41d). The presence of these features in the median spectra means that they must occur in >50% of single spectra in their respective scans and the fact that they are observed on every target means that the spectra are ubiquitously observed. This suggests that the explanation for these spectral signatures is the presence of instrumental spectral effects.

SHERLOC Raman measurements in the absence of a target were collected to assess the instrument's spectral background. For these measurements, the SHERLOC arm was kept in the stowed position and the spectra were collected with the objective lens facing the horizon, which was dark at the time of collection (activity time: 20:04, local sunset: 17:06 LMST). Three scans, HDR_100_1, HDR_250_1, and HDR_500_1, were collected to simulate a Raman scan of a target, however, because no target was present, any spectral signatures observed in the data must be an instrumental feature. Figure S41a shows the median spectra of the stowed arm HDR_100_1, HDR_250_1, and HDR_500_1 scans. The spectra show bands at ~480, 800, 1060, and 1200 cm^{-1}. These bands are all consistent with the fused silica spectrum (Walrafen et al. 1981). Generally the strongest band observed in fused silica is broad and at ~400 cm^{-1}. However,

the SHERLOC laser injection filter cuts off most of this band resulting in the ~480 cm^{-1} band observed. The ~650 cm^{-1} band is the 252.9 nm emission line from the laser (Bhartia et al., 2021). A comparison between the stowed arm HDR_500_1 median spectrum and the median spectrum of fused silica collected from the Diffusil cal target on sol 368 confirms that this background is fused silica (Figure S4Xb). As observed in figure S41a, the intensity of the fused silica background increases linearly with pulses per point, further supporting that the background is instrumental. Though this background feature is easily observed in the median spectra, it is much weaker in the single spectra. No signal was observed in the single spectra of scan HDR_100_1, however, a weak signal could be observed in single spectra of HDR_250_1 and HDR_500_1. An example of a single spectrum of HDR_500_1 is shown in figure S41C and shows ~50 counts of intensity for the 800 cm^{-1} band with no other feature significantly above the noise.

The fused silica background spectra from the stowed arm scan significantly differs from that of the median scans of targets. For example, the median scan of Alfalfa HDR_500_1 is shown in figure S41d. The main feature of this spectrum is a broad band centered at ~1050 cm^{-1}, but this band is much broader, downshifted, and more intense than that of the fused silica

~1060 cm^{-1} band. The target median spectra also contain a band at ~800 cm^{-1} and a weak band at ~500 cm^{-1}. These bands are consistent with the fused silica background but the ~1050 cm^{-1} band is not consistent with fused silica background and must be from the targets and matches the spectrum we have assigned silicate .

S3. Subtraction Artifacts

In SHERLOC data collected during the Crater Floor Campaign, we observed narrow peaks occurring at specific pixels more frequently than would be expected if they were caused by

spectral noise and/or cosmic rays. Our current understanding is that the artifacts are caused by single pixels with a consistently high background intensity (over 1000 counts) in both the dark and active spectra. The single pixels with high intensity in the dark and active spectra also have increased noise. This noise can result in a large difference in intensity between the dark and active spectra for these pixels, resulting in either positive or negative single-pixel features in the reported Raman spectrum. The SHERLOC team is currently investigating the cause of the high background intensity in these pixels and determining how best to mitigate their impact on data interpretation.

As stated in the main text, most of the affected pixels correspond to wavenumbers that are irrelevant to the spectral assignments discussed in this paper. The affected pixels correspond to approximately 331 cm^{-1}, 694 cm^{-1}, 784 cm^{-1}, 970 cm^{-1}, 981 cm^{-1}, 1164 cm^{-1}, 1307cm^{-1}, 1431 cm^{-1}, 1477 cm^{-1}, 1534 cm^{-1}, 1580 cm^{-1}, 1636 cm^{-1}, 2563 cm^{-1}, 3002 cm^{-1}, 3360 cm^{-1}, 3504 cm^{-1}, 3528 cm^{-1}, 3763 cm^{-1}, 3802 cm^{-1}, 3847 cm^{-1}, 3863 cm^{-1}, and 3947 cm^{-1}. In most instances, it is easy to differentiate between these spectral artifacts and Raman bands because the spectral artifacts affect single pixels while Raman bands have a minimum FWHM of ~3 pixels. However, the spectral artifacts that occur at 970 cm^{-1} and 981 cm^{-1} make it difficult to make confident mineral assignments of low-intensity peaks in this region, particularly when they have no associated secondary peaks (see main text section 2.4).

S4. Raman Spectral Assignments

S4.1 Analogue Instruments

Raman spectral assignments are largely based on the comparison of SHERLOC spectra to that of terrestrial analogue instruments. There are currently four SHERLOC analogue instruments,

MOBIUS, Brassboard, MORIARITI, and ACRONM. MOBIUS (mineralogy and organic-based investigations using ultraviolet spectroscopy) was the initial benchtop SHERLOC prototype and was described previously (Abbey et al., 2017). The Brassboard is an analogue instrument built using hardware similar to the SHERLOC flight instrument and is described in a previous publication (Razzell Hollis et al., 2021a). MORIARTI (Mineralogy and Organics Raman Instrumentation for the Analysis of Terrestrial Illumination) is an analogue instrument built by the Asher research group at the University of Pittsburgh.

ACRONM (Analogue Complementary Raman for Operations oN Mars) was built and is housed in the Raman microprobe lab at NASA Johnson Space Center. It is modeled from MOBIUS and is thus similar in construction (Abbey et al., 2017). A PhotonSystems NeCu-70 hollow cathode laser is used to produce 248.5794 nm incident excitation, identical to that used by SHERLOC. Using a 5X objective, the incident beam is focused to a ~100 μm spot size on the sample, which is located on a motorized XYZ stage constructed from Zaber Technologies. A Horiba Scientific iHR 320 spectrometer with a 2400 g/mm grating is used to disperse the Raman scattered light, and the dispersed light is detected using a Horiba Scientific Synapse Plus CCD (SYN-PLUS-2048X512-BU) that is thermoelectrically cooled to -75º. This system uses the same e2v 42-10 back illuminated UV (BIUV) detector used in SHERLOC.

S4.2 Silicate

We observed broad bands with a FWHH of ~100-200 cm^{-1} and peak centers in the 1000 - 1150 cm^{-1} spectral range in the median spectra of all scans and in numerous single spectra, as indicated in the main text. The single spectrum detections are associated with different rock colors and

textures, depending on the scan in which they are observed. Generally, the fingerprint region of silicate spectra falls between 400 cm^{-1} and 800cm^{-1} (Fu et al., 2017). Such low- and mid-region peaks would be obscured by SHERLOC's laser-injection filter and 252.9 nm laser plasma lineand are not discernable in the SHERLOC points assigned to silicate. A detailed analysis of the silicate species that are associated with these spectra is beyond the scope of this text. However, this work is currently being done by the SHERLOC team and will be available in a forthcoming publication. The observation of these silicate bands in the median spectra of every scan on every target, including natural targets, suggests that silicates are common across the Crater Floor, perhaps as a component of dust.

S4.3 Olivine

The Raman spectrum of olivine with 248.6 nm excitation, collected on ACRONM, consists of two primary peaks at ~825 and ~850 cm^{-1} that are assigned to SiO_4 stretching modes (Figure S6; Keubler et al., 2006). The UVRR spectrum is similar to that observed with visible excitation, however, the slit functions of the SHERLOC analogue instruments have smaller FWHHs compared to that of SHERLOC (40 cm^{-1}; Uckert et al., 2021). The FWHHs of the olivine bands are ~8-12 cm^{-1} resulting in an observed band width primarily controlled by the SHERLOC and analogue instrument slit functions. Because of this, we observe both the ~825 and

~850 cm^{-1} bands in the ACRONM spectra, and a single broad (~75 cm^{-1} FWHH) unresolved band located at ~835 cm^{-1} in the SHERLOC spectra (Figure S6). The SHERLOC spectrum can be sufficiently modeled by convolving the ~8-12 cm^{-1} FWHH intrinsic olivine Raman bands with the 40 cm^{-1} SHERLOC slit function. The result produces a single broad peak with a peak position at ~835 cm^{-1} and a FWHH of ~75 cm^{-1}, which matches well what is observed in the SHERLOC spectra.

It is well known that the peak positions of the ~825 and ~850 cm^{-1} olivine bands provide information on the Fo# composition of olivines (Kuebler et al., 2006). In addition, the relative peak intensities of the ~825 and ~850 cm^{-1} bands are affected by both composition (Kuebler et al., 2006) and crystal orientation (Ishibashi et al., 2008). The effects of band intensities on crystal orientation will differ for SHERLOC because the NeCu laser is: (1) not linearly polarized (Bhartia et al., 2021) and (2) under a different resonance Raman condition compared to visible excitations, which results in different Raman polarizability tensor shapes. Determining olivine composition from the unresolved ~825 and ~850 cm^{-1} doublet observed by SHERLOC is difficult because the change in more than one of the individual ~825 and ~850 cm^{-1} band parameters can result in the same change in the unresolved band. For example, an upshift in the peak intensity of the unresolved band could result from either an upshift of both the ~825 and ~850 cm^{-1} bands or an increase in the intensity of the ~850 cm^{-1} band with respect to the ~825 cm^{-1} band. Thus, determining olivine composition from the SHERLOC data is not trivial and a deeper analysis of the spectra are required to investigate this possibility.

S4.4 Carbonate

Raman spectra of carbonate collected by SHERLOC and analogue instruments is shown in Figure S7. Carbonate minerals have a strong band at ~1085 cm^{-1} from CO_3 symmetric stretching motion (v1; Buzgar & Apopei, 2009). Weaker bands observed at ~1450 and ~1750 cm^{-1} derive from CO_3 v3 asymmetric stretching/v4 asymmetric bending and v1+v4 combination bands respectively (Buzgar & Apopei, 2009). The ~1600 cm^{-1} band could result from H-O-H bending or CO_3 vibrational motions (Buzgar & Apopei, 2009). Based on the S/N we observe in the SHERLOC spectra we expect to only observe the most intense carbonate Raman band, which is >1 order of

magnitude more intense than the two minor peaks. The position of the most intense carbonate Raman band, the CO_3 symmetric stretching band, shifts with carbonate composition (Buzgar & Apopei, 2009). Data from SHERLOC analogue instruments indicate that the calcite CO_3 symmetric stretching band is ~5 cm^{-1} downshifted compared to that of magnesite. SHERLOC spectra show a CO_3 stretching frequency at ~1085 cm^{-1} on all targets.

S4.5 Pyroxene

Raman spectra of pyroxene observed by SHERLOC and collected on the ACRONM analogue instrument is shown in Figure S8. As observed with ACRONM, the major pyroxene peaks observed with 248.6 nm excitation are found at 680 cm^{-1} and 1010 cm^{-1}. These bands correspond to the SiO stretching vibrations of the bridging and non-bridging oxygens respectively (Huang et al. 2000). In the pyroxene SHERLOC spectrum we observe bands at ~690 and 995 cm^{-1}. The ~690 cm^{-1} band overlaps with the ~650 cm^{-1} plasma emission line from the laser, hindering its identification. We observe the SiO non-bridging symmetric stretching band at ~995 cm^{-1} in SHERLOC in contrast to 1010 cm^{-1} as observed in ACRONM. However, these peak positions are highly variable with composition and both SHERLOC and ACRONM bands are well within the wavenumber range for these bands (1020±50 cm^{-1}; Huang et al. 2000).

S4.6 Phosphate

With ACRONM, we collected spectra of six fluorapatite, and one each of chlorapatite, hydroxylapatite, carbonate-rich fluorapatite, whitlockite, and synthetic Mg-merrillite. The six fluorapatite samples are natural samples that come from igneous and/or metamorphic rocks in (1) Durango, Mexico, (2) Atlas Mountains, Morocco, (3) Eagle County, Colorado, USA, (4) Lake

Baikal, Russia, (5) Pegmatite from an unknown locality in India, and (6) Mud Tank carbonatite, Australia. The compositions of these fluorapatites have been described in previous studies (Currie et al., 1992; McCubbin et al., 2012). The chlorapatite is a natural sample from Ødegården Verk, Norway and was described in Lieftink et al. (1994). The hydroxylapatite is a natural sample from Holly Springs, Georgia, USA and was described previously by Sudarsanan and Young (1969). The carbonate-rich fluorapatite is a natural sedimentary apatite from Staffel, Germany described previously by Mason et al., (2009). The whitlockite sample is from Big Fish River, Yukon, Canada and has a composition that sits along the whitlockite-merrillite join (McCubbin et al., 2018). The Mg-merrillite sample was synthesized following the procedures outlined in Adcock et al. (2014). The most intense band is observed at ~965 cm^{-1} corresponding to the PO4 symmetric stretching normal mode (O'Shea et al., 1974). Secondary bands are observed at 1050, 600, 650, and 450 cm^{-1} corresponding to v3 asymmetric stretching (1050 cm^{-1}) and bending modes, respectively (Litasov et al., 2017).

The SHERLOC spectrum of phosphate/perchlorate shows the major peak at ~950-960 cm^{-1} and shows low intensity bands in the 1000-1150 cm^{-1} range that are difficult to resolve. The lower frequency bands of phosphate (450-650 cm^{-1}) are not expected to be observed by SHERLOC for the spectral S/N observed because they occur either below the laser injection filter cutoff or overlapping the ~650 cm^{-1} (252.9 nm) laser emission line. This SHERLOC spectrum is designated as "phosphate/perchlorate" because the main peak is located at ~950-960 cm^{-1}, which could be argued to be on the low wavenumber end for phosphates or the high wavenumber end for perchlorates with a single major peak from 930-950 cm^{-1} (Zapata et al., 2018) and minor peaks in the 1000-1150 cm^{-1} spectral range. Thus, it is difficult to differentiate between the two species. In the ACRONM spectra, almost all of the phosphates examined have their PO4

symmetric stretch at 965 cm^{-1} with the exception of Staffel fluorapatite (~959 cm^{-1}), and hydroxylapatite (~960 cm^{-1}).

It was recently shown that phosphates containing trivalent cerium have a distinct fluorescence feature at ~340 nm (Scheller et al., 2022; Shkolyar et al., 2021). However, aromatic organic compounds can also fluoresce at this wavelength (Scheller et al., 2022). The phosphate/perchlorate Raman spectra in Garde and Bellegarde are spatially covariant with a ~340 nm fluorescence feature, and the relative intensities between the phosphate/perchlorate Raman spectra and the corresponding ~340 nm fluorescence band are constant, suggesting that the signal may come from trivalent cerium. However, another possible explanation is that organics preferentially occur in phosphate weathering/alteration zones. In the Guillaumes targets, the phosphate/perchlorate Raman spectra and ~340 nm fluorescence signal appear uncorrelated. Thus, the presence of a ~340 nm fluorescence feature accompanying a phosphate/perchlorate spectrum may indicate that the target is a phosphate, but does not provide a definitive assignment.

S4.7 Sulfate

The Sulfate Raman spectrum from SHERLOC and the brassboard instruments are shown in figure S10. We observe the main peak at ~1015 cm^{-1} corresponding to the SO_4 symmetric stretching band (Buzgar et al., 2009). Secondary peaks occur at 1120-1150 cm^{-1}, 680-700 cm^{-1}, and ~615 cm^{-1} corresponding to asymmetric stretching, asymmetric bending, and asymmetric bending motions respectively. In figure S10 we show sulfate spectra for two different SHERLOC targets, Dourbes 269 and Quartier 293, because they show two distinct sulfate features. Dourbes 269 has a main peak Raman shift at ~1015 cm^{-1} more consistent with magnesium sulfate while Quartier 293 has its main peak at ~1005 cm^{-1} more consistent with calcium sulfate. This is

demonstrated by comparison of the SHERLOC spectra with the brassboard analogue instrument spectra of magnesium and calcium sulfates. SHERLOC observes Raman bands in the hydrogen stretching spectral range for several sulfate spectra, indicating some degree of hydration. However, the exact nature of the hydration state and the extent of hydration is not examined in this work. We observed broad bands that peak at about 3200 and 3400 cm^{-1} for sulfates from both Dourbes and Quartier. This is qualitatively similar to that observed for Mg and Ca sulfates on the brassboard and consistent with sulfates. Further examination of the SHERLOC sulfate spectra will be performed to examine hydration state and cation species.

S4.8 Perchlorate

SHERLOC and brassboard Raman spectra of perchlorate are shown in figures S11 and S12. The samples collected on the brassboard include sodium perchlorate monohydrate that was in the form of a damp, gel-like powder and potassium perchlorate present as a fine white powder. In SHERLOC spectra we observe lower intensity spectra that only show a ~950 cm^{-1} band and cannot be differentiated from phosphates (see phosphate section above), high intensity spectra that can be positively identified as perchlorate with secondary bands in the 1000-1150 cm^{-1} spectral range (Fig. S11), and spectra with sulfate peaks that also show a ~935 cm^{-1} band (Fig. S12). The high intensity perchlorate spectra observed with SHERLOC were only present in scans of Guillaumes and appear to be consistent with sodium perchlorate. We observed the spectra with bands at ~935 cm^{-1} and sulfate peaks in scans from Dourbes and Quartier. These bands are consistent with the major peak of several different perchlorate species (Fig. S12). Significant further investigation is needed to identify the species associated with the ~935 cm^{-1}, as the major Raman peak of a given perchlorate species can shift by nearly 100 wavenumbers, depending on its hydration state and a peak at ~935 cm^{-1} could also be consistent with oxygen chloride salts

that have lower oxidation degrees than that of perchlorate. Sodium perchlorate spectra have a major peak at 930-950 cm^{-1} that derives from Cl-O symmetric stretching and less-intense peaks at 600-650 cm^{-1} corresponding to Cl-O deformation and ~1000-1150 cm^{-1} that corresponds to asymmetric Cl-O stretching (Zapata & Garcia-Ruiz, 2018). Raman spectra collected on the brassboard of potassium (Fig. S11), calcium, ferrous iron, and magnesium perchlorate have their strongest peaks at ~935 cm^{-1} (Fig. S12), while the spectrum of sodium perchlorate has a peak at 950 cm^{-1} (Fig. S11). In Guillaumes, we observe a ~950 cm^{-1} major band, indicating sodium perchlorate. Guillaumes perchlorate spectra that exhibit a high intensity primary band at ~950 cm^{-1} also have low intensity bands in the 1000- 1150 cm^{-1} region, further supporting the assignment of sodium perchlorate.

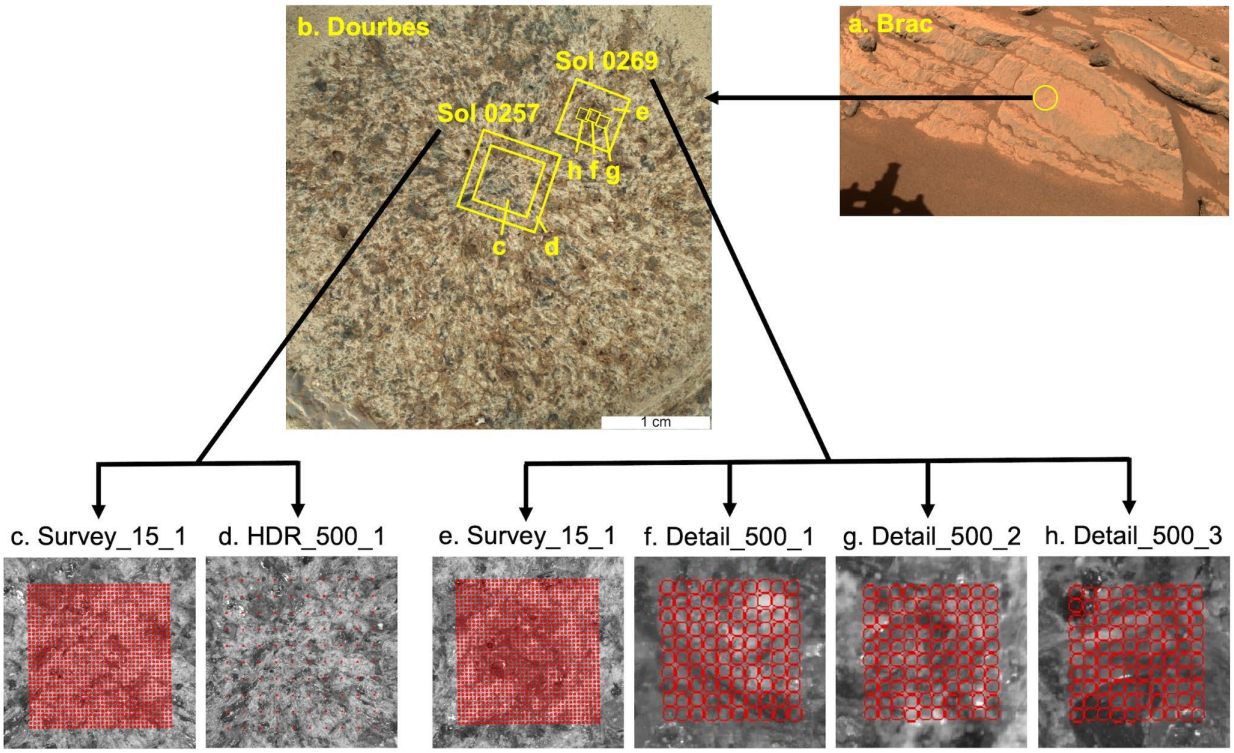

Figure S1. Diagram depicting the Raman scan nomenclature described in section 2.1 of the main text. (a) shows an image of Brac with a yellow circle indicating the location of the Dourbes target. (b) and (c)

show the different sols in which Raman scans were collected on Dourbes. (d)-(i) show the different SHERLOC scans collected on Dourbes. As discussed in the main text the Raman scan nomenclature has the form of Sol_Target ScanType_PulsesPerPoint_Scan#. For example, using our nomenclature, the scan in (g) is called 0269_Dourbes Detail_500_1.

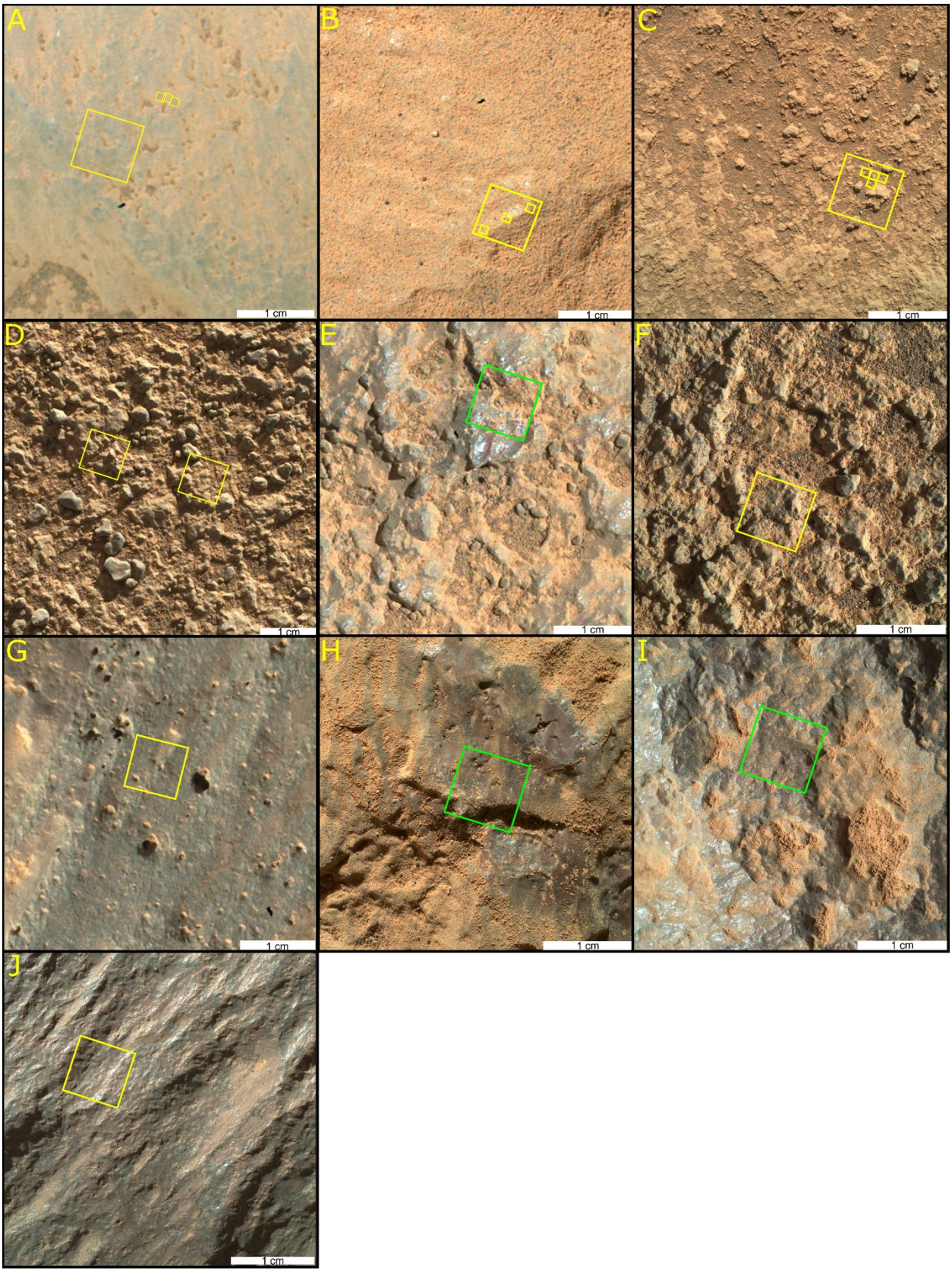
A
1 cm
B
1 cm
C
1 cm
D
1 cm
E
1 cm
F
1 cm
G
1 cm
H
1 cm
I
1 cm
J
1 cm

Figure S2. Shows all abraded targets discussed in this paper, prior to abrasion, and all natural targets discussed in this paper. Yellow boxes show the locations of scans performed on abraded surfaces. Green boxes show the locations of natural target scans. A) Dourbes B) Garde C) Quartier D) Guillaumes E) Foux F) Montpezat G) Bellegarde H) Nataani I) Bi la Sana J) Alfalfa

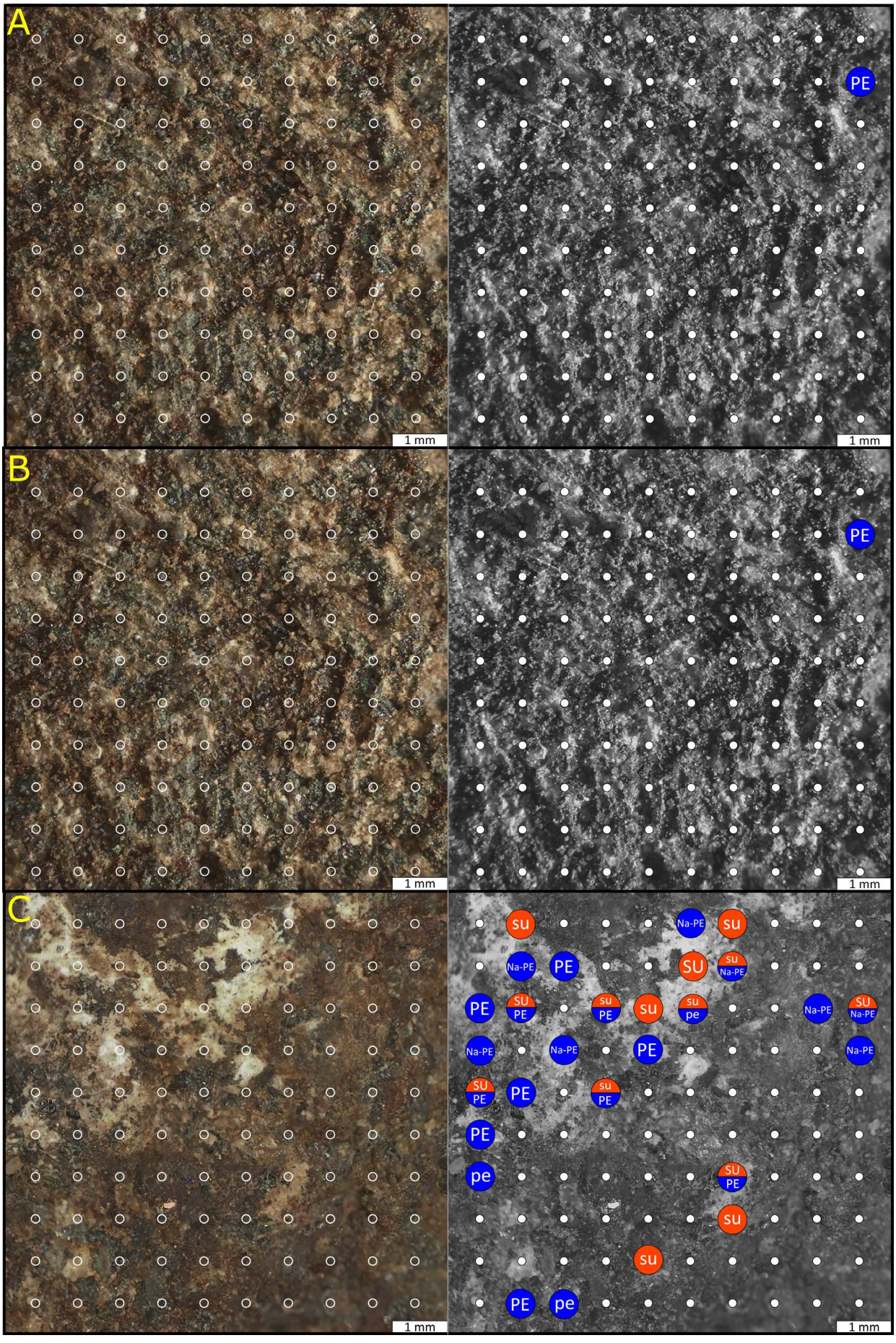
A
1 mm
PE
1 mm
B
1 mm
PE
1 mm
C
1 mm
su
Na-PE
su
Na-PE
PE
SU
su
Na-PE
PE
SU
PE
su
PE
su
su
pe
Na-PE
SU
Na-PE
Na-PE
Na-PE
PE
Na-PE
SU
PE
PE
su
PE
PE
pe
SU
PE
su
su
PE
pe
1 mm

Figure S3. Mineral assignment maps of scans A) 0161_Guillaumes HDR_100_2, B) 0161_Guillaumes HDR_300_1, and C) 0162_Guillaumes HDR_250_2. See section 3.2.1 in the main text for more details regarding the mineral assignments depicted here. SU = sulfate, PE = Perchlorate

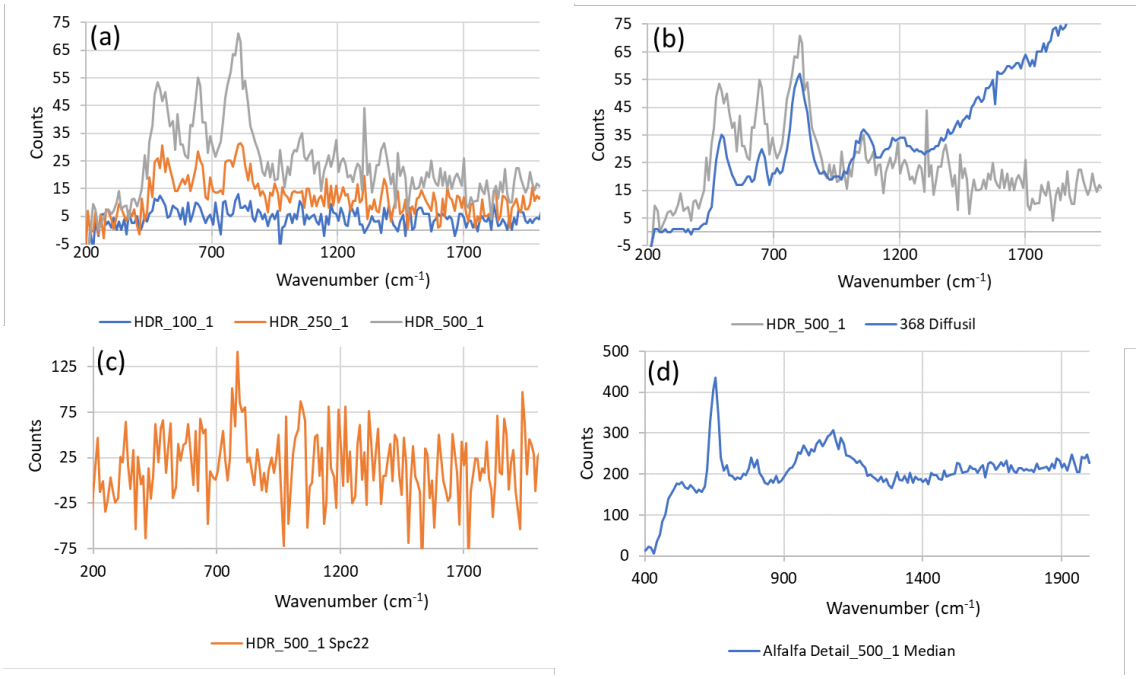

Figure S4. SHERLOC spectral background. (a) median spectra from the HDR_100_1, HDR_250_1, and HDR_500_1 scans of the stowed arm measurement. (b) comparison of the stowed arm HDR_500_1 median spectrum the the medium spectrum of fused silica from the Diffusil cal target (sol 368). (c) single spectrum from HDR_500_1 stowed arm scan. (d) Median spectrum from Alfalfa Detail_500_1.

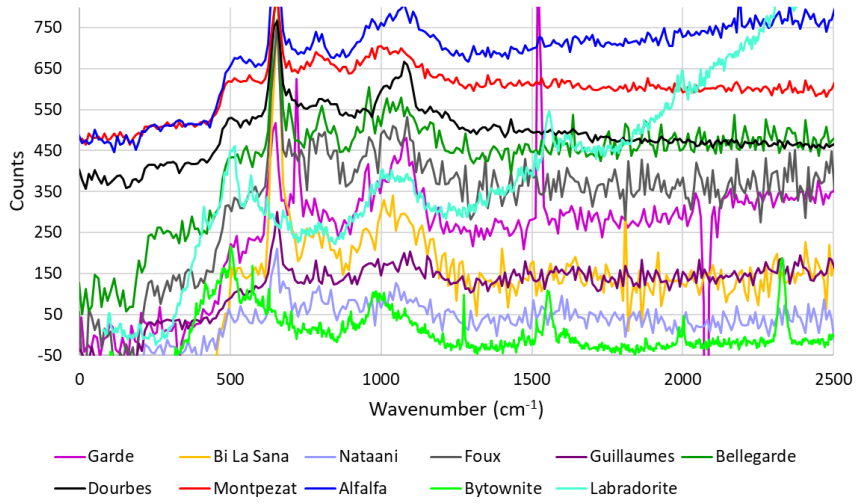

Figure S5. Median SHERLOC Raman spectra of silicate, from bottom to top, (bright green) ACRONM Bytownite, (light blue) 89_Nataani_HDR_100_1, (dark purple) 161_Guillaumes_HDR_300_1, (yellow) 98_Bi la Sana_HDR_300_1, (light purple) 208_Garde_Detail_1, (aqua) ACRONM Labradorite, (gray) 141_Foux_HDR_300_1, (green) 186_Bellegarde_HDR_250_1, (black) 269_Dourbes_Detail_500_1, (red) 349_Montpezat_Detail_500_1, and (blue) 270_Alfalfa_Detail_500_1. The dashed line is located at ~1050 cm^{-1}.

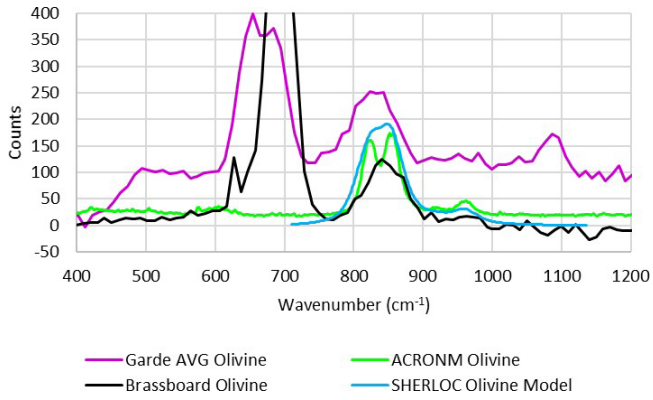

Figure S6. Olivine spectra collected on the ACRONM (green), the brassboard (black), and SHERLOC (purple) instruments. The SHERLOC spectrum is an average of all Olivine spectra collected on sol 208 Garde HDR_500_1. The ACRONM spectrum was collected on ~Fo 90 olivine (San Carlos, AZ; <150 µm size fraction) and the brassboard spectrum was collected on a natural olivine sample (Fo 82) from Hualālai, Hawai'i. The spectrum in blue is modeled from convolution of the olivine Raman bands and SHERLOC slit function as described in the text above.

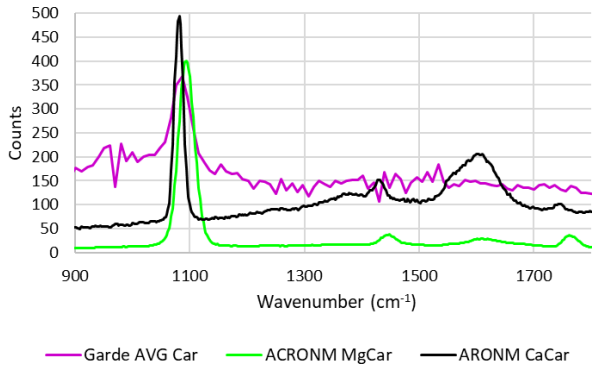

Figure S7. Carbonate mineral spectra. The black and green spectra are that of Ca and Mg Carbonate collected on ACRONM. The purple spectrum is the average of all carbonate spectra collected by SHERLOC on Dourbes sol 208 HDR_500_1. The ACRONM Ca carbonate spectrum was collected on calcite (Glen Rose formation, TX; <150 µm) and the ACRONM Mg carbonate spectrum was collected on magnesite (Riverside Co., CA; <45 µm).

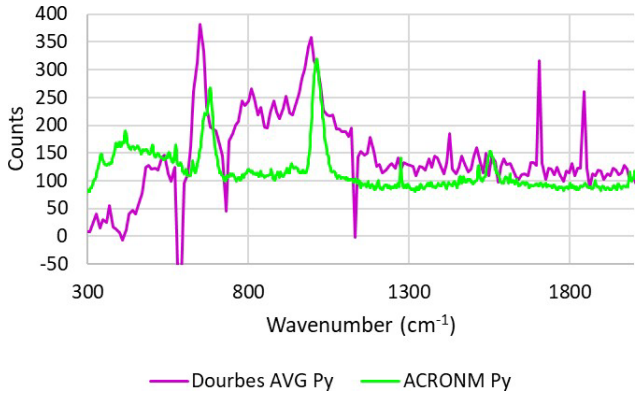

Figure S8. Raman spectrum of Pyroxene from (green) ACRONM and (purple) SHERLOC. The SHERLOC spectrum is an average of proposed pyroxene spectra collected on sol 257 Dourbes HDR_500_1. The ACRONM pyroxene spectrum was collected on enstatite (Bamble, Norway; 45-90 µm).

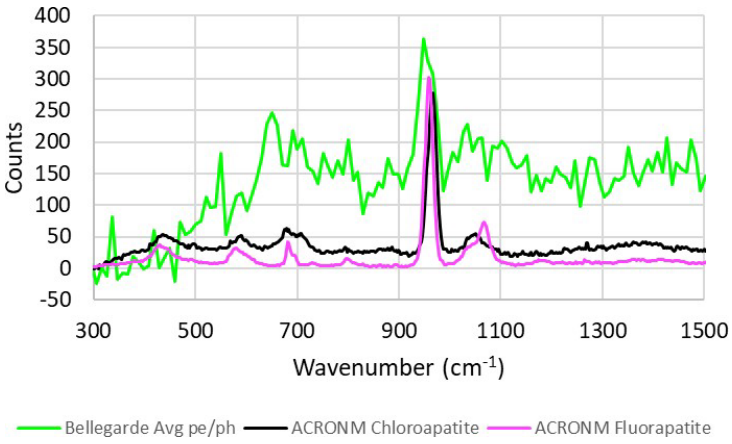

Figure S9. Spectra of phosphate collected by SHERLOC and ACRONM. (green) 0186_Bellegarde HDR_500_1 phosphate/perchlorate spectrum collected with SHERLOC. (black) chlorapatite collected on ACRONM. (purple) Carbonate-rich fluorapatite from Staffel, Germany collected on ACRONM.

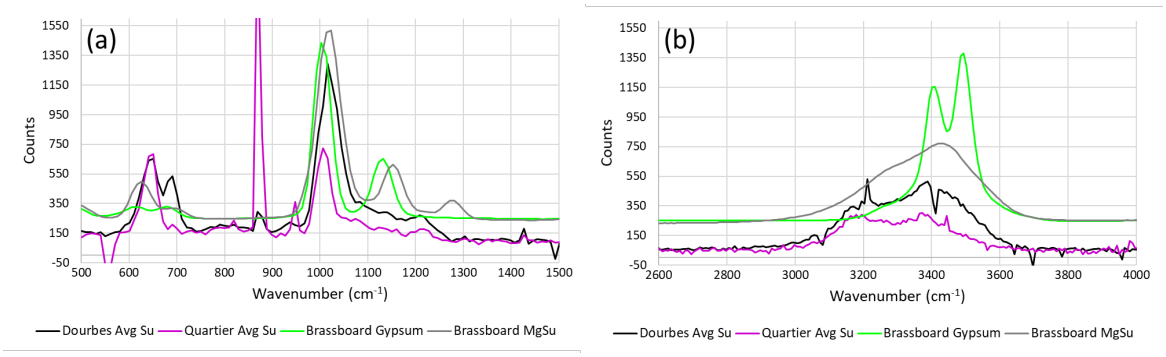

Figure S10. SHERLOC and analogue instrument spectra of sulfates in the (a) fingerprint and (b) hydrogen stretching spectral regions. (black) SHERLOC average spectrum of sulfate on 269 Dourbes Detail_500_1. (purple) SHERLOC average spectrum of sulfate on 293 Quartier HDR_500_1. (green) Brassboard spectrum of natural gypsum (WARDS #46–3798, from Tawas City, Michigan). (gray) Brassboard spectrum of synthetic magnesium sulfate (Macron Chemicals).

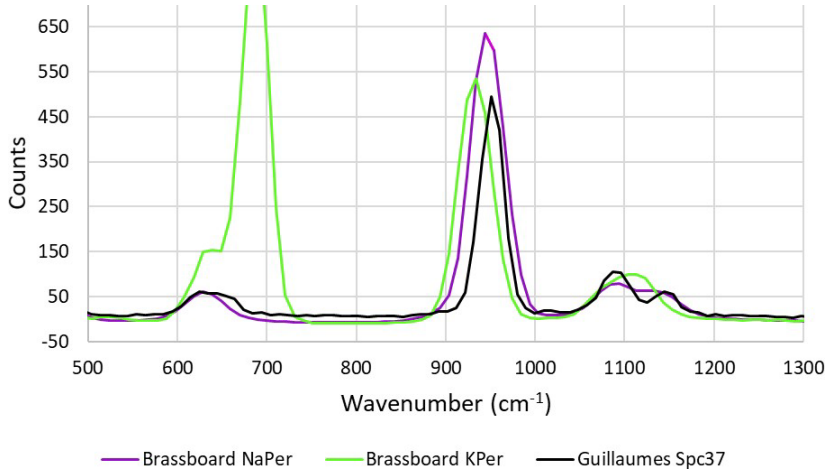

Figure S11. Spectra of perchlorates collected on SHERLOC and analogue instruments. (black) single intense spectrum of perchlorate observed in spectrum 37 of 0162_Guillaumes HDR_250_1, (green) spectrum of synthetic potassium perchlorate (Alfa Aesar A11296) collected on the brassboard, (purple) spectrum of synthetic sodium perchlorate monohydrate (Sigma Aldrich 310514) collected on the brassboard.

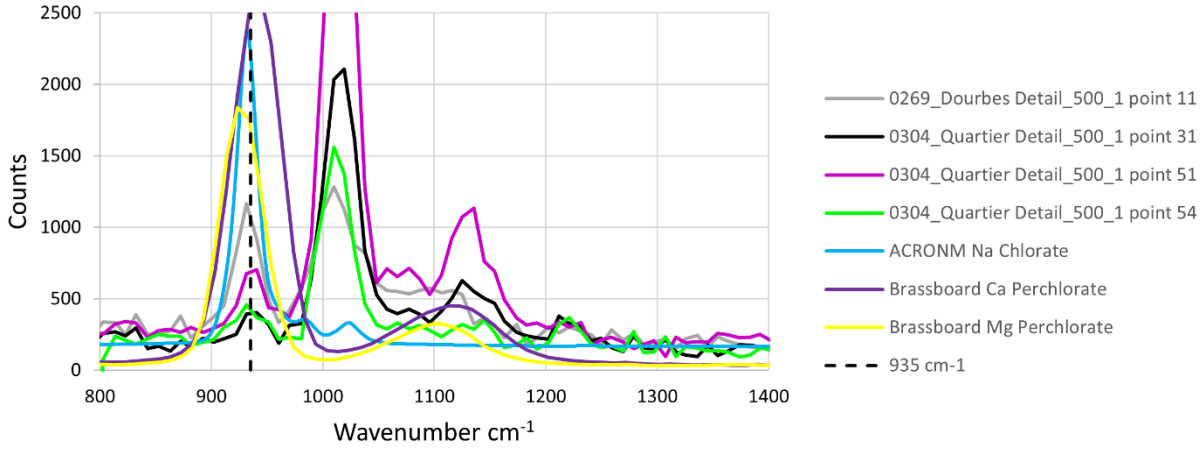

Figure S12. Spectra of perchlorates or chlorates collected on SHERLOC, Brassboard, and ACRONM. (gray) single spectrum of perchlorate/chlorate and sulfate observed in point 11 of 0269_Dourbes Detail_500_1, (black) single spectrum of perchlorate/chlorate and sulfate observed in point 31 of 0304_Quartier Detail_500_1, (magenta) single spectrum of perchlorate and sulfate observed in point 51 of 0304_Quartier Detail_500_1, (green) single spectrum of perchlorate and sulfate observed in point 54 of 0304_Quartier Detail_500_1, (blue) spectrum of sodium chlorate collected on ACRONM, (dark purple)

spectrum of calcium perchlorate collected on the brassboard, (yellow) spectrum of magnesium perchlorate collected on the brassboard. The dashed black line falls at 935 cm^{-1} for reference.